

**Studies on effect of chemical composition and  
microstructure on phase boundaries and physical and  
mechanical properties of dilute Zr-Nb alloys**

*By*

**R.V. Kulkarni**

**ENGG01200904030**

Bhabha Atomic Research Centre, Trombay, Mumbai

*A thesis submitted to the*

*Board of Studies in Engineering Sciences*

*In partial fulfillment of requirements*

*For the Degree of*

**DOCTOR OF PHILOSOPHY**

*of*

**HOMI BHABHA NATIONAL INSTITUTE**



**February 2016**

## Homi Bhabha National Institute

### Recommendations of the Viva Voce Board

As members of the Viva Voce Board, we certify that we have read the dissertation prepared by RAGHUVeer VIRUPAXRAO KULKARNI entitled “Studies on effect of chemical composition and microstructure on phase boundaries and physical and mechanical properties of dilute Zr-Nb alloys” and recommend that it may be accepted as fulfilling the dissertation requirement for the Degree of Doctor of Philosophy.

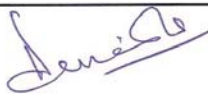
---

Chairman – Dr. Dinesh Srivastava

Date:

---

Guide / Convener – Dr. Dinesh Srivastava



Date: 15.2.16

---

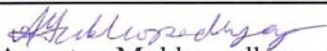
Co-Guide – Dr. G.K. Dey



Date: 15/2/16

---

Examiner – Prof. Amartya Mukhopadhyay, IIT Bombay



Date: 15/02/2016

---

Member 1 – Dr. Dr. K.B. Khan



Date:

---

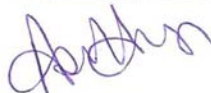
Member 2 – Dr. R.N. Singh



Date: 15.02.2016

---

Member 3- Dr. A. Arya



Date: 15/02/2016

---

Final approval and acceptance of this dissertation is contingent upon the candidate's submission of the final copies of the dissertation to HBNI. I hereby certify that I have read this dissertation prepared under my direction and recommend that it may be accepted as fulfilling the dissertation requirement.

Date: 15.2.16

Place: Mumbai

## **STATEMENT BY AUTHOR**

This dissertation has been submitted in partial fulfillment of requirements for an advanced degree at Homi Bhabha National Institute (HBNI) and is deposited in the Library to be made available to borrowers under rules of the HBNI.

Brief quotations from this dissertation are allowable without special permission, provided that accurate acknowledgement of source is made. Requests for permission for extended quotation from or reproduction of this manuscript in whole or in part may be granted by the Competent Authority of HBNI when in his or her judgment the proposed use of the material is in the interests of scholarship. In all other instances, however, permission must be obtained from the author.

R.V. Kulkarni

## **DECLARATION**

I, hereby declare that the investigation presented in the thesis has been carried out by me. The work is original and has not been submitted earlier as a whole or in part for a degree / diploma at this or any other Institution / University.

R.V. Kulkarni

*Dedicated to my parents*

*Late Shri. Virupaxrao Rangarao Kulkarni*

*Late Smt. Umabai Virupaxrao Kulkarni*

## ACKNOWLEDGEMENT

I express my deepest salutes and gratefulness to my guide Professor, D. Srivastava and co-guide Professor, G.K. Dey for their continuous supervision and guidance throughout the course of this study. Their advice about my shortcomings and appreciation about the achievements were highly encouraging without which I would not have made good learning and progress. During the years of this thesis, I was immensely benefited from their profound knowledge in the area of material science and structure-property correlations. I am thankful to Mr. K.V. Mani Krishna and Mr. S. Neogy of MSD, BARC, for their help in microstructure and microtexture measurements by electron microscopy. I would like to thank Dr. N. Saibaba and Mr. S.K. Jha of NFC, Hyderabad, India for providing the experimental materials and encouragement during the course of the study. I am also thankful to Mr. S. Anantharaman, Mr. E. Ramadasan and Dr. R. Kishore, Ex. Scientists of PIED, BARC for providing technical advice and encouragement throughout the study. I thank Mr. J.S. Dubey and Mr. R.S. Shrivastaw of PIED, BARC for helping me in carrying out all mechanical tests. I thank Mr. Sunil Kumar and Mr. B.N. Rath for helping me in measurements of texture of quite a number of Zr-2.5%Nb alloy samples used in the study. I thank Mr. M.S. Navage and Mr. J. Banerjee of RMD, BARC, Dr. J. Swaminathan and Mr. Bipin Das of NML of Jamshedpur for helping me in carrying out impression creep tests. Last but never the least, I am most thankful to Mr. Nirav Kumar who helped me in carrying out all the specimen preparations and experimental work. I would like to express special thanks to my daughter and wife and all relatives and friends for their constant encouragement and appreciation throughout the course of study. At the end I express my gratefulness to my institution, the Bhabha Atomic Research Centre, Trombay, Mumbai which provided me the opportunity to carry out this study.

<b>CONTENTS</b>		<b>Page No.</b>
<b>Synopsis</b>	.....	10
<b>Abstract</b>	.....	23
<b>List of Figures</b>	.....	26
<b>List of Tables</b>	.....	34
<b>CHAPTER 1: Introduction</b>		35
1.1 Objectives		39
1.2 Outline of thesis		39
<b>CHAPTER 2: Literature Review</b>		42
2.1 Zr-2.5%Nb pressure tubes in Pressurised Heavy Water Reactors (PHWRs)		42
2.1.1 Fabrication procedures of Zr-2.5%Nb pressure tubes		42
2.1.2 Parameters influencing phase transformation during manufacture of Zr-2.5%Nb pressure tubes		43
2.1.3 Microstructures of Zr-2.5%Nb pressure tubes		46
2.1.4 Crystallographic texture of Zr-2.5%Nb pressure tube		47
2.1.5 Chemical composition of Zr-Nb pressure tube alloy		49
2.2 Role of iron and oxygen concentrations on the properties of Zr-2.5%Nb alloy		49
2.2.1 Effect of iron and oxygen on $\beta/(\alpha+\beta)$ phase boundary of the alloy		49
2.2.2 CCT diagram for Zr-2.5%Nb alloy		52
2.2.3 Effect of iron and oxygen concentration and texture on in-reactor deformation behavior of Zr-2.5%Nb pressure tubes		54
2.3 Heat treatment and structure-property correlations		57
2.4 Thermal creep behavior of Zr-2.5%Nb pressure tube alloy		64
2.5 Inter-relationship of Coefficient of Thermal Expansion (CTE), Texture, 'Fe' and 'O' concentration in the Zr-2.5%Nb pressure tube alloy		67
2.6 Miniature specimen testing methods for evaluation of mechanical properties		70
<b>CHAPTER 3: Experimental Techniques and Procedures</b>		77
3.1 High Speed Quenching dilatometer (HSQD) and calibrations		77

3.1.1	Calibration of temperature measurement	79
3.1.2	Calibration of length change measurement	79
3.1.3	Evaluation of dilatometric curves for phase transformations and CCT diagram	81
3.1.4	Material and specimen preparation for determination of partial CCT diagram and heat treatments in the $\alpha+\beta$ phase field	82
3.1.5	Determination of partial CCT diagram for the Zr-2.5%Nb alloy	84
3.1.6	Heat treatments for microstructure and mechanical property correlation study	85
3.1.7	Determination of effect of 'Fe' and 'O' on $(\alpha+\beta)/\beta$ phase boundary of the alloy by dilatometry	85
3.1.8	Study on effect of 'Fe' and 'O' on the CTE and texture of Zr-2.5%Nb alloy	87
3.1.9	Heat treatment in the $(\alpha+\beta)$ phase field and compression testing	89
3.2	Heat treatment of bulk specimens for the study of correlation parameters for SPT and ABI	89
3.3	Automated Ball Indentation (ABI) test and Analysis of test data for mechanical property evaluation	92
3.4	Small Punch Test (SPT) and Analysis of test data for mechanical property evaluation	94
3.5	Specimen preparation for ABI and SPT	96
3.6	Electron Microscopy techniques for microstructural and microtextural study	97
3.7	Specimen preparation for microstructural and microtextural examination	97
3.8	Thermal creep study using miniature specimen testing techniques	98
3.8.1	Impression creep test for thermal creep study	99
3.8.2	Time dependent hot hardness tests for thermal creep study	101
3.9	Specimen preparation and texture measurements by X-ray diffraction method	102
<b>CHAPTER 4: Heat Treatment and Microstructural Evolution in the Zr-2.5%Nb Pressure Tube Material</b>		<b>108</b>
4.1	Objectives	108
4.2	Background	108
4.3	Determination of partial CCT diagram for Zr-2.5%Nb alloy	109
4.4	Heat treatments from the $(\alpha+\beta)$ phase field of Zr-2.5%Nb alloy	113

4.4.1	Dilatometric curves of ( $\alpha+\beta$ ) heat treatment experiments	113
4.5	Microstructural evolution in Zr-2.5%Nb alloy due to heat treatments	117
4.6	Texture evolution in Zr-2.5%Nb alloy due to heat treatments	124
4.7	Effect of cold working on texture modification of heat treated Zr-2.5% Nb alloy	125
4.7.1	Effect of cold deformation on texture evolution of ( $\alpha+\beta$ ) heat treated Zr-2.5%Nb alloy	126
4.8	Summary of the work	129
<b>CHAPTER 5: Determination of Correlation Parameters for Evaluation of Mechanical Properties by Small Punch Test and Automated Ball Indentation Test for Zr-2.5%Nb Pressure Tube Material</b>		133
5.1	Objectives	133
5.2	Background	133
5.3	Microstructures of heat treated specimens	134
5.4	Evaluation of Mechanical Properties of heat treated specimens	136
5.5	Determination of correlation parameters for ABI for evaluation of $\sigma_y$	148
5.6	Determination of correlation parameters for SPT for evaluation of $\sigma_y$ and $\sigma_{UTS}$	149
5.7	Discussion	149
5.8	Inter comparison of mechanical property data derived from tensile, ABI and SPT	152
5.9	Summary of the work	153
<b>CHAPTER 6: Mechanical Properties of Zr-2.5%Nb Pressure Tube Material Subjected to Heat Treatments in <math>\alpha+\beta</math> Phase Field</b>		156
6.1	Objectives	156
6.2	Background	156
6.3	Evaluation of mechanical properties of heat treated specimens by ABI and SPT	157
6.4	Discussion	166
6.4.1	Effect of cooling rates on microstructures and mechanical properties	168
6.4.2	Effect of soaking temperature on microstructures and mechanical properties	170
6.4.3	Effect of microstructural changes on the micro-hardness of heat treated Zr-2.5%Nb alloy sample	172

6.5	Summary of the work	174
<b>CHAPTER 7: Effect of Variation in Iron and Oxygen content on Phase Boundary, Physical and Mechanical Properties of Zr-2.5%Nb Pressure Tube Alloy</b>		177
7.1	Objectives	177
7.2	Effect of 'Fe' and 'O' contents on $(\alpha+\beta)/\beta$ transus temperature of the alloy	177
7.3	Effect of 'Fe' and 'O' on the thermal creep behavior of Zr-2.5%Nb alloy	184
7.3.1	Impression creep tests on the Zr-2.5%Nb alloy samples with varying 'Fe' contents	185
7.3.2	Hot hardness tests on the Zr-2.5%Nb alloy samples with varying 'O' contents	193
7.4	Effect of 'Fe' and 'O' on CTE and texture of Zr-2.5%Nb pressure tube alloy	201
7.4.1	CTE and texture measurements and microstructural examination	202
7.4.2	Effect of 'Fe' content on CTE and texture of Zr-2.5%Nb pressure tube alloy	213
7.4.3	Correlation of 'O' content with CTE and texture of Zr-2.5%Nb pressure tube alloy	215
7.4.4	Correlation of CTE and texture parameters	216
7.4.5	Inter-correlation of in-reactor axial creep rate, CTE, texture parameters, 'Fe' and 'O' contents in the alloy	216
7.5	Summary of the work	220
<b>CHAPTER 8: Conclusions</b>		226
<b>Future Work</b>		230

## SYNOPSIS

### Motivation and objectives of the studies

Zr-2.5% Nb alloy is presently being used as a pressure tube material in Pressurised Heavy Water Reactors (PHWRs) because of its higher strength, better creep and fracture strength in comparison to Zircaloy-2. During service, these pressure tubes undergo continuous dimensional changes mainly in the axial and circumferential directions due to the irradiation induced creep and growth. Therefore, satisfactory performance of a pressure tube is mainly dependent on its dimensional stability which is dictated by several of the metallurgical parameters such as microstructural features characterised by morphology, size and distribution of  $\alpha$  and  $\beta$  phases, crystallographic texture and dislocation density.

It has been reported that the heat treated Zr-2.5%Nb pressure tubes have shown superior performance in terms of creep rates which remained within the design criteria of the reactor (FUGEN type PWR reactor). Such superior creep rates must be attributed to the final microstructure and texture that resulted from heat treatments in the  $(\alpha+\beta)$  phase field of the alloy. In addition, earlier Post Irradiation Examination (PIE) studies on reactor operated Zr-2.5%Nb pressure tubes have indicated that, the elements, like iron and oxygen, have significant and advantageous influence on the in-reactor creep rates. These observations thus imply that, the control of metallurgical parameters through manufacturing schedules and selection of proper chemistry of the alloy are the key factors in evolving a superior creep resistant pressure tube material. Thus the thorough understanding of heat treatments on the Zr-2.5%Nb pressure tube alloy and the structure-property correlations in addition to the effect of important alloying elements, like iron and oxygen contents on the phase boundary, physical and mechanical properties gains significance.

It is well known fact that, increase in concentration of oxygen would raise the  $(\alpha+\beta)/\beta$  phase boundary of the Zr-Nb alloy, while iron would lower the same. Therefore, for a selected heat treatment temperature within the  $(\alpha+\beta)$  phase field, the fraction of  $\alpha$  and  $\beta$  phases would vary depending on the iron and oxygen contents of the alloy. This would influence the final microstructure of the alloy and hence would influence the short term as well as long term mechanical properties and also in-reactor deformation behaviour of the alloy.

The literature pertaining to heat treatments, microstructural and texture evolution and structure-property correlations of Zr-2.5%Nb alloy material [1] are discrete and also limited. Further, the literature pertaining to effects of iron and oxygen contents on the phase boundaries of Zr-Nb system is limited and also of qualitative in nature [2]. Literature on the subject domains of effect of iron and oxygen contents on the physical property such as Coefficient of Thermal Expansion (CTE), texture and the important mechanical property such as thermal creep of the Zr-2.5%Nb alloy have not been addressed adequately. Therefore the understanding in these subject domains is restricted. These gaps in the literature were the main motive behind the present studies. Hence in this thesis these issues have been dealt in two parts. One part is aimed to study microstructural and texture evolution in the Zr-2.5%Nb alloy due to various heat treatments and cold deformation followed by structure and property correlations. The other part is aimed to study the effects of iron and oxygen contents on the phase boundary, physical property such as CTE and texture and also the important mechanical property the thermal creep of the alloy material.

### **Summary of chapters**

The chapter-1 of the thesis introduces issues related with Zr-Nb alloy and effects of minor alloying elements iron and oxygen along with the objectives of the thesis. Chapter-2 deals with detailed literature review pertaining to heat treatments, structure and property correlations and the effect of iron and oxygen contents on the phase boundary, physical and mechanical properties of the alloy material. The chapter-3 describes different experimental techniques and procedures adopted in the study.

The chapter-4 discusses heat treatments and microstructural and texture evolution studies in addition to texture evolution of heat treated Zr-2.5%Nb alloy on cold deformation. To begin with the heat treatment studies, it was essential to have the accurate knowledge of  $\beta/(\alpha+\beta)$ -transus boundary for the selected Zr-2.5%Nb alloy for enabling selection of desired heat treatment temperatures within the  $(\alpha+\beta)$  phase field. Using a quenching dilatometer, a number of samples which were soaked at 1063°C in the  $\beta_{Zr}$  phase field of the alloy, were subjected to controlled cooling at different rates varying between 0.06°C/s and ~200°C/s.

The  $\beta \rightarrow \alpha + \beta$  start and end temperatures were determined for each cooling rate to establish the partial Continuous Cooling Transformation (CCT) diagram which is presented in the Fig. 1. The  $\beta \rightarrow \alpha + \beta$  start boundary in Fig.1 is the  $\beta$ -transus boundary for the alloy. Based on the highest  $\beta$ -transus temperature of 891°C established at the slowest cooling rate of 0.06°C/s, the heat treatment experiments were designed within the  $(\alpha + \beta)$  phase field and carried out using the quenching dilatometry technique. The microstructural evolution as a function of soaking temperatures and cooling rates has been studied on these samples using the transmission electron microscopy technique.

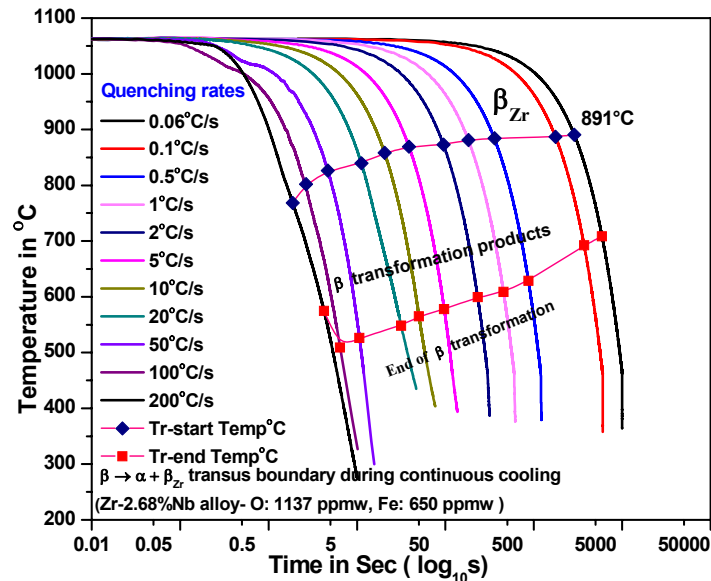


Fig.1: Partial CCT diagram for the Zr-2.5%Nb alloy

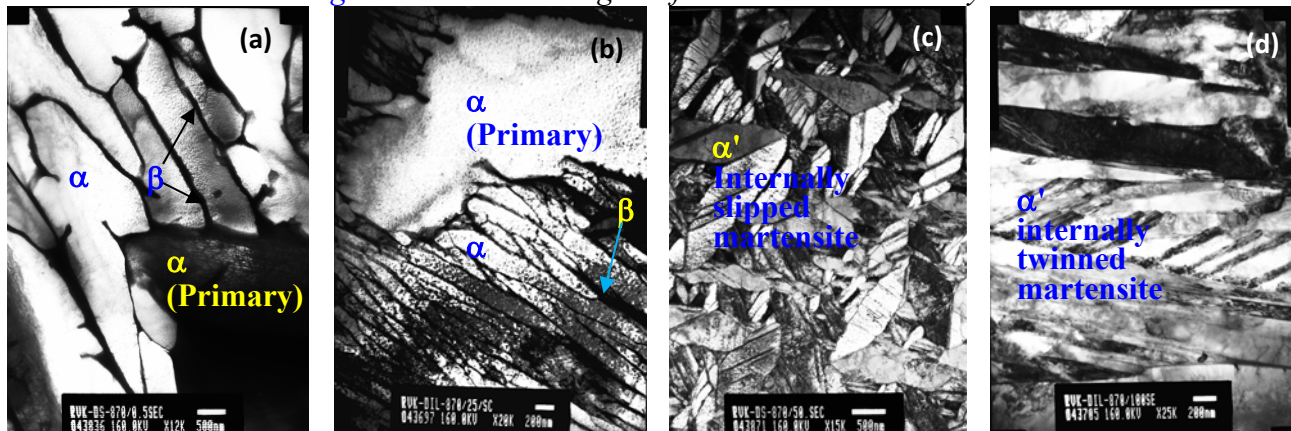


Fig.2 Microstructural evolution (heat treated in the  $\alpha + \beta$  phase field): (a) Widmanstätten  $\alpha$  (0.5°C/s), (b) Widmanstätten  $\alpha$  (25°C/s), (c) Martensitic structure (internally slipped) at (50°C/s) and (d) Martensitic structure (internally twinned) at (100°C/s)

Following are the important findings.

- (i) The microstructural study revealed that the small differences in soaking temperatures in the  $\alpha+\beta$  phase field were sufficient to produce distinct change in primary  $\alpha$  fractions attributing to sharp gradient in the solvus line of  $\alpha+\beta$  phase field in the Zr-Nb system.
- (ii) These experiments have shown that different cooling rates influenced the nature of  $\beta \rightarrow \alpha+\beta$  phase transformation that lead to martensitic or Widmanstätten type products. The morphology of Widmanstätten ' $\alpha$ ' progressively changed from being finer and straight to larger and irregular shaped as the cooling rates decreased (Fig.2 (a-b)).
- (iii) The samples quenched at 50°C/s and 100°C/s showed predominantly the martensitic products (Fig.2 (c-d)) along with the primary  $\alpha$ . At relatively slower quenching rates such as 50°C/s, internally slipped martensites were observed whereas at 100°C/s internally twinned martensites were the notable features. The martensite plates were seen to have formed in self accommodating morphologies that facilitate the formation of successive generation of martensitic plates through reduction in transformation strain energies [4].
- (iv) It was observed that decreasing the soaking temperature within the ( $\alpha+\beta$ ) phase field increased the probability of formation of martensite even at slower cooling rates such as 25°C/s which was attributed to increased 'Nb' content in the prior  $\beta_{Zr}$  phase. At lower soaking temperatures higher incidence of internally twinned martensite were observed due to the matrix ( $\beta_{Zr}$  phase) being stronger. In general, the Widmanstätten ' $\alpha$ ' plates became finer with the lowering of soaking temperatures attributing to increased heterogeneous nucleation sites due to finer structure of prior  $\beta$  grains. On the basis of these observations it was concluded that in order to obtain primary ' $\alpha$ ' and martensitic structures, a lower soaking temperature in the  $\alpha+\beta$  phase field followed by a minimum cooling rate of 25°C/s is required.
- (v) This chapter also deals with texture evolution study carried out using Electron Back Scattered Diffraction (EBSD) technique on few of the selected heat treated samples particularly those soaked at 883°C (closest to  $\beta$ -transus temperature of 891°C). The study revealed that quenching of samples with a rate of 50°C/s and 100°C/s, resulted in

considerable randomisation of the texture as indicated by nearly similar values of basal pole fractions ( $f_a$ ,  $f_r$ ,  $f_t$ ) in the three principal directions of the pressure tube. Such result could be attributed to the transformation of large number of randomly oriented fine  $\beta$  grains yielding various variants of martensitic ( $\alpha'$ ) plates which had Burgers' orientation relationship given by  $(0001)_\alpha // (110)_\beta$  and  $[2\bar{1}\bar{1}0]_\alpha // [111]_\beta$ . Texture analysis of the sample, cooled at 0.5°C/s, however, showed similar fraction of basal poles in the radial and circumferential directions ( $f_r$ ,  $f_t$ ) leaving axial component ( $f_a$ ) largely unaltered. This result can be attributed to the predominantly Widmanstätten nature of the transformation, coupled with relatively larger size of transformed  $\alpha$ , consequently fewer number of product grains (formed from the parent  $\beta$  grains). Hence, the degree of randomisation of texture was observed to be very low in this sample.

#### **Effect of cold deformation on texture evolution of ( $\alpha+\beta$ ) heat treated Zr-2.5%Nb alloy**

Further, the effect of cold deformation on texture evolution of the heat treated Zr-2.5%Nb alloy was studied using EBSD technique to understand the extent of texture modifications. For this purpose three of the samples soaked at 870°C and quenched at 25°C/s using quenching dilatometry, were subjected to cold working through compression testing at room temperature. The compression strains achieved in these samples were ~9.6%, ~12% and ~28.6%. It was observed that  $f_a$  value (*axial component of Kearn's texture parameters*) for ~9.6% and 12% of cold worked samples was nearly unaffected in comparison to the as heat treated condition and the starting material. This is similar to the observation in the previous study by Cheadle *et al.* [5]. With the increase in compression strain to ~28.6%, the modification in the texture was clearly evident through the increased values of  $f_a$ . Such texture modification may be attributed to the rotation of  $\alpha_{Zr}$  crystals towards the direction of compression axis and is in agreement with previous study by Cheadle *et al.* [5].

The chapter-5 deals with the determination of correlation parameters for evaluation of mechanical properties of anisotropic Zr-2.5%Nb alloy by Small Punch Test (SPT) and Automated Ball Indentation (ABI) test. These techniques were specifically chosen in the present study as these were suited for mechanical property characterisation of small size heat treated

dilatometry specimens. Since, both SPT and ABI are the non-conventional miniature specimen testing techniques, they required establishment of correlation parameters. The correlation parameters are specific to the technique and also specific to each class of materials and hence were required to be established experimentally for the Zr-2.5%Nb alloy. The literature in this subject domain has dealt with relatively isotropic materials like steels [6, 7]. There is no literature available which has dealt with the Zr-base alloys and in particular the issues of mechanical property characterisation of anisotropic materials like Zr-2.5%Nb alloy. Therefore, this part of the work bears importance as the correlation parameters established for these two techniques would provide direction specific mechanical properties of Zr-2.5%Nb alloy. This part of the work was necessary for characterising the mechanical properties of ( $\alpha+\beta$ ) phase heat treated Zr-2.5%Nb alloy samples referred in chapter-4.

As per the recommended procedures in the literature, the tensile specimens of dimensions conforming to ASTM E8 were extracted both from axial and circumferential directions of the Zr-2.5%Nb pressure tube spool piece. Five sets of these tensile specimens along with few bulk pieces were subjected to soaking at 880°C for 30 min (within the  $\alpha+\beta$  phase field of the alloy) followed by cooling to room temperature at different selected rates between 0.15°C/s and ~150°C/s using specially developed gas quenching system. One of the sets of these samples was subjected to water quenching as well.

These heat treated bulk specimens were subjected to SPT and ABI tests at room temperature for the two loading directions (axial and circumferential) adopting recommended procedures. It was noted that, in the case of SPT the yield and ultimate tensile strength representing values such as ( $P_y/t_0^2$ ) and ( $P_m/t_0^2$ ) for the axial loading condition were higher compared to the circumferential loading for the identical heat treated conditions. However, unlike the case of SPT, the conventional tensile tests and ABI tests exhibited higher strength values for the circumferential direction loading compared with axial direction for all the heat treated conditions. This observation was rationalised on the basis of disc specimen orientation experiencing relative texture effects in the two loading directions. Therefore, in the case of SPT, the strength representing values ( $P_y/t_0^2$ ) and ( $P_m/t_0^2$ ) obtained for the axial loading condition were correlated with the circumferential direction tensile strength data of same heat treated conditions and vice a

versa and linear relationships were established through regression analysis. In the case of ABI the yield strength representing value (*yield parameter A*) established for the axial and circumferential direction loading conditions were correlated with the tensile yield strength data for the same direction and the linear correlations were established through regression analysis. The experimentally established linear correlations for the determination of yield strength ( $\sigma_y$ ) and ultimate tensile strength ( $\sigma_{UTS}$ ) by SPT and ABI for the two directions of loading are presented in [Table-1](#) below.

**Table-1:** Correlation coefficients for the determination of mechanical properties by SPT and ABI

Linear correlations	Regression coefficient: ( $R^2$ )
$\sigma_{y(Ax)ABI} = -505.929 + 0.501 \times A_{(Ax)}$ (ABI axial loading)	0.962
$\sigma_{y(cir)ABI} = -436.89 + 0.498 \times A_{(cir)}$ (ABI-circumferential loading)	0.975
$\sigma_{y(cir)SPT} = 258.703 + 3.174 \times [P_y/t_0^2]_{Ax}$ (SPT-axial loading)	0.936
$\sigma_{UTS(cir)SPT} = -238.532 + 1.969 \times [P_m/t_0^2]_{Ax}$ (SPT-axial loading)	0.825
$\sigma_{y(Ax)SPT} = -221.352 + 5.901 \times [P_y/t_0^2]_{cir}$ (SPT-circumferential loading)	0.990
$\sigma_{UTS(Ax)SPT} = -796.518 + 3.365 \times [P_m/t_0^2]_{cir}$ (SPT-circumferential loading)	0.816

In chapter-6 the structure and mechanical property correlations of the ( $\alpha+\beta$ ) phase field heat treated Zr-2.5%Nb alloy has been discussed. The direction specific correlation parameters established in chapter-5 for SPT and ABI were used for characterisation of mechanical properties of these samples. Since all the heat treated dilatometry samples were extracted from axial direction of the pressure tube, the loading condition in both SPT and ABI tests was axial. Therefore, in the case of SPT the mechanical properties established for axial loading condition represented circumferential direction mechanical properties unlike the case of ABI testing which represented axial direction mechanical properties.

The results by SPT and ABI showed ([Fig.3 \(a\)](#) and [\(b\)](#)) increasing trend in mechanical properties with the cooling rates increasing from 0.5°C/s to 25°C/s which can be attributed to finer morphologies of transformed  $\alpha$  and  $\beta$  phases providing resistance to the deformation. The specimens with predominantly martensitic structures obtained at cooling rates 50 and 100°C/s showed higher strength values both by SPT and ABI, which can be attributed to solute

strengthening effect by supersaturated  $\alpha'$  (*martensite*), high dislocation density caused by rapid quenching in addition to increased barriers due to fine structure.

On the other hand, as the soaking temperature was increased from 840°C to 883°C, the SPT-derived mechanical properties showed an apparent decreasing trend, which is an expected result due to finer structure obtained at lower soaking temperatures. Whereas, the ABI derived strength values for the same conditions remained nearly unaffected, which may be attributed to averaging effect due to spherical indenter. The higher strength values observed at lower soaking temperatures in the case of SPT was mainly attributed to the solute strengthening effect due to ‘Nb’ enrichment of the  $\alpha$  and  $\beta$  phases, in addition to fineness of lamellar  $\alpha$  and  $\beta$  structure and martensitic structure obtained even at slower cooling rates. In order to verify the results obtained by ABI, the Brinell Hardness Number (BHN) obtained during ABI tests were correlated with the VHN values determined for the same sample conditions. The similar trends in hardness results by these two methods validated the measurements by ABI. This work has established that both ABI and SPT are sensitive to microstructural changes in the Zr-2.5%Nb alloy.

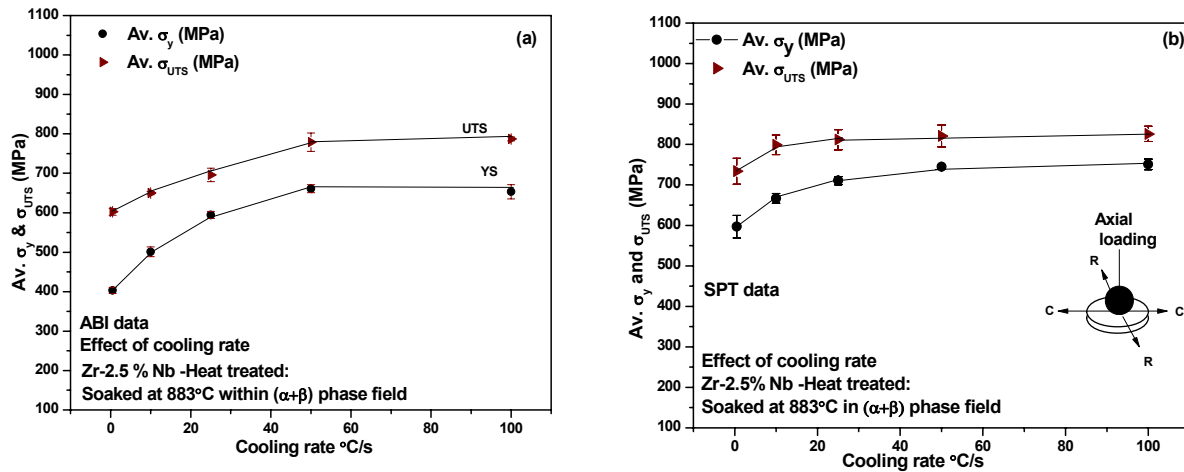


Fig.3 Mechanical properties of  $(\alpha+\beta)$  heat treated Zr-2.5%Nb alloy samples for one of the heat treatment condition, soaked at 883°C and cooled at different rates (a) by ABI, (b) by SPT

The chapter-7 deals with the effect of variation in iron and oxygen content (*within the specification range*) on the phase boundary, physical and mechanical properties of the Zr-2.5%Nb alloy. To study the effect of these elements on the  $(\alpha+\beta)/\beta$  phase boundary of the alloy, two sets Zr-2.5%Nb alloy samples having independent variation in iron and oxygen contents were selected and subjected to dilatometric scans in a linear temperature program up to 1063°C.

The  $\Delta l$  vs. *time* plots recorded for these samples for the heating cycle were analysed for  $(\alpha+\beta)/\beta$  transformation temperatures ( $T_\beta$ ). The results showed negative slope for the  $T_\beta$  vs. iron content linear fit which indicated a decrease in  $T_\beta$  by  $\sim 4^\circ\text{C}/100$  ppmw increase of ‘Fe’ attributing to its  $\beta$ -phase stabilising effect (see eq. (1)). Similarly, for oxygen variation set of samples a linear fit of  $T_\beta$  vs. oxygen content showed positive slope which indicated an increase in  $T_\beta$  by  $\sim 14^\circ\text{C}/100$  ppmw of oxygen which can be attributed to  $\alpha$ -phase stabilising effect (see eq. (2)). From eq.(1),  $T_\beta$  for an alloy with 650 ppmw of ‘Fe’ and 930 ppmw of ‘O’ would be  $867^\circ\text{C}$ . If the oxygen content is increased from 930 to 1137 ppmw, then according to eq.(2),  $T_\beta$  would increase by  $27^\circ\text{C}$ , i.e.  $T_\beta=(867^\circ\text{C}+27^\circ\text{C})=894^\circ\text{C}$  which is close to  $891^\circ\text{C}$  established for the alloy with 1137 ppmw of ‘O’ and 650 ppmw of ‘Fe’.

$$T_{(\alpha+\beta)/\beta} = T_\beta = (893.97 - \text{Fe}_{\text{ppmw}} \times 0.041) \text{ } ^\circ\text{C} \quad (R^2 = 0.84) \quad (1)$$

$$T_{(\alpha+\beta)/\beta} = T_\beta = (735.12 + \text{O}_{\text{ppmw}} \times 0.135) \text{ } ^\circ\text{C} \quad (R^2 = 0.93) \quad (2)$$

The effect of independent variation of ‘Fe’ and ‘O’ on the thermal creep behaviour of the as fabricated Zr-2.5%Nb pressure tube samples was studied at temperatures close to the reactor operation to understand the deformation behaviour of the alloy during service. For studying the effect of independent variation in ‘Fe’ content on thermal creep behavior, three Zr-2.5%Nb pressure tube alloy samples with iron content 165, 472 and 1566 ppmw were selected. These samples were subjected to impression creep tests at  $400^\circ\text{C}$  and 400 MPa punching stress using a flat punch of diameter 1.5 mm. The specimen loading condition was circumferential with respect to pressure tube axis. The literature [8] indicated that the test conditions selected belonged to the region dominated by dislocation climb plus glide mechanism of creep. The slope of impression creep strain vs. time plots (Fig. 4 (a)) for the three samples studied, showed decreasing steady state impression creep rates with the increase in ‘Fe’ content. Although ‘Fe’ is mainly associated with  $\beta_{\text{Zr}}$  phase of the dual phase Zr-2.5%Nb alloy, the increase in ‘Fe’ content in the alloy may be increasing the ‘Fe’ content of  $\alpha_{\text{Zr}}$  phase limiting to terminal solid solubility. Therefore, the observed decreasing trend in steady state creep rate can be attributed to solute strengthening of dominant  $\alpha_{\text{Zr}}$  phase by the interstitial ‘Fe’ content, in addition to strengthening of  $\beta_{\text{Zr}}$  phase.

The effect of oxygen content on the thermal creep behavior of the pressure tube alloy was studied using a high temperature Vicker's micro-hardness testing system (*indentation technique*). The oxygen content in the selected pressure tube samples had variation from 743 ppmw to 1587 ppmw. The time dependent hot hardness tests were performed at 300 and 400°C under vacuum with the indentation load of 500g and dwell time varying from 10 to 800s maximum during the test. The increase in diagonal i.e. the decrease in hardness as a function of time at a given test temperature is regarded as the measure of thermal creep of the alloy. The results of hardness verses dwell time of the indenter for the three samples are presented in the typical  $\ln(H)$  vs.  $\ln(t)$  plot in Fig. 4 (b). The results clearly showed higher hardness values for the higher oxygen content sample at all dwell times and also at both the test temperatures 300°C and 400°C which can be attributed to increased solute strengthening effect by the interstitial oxygen. The relative increase in slope of the linear fit of  $\ln(H)$  vs.  $\ln(t)$  at 400°C as compared with 300°C for a given sample can be attributed to increased recovery processes at 400°C. Thus, the study has shown that both iron and oxygen contents improved the thermal creep resistance of the alloy.

To study the effect of independent variation of iron and oxygen contents on the Coefficient of Thermal Expansion (CTE) and the texture parameters, two sets of pressure tube samples were selected. It was observed that the measured axial direction CTE and the texture parameter  $f_a$  values showed increasing trend with iron content (Fig.5 (a) and (b)) while circumferential direction CTE and the  $f_t$  values showed the opposite trend. These distinct trends in the CTE and texture parameters can be related to the influence of 'Fe' on the deformation mechanism of the  $\alpha_{Zr}$  phase of the alloy. As discussed earlier, the increase in 'Fe' content of the alloy would increase 'Fe' content of  $\alpha_{Zr}$  phase as well. This might decrease the stacking fault energy of the dominant  $\alpha_{Zr}$  phase similar to the case of addition of Al (*substitutional*) to  $\alpha$ -Ti [9, 10]. During the thermomechanical treatments due to decreased stacking fault energies the twinning ability of the alloy might be increasing [11] resulting in considerable rotation of  $\alpha_{Zr}$  crystals producing in texture modifications. As a result  $f_a$  values might be correlating with 'Fe' content with an increasing trend (Fig.5 (b)) and hence the axial CTE is also exhibiting same trend with 'Fe' content (Fig. 5 (a)) because CTE correlates with texture linearly as shown in Fig.5 (c). It was also observed that the in-reactor axial creep rates of the operating pressure tubes corresponding

to the samples studied for CTE and texture exhibited a good correlation with a decreasing trend with 'Fe' content increasing.

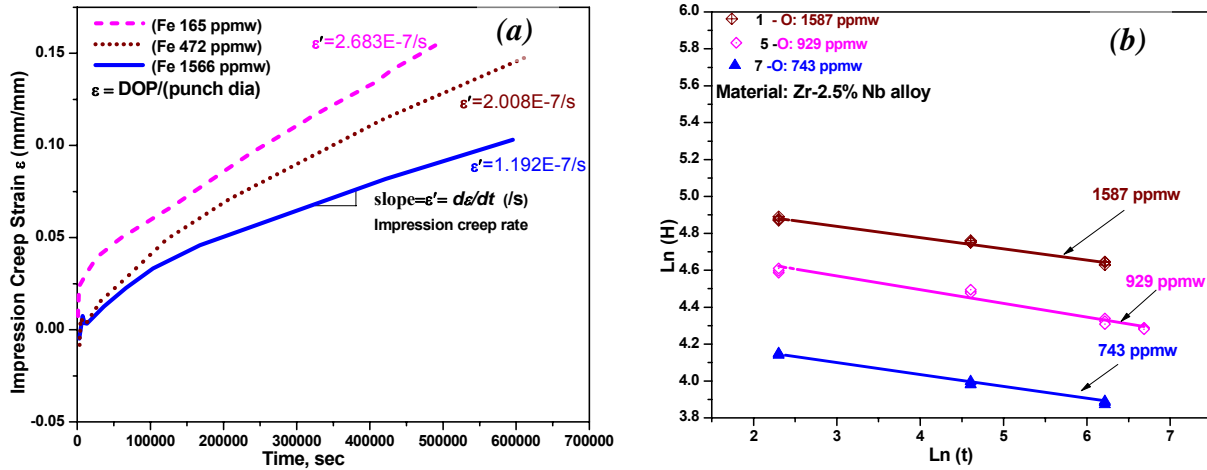


Fig. 4 (a) Effect of 'Fe' content on Impression creep behaviour (Creep stain ( $\epsilon$ ) vs. time curves, (b) Effect of oxygen on time dependent Vicker's hardness behaviour at 400°C

The inter correlation study showed that increasing 'Fe' content increased the  $f_a$  values and the corresponding CTE values and decreased the in-reactor axial creep rates. A good correlation of in-reactor axial creep rate with axial CTE in Fig.5 (d) and the linear correlation established between CTE and texture parameters in Fig.5 (c) in the present study indicated that CTE is sensitive to texture changes and can provide indications about the performance of the pressure tube. Therefore CTE can be used as surrogate parameter for texture. The effect of oxygen variation on the CTE and texture was studied in the similar way. The study showed that oxygen variation in the alloy showed no definite correlation with CTE, texture and also with in-reactor axial creep rates for the corresponding operating tubes. The reason could be, increased oxygen content in the alloy would increase its concentration in the  $\alpha_{Zr}$  phase (*octahedral sites*) and can reduce twinning ability of the  $\alpha_{Zr}$  phase and hence the texture modification, similar to the one observed in the case of  $\alpha$ -Ti alloys [9]. It was also observed that although 'Fe' content in the oxygen variation set of samples varied in a small range, the CTE data correlated with 'Fe' content, although with a relatively higher scatter, indicating that effect of oxygen on the texture and hence CTE is insignificant compared to the effect of 'Fe' content. The complete study has established that the effect of iron and oxygen on the mechanical properties of the alloy was distinct and also significant, while the effect of oxygen on the physical property, CTE was

insignificant, whereas the effect of iron was distinct and considerable. The chapter-8 finally summarises the conclusions of the complete thesis.

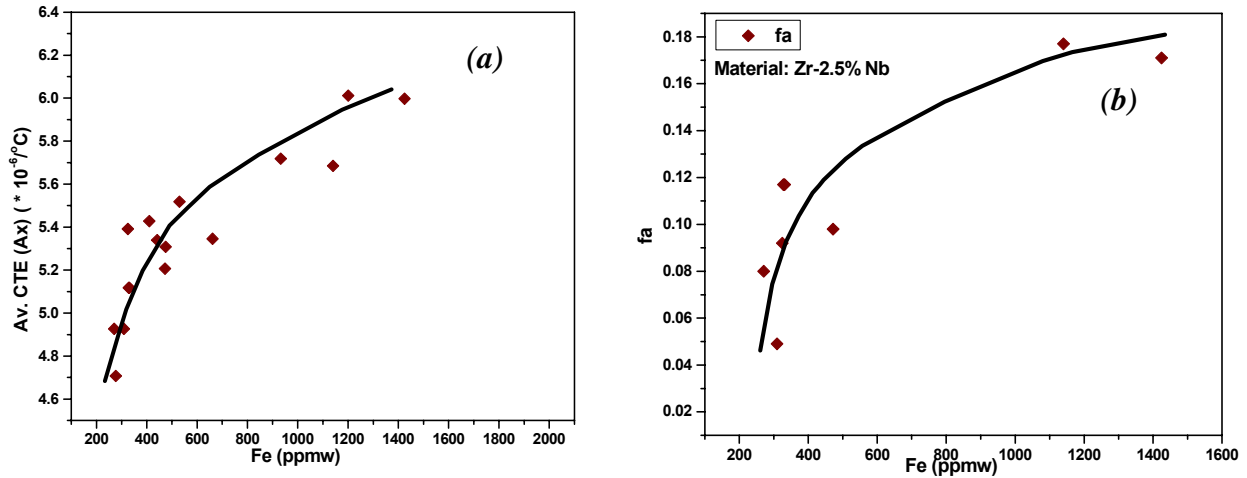


Fig.5(a) Effect of 'Fe' content on (a) Axial direction CTE, (b) Axial texture parameter ( $f_a$ )

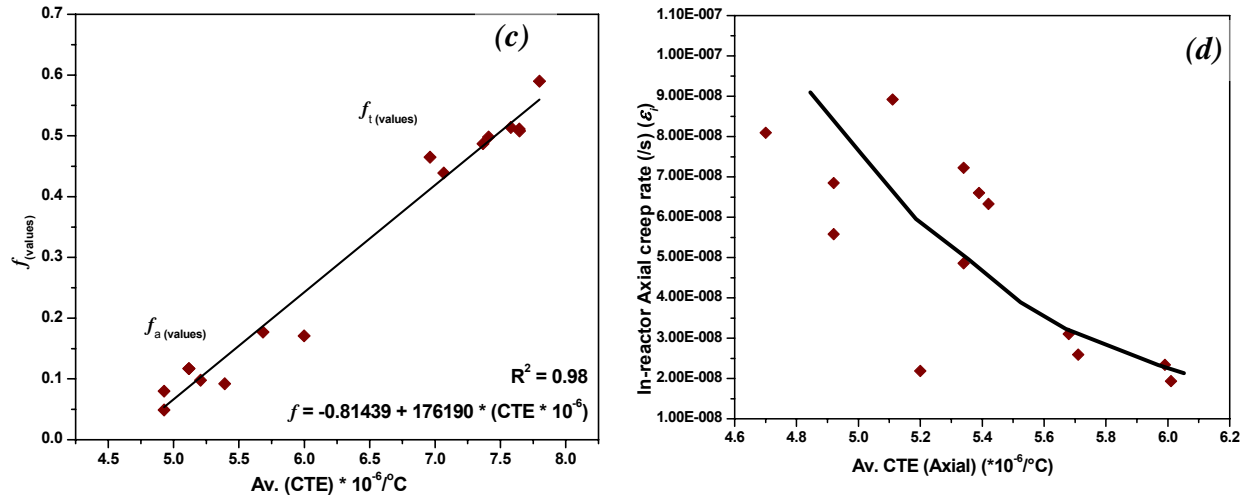


Fig.5(c) (Correlation of texture parameters  $f_a$  and  $f_t$  values with CTE , (d) Correlation of in-reactor axial creep rate ( $\dot{\epsilon}_i$ ) with their axial CTE

## References

1. R. Tewari, D. Srivastava, G.K. Dey, J.K. Chakravarty, S. Banerjee, *J. Nucl. Mater.*, 383 (2008)153-171
2. V. Fidleris, *J. Nucl. Mater.*, 54 (1974)199-211
3. E. Lee, Dissertation for PhD, The Ohio State University 2004, Document number, *osu1092756139*

4. D. Srivastava, PhD Thesis “ $\beta$ -phase transformation in dilute Zr-Nb alloys”, IISc, Bangalore, India (1996)
5. B. A. Cheadle, C. E. Ells, W. Evans, *J. Nucl. Mater* 23 (1967) 199-268
6. F.M. Haggag, “Nondestructive Determination of Yield Strength and Stress-Strain Curves of In-Service Transmission Pipelines Using Innovative Stress-Strain Microprobe Technology” Report No. ATC/DOT/990901, (1999)
7. X. Mao, H. Takahashi, *J. Nucl. Mater.*, 150 (1987) 42-52
8. K. L. Murty, J. Ravi, Wiratmo, *Nucl. Eng. Des.*, 156 (1995) 359- 371
9. C.J. Cochrane, PhD Thesis “Effect of Process Parameters on Deformation of Zr-2.5wt%Nb Alloy”, Department of Mechanical and Materials Engineering, Queen's University Kingston, Ontario, Canada, October 2013
10. R.W. Hayes, G.B. Viswanathan, M.J. Mills, *Acta Mater.*, 50 (2002) 4953-4963
11. C. Wang, H.Y. Zhang, H.Y. Wang G. J. Liu, Q.C. Jiang, *Scripta. Mater.*, 69 (2013) 445-448

**Publications in Referred Journals from This Work:**

1. R.V. Kulkarni, S. Neogy, B.N. Rath, K.V. Mani Krishna, D. Srivastava, N. Saibaba, I. Samajdar, E. Ramadasan, G.K. Dey, S. Anantharaman, DOI 10.1007/s12666-011-01047, *Trans Indian Inst. Met.* 64, Issue 4-5 (2011) 395-399
2. R.V. Kulkarni, K.V. Mani Krishna, S. Neogy, D. Srivastava, E. Ramadasan, G.K. Dey, N. Saibaba, S.K. Jha, R.S. Shriwastaw, S. Anantharaman, *Nucl.Eng.Des.*265(2013)1101- 1112
3. R.V. Kulkarni, K.V. Mani Krishna, S. Neogy, D. Srivastava, E. Ramadasan, R.S. Shriwastaw, B.N. Rath, N. Saibaba, S.K. Jha, G.K. Dey, *J Nucl. Mater.*,451 (2014)300-312

**Manuscripts prepared for publication**

1. “Effect of Variation in Iron and Oxygen Contents on the Thermal Expansion and Texture of the Zr-2.5%Nb pressure tube Alloy”
2. “Effect of variation in iron and oxygen contents on the thermal creep behaviour of the Zr-2.5%Nb pressure tube alloy”

Signature of Student:  
Date: 15<sup>th</sup> February, 2016

## ABSTRACT

During service, the Zr-2.5%Nb alloy pressure tubes in PHWRs undergo anisotropic dimensional changes mainly in the axial and circumferential directions due to irradiation induced creep and growth along with relatively small contribution from thermal creep. Such dimensional instability limits the service life of the pressure tubes. However, it has been observed that Zr-2.5%Nb pressure tubes in the heat treated condition have shown superior dimensional stability attributing to microstructure, texture and also the mechanical properties. In addition, it is also observed that the chemical composition particularly the iron and oxygen contents in the pressure tube alloy have shown advantageous influence on the in-reactor creep rates. Therefore, the complete study has been addressed in two parts, one part dealing with structure and property correlations and the other part dealing with effect of 'Fe' and 'O' contents on the phase boundary, physical and mechanical properties.

The Zr-2.5%Nb pressure tube material is a ( $\alpha+\beta$ ) dual phase alloy that can be used with variety of microstructures through controlled heat treatments. The concentrations of iron and oxygen are known to influence the ( $\alpha+\beta$ )/ $\beta$  phase boundary of the Zr-2.5%Nb alloy, which is important from the view point of design of suitable heat treatments to obtain desired structure and properties in the alloy. Secondly, the presence of these elements in the  $\alpha$  and  $\beta$  phases are also expected to influence the important physical property CTE and hence the texture. Thus, measured CTE in a certain direction can provide good indications about the effect of these minor alloying elements on texture and hence the in-reactor performance of the pressure tube. Further, the presence of these elements in  $\alpha$  and  $\beta$  phases is also expected to influence the thermal creep behavior which is important to improve the understanding of in-reactor creep behavior of the alloy, because these mechanisms are closely related.

The literature review has indicated that structure-property correlation study on the Zr-2.5%Nb alloy is discrete and also limited. The literature pertaining to the effect of independent variations in iron and oxygen concentrations on the phase boundary, CTE, texture and the thermal creep behaviour have not been addressed adequately. This has significantly restricted the understanding in these subject domains which was the main motive behind this study.

The extensive work reported in this thesis provides a valuable resource for understanding the microstructural and texture evolution in the Zr-2.5%Nb pressure tube alloy due to various heat treatments and the structure-property correlations, in addition to the influence of 'Fe' and 'O' contents on the phase boundary, physical and mechanical properties of the alloy.

To begin with, the partial Continuous Cooling Transformation (CCT) diagram was established to demark the  $\beta/(\alpha+\beta)$  transus boundary for the selected Zr-2.5%Nb alloy. Based on the highest  $\beta$ -transus temperature of 891°C established for the slowest cooling rate of 0.06°C/s, a systematic heat treatment study consisting of cooling the samples at different rates from different soaking temperatures within the  $(\alpha+\beta)$  phase field of the alloy was carried out using quenching dilatometry. The microstructural examination of these samples by TEM revealed that, for a given soaking temperature, morphology of Widmanstätten  $\alpha$  changed from finer and straight lamellae to wider and irregular shape as the cooling rate decreased from 25°C/s. For quenching rates 50°C/s and 100°C/s the microstructure was predominantly martensite along with primary  $\alpha$ . It was also observed that for a given cooling rate, the probability of martensite formation increased with decreasing soaking temperatures. The microtextural examination using EBSD on the samples soaked (883°C) close to  $\beta$ -transus temperature revealed that, texture tended to randomise at higher cooling rates such as 50°C/s and 100°C/s attributing to large number of randomly oriented fine  $\beta$  grains transforming to martensites with randomly oriented variants. Whereas, little change was seen at lower cooling rates, attributing mainly to Widmanstätten nature of structure and fewer  $\beta$  grains undergoing the transformation. To simulate the cold working of the pressure tubes during manufacturing, the samples heat treated at 870°C and cooled at 25°C/s were subjected to compression testing (in the axial direction of the PT). The textural evolution study using EBSD technique on these samples showed that the axial component of texture parameter ( $f_a$ ) increased with amount of CW increasing up to 28.6%. This is an important result considering thermomechanical treatments of the heat treated pressure tube. For studying evolution of mechanical properties of these small size heat treated dilatometry specimens, two miniature specimen testing techniques namely ABI and SPT were adopted. Since, both ABI and SPT are non-conventional techniques, initially the correlations were established adopting recommended procedures for evaluation of basic mechanical properties

such as yield strength and ultimate tensile strength. The study revealed that these established correlation parameters are specific to the technique and also to the class of materials i.e. Zr-2.5%Nb alloy. More importantly, since, Zr-2.5%Nb is an anisotropic material due to texture, special emphasis was given to establish direction specific correlations for the purpose of evaluation of direction specific mechanical properties in the present study.

Using these direction specific correlations for both ABI and SPT, the room temperature mechanical properties of the heat treated dilatometry samples was carried out. The subsequent structure-property correlation study addressed the issues of effect of cooling rates and effect of soaking temperatures on the morphologies of the transformed products and the corresponding change in mechanical properties.

The effect of independent variation of 'Fe' and 'O' contents on the  $(\alpha+\beta)/\beta$  phase boundary and the physical property CTE of the Zr-2.5%Nb alloy was studied using the dilatometry technique. The study showed that the temperature corresponding to  $(\alpha+\beta)/\beta$  phase boundary for the alloy increased at a rate of 13.5°C/100 ppmw of oxygen and decreased at a rate of 4°C/100 ppmw of 'Fe' content. This is an important result considering design of thermomechanical treatments of the alloy during the manufacture of pressure tube. The study of interrelationship of 'Fe' and 'O' concentrations on the CTE and bulk texture showed that increasing amounts of 'Fe' content up to around 1500 ppmw decreased the circumferential CTE and  $f_t$  values with a corresponding increase in axial CTE and  $f_a$  values, whereas no specific trend was observed as a function of 'O' content in the alloy. These results have been discussed in relation with deformation mechanisms as a function of Fe and O contents. This is another important result considering in-reactor performance evaluation of the alloy. Similarly, the effect of these elements on the thermal creep behavior of the alloy has been studied using miniature techniques such as impression creep tests and indentation creep tests. The study has revealed that both 'Fe' and 'O' contents have advantageous effect of the creep behavior. The probable mechanisms involved have been discussed to explain the observed creep resistant behavior as a function of 'Fe' and 'O' contents in the alloy. The large sets of experimental results in this thesis provide wide database to develop improved models for the assessment and prediction of performance operating pressure tubes.

<b>List of Figures</b>	<b>Page No.</b>
<a href="#">Fig.1</a> A schematic simplified view of PHWR core showing coolant channel assemblies	35
<a href="#">Fig.2.1</a> Simplified fabrication flow sheet adopted for manufacture of cold worked pressure tubes at Nuclear Fuel Complex (NFC), Hyderabad, India <a href="#">[7]</a>	43
<a href="#">Fig.2.2</a> Simplified fabrication flow sheet adopted for manufacture of cold worked / heat treated pressure tubes for RBMK <a href="#">[8]</a>	44
<a href="#">Fig. 2.3</a> Zirconium - Niobium Phase diagram	45
<a href="#">Fig.2.4</a> TEM microstructure of pressure tube <a href="#">(a)</a> after 1 <sup>st</sup> hot extrusion stages, <a href="#">(b)</a> after 2 <sup>nd</sup> hot extrusion stage	46
<a href="#">Fig.2.5 (a)</a> A schematic of typical distribution of fraction of basal poles of $\alpha_{Zr}$ crystals along three principal directions of the pressure tube <a href="#">(b)</a> typical (0002) pole figures for the Zr-2.5%Nb pressure tube with majority of basal poles in radial–transverse plane, <a href="#">[15]</a> <a href="#">(c)</a> (11 $\bar{2}$ 0) pole figure showing majority of prism poles in the radial- transverse plane. <a href="#">[15]</a>	48
<a href="#">Fig. 2.6 (a)</a> $\beta/(\alpha+\beta)$ transformation temperatures for zirconium-niobium alloys of differing oxygen concentrations ( <i>measured and calculated</i> ) <a href="#">[35]</a> , <a href="#">(b)</a> Phase boundary determination of dilute Zr–xNb alloys containing 1400 ppmw O and 700 ppmw ‘Fe’ <a href="#">[39]</a>	50
<a href="#">Fig. 2.7</a> Effect of oxygen on $(\alpha+\beta)/\beta$ phase boundary of zirconium-rich Zr-Nb alloys <a href="#">[59]</a>	51
<a href="#">Fig.2.8</a> Isothermal sections at the Zr-rich corner of the ternary Zr-Nb-Fe system, showing the tie-line construction used to determine the equilibrium concentrations of ‘Nb’ and ‘Fe’ in the $\alpha+\beta$ phase field at <a href="#">(a)</a> 873 K, <a href="#">(b)</a> 923 K <a href="#">[41]</a>	51
<a href="#">Fig. 2.9</a> CCT diagram for Zr-2.4%Nb alloy containing 1440 ppmw of oxygen <a href="#">[53]</a>	53
<a href="#">Fig.2.10 (a)</a> Correlation of elongation rate of cold worked Zr-2.5%Nb pressure tubes in CANDU reactor as a function of ingot iron analysis, <a href="#">(b)</a> Effect of ‘Fe’ on axial growth strain of Zr-2.5%Nb pressure tube material at fluence of $(1 \times 10^{26} \text{ n m}^{-2} > 1\text{MeV})$ , <a href="#">(c)</a> Correlation of elongation rate of cold worked Zr-2.5%Nb pressure tubes in CANDU reactor as a function of ingot oxygen analysis of two reactors <a href="#">[46]</a>	56
<a href="#">Fig.2.11</a> Various morphologies of martensite, <a href="#">(a)</a> and <a href="#">(b)</a> Massive martensite formed on quenching iodide pure zirconium from the $\beta$ -phase field, <a href="#">(c)</a> Packets of laths in a Zr-15% Nb	57

$\beta$ -quenched alloy showing irregular lath to lath interfaces, (d)  $\beta$ -quenched microstructure of Zr-5.5% Nb alloy, (e) and (f) are bright and dark-field micrographs showing alternately twin related laths in a Zr-2.5% Nb alloy, (g) Packets of martensitic structure with alternate laths twin related. (h) Lath of martensite with same orientation variants and lath boundaries showing dislocation structure, (i) and (j) Bright field TEM micrographs showing plate martensites (i) internally twined (*thick twins*) martensites, (j) internally twined martensite where the minor twin fraction is very thin, (k) Microstructure of the beta quenched sample of Zr-2.5% Nb alloy showing arrangement of primary and secondary plates, (l) Schematic presentation of the plate arrangements shown in (i-k) [56].

Fig. 2.12 Microstructure after hot extrusion. Bimodal grain size distribution of  $\alpha$  is visible in the microstructure [61] 60

Fig. 2.13 (a) Length change of the HT and CW PTs of NPD as function of fluence [66], (b) Transverse stain rate vs axial position of HT and CW PTs [66], (c) Diametral strain vs. neutron fluence measured for the operating pressure tube of FUGEN reactor [6], (d) Diametral creep rate of Zr-2.5%Nb heat treated PT of RBMK [67] 61 62

Fig. 2.14 Effect of 'Nb' concentration on thermal creep of Zr-Nb alloy at 400°C and 150 MPa [70] 64

Fig. 2.15(a) Typical creep curve, Curve A, constant-load test; Curve B, constant-stress test, (b) Experimental steady-state creep rate ratios between the axial and transverse directions versus texture parameters ( $f_t-f_r$ ) under a nominal transverse stress of 300MPa at 350°C under different stress ratios ( $\sigma_A/\sigma_T$ ) [15]. 65

Fig. 2.16 The effect of oxygen concentration on the variation of creep rate at 723 K and 207 MPa of Zr-2.5 wt% Nb with solution temperature [40] 66

Fig. 2.17 (a) Correlation of expansivity with X-ray measurements of preferred orientation (after Kearns) [78], (b) Growth strain at 80°C against and parameter (after Rogerson and Murgatroyd) [79, 80] 69

Fig. 3.1(a) A view of test chamber of DIL 805A and a schematic view of push rod arrangement for measuring the length change, (b) Specimen dimensions used in the study 77

Fig. 3.2 (a) CTE vs. Temperature curve for pure 'Ni' (99.999% purity) showing Curie 78

temperature ( $T_c$ ) at 354°C, (b) The  $\Delta l$  and Temperature vs. time curve showing  $\alpha \rightarrow \beta$  allotropic transformation of pure Uranium (99.9%) at 663°C

Fig. 3.3 (a) The plot showing  $(dL/L_0)$  measured, recommended and calibration vs. temperature 80 for the pure iron (99.999%) sample. Recommended relative length change relationship for the pure 'Fe' is expressed as,  $(dL/L_0)_{standard} = -2.89E-3 + 7.35E-6 T + 9.33E-9 T^2 - 3.14E-12 T^3$  [4],

(b) CTE measured and CTE after correction vs. temperature for the pure 'Fe' sample

Fig. 3.4 Schematic representation of dilation curve during cooling, Points A and B represent the 82 start and end of transformation. The three tangent method is shown for determining the transformation temperatures as identified by points C and D

Fig. 3.5 (a) A sketch showing scheme of extraction of dilatometry specimens from the spool 83 piece, (b) A schematic of temperature programs used for determination of partial CCT diagram, (c) Typical thermogram and dilatogram recorded during one of the experiments 84

Fig. 3.6 (a) Schematic of heat treatment cycles adopted for the study, (b) Scheme of specimen 86 preparation from the heat treated dilatometry sample

Fig. 3.7 (a) Schematic of specimen preparation for CTE studies (b) A typical experimental 88 output of Thermogram and dilatogram obtained for a sample.

Fig. 3.8 Schematic of specimen preparation from the heat treated dilatometry specimens for 89 Compression testing and EBSD scanning

Fig. 3.9 (a) Schematic of Heat Treatment setup, (b) Scheme of extraction of axial and 90 circumferential tensile specimens having gauge length  $7.62 \pm 0.02$  mm ( $7.62/\sqrt{(1.78 \times 1.52)} = 4.6 \pm 0.1$ ) [25], from the Zr-2.5%Nb alloy spool piece, (c) Schematic of specimen preparation from heat treated bulk pieces for SPT and ABI tests and TEM examination.

Fig. 3.10 (a) Ball indentation geometries before and after load application (*the material pileup is exaggerated*), (b) Typical Load vs. Depth curve for an ABI Test (c)  $(P/d_i^2)$  vs.  $(d_i/D)$  plot 92 used for determining Yield parameter "A", (d) A typical  $\ln(\sigma_i)$  vs.  $\ln(\epsilon_p)$  plot used for the determination of UTS ( $\sigma_{UTS}$ ). 93

Fig. 3.11(a) A schematic view of a jig used for Small Punch test, (b) A typical load-deflection 95 curve obtained for a Zr-2.5%Nb alloy specimen in the present study showing four different regimes during the progress of deformation I : Elastic bending regime, II: Plastic bending

regime, III: Plastic membrane stretching regime, IV: Plastic Instability regime. The plot also shows graphical method of determining the Yield load ( $P_y$ ) and Load maximum ( $P_m$ )

- Fig. 3.12 A schematic view of setup used for electropolishing Zr-2.5%Nb alloy samples 98
- Fig. 3.13 A schematic diagram of the impression creep test equipment 99
- Fig. 3.14 Specimen preparation for texture parameter determination by Kearns method, (a) 103  
Sample cutting plan to obtain samples from three principal directions from the pressure tube off cut, (b) method for obtaining rectangular flat samples from mid thickness of the tube by removing the outer and inner surface layers using EDM as shown by thick lines
- Fig. 4.1 (a) Analysis of cooling part of a typical  $\Delta l$  vs. T curve for  $\beta_{Zr} \rightarrow \alpha_{Zr} + \beta_{Zr}$  transformation 111  
start and end points, (b) analysis for  $\beta_{Zr} \rightarrow \alpha_{Zr} + \beta_{Zr}$  transformation start and end points for the cooling rates, between 0.5 °C/s and 20°C/s
- Fig.4.2 Partial CCT diagram for the Zr-2.5% Nb PT alloy selected for the heat treatment study 112
- Fig. 4.3 Schematic presentation of Zr- rich region of the Zr-Nb system showing effect of 113  
soaking temperature on fractions of  $\alpha$  and  $\beta$  phases and their compositions
- Fig. 4.4 (a) Typical thermogram and dilatogram recorded for one of the samples that was 115  
soaked at 883°C (*within the  $(\alpha+\beta)$  phase field*) and quenched at 25°C/s, (b) Slope changes in the cooling part of dilation curves showing transformation of  $\beta_{Zr} \rightarrow \alpha_{Zr} + \beta_{Zr}$  phase for the cooling rate 10°C/s from different soaking temperatures
- Fig. 4.5 (a) The slope changes in the cooling part of dilatograms showing transformation of  $\beta_{Zr}$  116  
phase when cooled at different rates from the soaking temperature 883±0.5°C. The significant increase in volume (i.e. increase in length) during cooling may be attributed to formation of  $\alpha_{Zr}$  at slower cooling rates and  $\alpha'$  at relatively higher cooling rates, (b) A partial CCT diagram for the Zr-2.5%Nb alloy for the condition soaked in  $(\alpha+\beta)$  phase field at 883°C and quenched at different rates. The martensite start temperature is observed at 681°C for this alloy and is also observed to be independent of cooling rates beyond 50°C/s.
- Fig. 4.6 Bright field TEM micrographs showing distribution and morphology of primary  $\alpha$  and 120  
 $\beta$ -phase transformed products  $\alpha$ ,  $\beta$  and  $\alpha'$  for the samples soaked 883±0.5°C and cooled at, (a) 0.5°C/s, (b) 10°C/s, (c) 25°C/s, (d) 50°C/s and (e) 100°C/s.

- Fig. 4.7 Bright field TEM micrographs showing distribution and morphology of primary  $\alpha$  and  $\beta$ -phase transformed products  $\alpha$ ,  $\beta$  and  $\alpha'$  for the samples soaked  $870\pm 0.5^\circ\text{C}$  and cooled at, (a)  $10^\circ\text{C/s}$ , (b)  $25^\circ\text{C/s}$  and (c)  $50^\circ\text{C/s}$  121
- Fig. 4.8 Bright field TEM micrographs showing distribution and morphology of primary  $\alpha$  and  $\beta$ -phase transformed products  $\alpha$ ,  $\beta$  and  $\alpha'$  for the samples soaked  $863\pm 0.5^\circ\text{C}$  and cooled at, (a)  $10^\circ\text{C/s}$ , (b)  $25^\circ\text{C/s}$ , (c)  $50^\circ\text{C/s}$  and (d)  $100^\circ\text{C/s}$  122
- Fig. 4.9 Bright field TEM micrographs showing distribution and morphology of primary  $\alpha$  and  $\beta$ -phase transformed products  $\alpha$ ,  $\beta$  and  $\alpha'$  for the samples soaked  $840\pm 0.5^\circ\text{C}$  and cooled at, (a)  $10^\circ\text{C/s}$ , (b)  $25^\circ\text{C/s}$  and (c)  $50^\circ\text{C/s}$  123
- Fig.4.10 Image quality maps obtained from EBSD of (a) sample quenched from  $883^\circ\text{C}$  at a rate of  $100^\circ\text{C/s}$ , (b) sample quenched from  $883\pm 0.5^\circ\text{C}$  at a rate of  $0.5^\circ\text{C/s}$  124
- Fig. 4.11 Image quality maps from the EBSD scans for the Zr-2.5%Nb alloy samples heat treated at  $870\pm 0.5^\circ\text{C}/30$  min and cooled at  $25^\circ\text{C/s}$  followed by Cold Working (CW) to different levels (a) as heat treated (0% CW) (b)  $\sim 9.6\%$  CW, (c)  $\sim 12\%$  CW, (d)  $\sim 26.8\%$  CW, (e) Correlation of Texture parameter ( $f_a$ ) with %CW showing increasing trend 127
- Fig. 5.1 Bright field TEM micrographs showing distribution and morphology of primary  $\alpha$  and  $\beta$ -phase transformed products  $\alpha$ ,  $\beta$  and  $\alpha'$  for the samples soaked  $880^\circ\text{C}$  and cooled at, (a) furnace cooled ( $0.15^\circ\text{C/s}$ ), (b)  $28^\circ\text{C/s}$ , (c)  $55^\circ\text{C/s}$  and (d) water quenched sample 135
- Fig. 5.2 SPT Load vs. displacement curves obtained for Zr-2.5%Nb alloy specimens heat treated at  $880^\circ\text{C}$  (*axial loading*), (a) Quenched at  $28^\circ\text{C/s}$ , (b) Quenched at  $55^\circ\text{C/s}$ , (c) Quenched at  $151^\circ\text{C/s}$ , (d) Cooled at  $0.15^\circ\text{C/s}$  and (e) Water quenched ( $\sim 800^\circ\text{C/s}$ ) 136
- Fig. 5.3 SPT Load vs. displacement curves obtained for Zr-2.5%Nb alloy specimens heat treated at  $880^\circ\text{C}$  (*Circumferential loading*), (a) Quenched at  $28^\circ\text{C/s}$ , (b) Quenched at  $55^\circ\text{C/s}$ , (c) Quenched at  $151^\circ\text{C/s}$ , (d) Cooled at  $0.15^\circ\text{C/s}$ , (e) Water quenched ( $\sim 800^\circ\text{C/s}$ ) 137
- Fig. 5.4 Correlation parameters for determination of  $\sigma_y$  by ABI (a) Axial-loading and (b) Circumferential loading 138
- Fig. 5.5 (a) SPT: Correlation parameters for evaluation of  $\sigma_y$  for - (*Axial loading*), (b) SPT; Correlation parameters for evaluation of  $\sigma_{UTS}$  - (*Axial loading*) 139

Fig. 5.6 (a) SPT, Correlation parameters for evaluation of $\sigma_y$ for -(Circumferential loading),	144
(b) SPT, Correlation parameters for evaluation of $\sigma_{UTS}$ – (Circumferential loading)	
Fig. 5.7 (a) Comparison of Tensile and SPT derived directional $\sigma_y$ values for different heat	145
treated conditions, (b) Comparison of Tensile and ABI derived directional $\sigma_y$ values for	
different heat treated conditions	
Fig. 5.8 (a) Comparison of Tensile and SPT derived directional $\sigma_{UTS}$ values for different heat	146
treated conditions, (b) Comparison of Tensile and ABI derived directional $\sigma_{UTS}$ values for	
different heat treated conditions	
Fig. 5.9 Comparison of axial and circumferential direction mechanical property data, (a) SPT	147
and ABI- derived $\sigma_y$ data with tensile $\sigma_y$ data, (b) SPT and ABI- derived $\sigma_{UTS}$ data with	
tensile $\sigma_{UTS}$ data	
Fig. 5.10 (a and b) A schematic of SPT specimen deformation during a test compared to	150
tensile deformation in the radial direction.	
Fig.6.1 Effect of cooling rate on mechanical properties $\sigma_y$ and $\sigma_{UTS}$ of the Zr-2.5%Nb	158
pressure tube samples by ABI for the samples soaked within the ( $\alpha+\beta$ ) phase field at, (a)	159
883°C, (b) 870°C, (c) 863°C, (d) 840°C	
Fig. 6.2 Effect of cooling rate on mechanical properties $\sigma_y$ and $\sigma_{UTS}$ of the Zr-2.5%Nb	160
pressure tube samples by SPT for the samples soaked within the ( $\alpha+\beta$ ) phase field at (a)	161
883°C, (b) 870°C, (c) 863°C, (d) 840°C	
Fig. 6.3 Effect of soaking temperatures on mechanical properties $\sigma_y$ and $\sigma_{UTS}$ of the ( $\alpha+\beta$ )	162
heat treated Zr-2.5%Nb pressure tube samples by ABI, for the cooling rates, (a) 10°C/s, (b)	163
25°C/s, (c) 50°C/s, (d) 100°C/s	
Fig. 6.4 Effect of soaking temperatures on mechanical properties $\sigma_y$ and $\sigma_{UTS}$ of the ( $\alpha+\beta$ )	164
heat treated Zr-2.5%Nb pressure tube samples by SPT, for the cooling rates (a) 10°C/s, (b)	165
25°C/s, (c) 50°C/s, (d) 100°C/s	
Fig. 6.5 (a) Effect of cooling rate on the Vicker’s hardness (VHN) of the heat treated Zr-	173
2.5%Nb alloy samples soaked at 883, 870, 863 and 840°C, (b) Effect of cooling rate on the	
Brinell hardness (BHN) of the same alloy samples obtained during ABI tests	

Fig. 7.1 The $(\alpha+\beta)/\beta$ transus temperature for the Zr-2.5%Nb alloy sample containing, (a) 301 ppmw of 'Fe' (Ph-1), (b) 402 ppmw of 'Fe' (Ph-2), (c) 1100 ppmw of 'Fe' (Ph-3), (d) 1336 ppmw of 'Fe' (Ph-4), (e) Linear fit of $(\alpha+\beta)/\beta$ transus temperature vs. 'Fe' content in the Zr-2.5%Nb alloy samples	178 179 180
Fig. 7.2 The $(\alpha+\beta)/\beta$ transus temperature for the Zr-2.5%Nb alloy sample containing, (a) 930 ppmw of oxygen (Ph-5), (b) 963 ppmw of oxygen (Ph-6), (c) 967 ppmw of oxygen (Ph-7), (d) 1003 ppmw of oxygen (Ph-8), (e) 1073 ppmw of oxygen; (Ph-9), (f) Linear fit of $(\alpha+\beta)/\beta$ transus temperature vs. 'O' content in the Zr-2.5%Nb alloy	181 182 183
Fig.7.3 Impression creep test results (a) Depth Of Penetration (DOP) vs. time, (b) creep stain ( $\varepsilon$ ) vs. time	185
Fig. 7.4 Increasing 'Fe' content in the Zr-2.5%Nb alloy showing decreasing trend in, (a) Steady state impression creep strain rate $\dot{\varepsilon}$ (at 400°C), (b) In-reactor axial creep rate, $\dot{\varepsilon}_i$ of the pressure tubes ( <i>reactor operating temperature 300°C</i> )	188
Fig. 7.5 (a-c) typical microstructure of the off cut samples used for the thermal creep study indicating similar distribution and features of $\alpha_{Zr}$ and $\beta_{Zr}$ phases	189
Fig. 7.6 Room temperature Vicker's Hardness of Zr-2.5%Nb alloy samples showing increasing trend with oxygen content in the range 743 to 1587 ppmw	197
Fig. 7.7 (a) $\ln(H)$ vs. $\ln(t)$ showing decrease in hardness with dwell time for all the three Zr-2.5%Nb alloy samples at the test temperature (a) 300°C, (b) 400°C	198
Fig. 7.8 $\ln(H)$ vs. $\ln(t)$ plot showing decrease in hardness with time at the test temperatures 300°C and 400°C for the Zr-2.5%Nb alloy sample containing, (a) 1587 ppmw of oxygen, (b) 929 ppmw of oxygen, (c) 743 ppmw of oxygen ( <i>Oxygen measurement Std. dev. <math>6 \times 10^{-4}</math> ppmw</i> )	199 200
Fig.7.9 Typical experimental CTE curves ( <i>up to 400°C</i> ) for the axial and circumferential directions of Zr-2.5%Nb pressure tube samples (a) as fabricated showing large difference slopes indicating texture effects, (b) heat treated ( <i><math>\beta</math>-quenched from 1063°C</i> ) showing similar slopes indicating similar texture	201
Fig. 7.10 (a-f) Typical microstructure of the off cut samples used for the thermal expansion studies indicating similar distribution and features of the $\alpha_{Zr}$ and $\beta_{Zr}$ phases	203

Fig. 7.11 Effect of increasing 'Fe' content in Zr-2.5%Nb alloy showing (a) increasing trend in axial direction CTE, (b) decreasing trend in circumferential direction CTE. This plot also shows nearly similar values of CTE for both axial and circumferential directions for a sample containing 579 ppmw of 'Fe' after heat treatment at 880°C in the ( $\alpha+\beta$ ) phase field followed by quenching at 150°C/s, (c) Correlation of axial texture parameter ( $f_a$ ) with 'Fe' content of as fabricated Zr-2.5%Nb pressure tube samples, (d) Correlation of circumferential texture parameter ( $f_t$ ) with 'Fe' content of as fabricated Zr-2.5%Nb pressure tube samples, (e) Correlation of texture parameters  $f_a$  and  $f_t$  values with CTE (*Fe-variation set of samples*)

Fig. 7.12 (a) Effect of oxygen on CTE of as fabricated Zr-2.5%Nb pressure tube samples for the (a) axial direction (b) for the circumferential direction, (c) Correlation of texture parameter ( $f_a$ ) with oxygen content showing scatter, (d) Effect of small variation of 'Fe' content on the axial CTE of oxygen variation samples

Fig. 7.13 Correlation of  $f_{values}$  vs. CTE (*randomly selected samples*) showing linear fit

Fig. 7.14 A conceptual plot of potential energy versus intratomic distance, demonstrating the anharmonic increases in intratomic separation with rising temperature.

Fig. 7.15 (a) Correlation of irradiation creep rate ( $\dot{\epsilon}_i$ ) of Zr-2.5%Nb pressure tubes with their (a) 'Fe' content, (b) axial direction CTE (*'Fe' variation samples*), (c) Correlation of ( $\dot{\epsilon}_i$ ) with circumferential CTE (*'Fe' variation samples*),

Fig. 7.16 (a) Effect of oxygen on ( $\dot{\epsilon}_i$ ) of Zr-2.5%Nb pressure tubes. (b) Correlation of ( $\dot{\epsilon}_i$ ) with axial direction CTE (c) with circumferential direction

<b>List of Tables</b>	<b>Page No.</b>
<a href="#">Table-1:</a> Correlation coefficients for determination of mechanical properties by SPT and ABI	16
<a href="#">Table-2.1</a> Specification of chemical composition of Zr-2.5wt%Nb pressure tubes	49
<a href="#">Table-3.1:</a> Chemical composition of Zr-2.5%Nb pressure tube spool piece used in the study	82
<a href="#">Table 3.2</a> Composition range of the samples selected for CTE and texture	87
<a href="#">Table-3.3:</a> Heat treatment conditions adopted on the Zr-.5%Nb pressure tube samples	91
<a href="#">Table 3.4 (a)</a> Description and microstructures of Zr-2.5% Nb pressure tube samples with ‘Fe’ content variation used for thermal creep study by impression creep test and in-reactor axial creep rate data for the corresponding operating channels.	100
<a href="#">Table-3.4 (b)</a> Impression creep test parameters	101
<a href="#">Table-4.1:</a> Effect of cooling rate on microstructural features for 883±0.5°C soaked specimens	119
<a href="#">Table-4.2:</a> Effect of cooling rate on microstructural features for 870±0.5°C soaked specimens	119
<a href="#">Table-4.3:</a> Effect of cooling rate on microstructural features for 863±0.5°C soaked specimens	120
<a href="#">Table-4.4:</a> Kearns texture parameters for the samples subjected to various cooling rates	125
<a href="#">Table -4.5:</a> Kearns Texture parameter ( $f_a$ ) for the cold worked samples after heat treatment	126
<a href="#">Table-5.1:</a> Kearns texture parameters for the starting material Zr-2.5%Nb PT spool piece	134
<a href="#">Table-5.2:</a> Correlation parameters for evaluation of axial and circumferential $\sigma_y$ by ABI	148
<a href="#">Table-5.3:</a> Correlation parameters for evaluation of axial and circumferential $\sigma_y$ , $\sigma_{UTS}$ by SPT	149
<a href="#">Table-6.1 (a):</a> Correlation parameters for evaluation of $\sigma_y$ and $\sigma_{UTS}$ by SPT for loading along axial direction of the pressure tube (for tensile $\sigma_y$ range 600 and 810 MPa and $\sigma_{UTS}$ range, 683 and 835 MPa), <a href="#">(b)</a> Correlation parameters for evaluation of $\sigma_y$ by ABI for loading along axial direction with of the pressure tube (for tensile $\sigma_y$ range 412 and 735 MPa)	157
<a href="#">Table-7.1</a> Zr-2.5%Nb alloy samples used for the study of effect on $(\alpha+\beta)/\beta$ Transus temperature due to variation in <a href="#">(a)</a> ‘Fe’ content in the alloy <a href="#">(b)</a> oxygen content in the alloy	181
<a href="#">Table-7.2(a):</a> Zr-2.5%Nb pressure tube samples with ‘O’ variation and their room temperature hardness values by Vicker’s, <a href="#">(b):</a> Description and microstructures of Zr-2.5% Nb pressure tube samples with ‘O’ content variation used for thermal creep study by indentation creep test	194

## CHAPTER 1: Introduction

---

The pressure tube is a part of coolant channel assembly in the PHWRs. Each coolant channel assembly comprises of a Calandria Tube (CT) inside which a Pressure Tube (PT) is held centrally and the garter springs are placed at certain intervals within the annulus gap to prevent PT and CT contact during operation [1, 2]. Natural uranium dioxide powder compacted and sintered in the form of cylindrical pellets and encapsulated in thin walled Zircalloy-4 cladding tube, forms the fuel pins of the PHWRs. Several such pins assembled in the form of fuel bundles are loaded in horizontal pressure tubes [1-5]. In PHWRs, these PTs act as miniature pressure vessels for the primary containment of hot heavy water  $D_2O$  (*deuterium oxide*) which serves as moderator and also coolant. The  $D_2O$  flows at a pressure of around 10 MPa and at a temperature in the range of 250-300°C during operation [2-9]. Fig.1 shows the simplified schematic view of the PHWR core and the coolant channel assembly where only two coolant channels are shown for the sake of clarity.

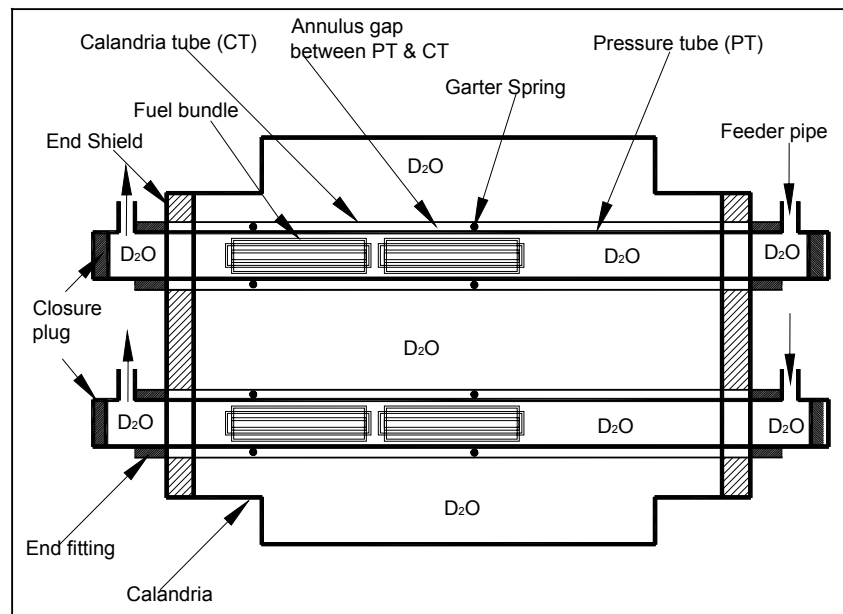


*Fig.1 A schematic simplified view of PHWR core showing coolant channel assemblies*

Zr-2.5% Nb alloy is presently being used as a pressure tube material in the PHWRs because of its higher strength, better creep and fracture strength and low hydrogen pickup rate compared to

Zircaloy-2 [3-6, 10-16]. Zr-2.5%Nb pressure tube is manufactured by a series of thermo-mechanical treatments involving, hot extrusion, cold-working and is used in stress-relieved condition [4-8, 12]. The as-fabricated microstructure in these pressure tubes usually consists of elongated hexagonal-close-packed (*hcp*)  $\alpha_{Zr}$  (*i.e. anisotropic*) that contains  $\sim 0.6\%$ Nb, partially surrounded by a thin network of filaments of (*bcc*)  $\beta_{Zr}$  (*relatively isotropic*) that contains  $\sim 20\%$ Nb [4, 15] and also 'Nb'-depleted hexagonal  $\omega$ -phase [4]. The pressure tubes have strong transverse crystallographic texture with the basal plane normals predominantly concentrated in the transverse direction of the tubes attributing to preferred orientation of  $\alpha_{Zr}$  phase that constitutes over 90% of the pressure tube material volume [3, 4, 17].

During the service, the pressure tubes in PHWRs experience a biaxial stress state due to pressurised coolant ( $\sim 10$  MPa) with transverse stress nearly double the axial stress [5, 6] and neutron flux of  $\sim 10^{17}$  n/m<sup>2</sup>/s [6]. Under such severe operating conditions, anisotropic irradiation growth and creep occur leading to continuous dimensional change, mainly in the circumferential and axial directions of the pressure tubes [3, 4]. These dimensional changes are actually the net effect of irradiation creep, irradiation growth and the thermal creep [4, 12]. However, the major source of deformation in pressure tubes is due to irradiation creep and growth, while the contribution of thermal creep is relatively much less [4]. Irradiation growth causes the shape change at constant volume under no external stress and thermal and irradiation creep cause the shape change at constant volume due to an applied stress [4].

The diametral creep leads to increased coolant flow bypass condition which can lead to inefficient heat extraction from the fuel bundles [5, 18, 19]. The decrease in wall thickness with time would cause an increase in stress in the circumferential direction which can further accelerate the degradation process of the pressure tubes [3, 4, 9, 18, 19]. The pressure tubes also elongate several millimeters per year in the axial direction which can cause interference with the other structural components such as feeder pies. In addition, the weight of heavy water and the fuel bundles cause the tube to deflect downwards which is termed as creep-sag [4].

The irradiation induced growth and creep are functions of the operating conditions such as coolant pressure (*stress*), temperature, and neutron flux [20], and material properties such as microstructure and crystallographic texture. The microstructural features which include

dislocation density, types of dislocations, grain size and shape distribution and morphologies of different phases are determined by the history of thermo-mechanical treatments during fabrication [3, 12]. However, for a given set of operating conditions there is considerable variability observed in the in-reactor deformation rates. The variations in microstructure and texture within the tube, temperature and neutron flux along the tube and variation in chemistry from tube-to-tube leads to the variability in deformation rates of the tubes [12, 20].

In recent years, it has been reported that the heat treated Zr-2.5%Nb pressure tubes being used in Reaktor Bolshoy Moshchnosti Kanalniy (RBMK) and the FUGEN type reactors have shown superior performance in comparison to cold worked pressure tubes [21]. Further, several of the Post Irradiation Examination (PIE) studies have indicated that, the in-reactor deformation behavior (*creep*) of the pressure tubes is a strong function of 'Fe' and 'O' content in the alloy [22-24]. Holt's [22] PIE studies have shown that 'Fe' content in particular has shown marked effect in lowering the axial creep rates of the tubes during service [22]. Thus, both control of microstructure and texture through manufacturing schedules and selection of tube chemistry particularly 'Fe' and 'O' contents can play an important role in evolving the creep resistant Zr-2.5%Nb alloy for the pressure tube application.

It is well known that 'Fe' and 'O' are  $\beta$  and  $\alpha$  phase stabilisers respectively and therefore have opposite effect on the  $\beta$ -transus boundary of the Zr-2.5%Nb alloy [16], the knowledge of which is important from the view point of thermomechanical treatments during the manufacture of a pressure tube. Fundamentally, 'Fe' and 'O' concentrations in the  $\alpha$  and  $\beta$  phases are expected to influence the important physical property, the CTE which represents the texture of the alloy. Therefore, CTE measured in a given direction can serve as a surrogate parameter in place of texture for the assessment and prediction of irradiation behavior of pressure tubes. Further, these minor alloying elements are also expected to have influence on the important mechanical properties, particularly the thermal creep behavior of the pressure tubes. The study of thermal creep behavior particularly at the temperature and stress levels close to reactor operation are important for developing better understanding of irradiation creep behavior of the alloy as these two mechanisms are closely related [4]. In the previous studies, the data available on the heat treatments and microstructural evolution in Zr-2.5%Nb alloy pressure tube material was limited

and also discrete. The literature pertaining to effect of minor alloying elements 'Fe' and 'O' contents on the phase boundary, is qualitative in nature. The effect of independent variation of 'Fe' and 'O' contents on the thermal creep at temperatures and stress levels close to reactor operating condition have not been reported. These literature gaps in these subject domains restricted the understanding of alloy behavior, which is important from the view point of development of creep resistant Zr-2.5%Nb alloy for the pressure tube application. This was the main motive behind the initiation of the present work. To address these issues, the thesis has been dealt in two parts. One part is aimed to study structure property correlations through precise heat treatments on the alloy material and also on cold deformation of alloy samples after heat treatment. The other part is aimed to study the effect of independent variations of minor alloying elements 'Fe' and 'O' contents within the specification range on the phase boundary, physical and mechanical properties. The complete work is also aimed to provide wider data and knowledge base for the development of improved models for the prediction and assessment of alloy behavior under reactor operating conditions.

Under this program an elaborate laboratory scale heat treatments were carried out within the ( $\alpha+\beta$ ) phase field of the alloy after establishing partial CCT diagram for the alloy using the quenching dilatometry technique. These heat treated dilatometry specimens were studied for microstructural and texture evolution using electron microscopy techniques. Since these specimens were small in size the miniature specimen testing techniques such as ABI and SPT were adopted for evaluation of basic mechanical properties such as YS and UTS after experimentally establishing the correlations. The structure and mechanical property correlation study was then carried out which forms one part of the work reported in this thesis.

In the second part, a number of Zr-2.5%Nb pressure tube samples having independent variation in 'Fe' and 'O' contents were selected. A number of these samples were studied for effect on  $\beta$ -transus boundary and CTE in axial and circumferential directions using dilatometry technique. The texture was studied using X-ray diffraction method, the thermal creep behavior was studied using miniature creep testing techniques such as impression and indentation creep tests at temperatures close to reactor operation such as 300°C and 400°C. An attempt also has been

made to correlate the results obtained with the observed in-reactor axial creep rates of the corresponding operating pressure tubes.

## **1.1 Objectives**

In summary, the objectives of this research work were to study the;

1. Microstructural and texture evolution in the alloy samples as a function of soaking temperatures and cooling rates through various heat treatments in the  $(\alpha+\beta)$  phase field.
2. Effect of cold deformation on texture evolution of  $(\alpha+\beta)$  heat treated Zr-2.5%Nb alloy
3. Determination of material specific correlation parameters for the miniature specimen testing techniques SPT and ABI for evaluation of key mechanical properties of anisotropic Zr-2.5%Nb pressure tube alloy.
4. Correlation of microstructure and room temperature mechanical properties of the samples heat treated in the  $(\alpha+\beta)$  phase field of the alloy.
5. Effect of independent variation in 'Fe' and 'O' contents on the  $(\alpha+\beta)/\beta$  phase boundary of the Zr-2.5%Nb alloy.
6. Role of 'Fe' and 'O' contents on the important mechanical property, the thermal creep
7. Inter-correlationship of 'Fe' and 'O' contents, CTE and texture in the as fabricated Zr-2.5%Nb pressure tube alloy.

## **1.2 Outline of the thesis**

The thesis is structured as follows;

Chapter-2 provides literature review pertaining to this study. In this chapter, the various techniques adopted by previous authors for establishing the data relevant to all the areas of this work and also the gap in the literature in these subject domains have been discussed. A problem definition has been made relevant to each area of the work. The chapter-3 deals with materials and experimental procedures adopted at various stages of the study. In chapter-4 an elaborate description has been made on the heat treatment studies on the Zr-2.5%Nb alloy samples using quenching dilatometry technique. A discussion has been presented on the microstructural and texture evolution in the alloy that resulted due to various heat treatments. The chapter-5 describes the determination of correlation parameters for evaluation of mechanical properties of

the anisotropic Zr-2.5%Nb pressure tube alloy by Automated Ball Indentation Technique (ABI) and Small punch Test (SPT). The chapter-6 deals with mechanical property evaluation of the heat treated specimen by the two miniature techniques ABI and SPT and the discussion on structure–property correlations. In the chapter-7 an elaborate study on effect of independent variation in iron and oxygen contents on the CTE, texture, the thermal creep of the Zr-2.5%Nb alloy has been discussed. Finally in chapter-8 a summary of all the new conclusions from the complete study has been presented.

### References-Chapter-1

1. S.S. Bajaj, A.R. Gore, *Nucl. Eng. Des.*, 236 (2006) 701-722
2. R.N. Singh, J.K. Chakravartty, S. Banerjee, *Founder's Day Special Issue No. 309* (2009) 71-89
3. S. Cai, PhD Thesis, "Evolution of Interphase and Intergranular Strain in Zr-Nb alloys During Deformation at room Temperature", Oct 2008, Dept. of Mechanical and Materials Eng. University Kingston Canada, Publication Ref; ISBN, 0494443162, 9780494443163
4. W. Li, PhD Thesis "Effect of Texture on Anisotropic Thermal Creep of Pressurised Zr-2.5%Nb Tubes" Queen's University Kingston, Ontario, Canada August, 2009
5. W. Li, R.A. Holt, *J.Nucl. Mater.*, 401 (2010) 25-37
6. R.N. Singh, R. Kishore, S.S. Singh, T.K. Sinha, B.P. Kashyap, *J. Nucl. Mater.*, 325 (2004) 26-33
7. R.N. Singh, U.K. Viswanathan, S. Kumar, P.M. Satheesh, S. Anantharaman, J.K. Chakravartty, P. Stähle, *Nucl. Eng. Des.*, 241 (2011) 2425-2436
8. D.K. Rodgers, C.E. Coleman, M. Griffiths, G.A. Bickel, J.R. Theaker, I. Muir, A.A. Bahurmuz, S. St. Lawrence, M. Resta Levi, *J. Nucl. Mater.*, 383 (2008) 22-27
9. E.F. Ibrahim, *J. Nucl. Mater.*, 118 (1983) 260-268
10. Y. Ding, D.O. Northwood, *Corros. Sci.*, 36, No. 2, (1994) 259-282
11. S.L. Wadekar, V.V. Raman, S. Banerjee, M.K. Asundi, *J. Nucl. Mater.*, 151 (1988) 162-171
12. N. Saibaba, S.K. Jha, S. Tonpe, Kumar Vaibhaw, V. Deshmukh, S.V. Ramana Rao, K.V. Mani Krishna, S. Neogy, D. Srivastava, G.K. Dey, R.V. Kulkarni, B.N. Rath, E.

- Ramadasan, S. Anantharaman, *J. American Society for Testing and Materials (ASTM), International, (JAI) Paper, ID JAI103213, DOI: 10.1520/JAI103213, 8, No. 6, (2011)*
13. S. A. Aldridge, B.A. Cheadle, *J. Nucl. Mater.*, 42 (1972) 32-42
  14. D.O. Northwood, X. M. Burany, Brian D. Warr, *American Society for Testing and Materials (ASTM), STP-1132 (1991) 156-176*
  15. V. Perovic, G. C. Weatherly, C. J. Simpson, *Acta Metall.*, 31, No. 9 (1983)1381-1391
  16. M. Griffiths, J.E. Winegar, A. Buyers, *J. Nucl. Mater.*, 383 (2008) 28-33
  17. M. Griffiths, R.A. Holt, J. Li, S. Saimoto, *Micro. Sci.*, 26 (1998) 293-301
  18. E.F. Ibrahim, *J. Nucl. Mater.*, 102 (1981) 214-219.
  19. E.F. Ibrahim, R.A Holt, *J. Nucl. Mater.*, 91 (1980) 311-321
  20. M. Griffiths, N. Christodoulou, S.A. Donohue, *J. (ASTM), International, (JAI) Paper ID JAI12432, 2, No.7 (2005)*
  21. K. Takayama “*Post-Irradiation Examination and Evaluation of Zr-2.5%Nb Pressure Tube of FUGEN*”, XA9846758, 181-192
  22. R.A. Holt, *J. Nucl. Mater.*, 372 (2008) 182-214
  23. V. Fidleris, *J. Nucl. Mater.*, 54 (1974) 199-211
  24. V. Fidleris, *J. Nucl. Mater.*, 159 (1988) 22-42

## CHAPTER 2: Literature Review

---

### 2.1. Zr-2.5%Nb pressure tubes in Pressurised Heavy Water Reactors (PHWRs)

Zr-2.5%Nb alloy is being used as pressure tube material in PHWRs because of superior mechanical properties and low hydrogen pickup rates compared to Zircaloy-2 [1-3]. Urbanic *et.al* [4] and Couet [5] have also shown that corrosion of Zr-2.5%Nb tubes was about one-third of that in Zircaloy-2 under similar operating conditions, and the deuterium uptake was only ~2%-4% of that of Zircaloy-2. The fabrication of cold worked pressure tube used in Indian and Canadian PHWRs mainly involves hot extrusion and cold working and they are used in the stress relieved condition. However, it has been observed in FUGEN and RBMK type of reactors that the heat treated pressure tubes fabricated from combination of heat treatments and deformation processes have shown superior performance with their deformation rates much lower compared to cold worked pressure tubes [6]. The major difference in these two types of pressure tubes is the microstructure and texture. Several studies have shown that both, tube chemistry and the microstructure of the dual phased alloy resulting from the type of thermo-mechanical treatments strongly influence the performance of the pressure tube during service. This chapter gives a brief review of previous studies that are relevant to the current research. The review subjects include the different pressure tube processing, the heat treatments, microstructures, texture and properties, and also the influence of 'Fe' and 'O' contents on the performance of the alloy.

#### 2.1.1. Fabrication procedures of Zr-2.5%Nb pressure tubes

Fig. 2.1 shows the main fabrication process steps adopted for the manufacture of cold worked and stress relieved pressure tube at Nuclear Fuel Complex (NFC), India [7]. Fig.2.2 schematically shows different fabrication flow outlines adopted at RBMK for the manufacture standard cold worked route (CW-A) and two heat treatment routes TMT-1 and TMT-2 which represent the water quenching and gas quenching route after holding at 850-870°C within the ( $\alpha+\beta$ ) phase field [7, 8]. The different series of thermomechanical treatments adopted as shown in Fig. 2.1 and Fig. 2.2 dictate the morphologies of the final microstructures which influence the short term and long term properties and consequently the in-reactor performance of the alloy [9-12]. The

primary aim of such heat treatment is to obtain the microstructure and texture that may be resistant to in-reactor deformations without seriously affecting the efficiency of heat-transfer property of the coolant channel assembly [8].

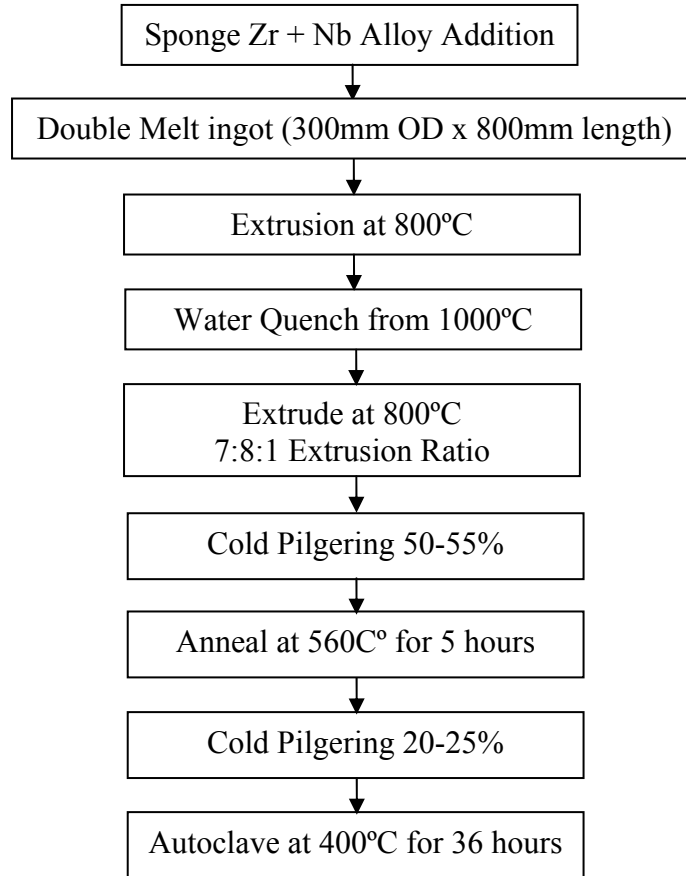


*Fig.2.1 Simplified fabrication flow sheet adopted for manufacture of cold worked pressure tubes at Nuclear Fuel Complex (NFC), Hyderabad, India [7]*

### **2.1.2. Parameters influencing phase transformation during manufacture of Zr-2.5%Nb pressure tubes**

The equilibrium phase diagram presented in Fig. 2.3 shows the presence of Zr-rich ( $\beta_{Zr}$ ) phase at high temperature and ‘Nb’ rich ( $\beta_{Nb}$ ) phase at room temperature [13]. The decomposition of  $\beta_{Zr}$  phase to  $\alpha_{Zr} + \beta_{Nb}$  (equilibrium) is kinetically slower, therefore, the transformation of  $\beta_{Zr}$  during normal cooling does not reach to the equilibrium phases. In the case of higher cooling rates metastable phases such as martensite ( $\alpha'$ ) and under certain conditions omega ( $\omega$ ) phase can also be formed.

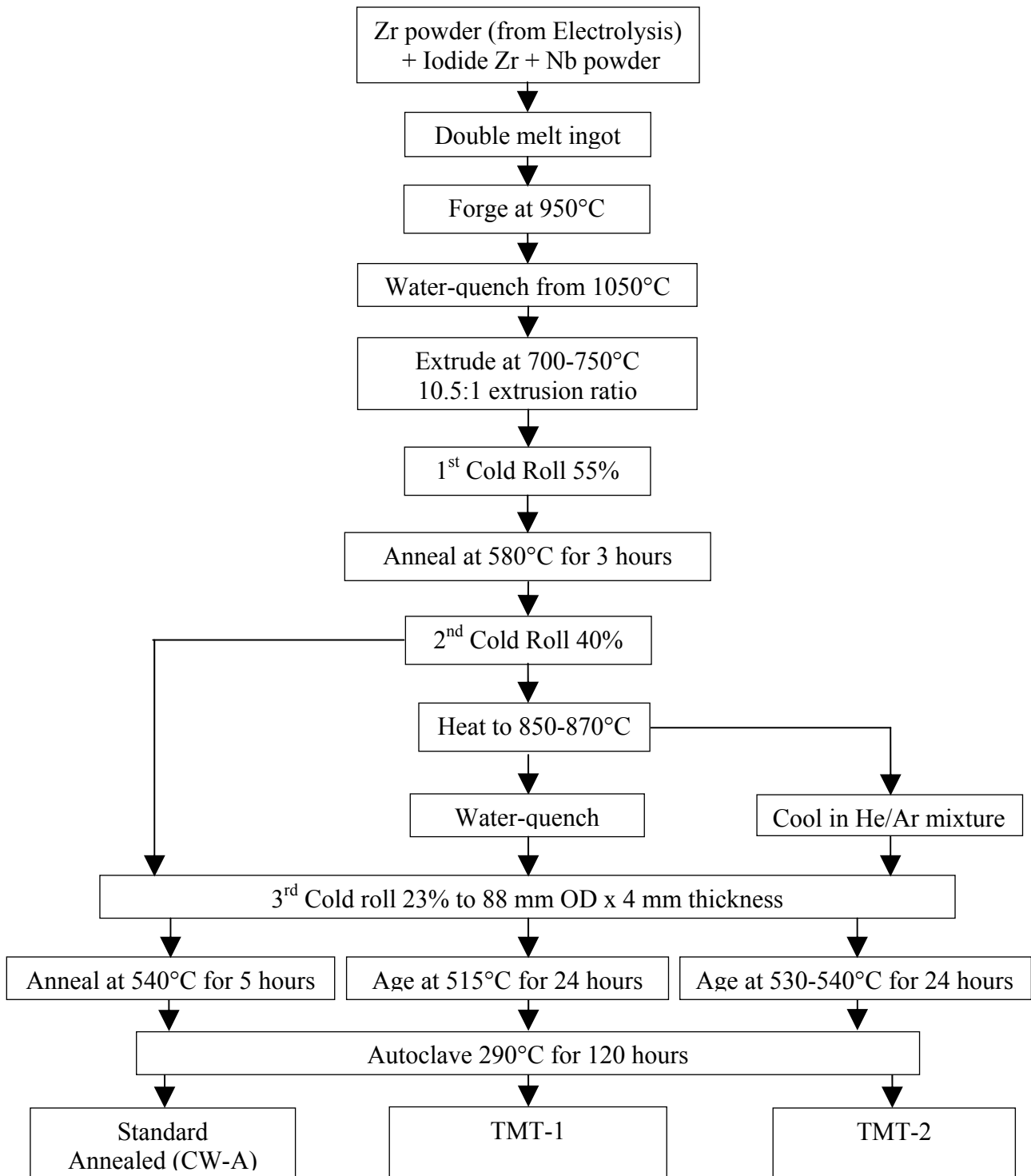


*Fig.2.2 Simplified fabrication flow sheet adopted for manufacture of cold worked / heat treated pressure tubes for RBMK [8]*

The occurrence of these phases is also dictated by the ‘Nb’ content in the  $\beta$  phase which is a function of soaking temperature within the  $(\alpha+\beta)$  phase field. Hence the retention of primary  $\alpha$  and transformation behavior of  $\beta_{Zr}$  leading to formation of  $\alpha$  and  $\beta$  phases or  $\alpha'$  phases and their morphologies are dictated by the nature of thermomechanical treatments adopted during the manufacture of pressure tube. The as-fabricated Zr-2.5%Nb pressure tube material fabricated from cold worked route is a two phase alloy with predominantly  $\alpha_{Zr}$  that constitutes over 90% volume and ~10% of  $\beta_{Zr}$  phase that is present as fine network around  $\alpha_{Zr}$ . The  $\alpha_{Zr}$  phase is crystallographically anisotropic with  $c/a$  axial ratio of 1.593. The preferred orientation of  $\alpha_{Zr}$  phase resulting from the thermo-mechanical treatments makes the alloy highly textured [14, 15]. From the phase diagram in Fig. 2.3, it can be seen that, the  $\alpha+\beta$  phase field of Zr-2.5wt%Nb expands from about 610°C to ~862°C [15]. The extrusion temperature of 800°C is therefore within the two phase field. At this temperature the estimated prior  $\alpha_{Zr}$  or pro-monotectoid  $\alpha_{Zr}$  is about 40% (*by volume*) and remaining ~60% is  $\beta_{Zr}$ . However, the presence of minor alloying elements such as oxygen in the commercial Zr-2.5%Nb alloy is expected to rise the  $\alpha+\beta \rightarrow \beta$  phase boundary resulting in higher volume fraction of  $\alpha$ -phase at 800°C [15, 16], whereas ‘Fe’ content may lower the same. Therefore knowledge of  $\alpha+\beta \rightarrow \beta$  phase boundary for the given alloy is important for the selection of suitable thermomechanical treatments during the manufacture of pressure tube.

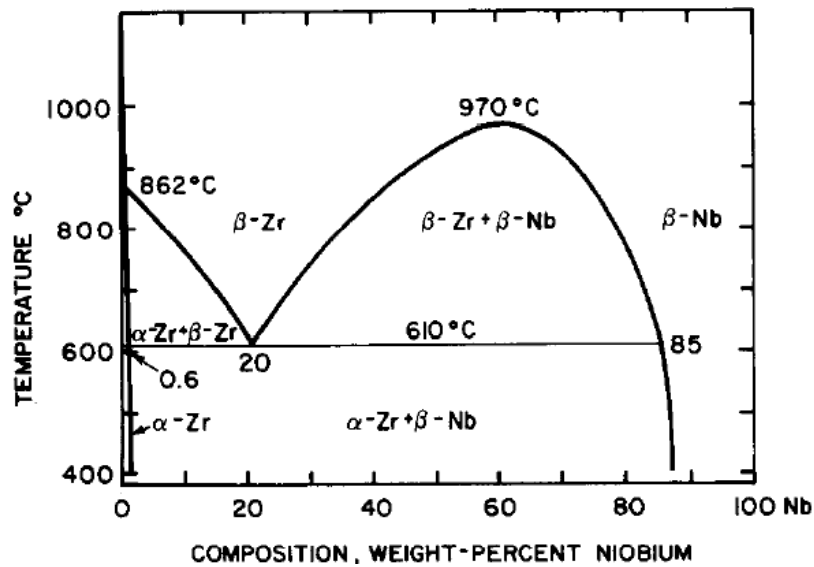


Fig. 2.3 Zirconium - Niobium Phase diagram [15]

### 2.1.3. Microstructures of Zr-2.5%Nb pressure tubes

Because of relatively large deformation in the axial direction of the tube during hot extrusion process the  $\alpha_{Zr}$  grains are elongated in the axial direction and flattened in the radial direction resulting in preferred orientation and hence the texture. Therefore, extrusion ratio is one of the factors that control the microstructure and texture in the alloy. Typical microstructures of the extruded Zr-2.5%Nb alloy generally consist of  $\sim 90\%$   $\alpha_{Zr}$  and  $\sim 10\%$   $\beta_{Zr}$  distributed around the  $\alpha$ -phase as thin grain boundary filaments [14, 15] which are shown in Fig. 2.4 (a), (b). The overall 2.5%Nb in the alloy mainly gets partitioned between the predominant  $\alpha_{Zr}$  and  $\beta_{Zr}$  phases, where  $\alpha_{Zr}$  may contain ‘Nb’ content less than 1wt%, while the  $\beta$ -phase may contain  $\sim 20\text{wt}\%$  Nb [14].

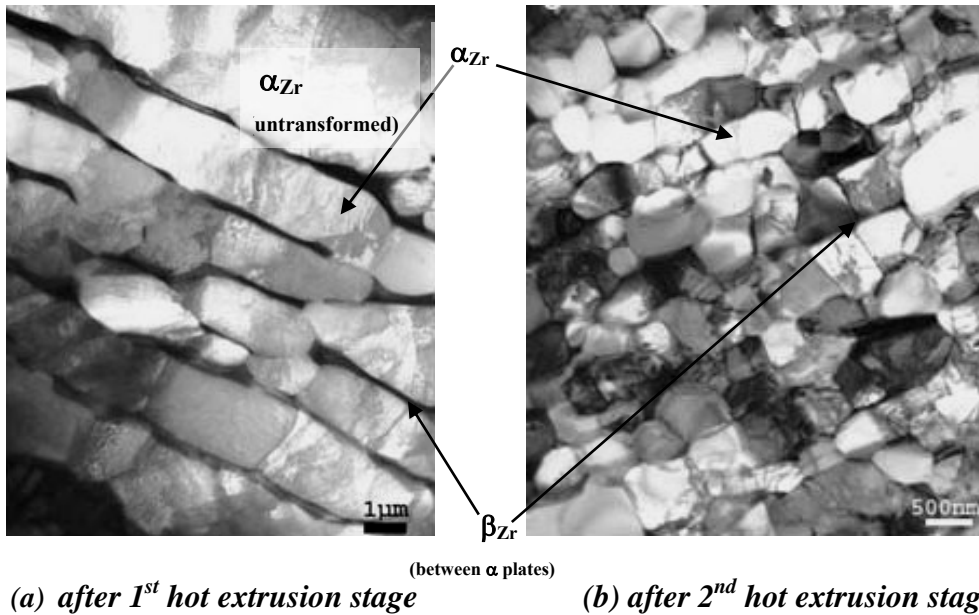


Fig.2.4 TEM microstructure of pressure tube (after hot extrusion stages)

The phase transformation of  $\beta$  to  $\alpha_{Zr}$  occurs during the cool down of the alloy and the  $\alpha$ -phase may inherit the texture from the  $\beta$ -phase according to the Burgers’ orientation relationship,  $\{110\}_{\beta} // \{0002\}_{\alpha}$  and  $[111]_{\beta} // [11\bar{2}0]_{\alpha}$  [15]. During the final autoclaving / stress-relief treatment at 400°C for 36 hours, the metastable  $\beta_{Zr}$  partially transforms towards the equilibrium  $\alpha_{Zr}$  ( $<1\%$  Nb) and  $\beta_{Nb}$  ( $\sim 95\%$  Nb). The  $\beta_{Zr}$  formed in this process may contain a combination of ‘Nb’-depleted hexagonal  $\omega$ -Zr (a metastable hexagonal phase of intermediate ‘Nb’ content) and Nb-enriched ( $\sim 50\%$ )  $\beta_{Zr}$  [14, 15]. The subsequent cold working (*pilgering*) may further elongate the

$\alpha$ -grains and more ‘ $a$ ’ and ‘ $c$ ’ component dislocations are introduced into the grains [15]. The  $c$ -component dislocations refer to the one’s having a component of their Burgers’ vector perpendicular to the basal plane and  $a$ -component dislocations have their Burgers’ vector in the basal plane. Dislocations having Burgers’ vectors with  $b=1/3\langle 11\bar{2}0 \rangle$  ( $\langle a \rangle$ -type) and  $b=1/3\langle 11\bar{2}3 \rangle$  or  $\langle 0001 \rangle$  ( $\langle c+a \rangle$  or  $\langle c \rangle$ -type) are generally present in most grains [15]. The exact dislocation structure varies in individual grains with different orientations and also as a function of position along the circumference of the tube [15, 17]. The dislocation density and type are known to influence the in-reactor deformation behavior of the pressure tube.

#### 2.1.4. Crystallographic texture of Zr-2.5%Nb pressure tube

The tendency of orientation of crystals in a specific direction is called “preferred orientation” or “crystallographic texture” [18]. In Zr-2.5%Nb alloy, due to the limited slip systems operative under ordinary conditions, the deformation during extrusion process is aided by twinning activity which leads to rotation of  $\alpha_{Zr}$  crystals resulting in crystallographic texture [19]. As a result of extrusion process, most of the  $hcp$   $\alpha$ -grains are oriented with their  $\{0002\}$  basal plane normals in the transverse direction,  $\{11\bar{2}0\}$  plane normals in the radial direction, and  $\{10\bar{1}0\}$  plane normals in the axial direction of the tube as shown schematically in Fig. 2.5 (a) [14, 15]. Fig. 2.5 (b) and (c) show typical (0002) and (11 $\bar{2}$ 0) pole figures for the common microstructure generally present in the pressure tubes fabricated from cold worked route. The strong crystallographic texture results in strong anisotropy in the physical and mechanical properties which ultimately influence the in-reactor deformation behavior of the pressure tubes [20].

It is well known that strong (0002) texture of typical PHWR pressure tube results in good transverse tensile strength and also low circumferential strain resulting from irradiation induced creep [15, 21]. However, the tubes with higher transverse texture exhibit relatively higher axial elongation rates and are also more susceptible to delayed hydride cracking (DHC) as the majority of basal planes are oriented perpendicular to the hoop’s direction (*radial-axial plane*) [22- 24]. It is observed that the texture developed at the extrusion stage, is generally not affected considerably even during subsequent cold drawing and stress relieving operations [25]. The studies by Holt and Aldridge [25] established that increasing extrusion ratio and extrusion

temperature reduced the proportion of basal plane normals in the longitudinal direction. Later by Holt and Zhao [26] found that morphology of prior  $\beta$ -phase plays an important role in the development of texture in the alloy. Thus cooling of the billet during extrusion process invariably influences the distribution of texture along the tube length.

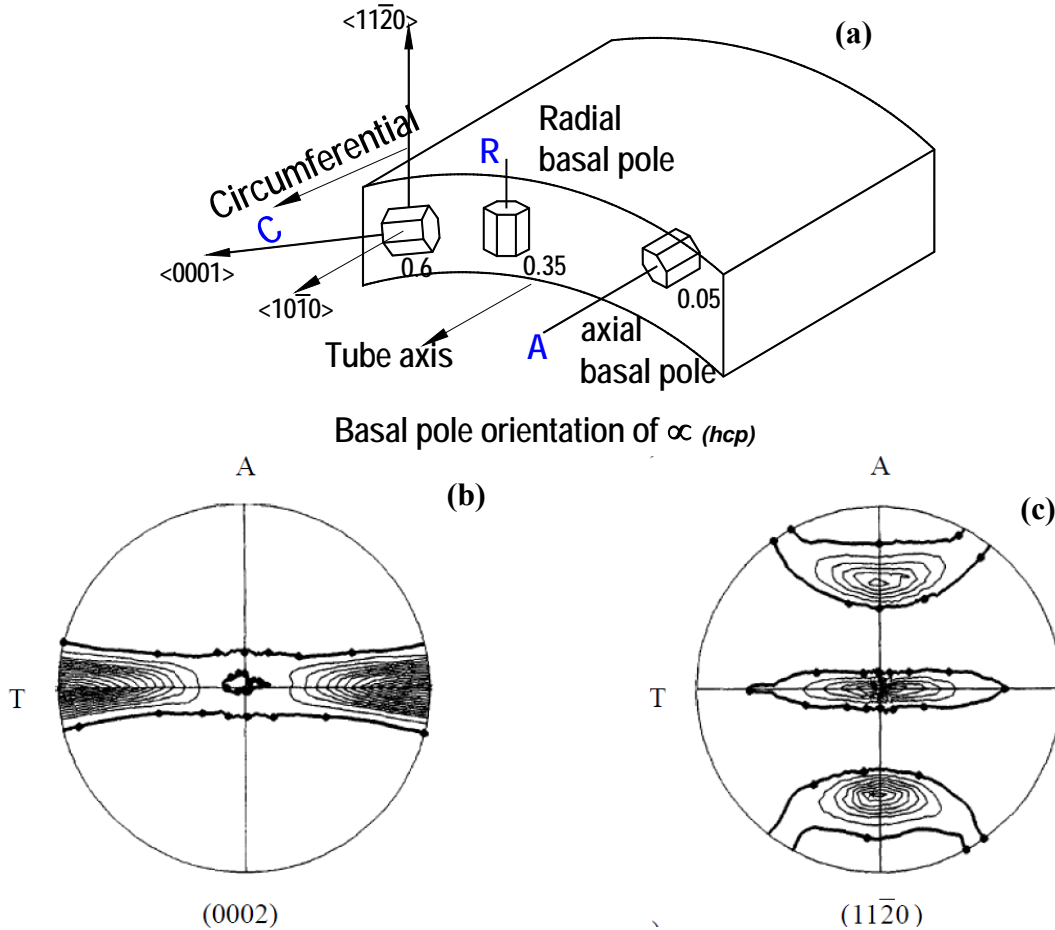


*Fig. 2.5 (a) A schematic of typical distribution of fraction of basal poles of  $\alpha_{Zr}$  crystals along three principal directions of the pressure tube (b) typical (0002) pole figures for the Zr-2.5%Nb pressure tube with majority of basal poles in radial–transverse plane, [15] (c)  $(11\bar{2}0)$  pole figure showing majority of prism poles in the radial- transverse plane. [15]*

The crystallographic texture in the Zr-2.5%Nb alloy is also known to have remarkable influence on the important properties such as Coefficient of Thermal Expansion, Young’s modulus, Poisson’s ratio, strength, ductility and toughness and also on the performance of the pressure tubes in the reactor [14, 15]. Thus, the texture is one of the controlling factors which play an important role in the design of creep resistant Zr-2.5%Nb alloy for pressure tube application.

### 2.1.5 Chemical composition of Zr-Nb pressure tube alloy

The current specification of chemical composition of the PHWR pressure tubes used in India is provided in the [Table-2.1](#). Niobium ('Nb') is the main alloying element while carbon, oxygen and iron are the minor alloying elements in the pressure tube alloy.

*Table-2.1 Specification of chemical composition of Zr-2.5wt%Nb pressure tubes*

Elements	Composition range (by weight)	Remark
Niobium	2.4~2.8 wt%	Alloying element
Oxygen	900-1300 ppmw	Alloying element
Iron	900-1300 ppmw	Alloying element
Carbon	40-80 ppmw	Alloying element
Chromium	<200 ppmw	Impurity
Hydrogen	<5	Impurity
Zirconium	Balance	---

### 2.2 Role of iron and oxygen concentrations on the properties of Zr-2.5%Nb alloy

The main alloying element 'Nb' acts as a  $\beta$  phase stabiliser and therefore the alloy has two phase ( $\alpha+\beta$ ) microstructure. The other elements, oxygen and iron are now regarded as minor alloying elements considering their advantageous effects on the in-reactor creep behavior of the alloy. Oxygen gets introduced into the material at different stages of pressure tube manufacturing. Oxygen also acts as  $\alpha$  phase stabiliser and strengthening agent. On the other hand 'Fe' is mainly associated with the alloy from the Zr-sponge stage itself and it acts as  $\beta$  phase stabiliser. It has been observed that these two elements have considerable influence on the phase boundaries, physical and mechanical properties and also on the in-reactor deformation behavior of the Zr-Nb pressure tube alloy. The following subsections discuss the literature pertaining to the effect of these alloying elements on the properties and to the scope of the work.

#### 2.2.1 Effect of iron and oxygen on $\beta/(\alpha+\beta)$ phase boundary of the alloy

The Zr-Nb phase diagram has been studied by many authors [27- 32]. The effect of oxygen and iron contents on the  $\beta/(\alpha+\beta)$  transformation temperature of the Zr-Nb system has been studied by several authors [16, 31- 41]. Since, oxygen and iron are  $\alpha$  and  $\beta$  phase stabilisers respectively, they have opposite effects on the  $\beta/(\alpha+\beta)$  phase boundary of the Zr-Nb binary system [33]. Oxygen in particular is known to have marked effect, as it increases the  $\beta/(\alpha+\beta)$  transus

temperature [31, 34, 35, 39]. The effect of ‘Nb’ and also ‘O’ on the  $\beta/(\alpha+\beta)$  transus temperature calculated theoretically and measured by Hunt and Nissen [34, 35] is shown in Fig. 2.6 (a). The figure shows that  $\beta/(\alpha+\beta)$  transus temperature is a strong function of ‘Nb’ and ‘O’ contents.

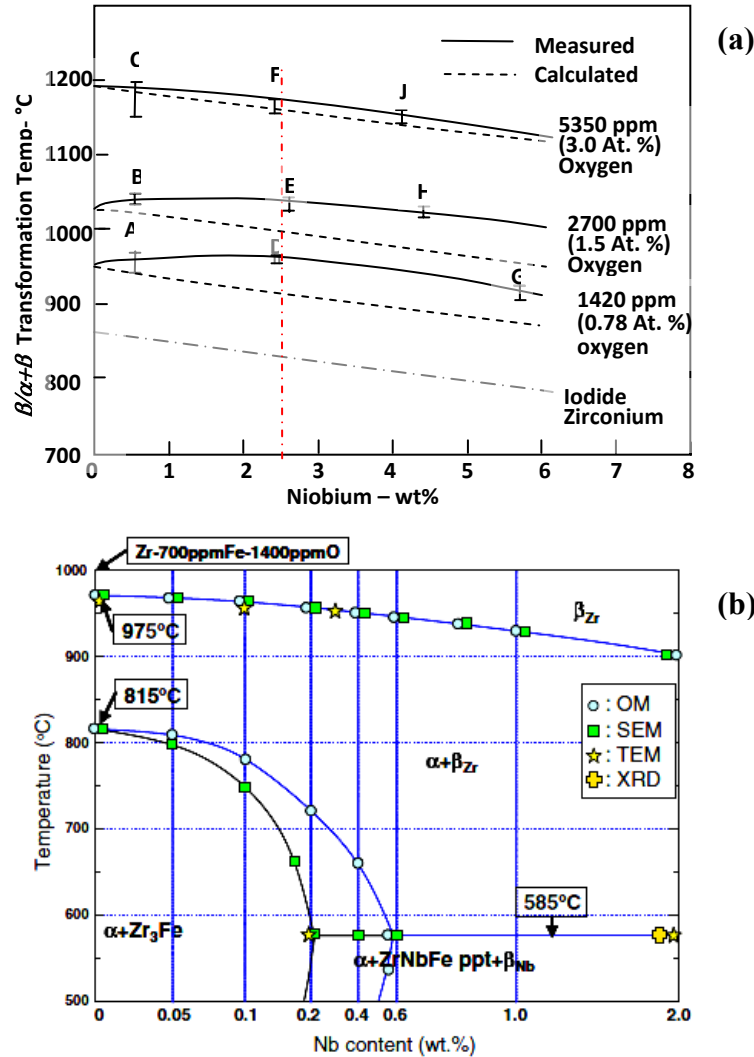


Fig. 2.6 (a)  $\beta/(\alpha+\beta)$  transformation temperatures for zirconium-niobium alloys of differing oxygen concentrations (measured and calculated) [35], (b) Phase boundary determination of dilute Zr-xNb alloys containing 1400 ppmw O and 700 ppmw ‘Fe’ [39]

Toffolon *et.al* [38] reported that increase in oxygen content from about 0.1 wt.% to 0.27 wt.% in the Zr-1%Nb alloy lead to increase in  $(\alpha+\beta)/\beta$  transition temperature from 1185 K to 1265 K. The Fig. 2.6 (b) shows the phase boundary of the Zr-rich region established by Kim *et.al* [39]. The Figure also shows the  $(\alpha+\beta)/\beta$  transformation temperature of the commercial grade ‘Zr’

containing 1400 ppmw ‘O’ and 700 ppmw ‘Fe’ to be  $970\pm 3^\circ\text{C}$ , which was attributed to the high ‘O’ concentration.

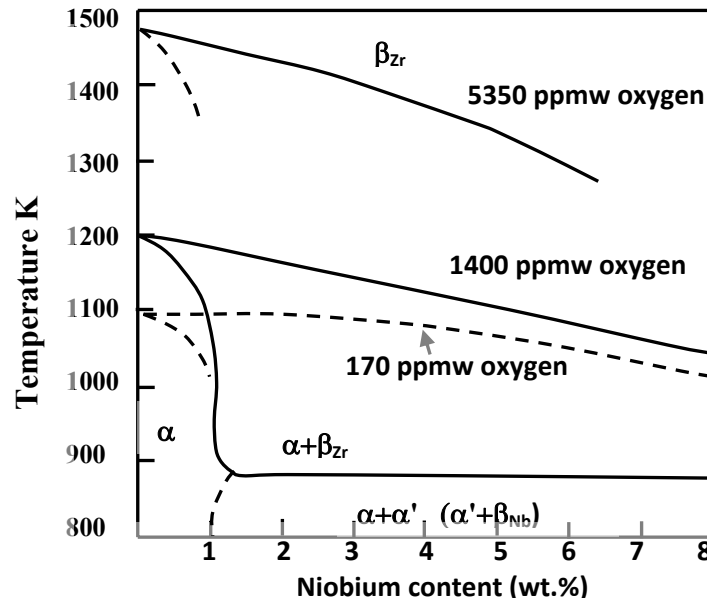


Fig. 2.7. Effect of oxygen on  $(\alpha+\beta)/\beta$  phase boundary of zirconium-rich Zr-Nb alloys [59]

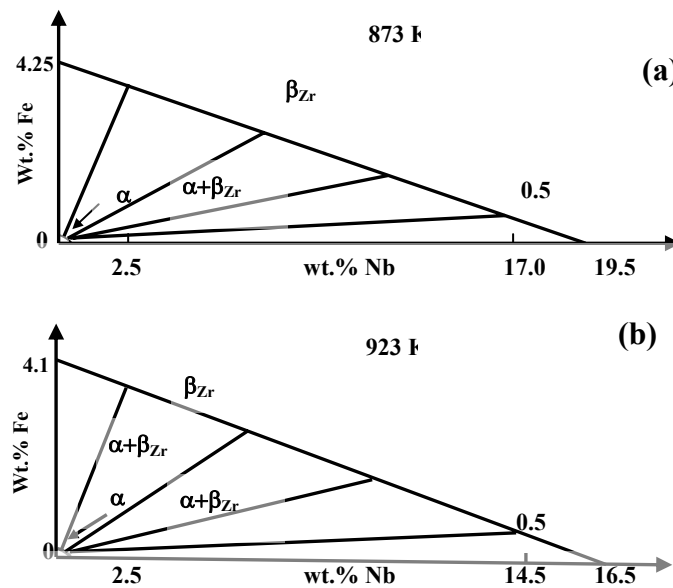


Fig.2.8 Isothermal sections at the Zr-rich corner of the ternary Zr-Nb-Fe system, showing the tie-line construction used to determine the equilibrium concentrations of ‘Nb’ and ‘Fe’ in the  $\alpha+\beta$  phase field at, (a) 873 K, (b) 923 K [41]

The lower value of  $815\pm 3^\circ\text{C}$  for the  $\alpha/(\alpha+\beta)$  phase transformation temperature in the commercial ‘Zr’ sponge compared with iodide ‘Zr’, was attributed to high ‘Fe’ content that acted as  $\beta$  phase

stabilizer [39]. Fidleris [40] reported from the phase diagram calculations that (See Fig. 2.7) increase in oxygen content by 0.10 wt% (1000 ppmw) in solution raises the  $\beta/(\alpha+\beta)$  transus temperature by about 70 K. Fidleris [40] also reported that  $\alpha$  content decreased from 20% to 2-3% when oxygen content was increased from 100 ppmw to ~1000 ppmw at 10-15K below the  $\beta$ -transus.

Study by Perovic, *et.al* [41] provided a rough estimate of the influence of 'Fe' on the  $\alpha+\beta/\beta$  equilibrium above the monotectoid temperature in the Zr-Nb system. A maximum of 0.02 wt% Fe is soluble in  $\alpha_{Zr}$  while values between 0.2 and 0.5 wt% Fe are soluble in  $\beta_{Zr}$  in the temperature range 873-1073K. A graphical method used to generate tie lines at the Zr-corner of the Zr-Nb-Fe ternary system shows the effect of 'Fe' on  $\beta$ -transus boundary as shown in the Fig.2.8 (a), (b). These literature indicate that the knowledge of effect of minor alloying elements on the  $(\alpha+\beta)/\beta$  phase boundary is important for the design of thermomechanical treatments.

Many authors have dealt the effect of 'Fe' and 'O' concentrations on the  $\beta$ -transus boundary qualitatively. Pe'rez and Massih [36] showed Arrhenious relationship of  $\beta$ -transus temperature with the oxygen in the concentrations range much higher than the current specification limit for the alloy. Thus, for the given composition of these alloying elements in the Zr-2.5%Nb alloy, the accurate knowledge of  $\beta/(\alpha+\beta)$  phase boundary is necessary for the design of heat treatment experiment. Generally, the Continuous Cooling Transformation (CCT) diagram serves the basis for the design of thermomechanical treatments. Therefore, initially the determination of CCT diagram for the Zr-2.5%Nb pressure tube alloy selected for the heat treatment study was initiated.

### **2.2.2 CCT diagram for Zr-2.5%Nb alloy**

The transformation behavior of Zr-Nb alloy systems and CCT diagram for the Zr-2.5%Nb alloy has been previously studied by Hunt and Niessen [35], Stewart *et.al* [42], Slattery [43] and Higgins and Banks [44]. The study by these authors in general was based on monitoring the thermal arrest points using the spot welded thermocouples. However, considerable scatter observed in the results has been attributed mainly to the following reasons.

- i. alloying effect of spot welded thermocouple material at higher temperatures lead to discrepancies in the measured thermal arrest points
- ii. effect of variation in oxygen content in the alloy samples

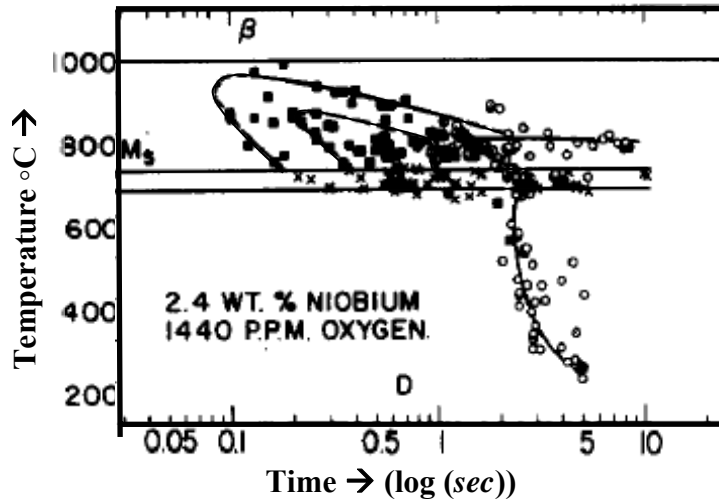


*Fig. 2.9* CCT diagram for Zr-2.4%Nb alloy containing 1440 ppmw of oxygen [53]

Hunt *et al.* [35] work, established that, increasing ‘Nb’ content in the alloy shifted the C-curve nose of the CCT curve to the right, while increasing oxygen content raised the  $\beta_{Zr} \rightarrow \alpha_{Zr} + \beta_{Nb}$  transformation temperature. Hunt *et al.* [35] presented the CCT curves for the Zr-Nb alloy as shown in (Fig. 2.9). The figure shows considerable scatter in the thermal arrest points and also the minimum oxygen content in the alloy studied was 1440 ppmw. In addition the effect of concentration of other important alloying element iron which is expected to have opposite effect on the  $\beta$ -transus boundary of the Zr-Nb alloy has not been considered. In the recent years, Griffiths *et al.* [33] reported the TTT diagram for the Zr-2.5%Nb pressure tube alloy. Although this work provides the equilibrium phase regions for the pressure tube alloy, it is of lesser relevance because majority of heat treatments are based on continuous cooling. Therefore CCT diagrams are the basis for design of thermomechanical treatments. Hence, in the present study, the determination of partial CCT diagram was initiated with the aim to determine the  $\beta/(\alpha + \beta)$  transus boundary for the selected Zr-2.5%Nb alloy using quenching dilatometry technique.

### 2.2.3 Effect of iron and oxygen concentration and texture on the in-reactor deformation behavior of Zr-2.5%Nb pressure tubes

It is known that irradiation induced creep and growth lead to continuous and anisotropic dimensional changes mainly in the circumferential and axial directions of the pressure tube during service [14, 15, 45]. The axial strain (*elongation*) beyond the accommodation limits of the end hardware design can lead to operational difficulties due to interference with other structural components such as feeder pipes. While, the increase in internal diameter of the pressure tube during service can increasingly bypass the coolant over the fuel bundles, leading to reduced efficiency of heat extraction by the coolant [23, 46, 47]. Thus dimensional changes in both directions can be the life limiting factors.

These dimensional changes are actually the net effect of, irradiation induced creep, irradiation growth along with a small contribution from thermal creep [15, 10]. The irradiation growth causes the shape change at constant volume under no external stress whereas the thermal and irradiation creep cause the shape change at constant volume under the influence of an applied stress [15]. Such irradiation behavior is mainly attributed to the metallurgical factors such as morphologies and distribution of the  $\alpha$  and  $\beta$  phase, the crystallographic texture, dislocation density and type, in addition to the effect of minor alloying elements 'Fe' and 'O' in the alloy [46, 48]. The effects of irradiation on dimensional stability of the pressure tubes are generally acknowledged to be due to the 'displacement damage' of lattice atoms by the high energy neutrons ( $>1\text{MeV}$ ) [23, 46, 49, 50]. The damage is the result of residual vacant lattice sites (*vacancies*) and 'Zr' atoms in the interstitial sites known as Self Interstitial Atoms (SIAs) which form only a few per cent of the total number of atoms displaced because of effect of dynamic defect annihilation process.

It is known that crystallographic anisotropy affects irradiation deformation behaviour in two different ways, firstly at the polycrystalline level, through intergranular interaction and secondly at the single crystal level, through diffusional anisotropy [49]. The vacancies and SIAs exhibit anisotropic diffusion characteristics in the  $\alpha_{\text{Zr}}$  phase which is a natural consequence of the *hcp* crystal structure of  $\alpha_{\text{Zr}}$  with (*c/a ratio of 1.593*). Such diffusional anisotropy difference (DAD) provides driving force to segregate the residual defects amongst sinks of different orientation and

causes an imbalance in their fluxes resulting in extended defects in the crystal such as voids, dislocation loops, and network of dislocations [15, 46, 49, 50]. Thus because of strong crystallographic texture, it has been observed that the pressure tubes tend to grow in a direction with higher concentration of <a>-axis (*i.e. mainly axial direction of pressure tubes*) and shrink in the direction with higher concentration of <c>-axis distribution (transverse direction of pressure tubes) due to the mechanism called DAD of vacancies [46, 51]. Growth results when the strain direction of a sink correlates with its orientation [15, 49, 52].

The absorption of excess of one type of point defects by the sinks causes microstructural evolution during irradiation, which consequently result in macroscopic deformation of crystalline materials [49, 50]. Because of low crystal symmetry and limited dislocation slip systems in Zr-alloys at the reactor operating temperatures, it is proposed that the climb-induced glide mechanism can be active, where the irradiation induced point defects and defect clusters play important role in irradiation creep in the polycrystalline alloy [49, 50, 52, 53]. Most established irradiation deformation theories are based on this concept.

In the mean while, the microchemistry such as the redistribution of niobium, iron and oxygen may get altered due to irradiation damage [15, 41]. The microstructural study by Perovic *et. al* [41] on reactor operated pressure tube samples by analytical electron microscopy reported that the  $\beta_{\text{Nb}}$  precipitates were observed in  $\alpha_{\text{Zr}}$  phase after irradiation. This observation by Perovic *et. al* [41] infers that irradiation enhanced diffusion of solute atoms of the alloying elements occurs leading to microstructural evolution which eventually can influence the performance of the alloy during service. Holt [46] study has shown the advantageous effect of 'Fe' and 'O' on the irradiation behaviour of the pressure tubes. Fig. 2.10 (a) shows good correlation of elongation rate of cold worked pressure tubes with an apparent decreasing trend with increase in 'Fe' content, while Fig.2.10 (b) shows effect of 'Fe' on the axial growth strain of the Zr-2.5%Nb pressure tubes at a fluence of ( $1 \times 10^{26} \text{nm}^{-2} > 1 \text{MeV}$ ) [46]. Similarly, Fig. 2.10 (c) shows a good correlation of elongation rate of cold worked Zr-2.5%Nb pressure tubes with oxygen content [46]. The effect of 'Fe' on irradiation behavior of the alloy has not been satisfactorily explained yet. However, it is proposed that 'Fe' in solution can interact with vacancies and in the form of precipitate it might provide sites for recombination of vacancies and interstitials and thus can

delay the irradiation induced deformation process [54, 55]. Further, 'Fe' is also expected to change the volume fractions of  $\alpha$  and  $\beta$  phases at the extrusion stage itself, and hence can have an indirect influence on texture due to  $\beta$  phase stabilising effect [46]. On the other hand oxygen is known to occupy interstitial positions in the  $\alpha_{Zr}$  lattice and provide solute strengthening effect. Thus oxygen may play an important role in retarding the creep rates by providing obstacles to the dislocation motion.

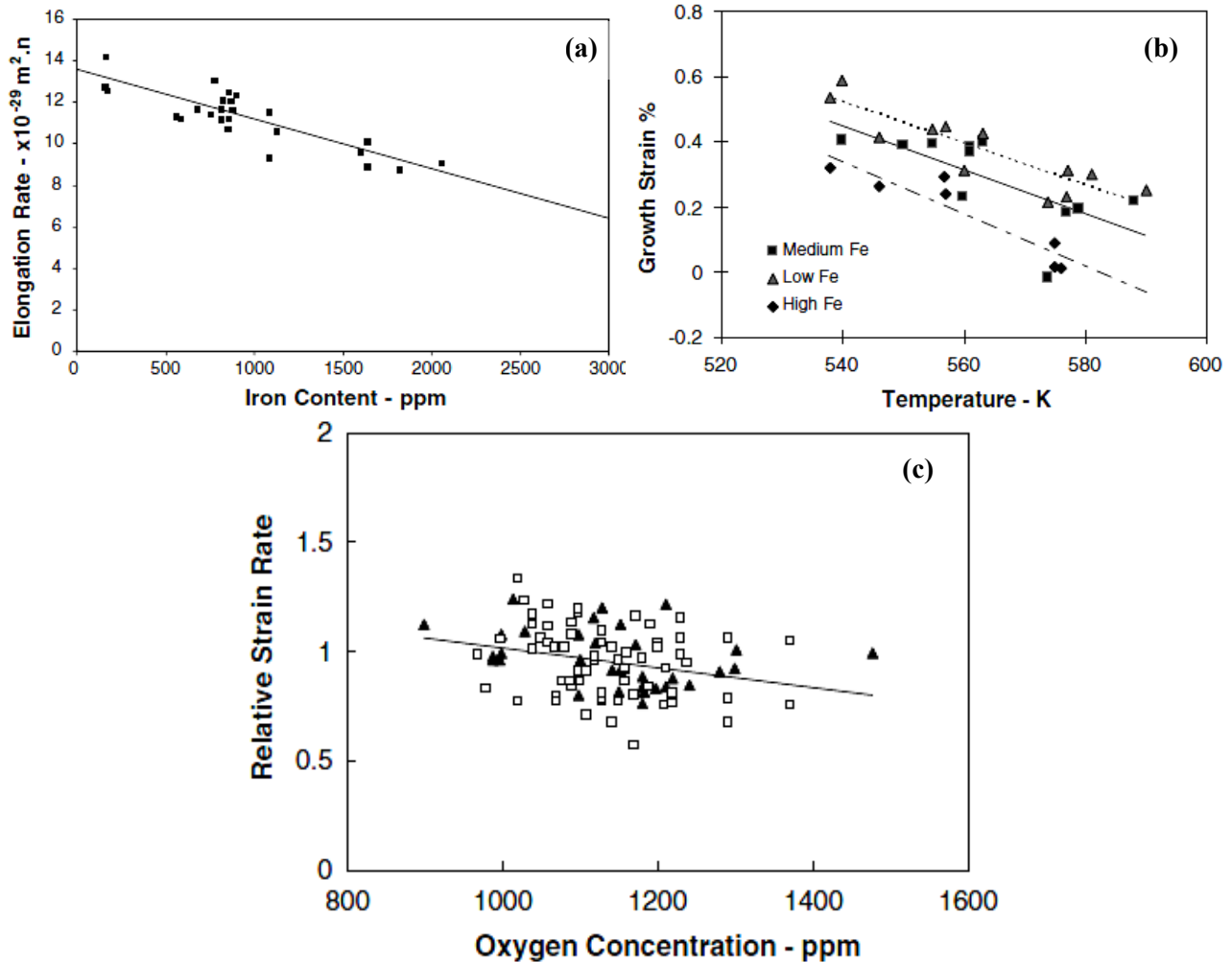


*Fig.2.10 (a) Correlation of elongation rate of cold worked Zr-2.5%Nb pressure tubes in CANDU reactor as a function of ingot iron analysis, (b) Effect of 'Fe' on axial growth strain of Zr-2.5%Nb pressure tube material at fluence of  $(1 \times 10^{26} \text{ n m}^{-2} > 1\text{MeV})$ , (c) Correlation of elongation rate of cold worked Zr-2.5%Nb pressure tubes in CANDU reactor as a function of ingot oxygen analysis of two reactors [46]*

### 2.3 Heat treatment and structure-property correlations

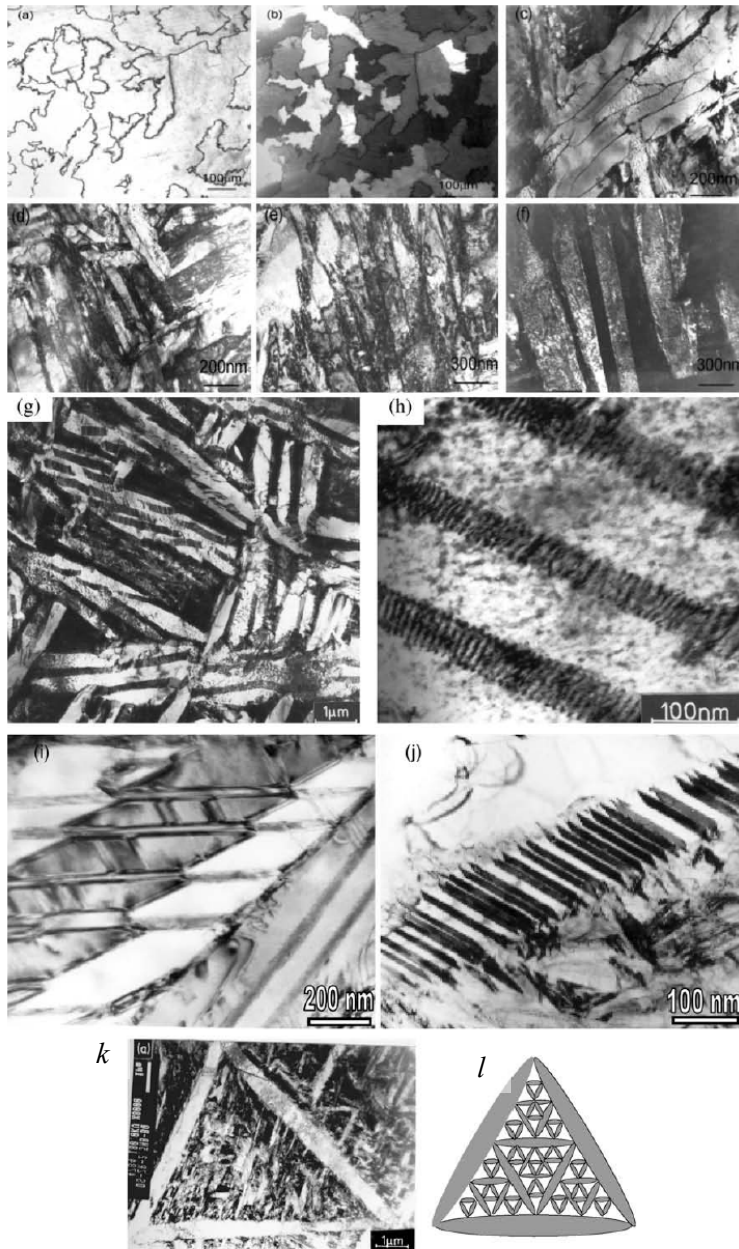
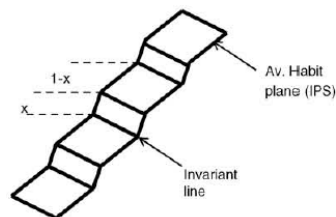


*Fig.2.11 Various morphologies of martensite. (a) and (b) Massive martensite formed on quenching iodide pure zirconium from the  $\beta$ -phase field. (c) Packets of laths in a Zr-15% Nb  $\beta$ -quenched alloy showing irregular lath to lath interfaces (d)  $\beta$ -quenched microstructure of Zr-5.5% Nb alloy. (e) and (f) are bright and dark-field micrographs showing alternately twin related laths in a Zr-2.5% Nb alloy. (g) Packets of martensitic structure with alternate laths twin related. (h) Lath of martensite with same orientation variants and lath boundaries showing dislocation structure. (i) and (j) Bright field TEM micrographs showing plate martensites (i) internally twined (thick twins) martensites (j) internally twined martensite where the minor twin fraction is very thin. (k) Microstructure of the beta quenched sample of Zr-2.5% Nb alloy showing arrangement of primary and secondary plates (l) Schematic presentation of the plate arrangements shown in (i-k) [56].*



Heat treatment and structure-property correlation study is an important part of this research which is aimed to address the issues related to the development of creep resistant Zr-2.5%Nb pressure tube alloy for the pressure tube application. As discussed in previous sections the Zr-2.5%Nb pressure tube alloy is a dual phase material and is amenable to various heat treatments and hence can be used with variety of microstructure. The final microstructure, crystallographic texture and dislocation density achieved due to a series of thermomechanical treatments adopted during the manufacture of pressure tube dictates the short term and long term mechanical properties and also the performance in the reactor. It is observed that the pressure tubes fabricated from cold worked route have shown higher creep rates compared to the heat treated one's operating in FUGEN and RBMK. The obvious reason for such lower creep rates must be attributed to the final microstructure and properties. In the following a brief review of literature pertaining to heat treatments, microstructural and textural evolution and the structure property correlation has been presented.

Northwood and Fong [13] studied the relationship of microstructure and room temperature mechanical properties of cold-worked Zr-2.5wt% Nb pressure tube alloy after heat treatments at 750 and 800°C in the  $\alpha_{Zr}+\beta_{Zr}$  phase field followed by aging treatment at 560°C in the  $\alpha_{Zr}+\beta_{Nb}$  phase field. This work was aimed to achieve the microstructure with improved mechanical properties in the pressure tube alloy.

Tewari *et. al* [56] work describes the mechanism by which the martensitic transformation would take place under certain heat treatment conditions. The various microstructural details obtained by Tewari *et. al* [56] are shown in Fig.2.11 (a-f). The authors Tewari *et. al* [56] have also shown that plate shaped  $\alpha$ -phase obtained for the heat treatment in the  $\alpha+\beta$  phase field maintained strict orientation relation and habit plane with the parent  $\beta$  matrix. This work has shown that, the morphology and orientation of transforming  $\beta$  grains is the key factor in controlling the texture of the heat treated pressure tube alloy.

Srivastava *et.al* [57, 58] studied the  $\beta$ -phase transformation leading to different morphologies of martensite in the Zr-2.5wt%Nb alloy. The authors [57, 58] have also reported the crystallographic descriptions of different variants of martensites. The "indentation mark" morphology was seen frequently in three variant groups, when viewed along  $\langle 111 \rangle_{\beta}$  directions

in the transmission electron microscope. These variant groups were seen to have highest degree of self accommodation of the strain resulting from previous generation of martensitic plates.

Dey *et. al* [59] studied the effect of ‘Nb’ concentration in  $\beta$ -phase on the transformation behavior of Zr-rich Zr-Nb alloys. The composition of ‘Nb’ in the  $\beta$ -phase was varied by suitably designing heat treatments. This work has indicated that the selection of soaking temperatures within the  $(\alpha+\beta)$  phase field for the purpose of heat treatment is critical, as the ‘Nb’ content of  $\beta$ -phase plays important role in the nature of  $\beta$ -phase transformation.

Kumar *et. al* [60, 61] study established that the changes in the bulk texture of Zr-2.5 wt% Nb alloy on cold rolling was insignificant compared to the single-phase material. The authors Kumar *et. al* [60, 61] concluded from the microtexture studies that  $\alpha$  plates remained approximately undeformed after cold rolling, while the  $\beta$  matrix underwent significant orientation changes resulting in insignificant textural changes. In some cases, where the textural changes occurred in the dual phase alloy was attributed the local discontinuity in the  $\beta$ -phase allowing rotation of  $\alpha$ -crystals during cold deformation. This work has provided input for the present study on the characteristics of textural changes in the dual phase alloy.

The authors Kumar *et.al* [61], Kapoor *et.al* [62] and Srivastava *et. al* [63] studied the microstructural changes by modifying the fabrication process parameters of Zr-2.5%Nb alloy pressure tubes. Kumar *et.al* [61] observed bimodal distribution of  $\alpha_{Zr}$  phase in the microstructures. They attributed larger  $\alpha_{Zr}$  plates to the one nucleated at early stages of hot extrusion from the parent  $\alpha_{Zr}$  grains, and relatively smaller  $\alpha_{Zr}$  plates to the one transformed subsequently during cooling from Zr-rich  $\beta$  to  $\alpha+\beta_{Nb}$  (*Nb-rich phase*). Fig.2.12 shows the microstructure after hot extrusion stage. The bimodal grain size distribution of  $\alpha$  is visible in the microstructure. Srivastava *et. al* [63] described that elongated  $\alpha$  phase in the  $\alpha+\beta$  microstructure is required for obtaining desired level of strength at 310°C. They also recommended lower extrusion ratio and two stage pilgering to have finer control on the microstructure, mechanical properties and better dimensional tolerance. Further, Srivastava *et. al* [63] have shown that the phase separation tendency of the  $\beta$  phase (*into Zr-rich ( $\beta_I$ ) and Nb-rich ( $\beta_{II}$ ) constituents*)

influences the microstructural evolution. This work provides input for carrying out the heat treatment and microstructural studies in the present work.

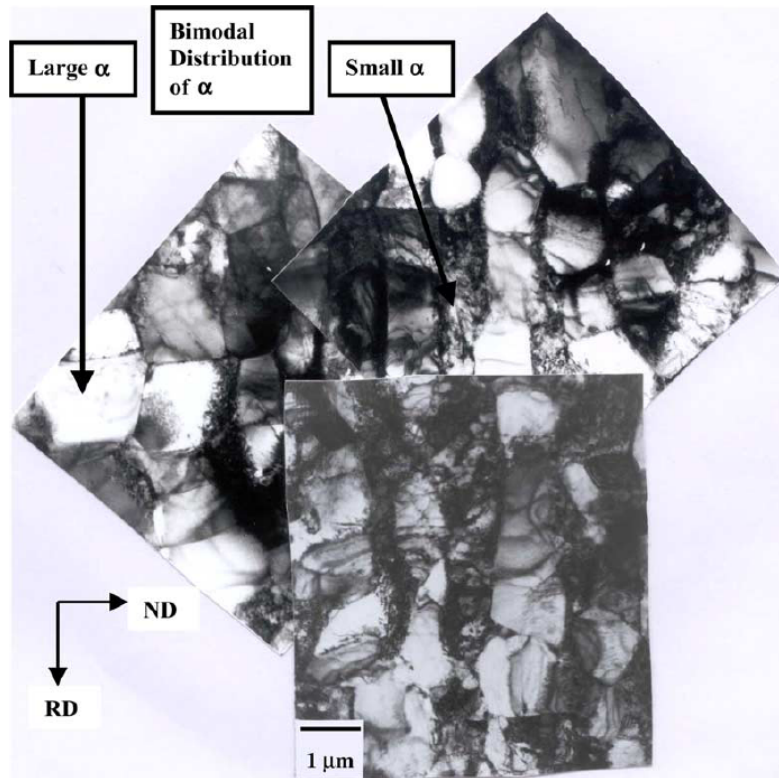


*Fig. 2.12* Microstructure after hot extrusion. Bimodal grain size distribution of  $\alpha$  is visible in the microstructure [61]

Choubey and Jackman [64] used Secondary Ion Mass Spectrometry (SIMS) and demonstrated that the grain coarsening of primary  $\alpha$  is accompanied by preferential oxygen enrichment of the  $\alpha$  grains with a corresponding decrease in oxygen content in the prior- $\beta$  matrix of the Zr-2.5%Nb alloy. In their work the authors have discussed in detail the effect of oxygen concentration on the microstructure, solid-solution hardening, strain aging that can adversely affect the ductility and toughness of the alloy.

Hong *et. al* [65] study on Zircalloy-4 reported that increasing the oxygen content increased the width of  $\alpha_{Zr}$  plates and in some cases, even the basket weave structure changed to parallel-plate structure. This result is similar to the one observed in the study by Choubey *et al.* [64] for the Zr-2.5%Nb alloy.

Chow *et. al* [66] described the processing steps for the fabrication of Heat Treated (HT) pressure tube which involved hot extrusion at 840°C followed by solution treatment at 870°C and water quenching. The tube was then cold drawn to about 15% and tempered at 500°C for 24 h. To achieve the final dimensions the tube was machined and then subjected to autoclaving for 72 h at 400°C. This procedure produced a mixture of primary- $\alpha$  grains in a matrix of martensite with more random texture compared to the Cold Worked (CW) tubes.

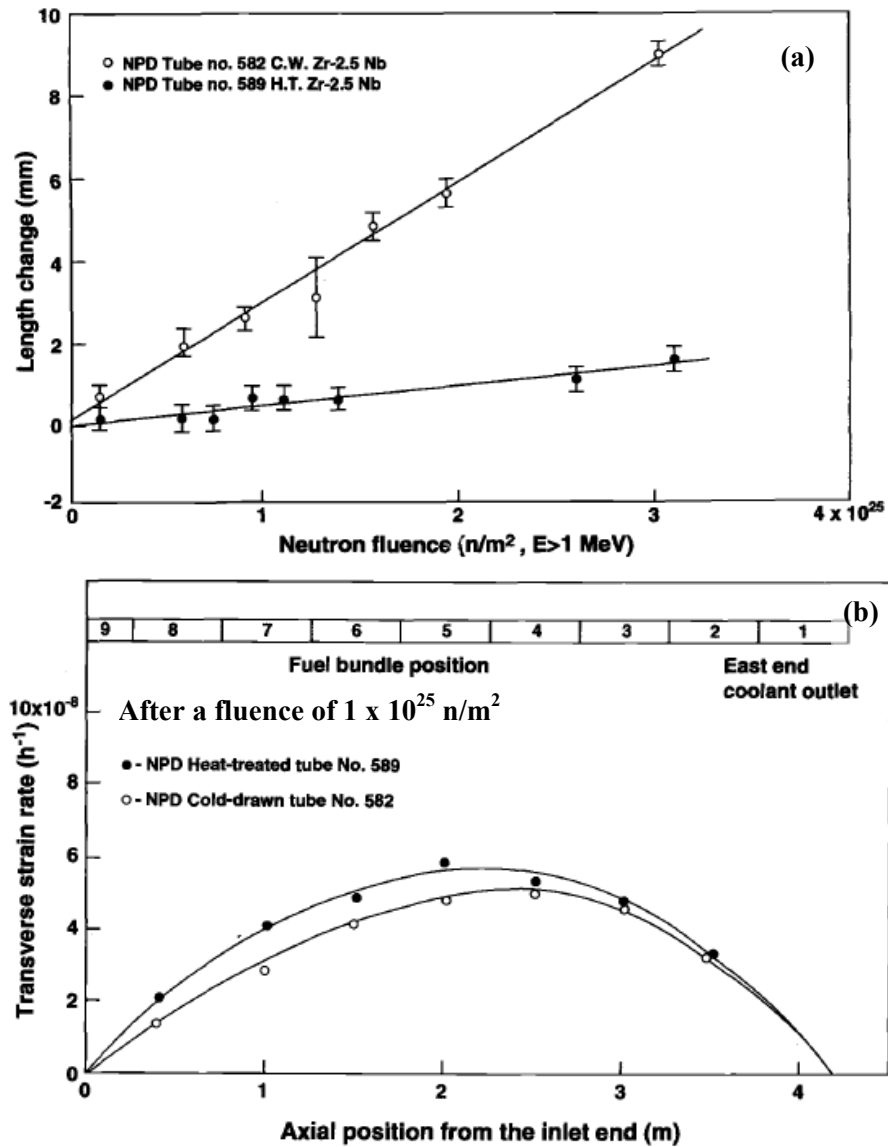
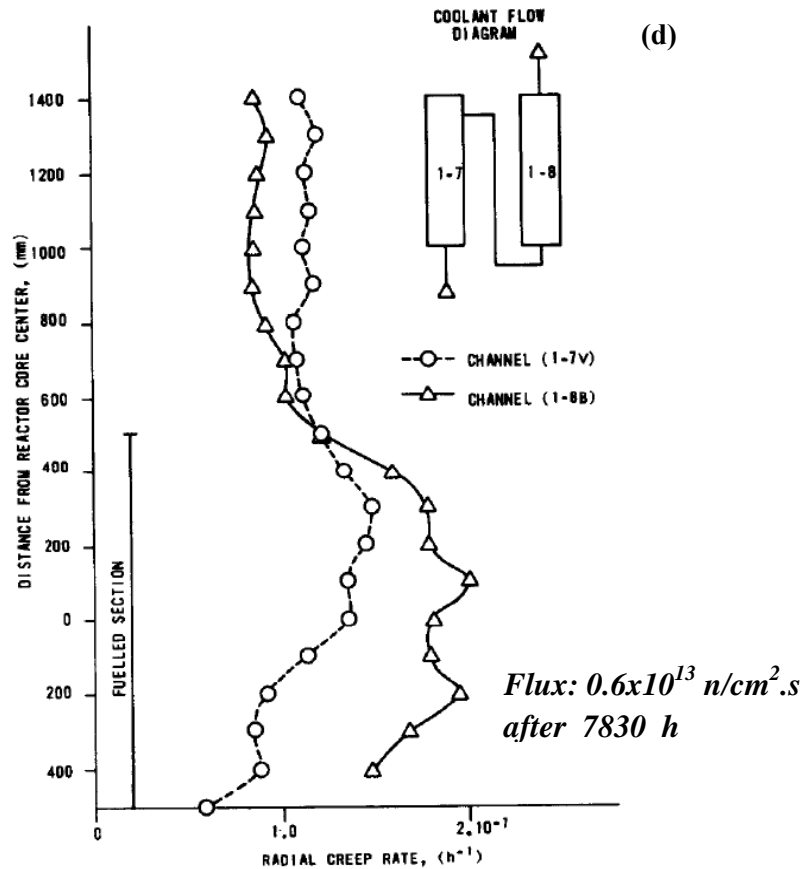
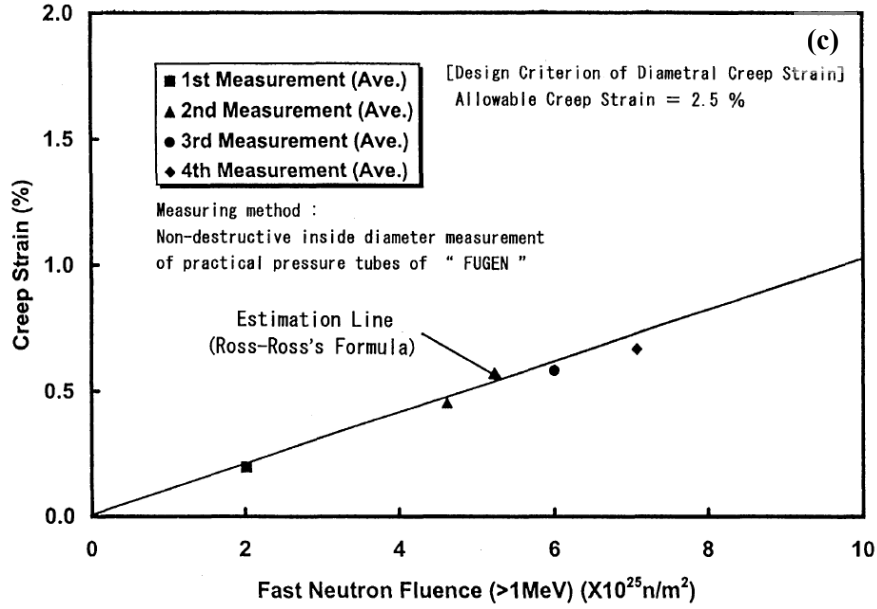


Fig. 2.13 (a) Length change of the HT and CW PTs of NPD as function of fluence [66],  
 (b) Transverse strain rate vs axial position of HT and CW PTs (After a fluence of  $1 \times 10^{25}$   $n/m^2$ ) [66]



2.13 (c) Diametral strain vs. neutron fluence measured for the operating pressure tube of FUGEN [6], (d) Radial creep rate of Zr-2.5%Nb heat treated PT of RBMK [67]

Chow *et. al* [66] presented the comparison of irradiation behavior of CW and HT pressure tubes. The study showed that axial elongation rate of HT pressure tubes was considerably lower compared to the CW pressure tubes of similar irradiation conditions (see Fig. 2.13 (a)). However, the circumferential creep rate for the HT tubes was observed to be marginally higher compared to the CW pressure tubes (See in Fig. 2.13 (b))

In another post irradiation study, Takayama [6] also reported the irradiation behaviour of HT pressure tubes. The author's study [6] observed that the measured diametral strain rate did not exceed the design criteria and also matched the Ross-Ross estimation. This result is shown in Fig.2.13 (c).

Goncharov *et.al* [67] reported the in-reactor diametral creep after 7830 h of operation for the Zr-2.5%Nb channel tubes heat treated at 550°C for 5h which is shown in Fig.2.13 (d). The authors Goncharov *et.al* [67] evaluated a safe design limit of 3% of diametral increase based on the observation that the tubes with higher strains up to 4.8% showed no signs of rupture.

In the summary, many authors [46, 56-65, 68] studied the microstructure and property correlations of dilute Zr-Nb alloys while some authors [56-59] discussed the nature of  $\beta$  phase transformation that resulted in martensitic structure with different morphologies and their crystallographic relationship with the parent  $\beta$ -phase. Some authors [13, 60-63] have discussed the microstructural developments and mechanical properties at various stages of manufacturing of Zr-2.5%Nb alloy pressure tube. Some [40, 65] discussed the effect of oxygen content on the microstructure. The effect of texture on the mechanical properties has been dealt with by Cai. *et. al* [68]. Some authors [6, 46, 66, 67] provided the valuable input on irradiation performance of the Zr-2.5%Nb pressure tubes fabricated from cold worked and heat treated routes in addition to the influence of minor alloying elements 'Fe' and 'O' contents in the alloy [6, 46, 66, 67].

The available data base on heat treatments, the microstructural and textural evolution and structure and property correlations is discrete which has significantly restricted the understanding of Zr-2.5%Nb alloy under irradiation. Therefore, the objective of this part of the work was to carry out a systematic study comprising of effect of soaking temperatures and cooling rates on the nature of  $\beta$ -phase transformation leading microstructural and textural evolution followed by structure and mechanical property correlations.

## 2.4 Thermal creep behavior of Zr-2.5%Nb pressure tube alloy

The thermal creep behavior of a material is strongly dependent on several metallurgical variables, such as microstructure, preferred orientation (*texture*), extent of cold work prior to creep, material chemistry and impurity contents. In Zr-2.5%Nb alloy ‘Nb’ plays an important role in creep resistance due to low diffusion rate of ‘Nb’ in  $\alpha_{Zr}$  phase [69]. In addition ‘Nb’ also improves corrosion resistance, strength and lowers the hydrogen pickup rate significantly during service in comparison to Zircaloy-2. Nam *et. al* [70] study of thermal creep at 400°C and 150 MPa showed that addition of 0.5%Nb to Zr drastically reduced the thermal creep rates. However, further addition of ‘Nb’ showed insignificant change in creep rates (see Fig. 2.14.)

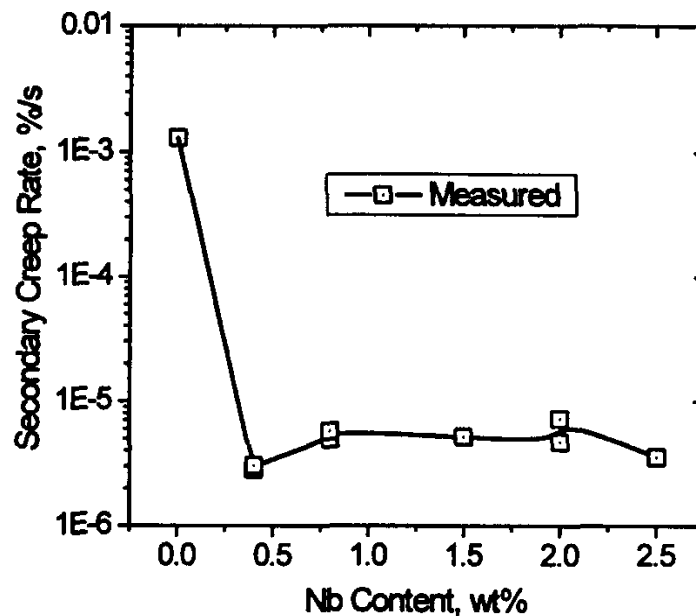


Fig. 2.14 Effect of ‘Nb’ concentration on thermal creep of Zr-Nb alloy at 400°C and 150 MPa [70]

The effect of independent variation of other minor alloying elements ‘Fe’ and ‘O’ on the thermal creep behavior of Zr-2.5%Nb pressure tube alloy at temperatures and stress levels close to reactor operation is an important part of this study. In the following a brief review of literature on the influence of these minor alloying elements on the thermal creep of the alloy is presented. A typical creep curve generally obtained in a conventional creep test comprises of three stages of creep viz: primary creep, secondary creep and the tertiary creep as shown Fig.2.15 (a). The primary creep is characterised by decreasing creep rate. The secondary creep is characterised by

steady state creep rate which is of practical significance considering the design and application of a component. The tertiary creep is marked by the accelerated creep rate is often associated with metallurgical changes, such as coarsening of precipitates and formation of voids which may lead to accelerated creep rates and eventual failure [15].

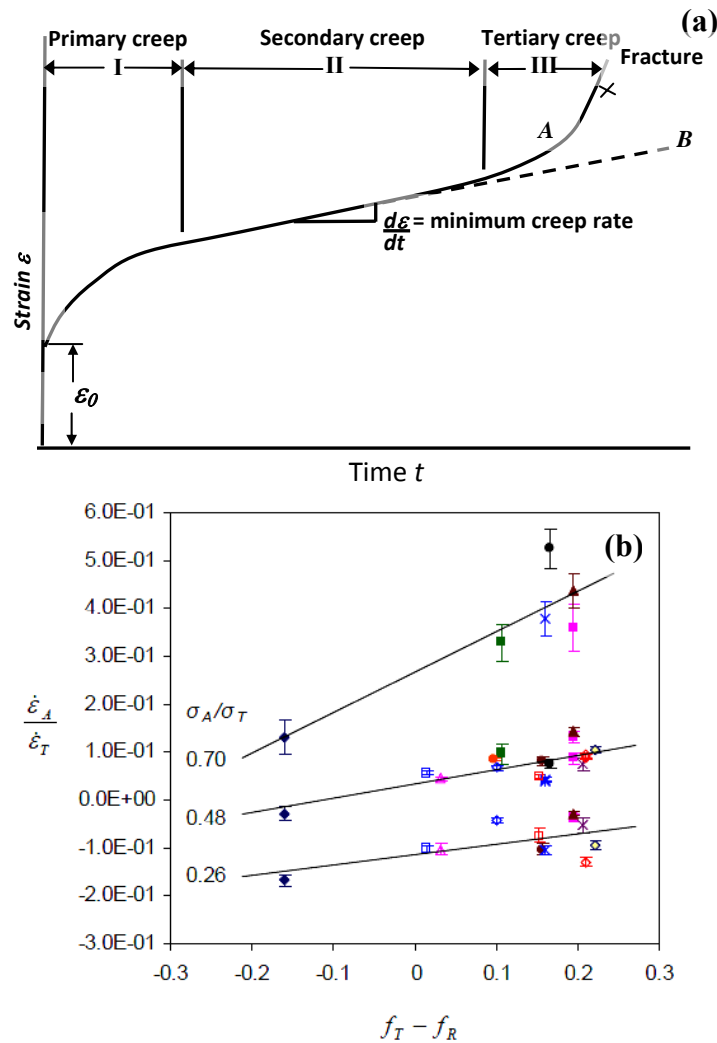
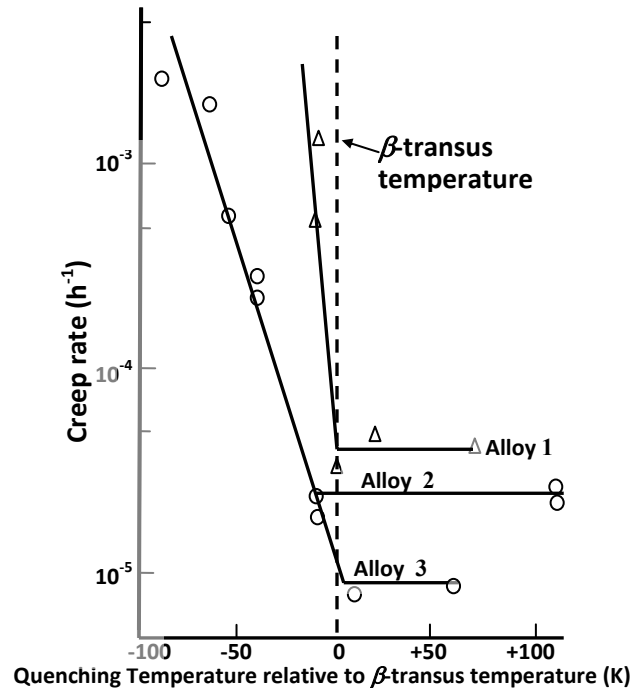


Fig. 2.15 (a) Typical creep curve, Curve A, constant-load test; Curve B, constant-stress test, (b) Experimental steady-state creep rate ratios between the axial and transverse directions versus texture parameters ( $f_t-f_r$ ) under a nominal transverse stress of 300MPa at 350°C under different stress ratios ( $\sigma_A/\sigma_T$ ) [15]

Li's [15] study used the biaxial creep tests on Zr-2.5%Nb alloy at 350°C and 300MPa (see Fig.2.15 (b)). The results showed the effect of texture variation i.e. ( $f_t-f_r$ ) on the creep rate ratio

$\dot{\epsilon}_A/\dot{\epsilon}_T$ . The results indicated direction of load applications is an important factor while assessing the mechanical behavior of anisotropic material like Zr-2.5%Nb pressure tube alloy.



*Fig. 2.16 The effect of oxygen concentration on the variation of creep rate at 723 K and 207 MPa of Zr-2.5 wt% Nb with solution temperature. [40]*

Kim *et. al* [71] studied the effect of minor alloying elements ‘Cu’, ‘Fe’ and ‘Nb’ on the thermal creep behavior of Zr-based alloys under constant stress in the range of 100 and 140 MPa at temperatures 280 and 330°C. The results showed that ‘Nb’ as an alloying element exhibited the strongest effect on the creep resistance followed by ‘Fe’ and ‘Cu’. Although the alloy materials used was not the Zr-2.5%Nb alloy, the relative influence of ‘Nb’, ‘Fe’ and ‘Cu’ on the steady state creep rates of the alloy has provided important input for the thermal creep studies planned in this work.

Fidleris [40] showed that the Zr-2.5wt%Nb alloy with oxygen content variation in the range of 800 and 1100 ppmw influenced the  $\beta$ -transus temperature. This resulted in variation in the fraction of primary  $\alpha$ -grains which influenced the thermal creep behavior studied at 723 K (see Fig. 2.16). This is an important result considering the fact that,  $\alpha$ -fraction controls the mechanical properties of the Zr-2.5wt%Nb alloy. Thus, literature study indicates that the effect of independent variation in ‘Fe’ and ‘O’ contents on the thermal creep of Zr-2.5%Nb alloy has

not been addressed adequately particularly at stress levels and temperatures close to reactor operation.

## **2.5 Inter-relationship of Coefficient of Thermal Expansion (CTE), Texture, ‘Fe’ and ‘O’ concentration in the Zr-2.5%Nb pressure tube alloy**

The thermal expansion behavior of Zr-2.5%Nb pressure tube alloy is strongly dependent on the direction of the component due to the preferred orientation of anisotropic  $\alpha_{Zr}$  phase. Therefore, it is expected that CTE would correlate with texture parameter  $f$  for the given direction of the tube. The phenomenon of irradiation growth is known to be related to the anisotropic thermal expansion [72] of the  $\alpha_{Zr}$  phase. Therefore, texture and CTE can exhibit similar kind of inter-relationship with irradiation behavior. Further, presence of alloying elements in the  $\alpha$  and  $\beta$  phases of the alloy is expected to change the lattice parameter and hence the CTE characteristics of the alloy. Nevertheless, the ‘Fe’ and ‘O’ concentrations in the alloy are known to influence irradiation behavior of the alloy [46]. Therefore in this thesis, it was of interest to study the inter-correlation of these parameters to ascertain that CTE can be used as a surrogate parameter for texture for the assessment and prediction of behavior of irradiated pressure tubes. In the following, a brief review of literature pertaining to the effect of ‘Fe’ and ‘O’ concentrations on CTE, texture and in-reactor deformation of Zr-2.5%Nb pressure tube is presented.

The thermal expansion of a solid is a property arising strictly due to the anharmonicity of the lattice vibrations [73]. In the case of anisotropic crystals like  $\alpha_{Zr}$  the anharmonicity of lattice vibrations along ‘ $c$ ’ and ‘ $a$ ’-axes differ drastically due to wide difference in atomic separation in these directions. It has been established that the CTE along < $c$ >-axis of the  $\alpha_{Zr}$  (*hcp*) is  $\sim 10.3 \times 10^{-6}/K$ , which is almost double the value for the < $a$ >-axis ( $\sim 5.8 \times 10^{-6}/K$ ) [14, 74]. Hull *et.al* [75] study on effect of composition on thermal expansion of Ti-alloy which is crystallographically similar to  $\alpha_{Zr}$  has shown that the minor alloying elements either in interstitial or substitutional position can influence the CTE significantly attributing to change in lattice parameter.

Holmberg and Dagerhamn [76] studied the effect of oxygen on lattice parameters of  $\alpha_{Zr}$  in the temperature range 400 and 800°C. It was shown that the  $a$ -axis of  $\alpha$ -zirconium increased with the increase in oxygen content from 3.232 Å to 3.256 Å at 20 at.%, then decreased to 3.245 Å at

the solubility limit (28.6 at.%), whereas the lattice parameter for *c*-axis increased continuously to 5.207 Å at the solubility limit. Similarly, the lattice parameter of  $\beta$ -zirconium-niobium solid solution reported by Rogers and Atkins [30], showed a linear increase with increase in zirconium content. However addition of oxygen to  $\beta_{Zr}$  phase showed nearly linear decrease with increasing oxygen concentration. This result is important indication for assessment of CTE as a function of oxygen and iron in the Zr-2.5%Nb pressure tube alloy.

In one of the models of irradiation growth in zirconium, it has been proposed that the collision of fast neutrons removes atoms from the basal plane and redistributes them on the prism planes [77]. Therefore, the direction which shrinks during irradiation corresponds to the direction of highest thermal expansion coefficient [72]. In the case of Zr-2.5%Nb pressure tube alloy, the irradiation growth causes shrinking along the  $\langle c \rangle$ -axis i.e. along [0001] direction and expansion along the  $\langle a \rangle$ -axis i.e. along  $[11\bar{2}0]$  which can be attributed to the mechanism called Diffusional Anisotropy Difference (DAD) [14, 46, 72, 77]

The anisotropy of a material is best represented by the Kearn's texture parameters [78] for any selected crystallographic plane which is known as texture factor  $f$ . The  $f$  texture factor was developed by Kearn's [78] to provide a means to resolve basal pole [0001] distribution into an effective fraction in each of the three principal directions ( $f_a, f_r, f_t$ ) of an as-fabricated component of *hcp* type materials such as Zr-alloys. The sum of  $f$  values from all three directions is 1.0 regardless of texture. For a single crystal the basal poles in one direction yields an  $f$  value of 1.0 and zero in other two directions. A value of  $f = 1/3$  for all the three directions would mean random orientation of the crystals in the matrix. The  $f$  values may be used to account quantitatively the texture effects in properties such as thermal expansion, irradiation growth and other physical and mechanical properties.

Tempest [79] put forward the idea that, in a polycrystalline aggregate the randomly oriented anisotropic crystals can provide no shape change under neutron irradiation as effective dimensional changes can be negligible in any direction. However, fabrication processes of Zr-based alloys can lead to preferred orientation of anisotropic  $\alpha_{Zr}$  phase resulting in strong texture in the final product. As a result physical and mechanical properties and in-reactor deformation behavior of the component are anisotropic. A detailed investigation of relationship between

preferred orientation (*texture*) and thermal expansion in the polycrystalline Zircaloy-2 and Zircaloy-4 reported by Kearns [78] is shown in Fig. 2.17 (a).

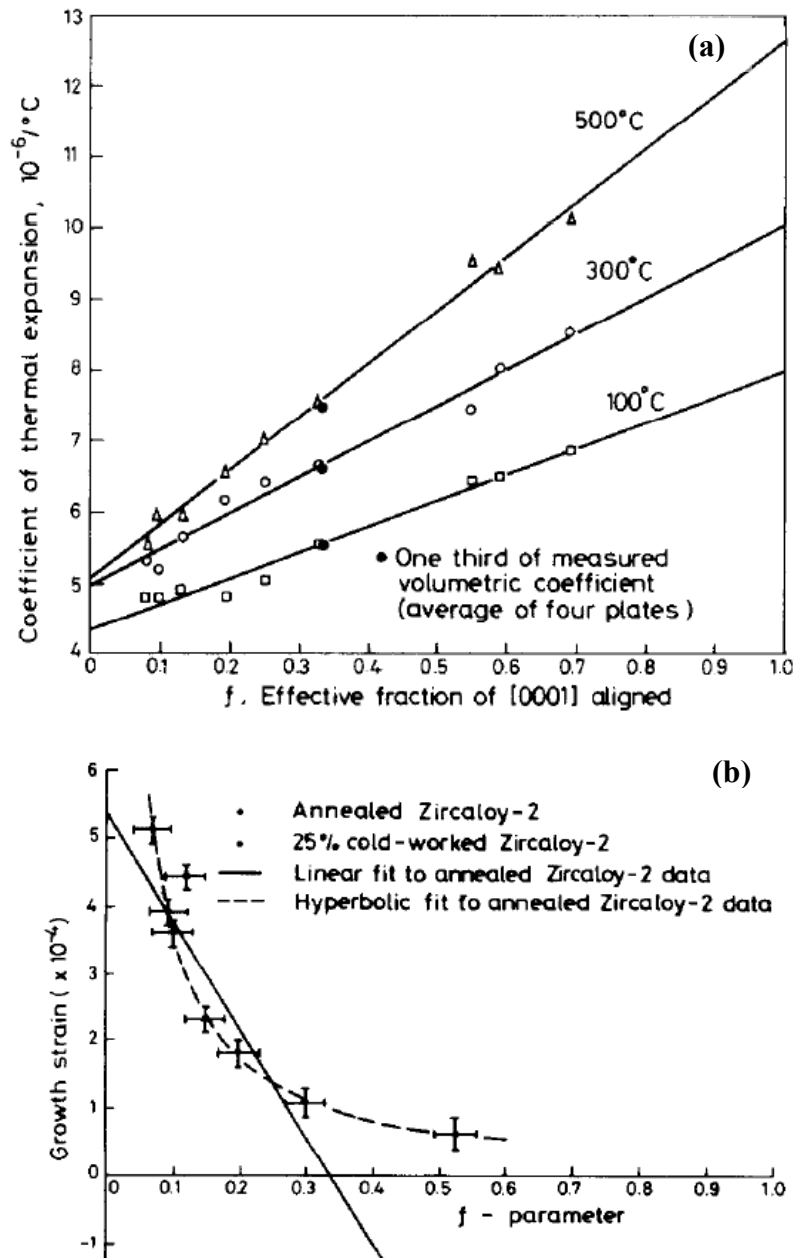


Fig. 2.17 (a) Correlation of expansivity with X-ray measurements of preferred orientation (after Kearns) [78], (b) Growth strain at 80°C against  $f$  parameter (after Rogerson and Murgatroyd) [79, 80]

The linear relationship of CTE vs. texture presented in Fig. 2.17 (a) for the single phase alloys is an important input for the present study. Rogerson and Murgatroyd [79, 80] reported the

important result of relationship of growth strain for the Zircaloy-2 material with the texture parameter ( $f$ ) which is shown in Fig. 2.17 (b). This result shows that the irradiation induced growth strain decreased approximately linearly as the  $f$ -parameter in the region of  $0 < f < 0.33$  for the alloy.

Thus the literature study indicates that there is a scope for studying inter-relationship of CTE, texture parameter  $f$  and also irradiation behavior as a function of minor alloying elements which was the motive behind this part of the work.

Therefore the objective of this part of the work was,

1. To study the correlation of CTE with texture parameters of the dual phased Zr-2.5%Nb pressure tube alloy in the as fabricated condition and ascertain the sensitivity of CTE to textural changes.
2. To study the effect of independent variation of 'Fe' and 'O' concentrations on the axial and circumferential CTE and also the texture parameters of the as fabricated Zr-2.5%Nb pressure tube samples
3. To study the inter-relationship of CTE, texture and in-reactor deformation behaviour and 'Fe' and 'O' contents of the operating Zr-2.5%Nb pressure tubes.

## **2.6 Miniature specimen testing methods for evaluation of mechanical properties**

In the present study, since the specimens used were small in size, the miniature specimen testing techniques such as the Small Punch Test (SPT), Automated Ball Indentation (ABI) and impression / indentation creep tests were employed for establishing mechanical properties. A brief review of literature pertaining to these miniature techniques is presented in the following.

The miniature specimen testing techniques are essentially innovative and nonconventional techniques developed for evaluation of key mechanical properties through establishment of correlation parameters using some conventional testing methods such as ASTM [81-84]. Many authors [81- 85] have used the ABI technique for evaluation of key mechanical properties of test pieces and the operating steel pipelines insitu, and successfully adopted the results for performance evaluation and life management of operating components. Similarly, some authors [86, 87] used the SPT technique and systematically established correlation parameters for the steel materials and obtained mechanical property data for the alloy. The mechanical property

data established in this manner were in good agreement with the conventional tension test data. The authors at [81-87] describe that the correlation parameters for a given miniature testing technique are material specific and need to be determined separately for different class of materials adopting recommended procedure [84, 85, 88, 89]. Many authors [81-85, 88, 89] have dealt with correlation parameters for the steel materials which is a most common macroscopically isotropic alloy used in the industries for many applications. Generally the procedure for establishment of correlation parameters for evaluation of key mechanical properties such as yield strength and ultimate tensile strength involves regression analysis of different strength representing values with the corresponding tensile strength data (*conventional test data*) obtained for the same specimen condition. The literature review has indicated that no work pertaining to such correlation parameters for evaluation of mechanical properties of anisotropic Zr-base alloys using ABI and SPT has been reported in the open literature. Therefore the first objective of this part of the work was to establish the correlation parameters for evaluation of key mechanical properties of anisotropic Zr-2.5%Nb alloy material for ABI and SPT techniques. Since Zr-2.5%Nb alloy being anisotropic, the primary interest was to study the effect of direction of load application on the mechanical properties (*due to texture effects*). In addition the work was also aimed to understand the sensitivity of these techniques to variations in microstructures, so that these techniques can be adopted for performance evaluation of components.

## References- Chapter-2

1. W. Li, R.A. Holt, *J.Nucl. Mater.*, 401 (2010) 25-37
2. I.S. Lupakov, B.G. Parfenov, A.I. Gromova, (UDC 669.018.8:546.831), Translated from *Atomnaya Energlya*, 20, No. 4 (1966) 330-333
3. S.S. Bajaj, A.R. Gore, *Nucl. Eng. Des.*, 236 (2006) 701-722
4. V.F. Urbanic, M. Griffiths, *American Society for Testing and Materials (ASTM)*, STP 1354 (2000) 641-657
5. A. Couet, A Thesis in Nuclear Engineering for Master of Science, August 2011, The Pennsylvania State University The Graduate School Department of Nuclear Engineering
6. K. Takayama “*Post-Irradiation Examination And Evaluation of Zr-2.5%Nb Pressure Tube of FUGEN*”, XA9846758, 181-192
7. International Atomic Energy Agency, Vienna, TECDOC-1410, “Delayed hydride cracking in zirconium alloys in pressure tube nuclear reactors” *Final report of a coordinated research project 1998-2002, October 2004*
8. C. Coleman, M. Griffiths, V. Grigoriev, V. Kiseliiov, B. Rodchenkov, V. Markelov, *J. (ASTM), International, (JAI), Paper ID JAI101111, 4, No. 10 (2007)*
9. D. Srivastava, G.K. Dey, S. Banerjee, *Metall. Mater. Trans. A*, 26A (1995) 2707-2718
10. N. Saibaba, S.K. Jha, S. Tonpe, Kumar Vaibhaw, V. Deshmukh, S.V. Ramana Rao, K.V. Mani Krishna, S. Neogy, D. Srivastava, G.K. Dey, R.V. Kulkarni, B.N. Rath, E. Ramadasan, S. Anantharaman, *J. (ASTM), International, DOI:10.1520/JAI103213, (JAI) Paper ID JAI103213, 8 No. 6, (2011)*
11. Y. Ding, D.O. Northwood, *Corros. Sci.*, 36, No.2 (1994) 259-282
12. R.A. Holt, R. G. Fleck, *(ASTM), STP 1023 (1989) 705-721*
13. D.O. Northwood, W.L. Fong, *Metallography*, 13 (1980) 97- 115
14. S. Cai, PhD Thesis, “*Evolution of Interphase and Intergranular Strain in Zr-Nb alloys During Deformation at room Temperature*”, Oct 2008, Dept. of Mechanical and Materials Eng. University Kingston Canada, Publication Ref; ISBN, 0494443162, 9780494443163
15. W. Li, PhD Thesis “*Effect of Texture on Anisotropic Thermal Creep Of Pressurised Zr-2.5%Nb Tubes*”, Queen’s University Kingston, Ontario, Canada August, 2009

16. A. Peruzzi, T. Bolcich, *J. Nucl. Mater.*, 174 (1990) 1-15
17. V. Fidleries, *J. Nucl. Mater.*, 159 (1988) 22-42
18. G. E. Dieter, “*Mechanical Metallurgy*” McGraw Hill book Company, London (1988)
19. C.N. Rao, *J. Mater. Sci. Lett.*, 11 (1992) 1429-1430
20. P.M. Kelly, K.G. Watson, *J. Nucl. Mater.*, 44 (1972) 71-78.
21. D.O. Northwood, J.W. Robinson, Z. Jie, “*Textures and Microstructures*”, 13(1991)133-154
22. C. Coleman, M. Griffiths, V. Grigoriev, V. Kiseliov, B. Rodchenkov, V. Markelov, *J. (ASTM), STP 1505, (JAI) Paper ID: JAI101111, 4, Issue 10 (2007)*
23. R.A. Holt, N. Christodoulou, A.R. Causey, *J. Nucl. Mater.*, 317 (2003) 256-260
24. S. Kim, *Metall. Mater. Trans. A*, 37A (2006) 59-68
25. R.A. Holt, S.A. Aldridge, *J. Nucl. Mater.*, 135 (1985) 246-259
26. R.A. Holt, P. Zhao, *J. Nucl. Mater.*, 335 (2004) 520–528
27. I.T. Bethune, C.D Williams, *AECL-2715 (1968)*
28. C.E. Lundin, R.H. Cox, *USAEC Report No. 1/At(11-1)-752 (1960)*
29. H. Richter, P. Wincierz, K. Anderko, U. Zwicker, *J. Less Common Metals*, 4(1962)252-265
30. B.A. Rogers, D.F. Atkins, “*Zirconium-columbium diagram*”, *Trans. AIME*, 203 (1955)1034-1051
31. C.E. Lundin, R.H. Cox, “The determination of the equilibrium phase diagram, zirconium-niobium”, *U.S. Atomic Energy Comm. Technical Information Service Extension, Washington 25, D.C., Research and Development Rep. TID-11919 (1960)*
32. J.J. Jonas, B.H.E. Richter, M.J. Luton , *Metall. Trans. A*, 10A,(1979) 611-620
33. M. Griffiths, J.E. Winegar, A.J. Buyers, *J. Nucl. Mater.*, 383, No.1-2 (2008) 28-33
34. C.E.L. Hunt, P. Niessen, *J. Nucl. Mater.*, 35 (1970) 134-136
35. C.E.L. Hunt, P. Niessen, *J. Nucl. Mater.*, 38 (1971) 17-25
36. R. Jerlerud Pe´rez, A.R. Massih, *J. Nucl. Mater.*, 360 (2007) 242–254
37. D.O. Northwood, D.C. Gillies, *Microstruct. Sci.*, 7 (1979) 123-132
38. C. Toffolon, J.C. Brachet, C. Servant, L. Legras, D. Charquet, P. Barberis, J.P. Mardon, in, G. Moan, P. Rudling (Eds.), *American Society for Testing and Materials, STP 1423, (2002) 361-383*

39. H.G. Kim, J.Y. Park, Y.H. Jeong, *J. Nucl. Mater.*, 347 (2005) 140-150
40. V. Fidleris, *J. Nucl. Mater.*, 54 (1974)199-211
41. A. Perovic, V. Perovic, G.C. Weatherly, G.R. Purdy, R.G. Fleck, *J. Nucl. Mater.*, 199 (1993) 102-111
42. D. Stewart, B. A. Hatt, J. A. Roberts, *Brit. J. Appl. Phys.* 16 (1965) 1081
43. G. F. Slattery, *Electrochem. Tech.* 4 (1966) 336
44. G. T. Higgins, E. E. Banks, *BRIT. J. Appl. Phys.*, 17 (1966) 283-284
45. M.P. Puls, *Nucl. Eng. Des.*, 171 (1997) 137-148
46. R.A. Holt, *J. Nucl. Mater.*, 372 (2008) 182-214
47. E. F. Ibrahim, *J. Nucl. Mater.*, 96 (1981) 297-304
48. R.A. Holt *J. Nucl. Mater.*, 90 (1980) 193-204
49. C.H. Woo, *J. Nucl. Mater.*, 159 (1988) 237-256
50. R. Adamson, F. Garzarolli, C. Patterson, “In-Reactor Creep of Zirconium Alloys -2009”, September 2009 Advanced Nuclear Technology International Krongjutarvägen 2C, SE-730 50 Skultuna, Sweden
51. S. Neogy, D. Srivastava, G. K. Dey, J. K. Chakravartty, S. Banerjee, *Trans. Indian Inst. Met.*, 57, No. 5 (2004) 509-519
52. M. Griffiths, N. Christodoulou, S.A. Donohue, *J. (ASTM), International, (JAI) Paper ID JAII2432, 2 No. 7 (2005)*
53. R. A. Holt, E. F. Ibrahim, *Acta Metall.*, 27 (1979 )1319-1328
54. G.M. Hood, H. Zou, D. Gupta, R.J. Schultz, *J. Nucl. Mater.*, 223 (1995) 122-125
55. A.D. King, G.M. Hood, R.A. Holt, *J. Nucl. Mater.*, 185 (1991) 174-181
56. R. Tewari, D. Srivastava, G.K. Dey, J.K. Chakravarty, S. Banerjee, *J. Nucl. Mater.*, 383 (2008)153-171
57. D. Srivastava, P. Mukhopadhyay, S. Banerjee, S. Ranganathan, *Mater. Sci. Eng. A*, 288 (2000) 101-110
58. D. Srivastava, K. Madangopal, S. Banerjee, S. Ranganathan, *Acta metal, mater.*, 41, No. 12 (1993) 3445-3454

59. G. K. Dey, R. N. Singh, R. Tiwari, D. Srivastava, S. Banerjee, *J. Nucl. Mater.*, 22 (1995) 146-157
60. M.K. Kumar, I. Samajdar, N. Venkatramani, G.K. Dey, R. Tewari, D. Srivastava, S. Banerjee, *Acta Mater.*, 51 (2003) 625–640
61. M.K. Kumar, C. Vanitha, I. Samajdar, G.K. Dey, R. Tewari, D. Srivastava, S. Banerjee, *J. Nucl. Mater.*, 335 (2004) 48-58
62. K. Kapoor, K. Muralidharan, N. Saratchandran, *JMEPEG*, 8 (1999) 61-67
63. D. Srivastava, G.K. Dey, S. Banerjee, *Metall. Mater. Trans. A*, 26A (1995) 2707-2718
64. R. Choubey, J.A. Jackman, *Metall. Mater. Trans. A*, 27A (1996) 431- 440
65. H.S. Hong, S.J. Kim, K.S. Lee, *J. Nucl. Mater.*, 265 (1999) 108-111
66. C.K. Chow, C.E. Coleman, M.H. Koike, A.R. Causey, C.E. Ells, R.R. Hosbons, S. Sagat, V.F. Urbanic, D.K. Rodgers, (*ASTM*), *STP 1295* (1996) 469-491
67. V.V. Goncharov, P.A. Platonov, A.N. Ivanov, I.A Frolov, *J. Nucl. Mater.*,90(1980)224-231
68. S. Cai, M.R. Daymond, R.A. Holt, *Acta Mater.*, 57 (2009) 407-419
69. H.G. Kim, J.Y. Park, Y.H. Jeong, *J. Nucl. Mater.*, 345 (2005) 1-10
70. C. Nam, K.H. Kim, M.H. Lee, Y.H. Jeong, *J. Korean Nucl. Soc.*, 32, No.4(2000) 372-378
71. H.G. Kim, Y.H. Kim, B.K. Choi, Y. Jeong, *J. Nucl. Mater.*, 359 (2006) 268-273
72. P.R. Roy, D.N. Sah, *PRAMANA*, 24 Nos 1-2 (1985) 397-42
73. S. Sindhu, C.S. Menon, *PRAMANA, Indian Academy of Sciences, J. physics* 67, No.3 (2006) 535-540
74. C. N. Tomé, N. Christodoulou, P. A. Turner, M. A. Miller, C. H. Woo, J. Root and T. M. Holden: *J. Nucl. Mater.*, 227 (1996), 237-250
75. F.C. Hull, S.K. Hwang, J.M. Wells, and R.I. Jaffee, *J. Mater. Eng.*, 9 (1987) 81-92
76. B. Holmberg, T. Dagerhamn, “*X-ray studies on solid solutions of oxygen in  $\alpha$ -zirconium*”, *Acta Chem. Scand.*, 15 (1961) 919-925
77. N. T. Chebotarev, UDC 621.039.543.4, *Atomic Energy*, 85, No.1 (1998) 438-446
78. J.J. Kerans, *J. Nucl. Mater.*, 299 (2001) 171-174
79. P.A. Tempest, *J. Nucl. Mater.*, 92 (1980) 191-200
80. A. Rogerson, R.A. Murgatroyd, *J. Nucl. Mater.* 80 (1979) 253

81. F.M. Haggag, J. A. Wang, Proc., *“Nondestructive Evaluation of Aging Aircraft, Airports and Aerospace Hardware*, doi,10.1117/12.259096, SPIE 2945 (1996) 217-228
82. F.M. Haggag, L.D Phillips, IPC04-0345, *Proceedings of IPC 2004, American Society for Mechanical Engineering (ASME), International Pipeline Conference Oct, 2004*
83. F.M. Haggag, L.D Phillips, IPC04-0357, *Proceedings, IPC 2004, American Society for Mechanical Engineering (ASME), International Pipeline Conference Oct.2004*
84. W. R. Corwin, F. M. Haggag, W. L. Server, (ASTM), *STP 1204 (1993) 27-44*
85. F.M. Haggag, K.L. Murty *“The Minerals, Metals and Materials Soc. ,“Nondestructive Evaluation and Materials Properties III”*, (1997) 101-106
86. Y. Xu, G. Ning, C. Zhang, Q. Yu, *Int. J. Pressure Vessels and Piping*, 77 (2000) 715-721
87. X. Mao, H. Takahashi, *J. Nucl. Mater.*, 150 (1987) 42-52
88. K.L. Murty, M.D. Mathew, Y. Wang, V.N. Shah, F.M. Haggag, *Int. J. Pressure Vessels and Piping*, 75 (1998) 831–840
89. H. Takahashi, T. Shoji, X. Mao, Y. Hamaguchi, T. Misawa, M. Saito, T. Oku, T. Kodaria, F. Fukaya Kioshi, H. Nishi, M. Suzuki, *“Recommended practice for Small Punch (SP) testing of metallic materials (Draft), JAERI-M-88-172 (Report), September (1988)1-19*

## CHAPTER 3: Experimental Techniques and Procedures

---

The following subsections deal with brief description of all the techniques, specimen preparations and the calibration methods used in the present study.

### 3.1 High Speed Quenching Dilatometer (HSQD) and calibrations

The High Speed Quenching Dilatometer (*model DIL805A*) used in the study is a pushrod type dilatometer. The equipment has arrangement of a Linearly Variable Differential Transformer (LVDT) with resolution of  $0.1\mu\text{m}$  for length change measurement of a solid sample and a spot welded S-type thermocouple (*Pt/Pt-10%Rh*) having resolution of  $0.1^\circ\text{C}$  for temperature measurement as shown in Fig. 3.1 (a). The specimen dimensions used in the study is shown in Fig. 3.1 (b). The thermocouple wires were spot welded at the centre of the cylindrical surface of the specimen as per the standard procedure [1, 2] in all the experiments.

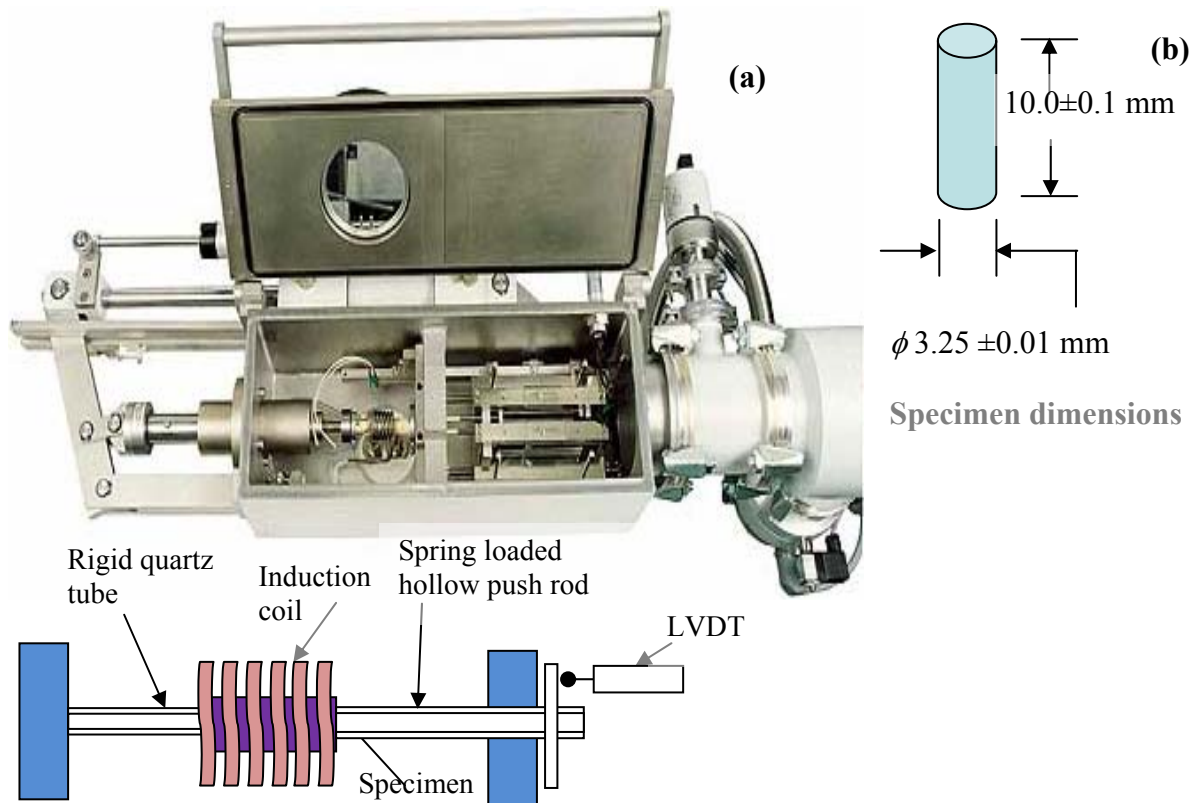


Fig. 3.1(a) A view of test chamber of DIL 805A and a schematic view of push rod arrangement for measuring the length change, (b) Specimen dimensions used in the study

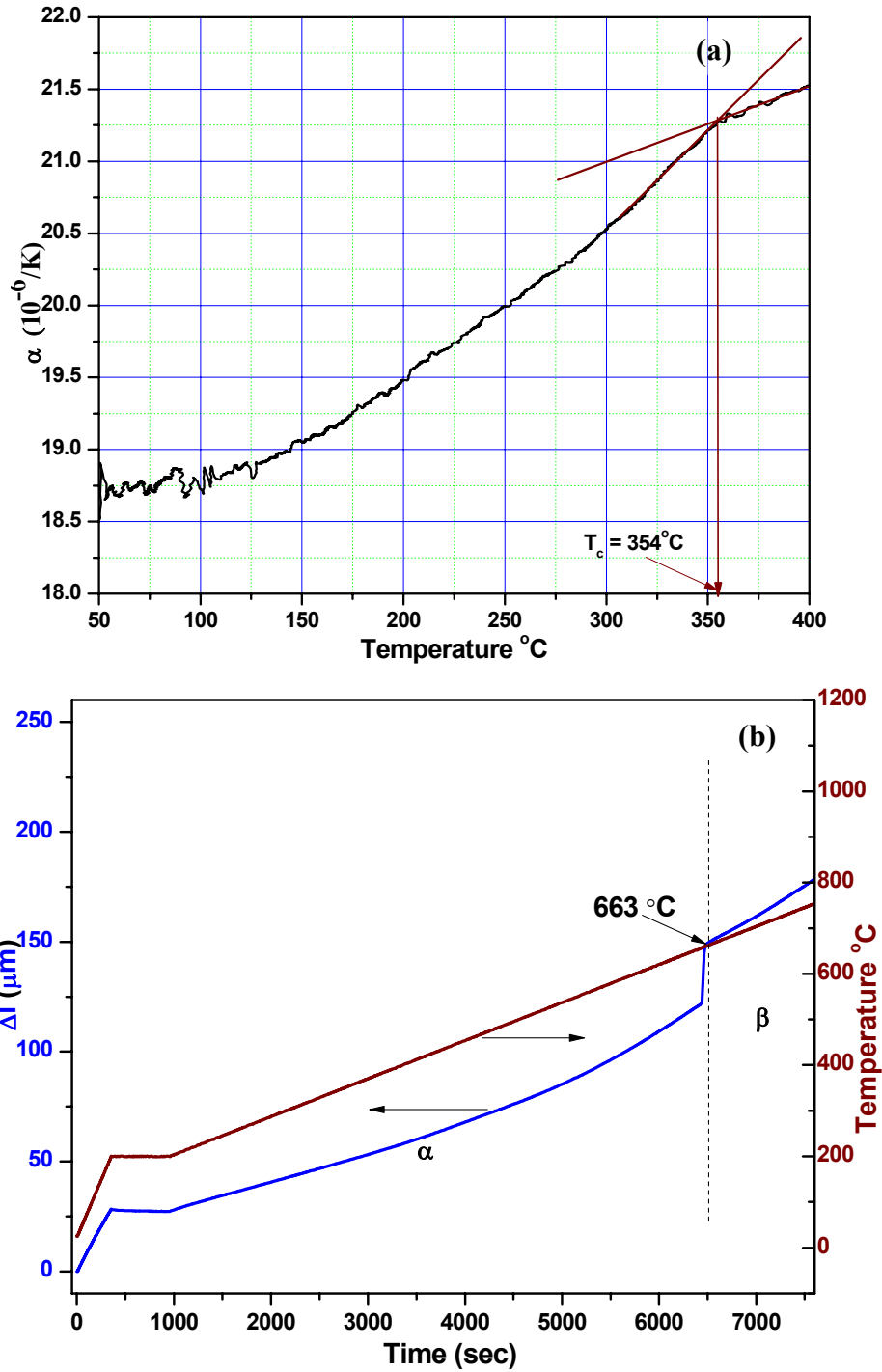


Fig.3.2 (a) CTE Vs Temperature curve for pure 'Ni' (99.999%) showing Curie temperature ( $T_c$ ) at 354 $^{\circ}C$ , (b) The  $\Delta l$  and Temperature vs. time curve showing  $\alpha \rightarrow \beta$  allotropic transformation of pure Uranium (99.9%) at 663 $^{\circ}C$

To minimise the errors associated with the length-change measurements, the quartz pushrods were used as quartz has low thermal conductivity as well as low linear thermal expansion coefficient (LTEC) of  $0.5 \times 10^{-5} \text{ }^\circ\text{C}^{-1}$  [3]. To achieve the programmed temperature a computer controlled Radio Frequency (RF) induction heating system was used. The change in length and temperature of the specimen were recorded as a function of time in a computerised data logging system during the experiment. It was established from a number of test experiments that a maximum quenching rate of  $\sim 20^\circ\text{C/s}$  could be achieved under the dynamic vacuum of  $\sim 2.0 \times 10^{-2}$  mbar, whereas under high purity ambient ‘He’ gas flow, the maximum quenching rate achievable was  $\sim 100^\circ\text{C/s}$ . For still higher cooling rates the controlled flow of liquid  $\text{N}_2$  chilled ‘He’ gas was used. This arrangement could provide a maximum cooling rate of  $\sim 300^\circ\text{C/s}$ .

### 3.1.1 Calibration of temperature measurement

The temperature measurement of the dilatometer was calibrated by Curie temperature method [3, 4] using a pure Ni sample (99.999%). Fig.3.2 (a) shows the measured Curie temperature ( $T_c$ ) of pure ‘Ni’ sample as  $354^\circ\text{C}$  which is similar to that reported in the literature [5, 6]. The temperature measurement was further verified by measuring  $\alpha \rightarrow \beta$  transition temperature of pure Uranium (99.9%) metal which also was similar to the one reported in the literature (see Fig. 3.2 (b)) [7]. Hence, all the phase transformation temperatures established using dilatometry in this study were corrected according to the above calibration figures.

### 3.1.2 Calibration of length change measurement

The LVDT of the dilatometer was calibrated using a pure ‘Fe’ sample (99.999%) employing standard procedure [3, 4, 8]. The heating rate of  $5^\circ\text{C/min}$  was used during calibration and also in the all experiments. Fig. 3.3 (a) shows the relative length change for the pure ‘Fe’ specimen measured as a function of temperature using the dilatometer. Fig.3.3 (a) also shows standard ( $dL/L_0$ ) values as a function of temperature for the pure ‘Fe’. The correction to the length change measurement for a given temperature was calculated using the standard procedure [3,4,8]. These results have been plotted as a function of temperature as shown in Fig. 3.3 (a). The correction to the measured length change of all the samples pertaining to the temperature range of calibration

has been incorporated as per the standard procedure [8]. Fig. 3.3 (b) shows the CTE results of the pure 'Fe' sample before and after applying the length change correction.

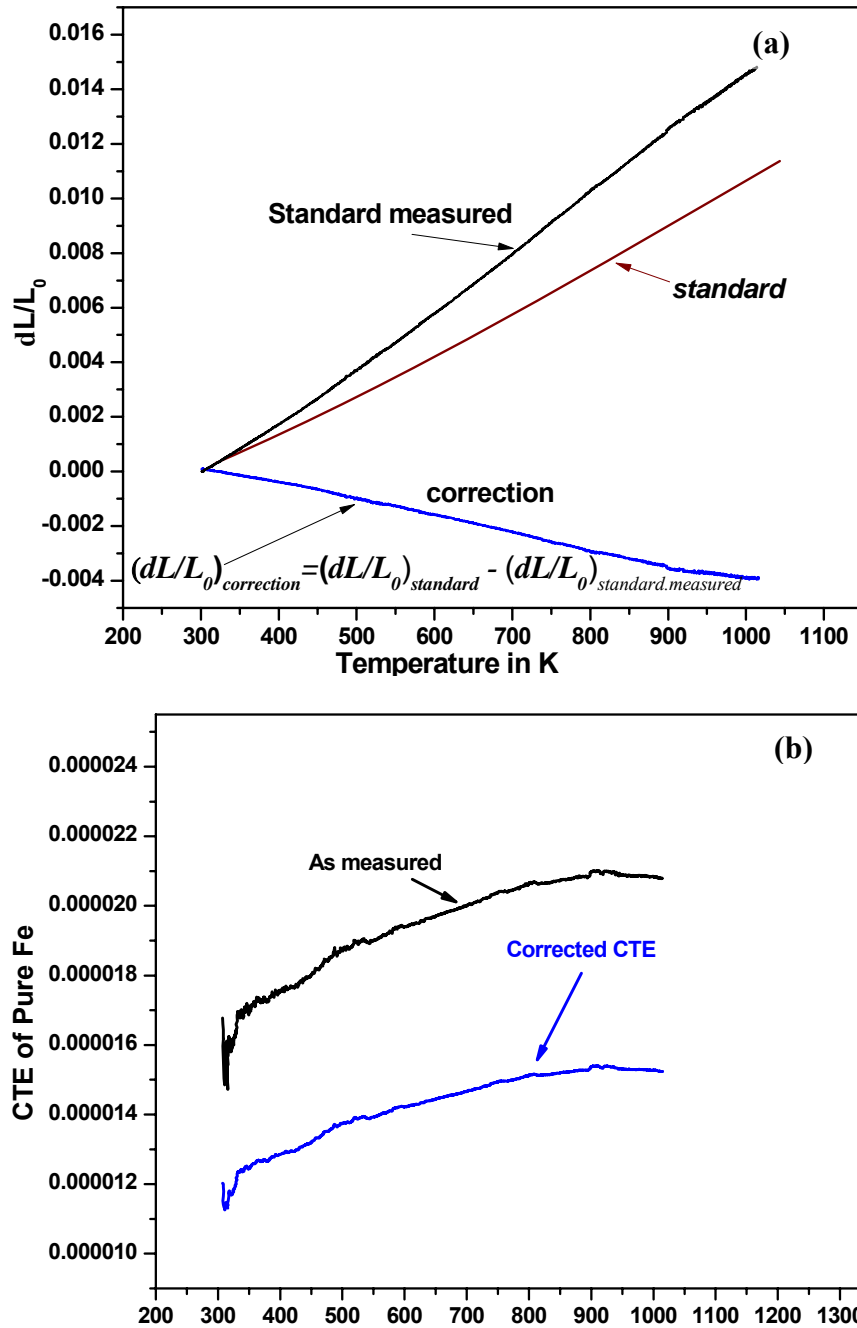


Fig. 3.3 (a) The plot showing  $(dL/L_0)$  measured, recommended and calibration vs. temperature for the pure iron sample. Recommended relative length change relationship for the pure 'Fe' is expressed as,  $(dL/L_0)_{\text{standard}} = -2.89E-3 + 7.35E-6 T + 9.33E-9 T^2 - 3.14E-12 T^3$  [4], (b) CTE measured and CTE after correction vs. temperature for the pure 'Fe' sample

### 3.1.3 Evaluation of dilatometric curves for phase transformations and CCT diagram

The phase change during phase transformations is usually accompanied by a significant change in specific volume which generally produces an observable dilatation that is different from the thermal expansion effect [3, 4, 9-15]. Therefore, dilatometry is a powerful technique for the study of phase transformations in alloys because it permits the real-time monitoring of the extent of transformation reactions in terms of dimensional changes [3, 4, 9-15]. Actually this technique allows us to determine kinetics of phase transformation [10, 12-18]. A schematic curve depicting normally observed dilation curve during phase transformation in a dilatometer is shown in Fig. 3.4. A straight line part of the curve indicates thermal dilation for the given phase of the material [3, 4, 9, 13]. The phase change in the sample produces change in specific volume during the phase transformation which is reflected by change in slope of the dilation curve as shown in Fig. 3.4. The change in specific volume is the consequence of product phases having different crystal structures with different lattice parameters, solubilities of solute atoms and thermal expansion coefficients of the product phases [13, 15, 19].

From the  $\Delta L$  vs.  $t$  curve during continuous heating/cooling, the beginning of a transformation range is signified by the deviation from the straight line as shown by tangents drawn at (*tangent method*) points A and B in Fig. 3.4). The tangent method of evaluation is based on progress of change in specific volume and it allows observing quantitatively the dynamics of transformation [20]. If the curve continues into another straight line, then the transformation in that field is considered to be finished. The points of departure from linearity of the dilation curve specify intervals of temperatures ( $T_A$  and  $T_B$ ) for the transformation. In the case of study on CCT diagram, the point of departure from linearity of the dilation curve [17, 18, 20] is of significance and hence has been used for identifying transformation start and finish temperatures of particular phase transformation.

The points C and D in Fig. 3.4 show the transformation region on  $\Delta l$  vs.  $t$  curve obtained from three tangents method. The temperature interval established from this method corresponds to the phase transformation taking place certainly in a substantial part of a specimen volume [20]. In the present study this method has been used for studying the effect of 'Fe' and 'O' content on the  $(\alpha+\beta)/\beta$  phase boundary of the alloy in the present study.

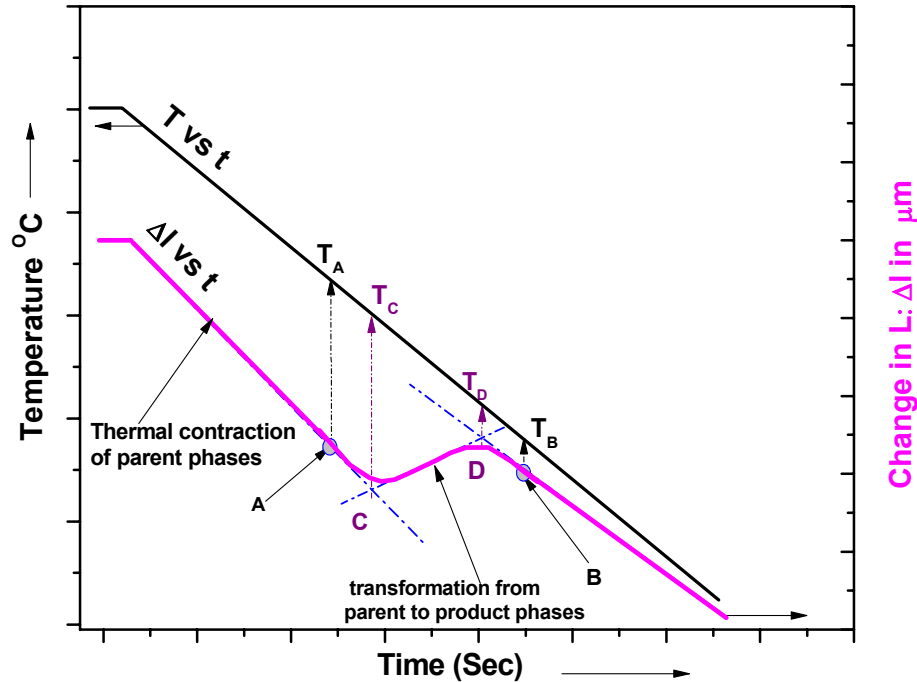


*Fig. 3.4 Schematic representation of dilation curve during cooling, Points A and B represent the start and end of transformation. The three tangent method is shown for determining the transformation temperatures as identified by points C and D.*

### 3.1.4 Material and specimen preparation for determination of partial CCT diagram and heat treatments in the $\alpha+\beta$ phase field

*Table-3.1: Chemical composition of the Zr-2.5%Nb pressure tube spool piece used in the study*

Element	Nb (%)	O (ppmw)	N (ppmw)	Fe (ppmw)	Sn (ppmw)
Composition	2.68	1137	28	650	25

The starting material used in the present study was a spool piece of Zr-2.5%Nb alloy obtained after the 1<sup>st</sup> pilgering stage of the typical pressure tube fabrication process adopted at NFC, Hyderabad, India (See Fig. 2.1). Table 3.1 provides the elemental composition of the alloy as determined by Glow Discharge optical Emission Spectrometry. The scheme of extraction of specimen and geometry of the specimen used for dilatometric studies in this study is shown in Fig. 3.5 (a).

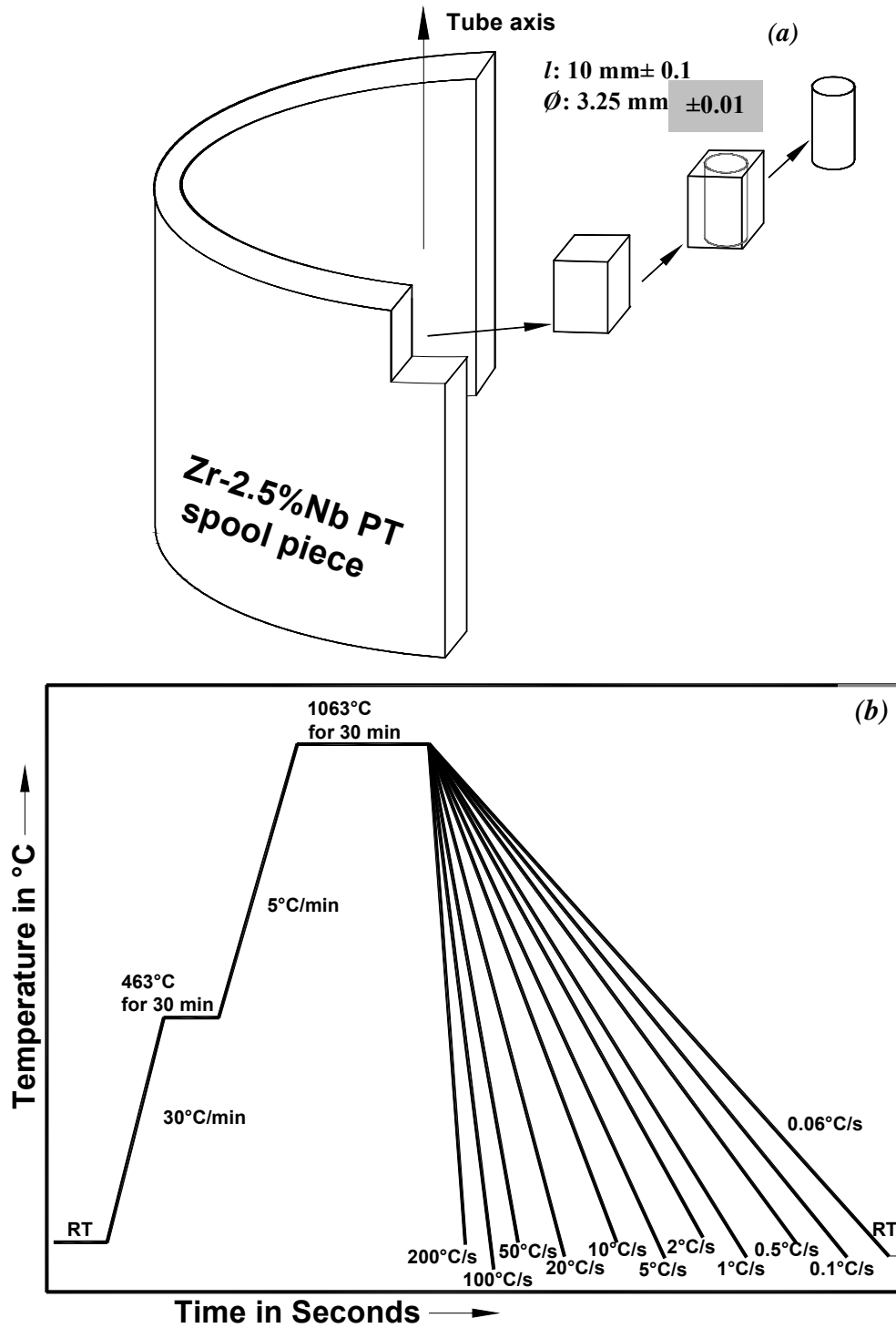


Fig. 3.5 (a) A sketch showing scheme of extraction of dilatometry specimens from the spool piece, (b) A schematic of temperature programs used for determination of partial CCT diagram

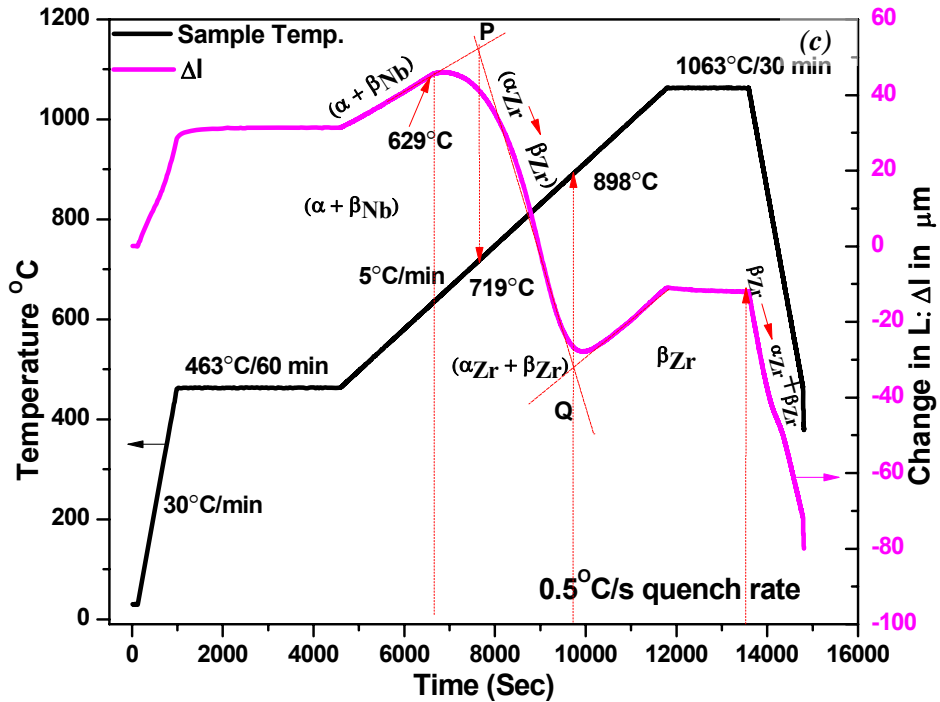


Fig. 3.5 (c) Typical thermogram and dilatogram recorded during one of the experiments

### 3.1.5 Determination of partial CCT diagram for the Zr-2.5%Nb alloy

Fig. 3.5 (b) schematically shows the details of  $\Delta l$  vs.  $t$  and  $T$  vs.  $t$  curves recorded during a heating and cooling cycle for one of the samples for determining CCT diagram using the quenching dilatometer. The heating part remained identical for all the samples while the different samples were cooled at different rates between  $0.06^\circ\text{C/s}$  and  $200^\circ\text{C/s}$ . During the thermal cycle the change in length of the sample and the sample temperature were recorded as a function of time. The cooling rates achieved were within  $\pm 2^\circ\text{C/s}$  for  $50^\circ\text{C/s}$  and higher while for slower cooling rates the deviation was within 3 to 5% of the programmed cooling rates. Fig.3.5 (c) shows a typical thermogram and dilatogram output recorded during one of the experiments. The negligible dilation observed in the  $\Delta l$  vs.  $t$  curve during soaking at  $463^\circ\text{C}$  indicated that a soaking period of 15 min effectively relieved the stresses (*flat portion of the  $\Delta l$  vs.  $t$  curve after 15 min of soak*). Similarly, soaking at  $1063^\circ\text{C}$  for 30 min also showed negligible volume change after nearly 15 min duration indicating that homogenisation of  $\beta$  phase has been effectively completed. Based on these findings the rest of the experiments were programmed with 30 min of soaking at both  $463^\circ\text{C}$  and  $1063^\circ\text{C}$  as shown in schematic temperature program in Fig. 3.5 (b).

During heating the onset of  $\alpha_{Zr} \rightarrow \beta_{Zr}$  transformation is indicated by the slope change in  $\Delta l$  vs.  $t$  curve at 629°C as shown in the Fig. 3.5 (c). As the temperature increased, the  $\alpha_{Zr} \rightarrow \beta_{Zr}$  phase change resulted in sharp decrease in the dilation curve which is associated with large decrease in volume as  $\beta_{Zr}$  is relatively much close packed structure compared to  $\alpha_{Zr}$  at these temperatures [21-23]. During cooling from 1063°C  $\beta_{Zr} \rightarrow \alpha_{Zr}$  transformation showed slope change in the  $\Delta l$  vs.  $t$  curve (*due to increase in volume*) in a certain temperature range for each sample depending on the cooling rate adopted.

### 3.1.6 Heat treatments for microstructure and mechanical property correlation study

A schematic of heat treatment cycles adopted for the study in the quenching dilatometer is shown in Fig.3.6 (a). The heat treatment program consisted of stress relieving at 463°C/30min and then soaking at selected temperatures such as 840, 863, 870, 883°C for 30 min within the ( $\alpha+\beta$ ) phase field followed by controlled cooling / quenching to room temperature at selected rates such as 0.5, 10, 25, 50 and 100°C/s. The temperature control during heating and soaking time was within  $\pm 0.5^\circ\text{C}$ . A scheme for obtaining samples from these heat treated dilatometry sample is shown in Fig. 3.6 (b). Each heat treated dilatometry specimen was sliced using slow speed diamond wheel cut off machine to obtain slices for SPT, TEM, EBSD and ABI, hardness measurements and also compression testing in some cases.

### 3.1.7 Determination of effect of ‘Fe’ and ‘O’ on ( $\alpha+\beta$ )/ $\beta$ phase boundary of the alloy by dilatometry

Two sets of Zr-2.5%Nb alloy pressure tube spool pieces having independent variation in iron and oxygen content (*within the specification range*) were selected. One set had ‘Fe’ variation from 301 ppmw to 1336 ppmw, while oxygen and ‘Nb’ content in these samples were within 1018  $\pm 20$  ppmw and 2.65  $\pm 0.05\%$  respectively. Similarly, the other set had variation in oxygen content between 930 and 1073 ppmw, whereas ‘Fe’ and ‘Nb’ content varied within 330 $\pm 20$  ppmw and 2.60  $\pm 0.04\%$ , respectively. In both the sets the variation of impurity elements such as ‘N’, ‘C’ varied in a range of 35  $\pm 5$  and 46 $\pm 5$  ppmw, respectively. The scheme of extraction of dilatometry specimen for the purpose of determining the transformation temperature from these selected sample spool pieces was identical to the one described in Fig. 3.5 (a).

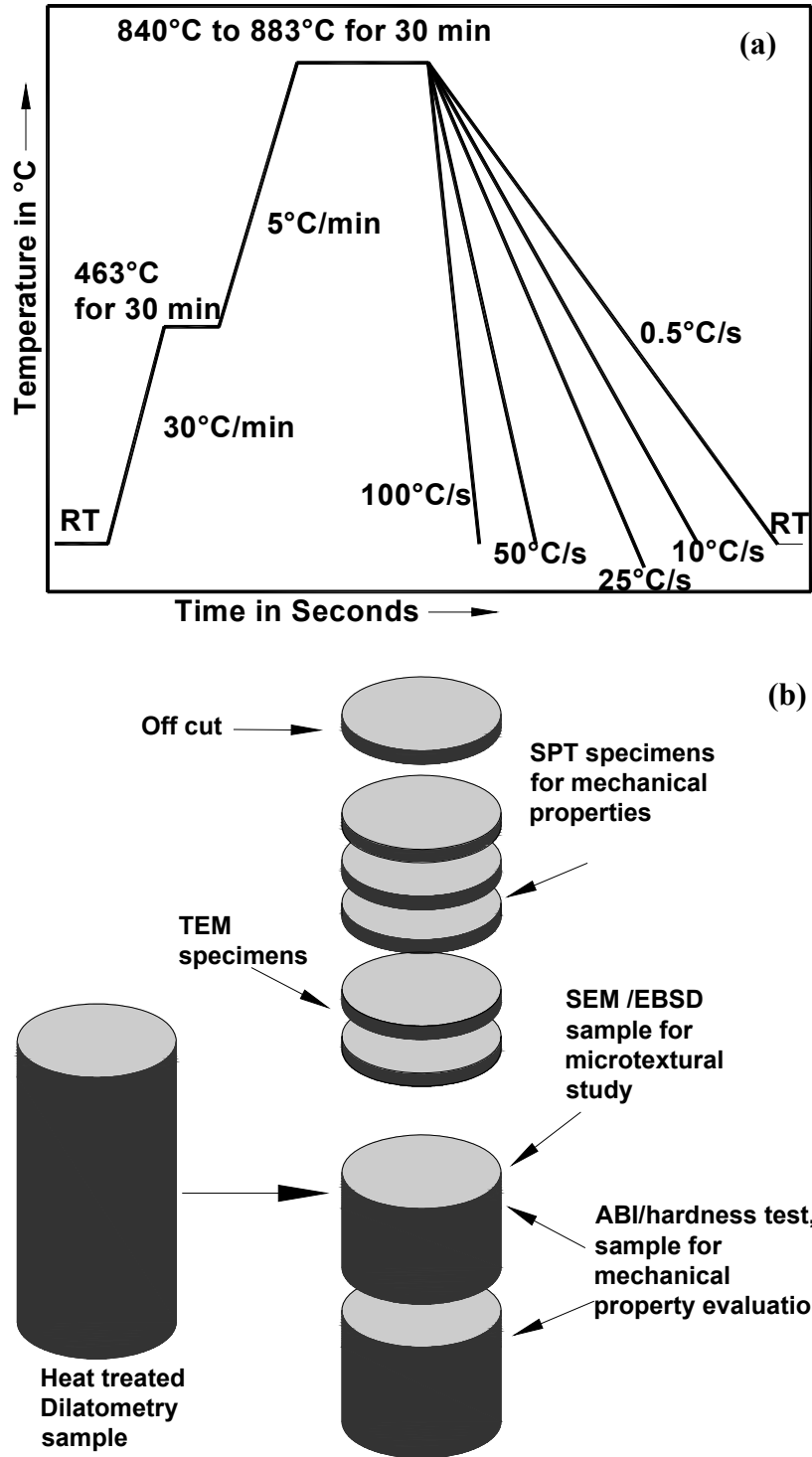


*Fig. 3.6 (a) Schematic of heat treatment cycles adopted for the study, (b) Scheme of specimen preparation from the heat treated dilatometry sample*

Each of the specimens belonging to ‘Fe’ and ‘O’ content variation sets were subjected to identical temperature program using the dilatometer as described in subsection 3.1.4. The dilation curves  $\Delta l$  vs.  $t$  recorded for each specimen were analysed for  $\alpha_{Zr} \rightarrow \beta_{Zr}$  transformation range using the three tangents method as explained in detail in subsection 3.1.3.

### 3.1.8 Study on effect of ‘Fe’ and ‘O’ on the CTE and texture of Zr-2.5%Nb alloy

In this work, all the sample materials were selected from the off cuts of the operating Zr-2.5%Nb pressure tubes fabricated under identical process parameters mainly for two reasons. First being the in-reactor axial creep data for many of these pressure tubes is available, which is essential for the correlation studies. Second being the correlation study will be relevant to the variations in ‘Fe’ and ‘O’ contents that is present within the specification range of the alloy which will be useful in assessment of performance of the operating pressure tubes and also for modeling.

In this work, a large number of samples from different Zr-2.5%Nb alloy pressure tube were selected for studying the CTE and texture as a function of ‘Fe’ and ‘O’ content. The composition range considered in this study is given in Table 3.2. The variation in Fe, O and Nb measurements by Glow Discharge Optical Emission Spectrometry (GDOES) in each sample had the standard deviation of  $3 \times 10^{-4}$ ,  $6 \times 10^{-4}$ , and  $2 \times 10^{-3}$  respectively. In addition, few more samples were also selected randomly for studying the correlation between texture and CTE of the pressure tube alloy. Fig. 3.7 (a) shows the schematic of extraction of dilatometry specimen from the axial and circumferential directions of pressure tube off cuts for the CTE studies.

*Table 3.2 Composition range of the samples selected for CTE and texture*

Fe-variation range 270 to 1425 ppmw (‘Fe’ measurement: Std. Dev. $3 \times 10^{-4}$ )		O-variation range 782 to 1180 ppmw (‘O’ measurement: Std. Dev. $6 \times 10^{-4}$ )	
Other elements		Other elements	
Nb (%)	O ppmw	Nb (%)	Fe ppmw
2.66±0.04	930±26	2.67 ±0.03	322±16

A typical experimental dilatogram and thermogram recorded for one of the specimens is shown in Fig.3.7 (b). The CTE of the specimen was calculated using the equation  $\alpha_T = (dL/L_0)/dT$  [24]. Each specimen was subjected to repeat runs under the same temperature program until, at least three closely reproducible CTE curves are obtained. The average value of CTE ( $\alpha_m$ ) in the

temperature range ( $\Delta T$ ) of 100°C and 400°C from each run was determined using the relationship

$$\alpha_m = (l/L_0) \times (\Delta L/\Delta T) \quad [24] \quad (1)$$

The  $\alpha_m$  values from a minimum of three tests on the same sample was further averaged and used as representative value of CTE of the given sample.

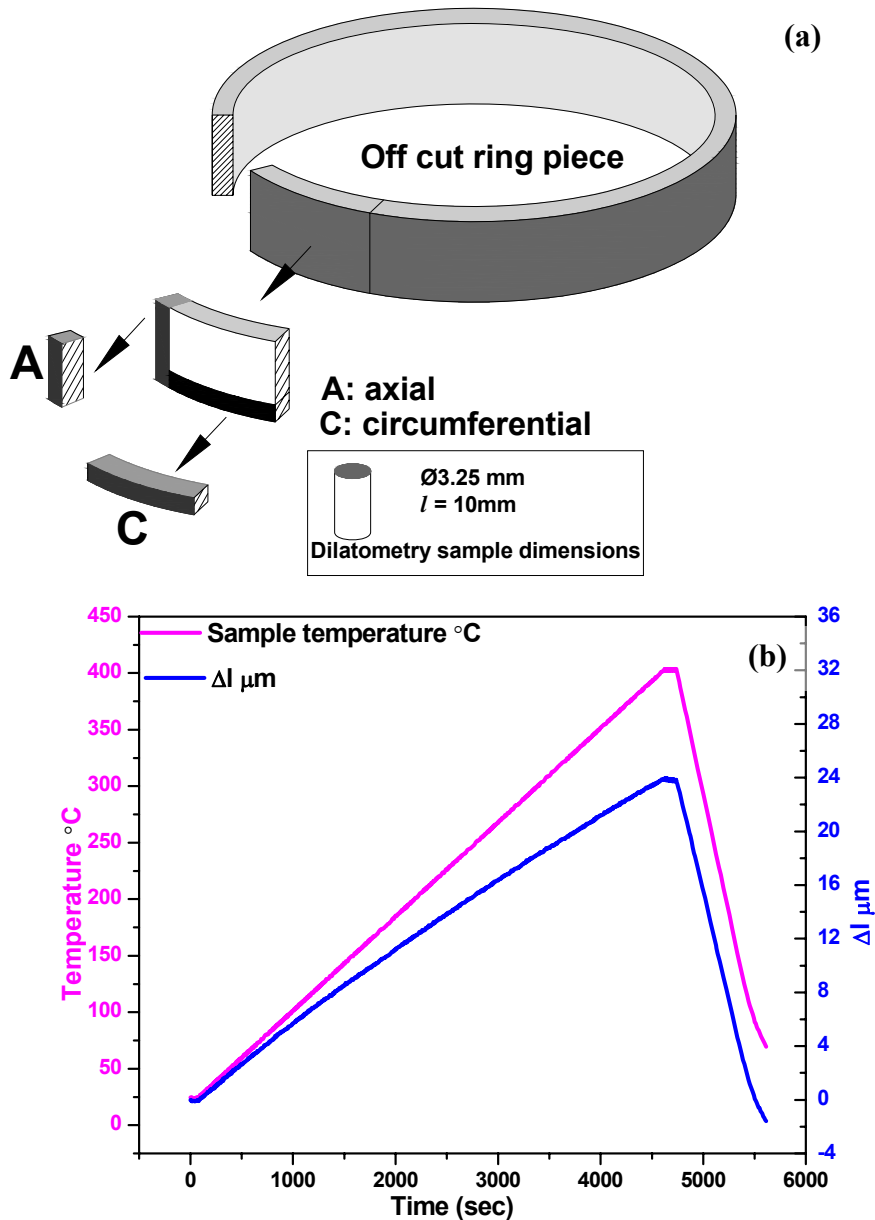
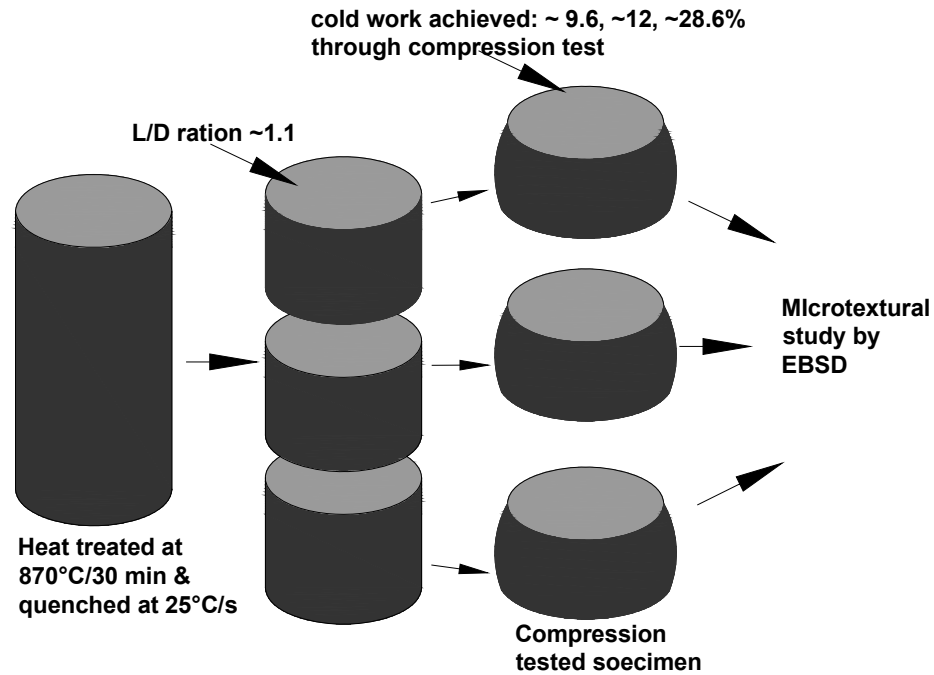


Fig. 3.7 (a) Schematic of specimen preparation for CTE studies (b) A typical experimental output of Thermogram and dilatogram obtained for a sample.

### 3.1.9 Heat treatment in the ( $\alpha+\beta$ ) phase field and compression testing

Few specimens extracted in the axial direction of the pressure tube (see Fig. 3.5 (a)) were soaked at 870°C/30 min followed by cooling to room temperature at 25°C/s using the quenching dilatometer. The compression test samples were extracted from these heat treated dilatometry specimens as schematically shown in Fig. 3.8. The cross sectional surfaces of these samples prepared metallographically to obtain flat and parallel faces and then subjected to compression testing using an Universal Testing Machine (UTM) to impart different amounts of cold work. These samples were subsequently prepared metallographically followed by electrolytic polishing for texture evolution study as a function of cold work using the EBSD technique.



*Fig. 3.8 Schematic of specimen preparation from the heat treated dilatometry specimens for Compression testing and EBSD scanning*

### 3.2 Heat treatment of bulk specimens for determining correlation parameters for SPT and ABI

A heat treatment setup that was specially developed for heat treating the miniature tensile specimens and small size bulk pieces is shown in Fig. 3.9 (a). The setup consisted of a vertical

tubular resistance furnace with a quartz tube held inside the furnace as shown schematically in Fig. 3.9 (a). The quartz tube had a T-connection on the top and a bottom cap with a B-34 cone and socket joint. The bottom socket had a small opening for the escape of purge / quench gas.

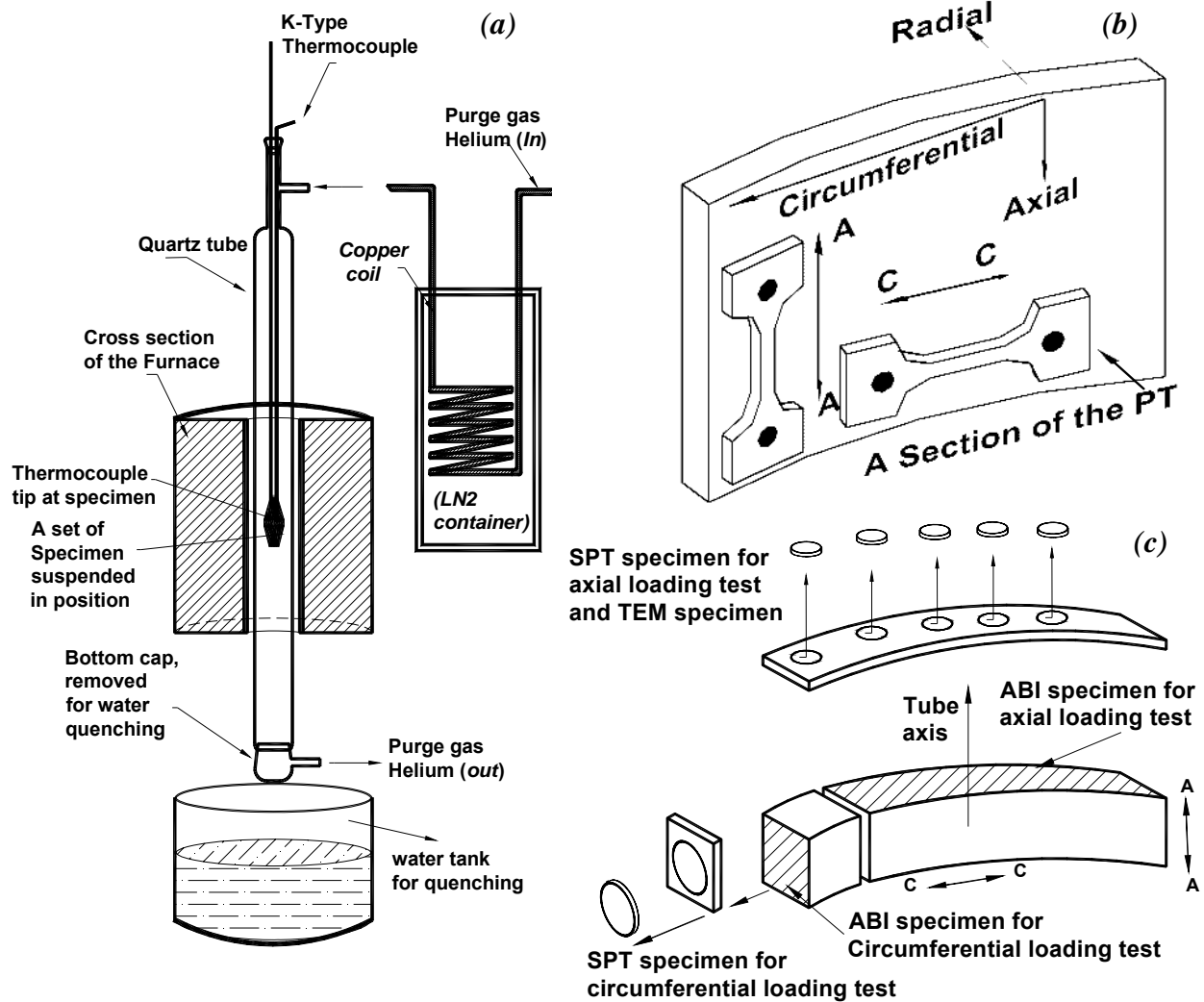


Fig. 3.9(a) Schematic of Heat Treatment setup, (b) Scheme of extraction of axial and circumferential tensile specimens having gauge length  $7.62 \pm 0.02$  mm ( $7.62 / \sqrt{(1.78 \times 1.52)} = 4.6 \pm 0.1$ ) [25] from the Zr-2.5%Nb alloy spool piece, (c) Schematic of specimen preparation from heat treated bulk pieces for SPT and ABI tests and TEM examination.

The scheme of extraction of tensile specimens from the axial and circumferential directions of the Zr-2.5%Nb pressure tube is shown in Fig. 3.9 (b). A set of specimens consisting of bulk pieces and tensile specimens along with a K-type thermocouple was heated to 880°C (within the

$\alpha+\beta$  phase field of the alloy) under the cover gas (He) followed by soaking for 30 min to achieve phase equilibration.

After the soaking period, the specimens were lifted to the neck of quartz tube (*maintained at room temperature outside the furnace*) along with the thermocouple and then cooled to room temperature at a desired rate by controlling the flow rate of ambient / LN<sub>2</sub> (*liquid nitrogen*) chilled helium gas. During the complete cycle the temperature output from the thermocouple was recorded as a function of time at an interval of 0.1s. In the case of water quenching, the bottom cap of the quartz tube was removed and the specimens were allowed to fall freely under Helium cover gas into the water tank kept below the system. The cooling rate was approximately 800°C/s as the specimen fell freely from the hot zone into the water tank in <0.5s. The details of heat treatment conditions for different sets are listed in Table-3.3. The heat treated bulk specimen were then subjected to specimen preparation for ABI and SPT tests both for the axial and circumferential loading conditions as shown schematically in Fig. 3.9 (c).

*Table-3.3: Heat treatment conditions adopted on the Zr-.5%Nb pressure tube samples*

Specimen ID	Cooling medium/flow rate	Cooling rate	Remarks
S1	Helium/4 lpm	28°C/s	Specimens were lifted away from hot zone to the neck of quartz tube maintained at room temperature and quench gas flow was allowed at controlled rates.
S2	Helium/15 lpm	55°C/s	
S3	Helium/30 lpm ( <i>Chilled in LN<sub>2</sub></i> )	151°C/s	
S4	Helium/4 lpm	0.15°C/s	Specimens held in hot zone with furnace power off ( <i>Furnace cooled</i> ).
S5	Water quenched	~ 800°C/s	Dropped from hot zone under (He) cover gas in the water tank kept below.

The heat treated axial and circumferential direction tension specimens were of gauge length 7.62 ±0.02 mm, width 1.78 ±0.02 mm and thickness 1.52±0.02 mm (with  $L_0/\sqrt{(W \times T)}$  ratio of  $7.62/\sqrt{(1.78 \times 1.52)} = 4.6 \pm 0.1$ ). The specimens of different heat treated condition were designated S1, S2, S3, S4 and S5 as described in Table-3.3. These specimens were subjected to tension tests at room temperature at a constant strain rate of  $2 \times 10^{-4}$ /s using a calibrated TIRA TEST 28250 UTM having load cell capacity of 1000 kg and strain gauge resolution of 1µm. The load vs. displacement curve obtained for each test were analysed for yield stress by 0.2% off set method as explained in ASTM E8 [26]. At least two tests were carried out for each of the heat treated and loading conditions and the average value was used for analysis.

### 3.3 Automated Ball Indentation (ABI) test and Analysis of test data for mechanical property evaluation

All the ABI tests were carried out at room temperature adopting standard procedure as described at [25, 27-37]. The UTM used for ABI testing had load cell capacity of 100 kg and LVDT resolution of 1 $\mu$ m. All the ABI tests were performed at a constant crosshead speed of 0.1mm/min on flat and polished surface, through strain controlled multiple indentation cycles at the same penetration location using a 0.508mm diameter spherical indenter. Fig. 3.10 (a) shows schematic sketch of the ball indentation geometries before and after load application with the exaggerated material pileup Fig.3.10 (b), (c) show a typical Load ( $P$ ) vs. depth ( $\delta$ ) curve obtained for an ABI test and  $P/d_t^2$  vs.  $d_t/D$  plot used for determining yield parameter “A” through the Mayer’s relationship  $P_m/d_t^2=A(d_t/D)^{m-2}$  [25, 27-37].

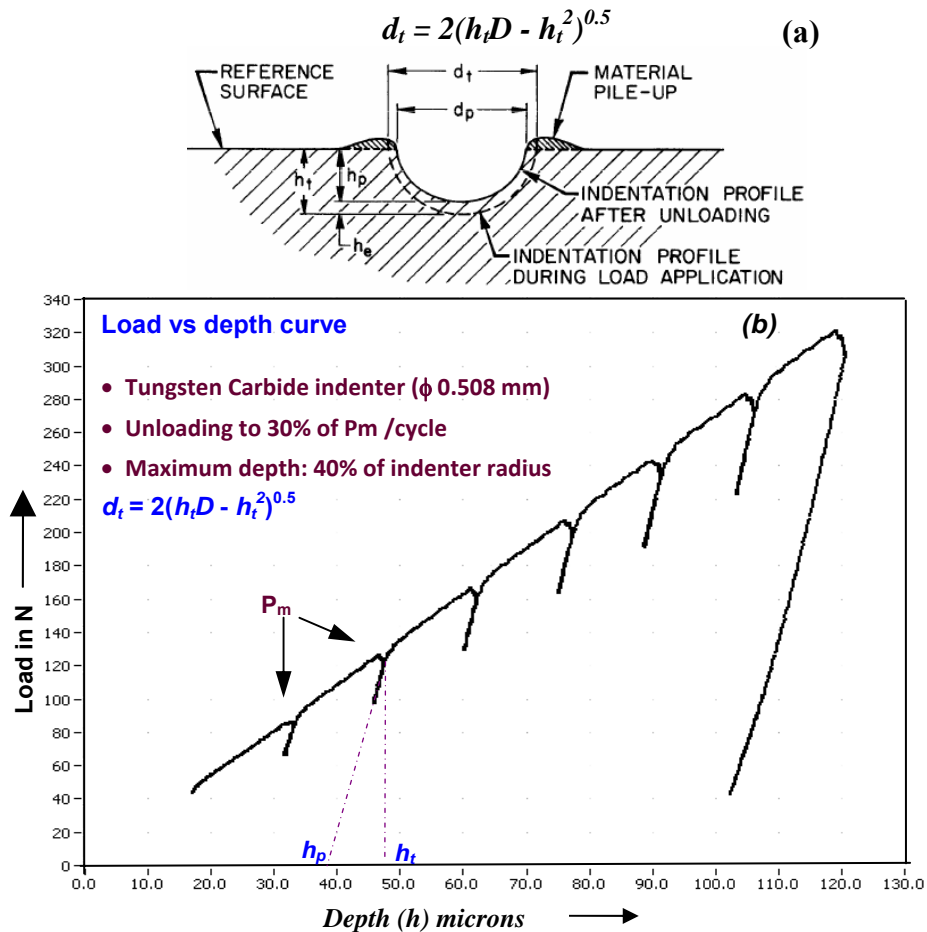


Fig. 3.10 (a) Ball indentation geometries before and after load application (the material pileup is exaggerated), (b) Typical Load vs. Depth curve for an ABI Test.

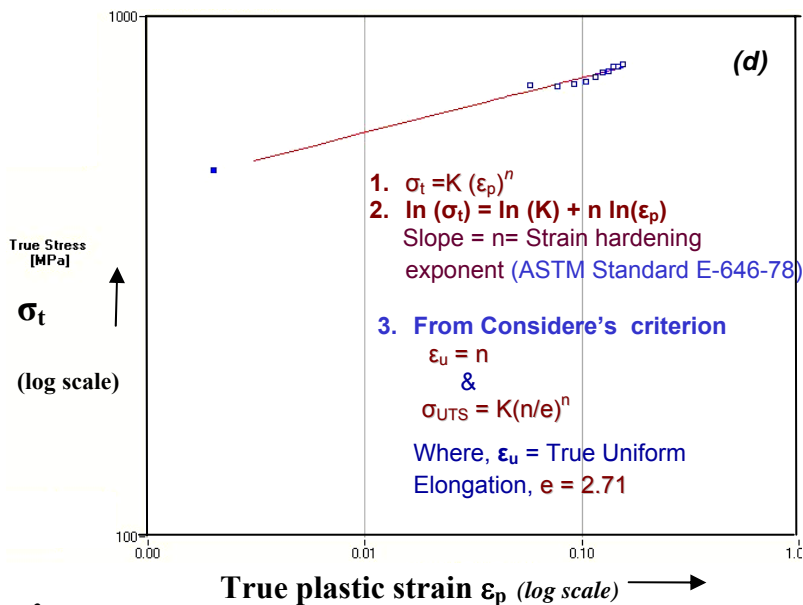
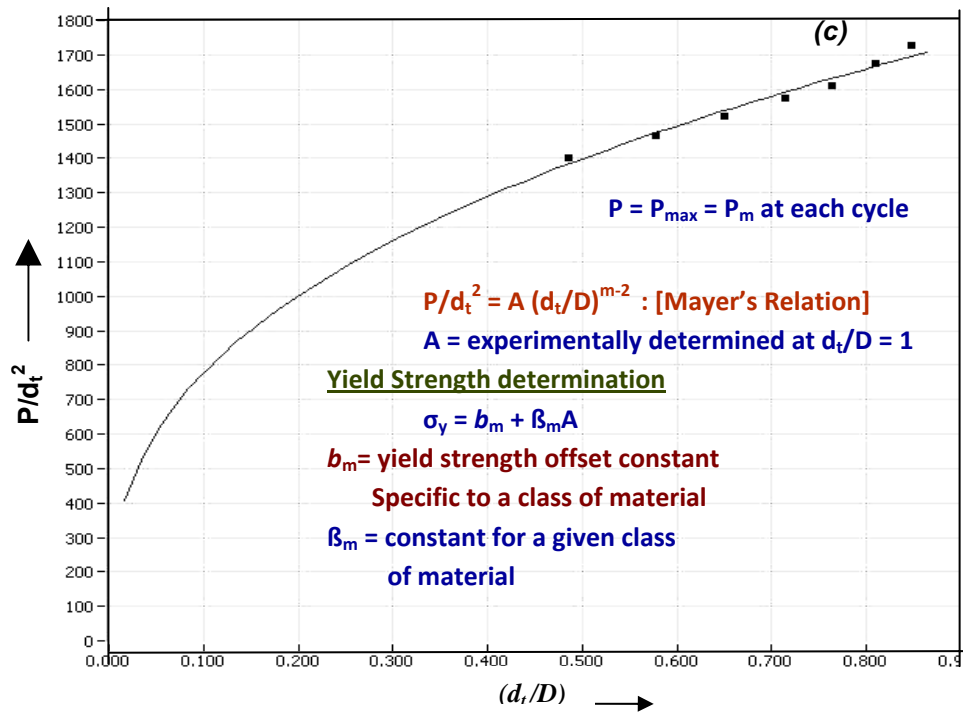


Fig. 3.10 (c)  $(P/d_t^2)$  vs.  $(d_t/D)$  plot used for determining Yield parameter “A”, (d) A typical  $\ln(\sigma_t)$  vs.  $\ln(\epsilon_p)$  plot used for the determination of UTS ( $\sigma_{UTS}$ ).

The yield parameter ( $A$ ) was then used to evaluate the yield strength ( $\sigma_y$ ) of the material using the following correlation;

$$\sigma_y = b_m + \beta_m A \quad (2)$$

where,  $b_m$  is the yield point offset constant specific to particular type or class of materials and  $\beta_m$  is a material-type constant which need to be determined separately for each class of materials. In the present study the value of  $\beta_m$  and  $b_m$  for the Zr-2.5%Nb pressure tube alloy were initially determined through regression analysis of tensile YS values from the specimens of different heat treatments the details of which has been discussed in chapter-5. The yield parameter value ‘A’ obtained for different specimens in each test in the entire study were then related to these correlations to establish the yield strength of the sample material. In eq. (2), the units of ‘A’ and  $\sigma_y$  are same. Assuming that the flow behavior of metallic materials generally follow the power law of the form  $\sigma_t = K(\epsilon_p)^n$  in the uniform elongation region of the conventional tension test, the ABI derived True Stress ( $\sigma_t$ ) and True Strain ( $\epsilon_p$ ) data was fitted to  $\ln(\sigma_t)$  vs.  $\ln(\epsilon_p)$  as shown in a typical plot in Fig. 3.10 (d). The linear regression of  $\ln(\sigma_t)$  vs.  $\ln(\epsilon_p)$  data is expressed in eq. (3)

$$\ln(\sigma_t) = \ln(K) + n \ln(\epsilon_p) \quad (3)$$

The flow properties K and n were determined from the intercept and the slope of the linear fit (eq.2). Then using the Considere’s criteria that, at the point of necking true strain  $\epsilon_u = n$  (*strain hardening exponent*) the UTS was determined using the relation  $\sigma_{UTS} = K (n/e)^n$  where  $e = 2.71$  [27, 30, 35, 37].

The Brinell hardness number (HB) can also be determined from the ABI test using the maximum indentation load ( $P_{max}$  in kgf) and the final impression diameter ( $d_f$  in mm) and the indenter diameter ( $D$  in mm) using the following equation [38].

$$HB = 2P_{max} / [\pi D ((D - (D^2 - d_f^2)^{0.5})] \quad (4)$$

### 3.4 Small Punch Test (SPT) and Analysis of test data for mechanical property evaluation

The setup for SPT consisted of a UTM having the load cell capacity of 500kg and a finger gauge of 0.001mm resolution for measurement of displacement of the punch. In the entire study, the small punch tests on all the specimens were performed as per the guidelines provided for testing metallic materials, in the report JAERI-M-88-172 [39]. During a SPT a disc specimen of  $\text{Ø}3.0$  mm and thickness  $0.25 \pm 0.01$  mm was circumferentially gripped using upper and lower dies as shown in Fig.3.11 (a) and a  $\text{Ø}1.0$ mm hardened steel ball positioned at the centre was forced at a constant cross head velocity of 0.1mm/min using a plunger.

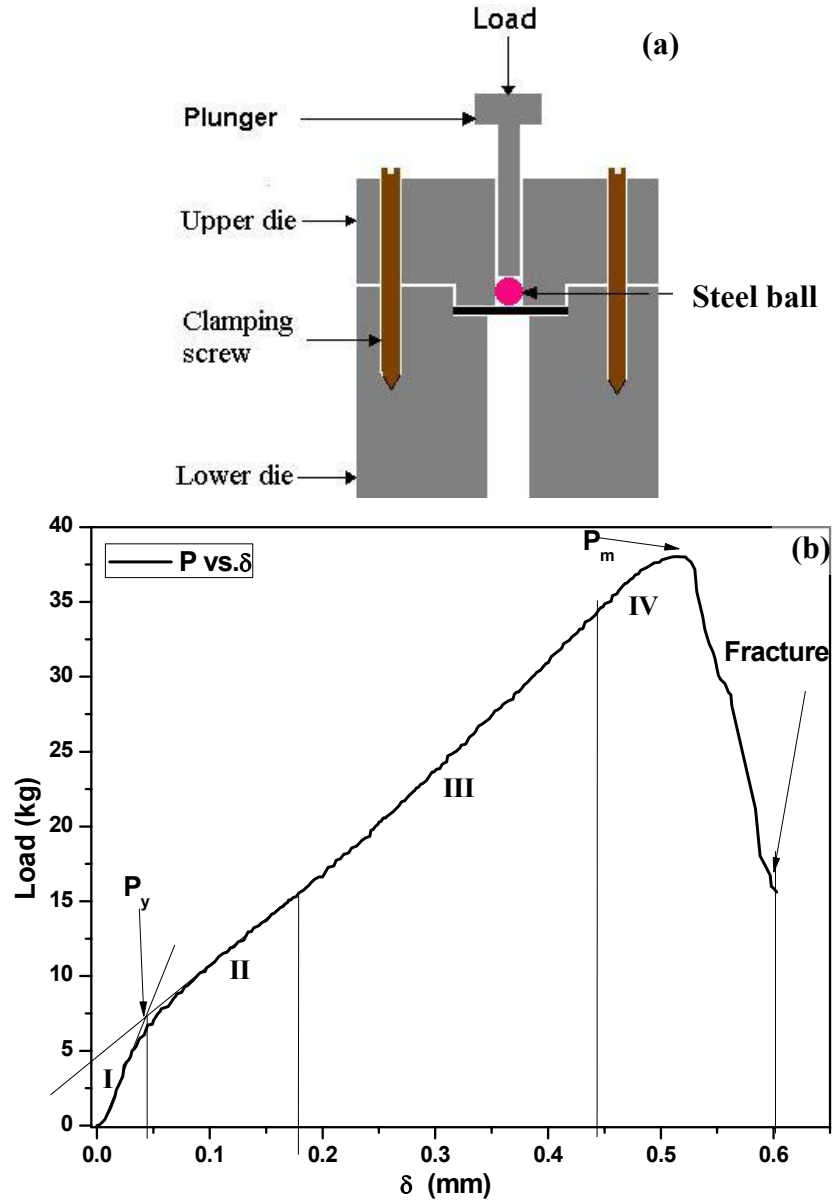


*Fig. 3.11 (a) A schematic view of a jig used for Small Punch test, (b) A typical load-deflection curve obtained for a Zr-2.5%Nb alloy specimen in the present study showing four different regimes during the progress of deformation I : Elastic bending regime, II: Plastic bending regime, III: Plastic membrane stretching regime, IV: Plastic Instability regime. The plot also shows graphical method of determining the Yield load ( $P_y$ ) and Load Maximum ( $P_m$ )*

The gripping by the dies at the circumference prevented the specimen from cupping upwards during punching, so that the plastic deformation was concentrated in the region below the punch. The load and central deflection of the specimen were recorded as a function of time during the

test until the specimen reached fracture. Fig.3.11 (b) shows a typical SPT output recorded during a test. Slopes measured in the elastic bending regime I and values of the load measured at the end of the elastic domain (*beginning of plastic bending regime II*) of the curves are compared to the Young's modulus and the yield stress, respectively. The regime III of the curve corresponds to the membrane stretching of the specimen during which the part of the disc specimen not in contact with the indenter stretches uniformly with a corresponding uniform decrease in thickness of the specimen. The regime IV corresponds to the plastic instability of the specimen, where the load decreases after reaching a maximum due to localised circumferential necking leading to decrease in load bearing capacity as in the case of uniaxial tension test. The circumferential necking is also known as through thickness thinning of the specimen. The specimen eventually reaches final circumferential fracture at the through thickness thinning regions. The  $P$  vs.  $\delta$  curve was analysed for yield load  $P_y$  and load maximum  $P_m$  using the recommended procedures at [39-42]. At least three tests were performed for each loading direction and heat treated condition.

As per the procedure described in the literature, load ' $P$ ' at initial localised plastic straining i.e. the yield load ' $P_y$ ' is determined by constructing the tangents as shown in Fig. 3.11 (b). Both yield load and load maximum obtained in a test depend on the specimen thickness ' $t_0$ '. Therefore ' $P_y$ ' and ' $P_m$ ' were first normalised with  $t_0^2$  to obtain yield strength and ultimate tensile strength representing values ( $P_y/t_0^2$ ) and ( $P_m/t_0^2$ ) which have the same units as stress. These strength representing values were then related to the linear correlations [40, 42] for the Zr-2.5%Nb alloy material, established in this work following the procedure for the evaluation of mechanical properties ( $\sigma_y$ ) and ( $\sigma_{UTS}$ ). Equations (5) and (6) show the general form of these linear correlation where  $C_1$ ,  $C_2$ ,  $C_3$  and  $C_4$  are the correlation parameters [40, 42]. The determination of these correlation parameters have been discussed in chapter-5.

$$\sigma_y = C_1 + C_2 \times (P_y/t_0^2) \quad (5)$$

$$\sigma_{UTS} = C_3 + C_4 \times (P_m/t_0^2) \quad (6)$$

### 3.5 Specimen preparation for ABI and SPT

The specimen preparation procedure for SPT and ABI tests has been described briefly in this section. The heat treated dilatometry specimens and bulk pieces of Zr-2.5%Nb pressure tube

samples were sliced in the predetermined directions as shown schematically in Fig. 3.6 (c) and Fig. 3.9 (c) to obtain blanks of ~0.4 mm thickness using a slow speed diamond wheel cut off machine. The cross sectional blanks from the heat treated dilatometry specimen belonged to the radial-transverse plane of the pressure tube. In the case of heat treated bulk samples, these blanks were extracted from the radial-transverse and radial-axial planes of the pressure tube with the aim to study the effects of texture on the mechanical properties of the anisotropic Zr-2.5%Nb alloy. The further steps involved lapping of both cross sectional surfaces of each blank successively with emery paper of grit sizes ranging from 400 to 1000, mechanical polishing to obtain uniform and flat mirror finish surface. The prepared blanks were punched to obtain discs of  $\phi 3\text{mm}$  and  $0.25 \pm 0.01$  mm thickness. For ABI tests, the heat treated bulk specimens were subjected to metallographic preparation on radial-circumferential and radial-axial surfaces (see Fig. 3.9 (c)) while in the case of heat treated dilatometry specimens the cross sectional surface was prepared metallographically. To ensure that the specimens are flat and also have parallel the opposite surfaces it was subjected to identical specimen preparation steps.

### **3.6 Electron Microscopy techniques for microstructural and microtextural study**

The microstructural characterisation of a number of heat treated Zr-2.5%Nb alloy samples was carried out using JEOL-2000FX Transmission Electron Microscope (TEM). The accelerating voltage was kept at 160 keV during the examination. The equipment was used in the bright field mode to study the finer morphological details of  $\alpha_{\text{Zr}}$  and  $\beta_{\text{Zr}}$  phases in the specimens. The Scanning Electron Microscope (SEM) model FEI-3DSEM equipped with Electron backscattered diffraction (EBSD) detector was used for microtexture characterisation of the heat treated Zr-2.5%Nb alloy specimens. The accelerating voltage of 20 keV was used to attain good intensity of backscattered electrons.

### **3.7 Specimen preparation for microstructural and microtextural examination**

The specimen preparation for TEM and EBSD examination was similar to the specimen preparation procedure adopted for SPT and ABI tests. The initial blanks of ~0.4mm thickness were obtained by slicing the specimen using a slow speed diamond wheel cut off machine. These blanks were subjected to standard metallographic preparation to obtain mirror finish surfaces.

The specimen for TEM examination were then prepared using Fischione twinjet electro polishing machine with an electrolyte consisting of a solution of 80% methanol and 20% perchloric acid at a temperature of  $-50^{\circ}\text{C}$  and 25V. In the case of specimen for EBSD examination, these metallographically prepared flat samples were subjected to electrolytic polishing for obtaining stress free surfaces using an in house developed arrangement as shown schematically Fig. 3.12. The electropolishing was carried out using the electrolyte of concentration 5% Perchloric acid + 95% Methanol, at the bath temperature of  $-49^{\circ}\text{C}$  and a DC current of  $\sim 0.12$  Amps and DC voltage between 9 and 14V.

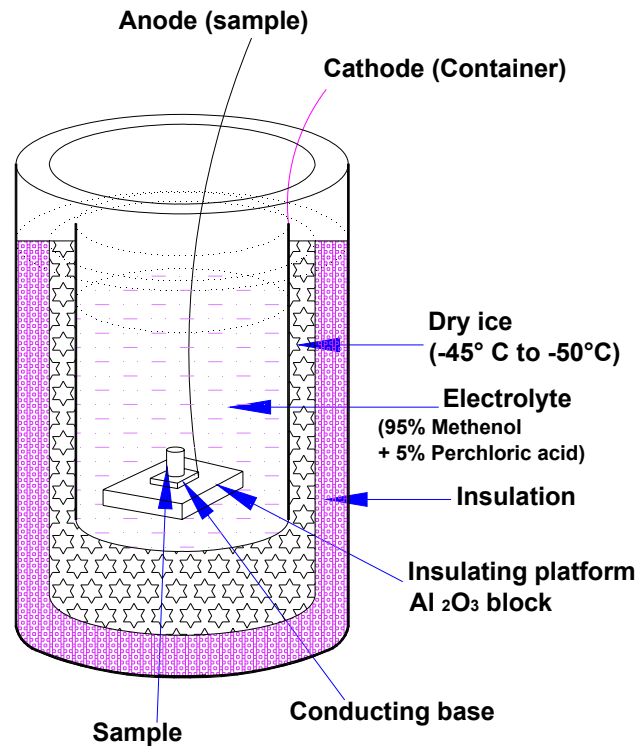


*Fig. 3.12 A Schematic view of setup used for electropolishing Zr-2.5%Nb alloy samples*

### 3.8 Thermal creep study using miniature specimen testing techniques

The thermal creep study was carried out using the miniature specimen testing techniques such as impression and indentation creep tests, considering suitability to study creep property of anisotropic alloy by selecting specific direction of load application on small size specimen. These indentation techniques are also sensitive to the variation in alloying additions [43], which

was essential for ascertaining the effect of variation in ‘Fe’ and ‘O’ contents on the thermal creep behavior of the alloy.

### 3.8.1 Impression creep test for thermal creep study

Impression creep technique is a modified indentation creep test wherein constant load and also a constant stress is essentially maintained during the test due to flat bottomed cylindrical punch, because the contact area of the punch with the specimen remains constant [44- 46]. Under this punching stress, if the indenter sinks into the material to a depth  $h$  in time  $t$ , then  $v_s = dh/dt$  signifies the punch velocity during the test [47].

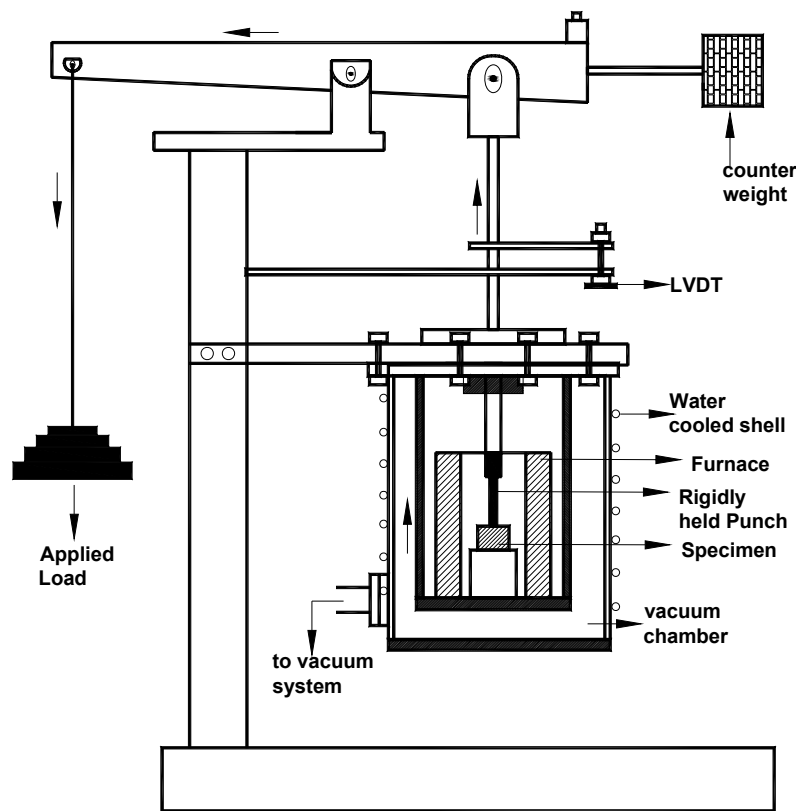


*Fig. 3.13 A schematic diagram of the impression creep test equipment*

The steady state velocity of the punch is related to the steady state creep rate of the material. It was observed during the initial impression creep tests at the test conditions of 300°C and punching stress  $\sigma_i < 400\text{MPa}$  that, the steady state impression creep rates were insignificant. This data has not been presented in this work. Based on this experience, the test temperature was raised to 400°C and punching stress ( $\sigma_i$ ) was increased to 400MPa with the intention to have

measurable creep rates, so that the effect of variation in minor alloying element on the thermal creep can be brought out. The  $\sigma_i=400\text{MPa}$  corresponds to  $\sim 115\text{ MPa}$  of uniaxial tensile stress through conversion factor which is close to hoop's stress value that generally exists in the pressure tube during operation. This stress value is nearly one third of the circumferential direction uniaxial tensile yield stress ( $\sigma_y$ ) of  $\sim 460\text{ MPa}$  and  $325 \pm 10\text{ MPa}$  for the Zr-2.5%Nb pressure tube at 300 and 400°C respectively [48].

*Table 3.4 (a) Description and microstructures of Zr-2.5% Nb pressure tube samples with 'Fe' content variation used for thermal creep study by impression creep test and in-reactor axial creep rate data for the corresponding operating channels.*

Sample ID	'Fe' ppmw Std. deviation: $3 \times 10^{-4}$ ppmw)	$f_t$	$f_r$	$f_a$	In-reactor axial creep rate (/s) normalised with peak fluence after 3340 EFPD of operation	Dislocation density ( $\text{m}^{-2}$ ) determined from X-ray line profile analysis	
						Plane: $[11\bar{2}0]$	Std. Devi.
1	1566	0.50	0.39	0.12	$6.17069 \times 10^{-12}$	$6.83 \times 10^{16}$	$3.45 \times 10^{16}$
2	472	0.51	0.39	0.09	$1.3215 \times 10^{-11}$		
3	165	0.52	0.38	0.09	$1.96365 \times 10^{-11}$		

The effect of 'Fe' on thermal creep behavior of the alloy was investigated using impression creep test method adopting the standard procedure described by many authors [44-47, 49-53]. A schematic diagram of the impression creep equipment is shown in Fig. 3.13 which consists of a test chamber inside which the specimen of maximum size of 10 x 10 mm cross sectional area and 10 mm height can be placed on the flat platform of the specimen holder. The punch with a primary load of  $\sim 0.5\text{ kg}$  was made to rest vertically on the flat specimen surface and the S-type thermocouple and the furnace were fixed in their positions. After attaining the steady vacuum of  $5 \times 10^{-5}\text{ mbar}$  and test temperature 400°C, a calculated amount of load was applied on the specimen through external lever arm as shown in the Fig. 3.13. The Depth of Penetration (DOP) of the punch was monitored using a calibrated LVDT (*with resolution  $1\mu\text{m}$* ) and recorded as a function of time during the test at the programmed intervals. Each creep experiments lasted for an approximate period of 165 hours. Table-3.4 (a) provides the iron content in the Zr-2.5%Nb pressure tube samples selected for impression creep study along with texture and dislocation density data and also the in-reactor axial creep data for the corresponding operating channels. The 'O' and 'Nb' content in these samples were  $877 \pm 40\text{ ppmw}$  and  $2.59 \pm 0.09\%$  respectively.

The samples of size ~ 4 x 4 x 5 mm were sliced from these spool pieces similar to the one shown in Fig. 3.7 (a) and the radial-axial surface of the specimens were prepared as explained in subsection 3.5.

The impression creep tests were performed on these prepared faces of the samples using test parameters described in Table-3.4 (b). The DOP of the punch measured as a function of time using an LVDT with resolution of  $\pm 1 \mu\text{m}$  was the basic output of the test that was analysed for the creep property of the sample material.

*Table-3.4 (b) Impression creep test parameters*

Test environment	Vacuum of $5 \times 10^{-5}$ mbar and $400^\circ\text{C}$
Direction of load application	Circumferential with respect to pressure tube axis
Punch diameter	$a = 1.5 \text{ mm}$ ( <i>Tungsten carbide punch</i> )
Punching Stress	$\sigma_i = 400 \text{ MPa}$
Load calculation	Applied dead load, $P = (\sigma_i / (g \times \text{Lever arm ratio})) \times (\text{cross sectional area of punch}) = (400 \text{ MPa} / 9.806 \times 10) \times (\pi \times 1.5^2) / 4 = 7.208 \text{ kg}$

### 3.8.2 Time dependent hot hardness tests for thermal creep study

The indentation creep tests using Vicker's hot hardness measuring technique was specifically adopted for studying the thermal creep behaviour of Zr-2.5%Nb pressure tube samples with 'O' content variation for the following reasons. The thermal creep data of the alloy at  $300^\circ\text{C}$  (*reactor operating temperature*) is an important data for the purpose of correlation study. The constant stress impression creep tests could not be used as the impression creep rates obtained at  $300^\circ\text{C}$  were insignificant as explained earlier. The hot hardness technique is sensitive to the test temperatures. Although, time dependent hot hardness is not a constant stress creep test the change in hardness with dwell time of the indenter at a given test temperature can provide a good measure of thermal creep behaviour of the alloy [54-57]. For a constant indentation load at a constant specimen temperature, if the penetration of the indenter into the solid increases with time then the solid is said to exhibit indentation creep [58-60]. According to Mulheran and Tabor [54] the hardness, temperature and time are related by the relation expressed in eq. (7).

$$H^{(-n+0.5)} = A[\exp(-Q/RT)]t \quad (7)$$

where, 'H' is the hardness, 'T' the temperature in (K), 'A' is the intrinsic hardness of the material at  $T = 0\text{K}$ . When hardness 'H' is plotted against dwell time (t) in a log-log scale, a series of linear

plots can be obtained for different test temperatures. In the present study, these plots were sufficient to explain the effect of oxygen on the time dependent deformation behavior of the alloy, hence no attempt was made to determine the activation energy ( $Q$ ) and stress exponent ( $n$ ). The alloy samples had oxygen content variation from 743 ppmw to 1587 ppmw, while ‘Nb’ and ‘Fe’ contents were in the range of 2.67 %  $\pm$ 0.06% and 321 ppmw $\pm$ 30 ppmw respectively.

The scheme of specimen extraction and preparation was identical to the one explained for impression creep tests. Initially the room temperature Vicker’s Micro-hardness measurements were made on the radial-axial surfaces of these samples using a 500g load and dwell time of 10 seconds. The results showed a clear increasing trend in hardness with the increase in oxygen content. Based on this result, three among these samples covering the entire range of oxygen content were selected for the indentation creep tests at 300 and 400°C using a Vicker’s hot hardness tester.

The arrangement for hot hardness studies consisted of heating the specimen and indenter independently to a same selected test temperature under vacuum ( $5 \times 10^{-5}$  mbar), through a computer controlled program. After the temperature stabilisation, the indenter along with the load (500g) was moved with a slow speed of 5 $\mu$ m/s (*to avoid effects of shock loading*) and made to rest on the area of the specimen identified using an online microscope. The dwell time of the indenter was varied between 10 and 800s through the online computer at each test temperature. The indentation images were then captured using an attached digital camera and the diagonal measurements of these indentations were accomplished through the calibration factor. For each specimen three indentations were made at each test condition of temperature and dwell time and the average values of the diagonals were used for evaluation of Vicker’s Hardness Number (VHN) as per the ASTM standard expression in eq. (8) [61].

$$\text{VHN} = 1854 \times P / (d_m^2) \text{ kgf/mm}^2 \quad (8),$$

where, P is the load in grams and  $d_m$  is the mean of the diagonals of the indentation in micrometers.

### **3.9 Specimen preparation and texture measurements by X-ray diffraction method**

The crystallographic texture describes the geometric arrangement of crystallites in a polycrystalline material [62]. In the present study the crystallographic texture measurements of a

number of Zr-2.5%Nb pressure tube samples was determined by X-ray diffraction method using a X-ray diffractometer (*Model HRD, ITAL structures*) adopting Kearn's method [63].

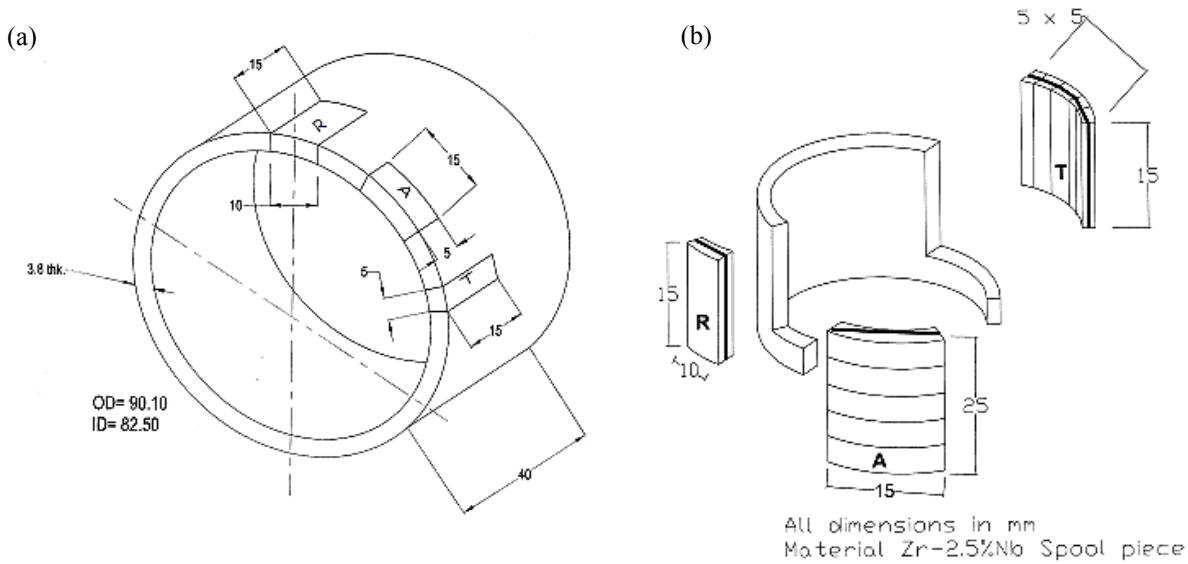


**Fig. 3.14** Specimen preparation for texture parameter determination by Kearn's method. (a) Sample cutting plan to obtain samples from three principal directions from the pressure tube off cut. (b) method for obtaining rectangular flat samples from mid thickness of the tube by removing the outer and inner surface layers using EDM as shown by thick lines

The specimen preparation involved slicing the off cut sample from three principal directions (*transverse, radial and axial*) of the pressure tube as shown schematically in Fig.3.14 (a). Since, the wall thickness of the tube was <4 mm, composite sample arrangement was adopted for the transverse and axial directions to ensure at least ~15mm x 10 mm area is available for exposure. From each of the three directions the mid thickness surfaces of the samples obtained (see 3.14 (a-b)) by slicing using Electro Discharge Machining (EDM) were mounted together to obtain composite specimen and subjected to metallographic preparation. The specimens were chemically polished using 45% HNO<sub>3</sub>+5% HF+50% H<sub>2</sub>O solution to obtain stress free sample surfaces for XRD studies. The specimens from each direction and the (*annealed*)  $\alpha$ -zirconium powder sample were scanned for 2 $\theta$  angles ranging from 30°-140° using Cu-K $\alpha$  radiation adopting the standard procedure. The texture parameter  $f_{[1002]}$  for the selected direction of the specimen was determined using Kearn's relationship in eq. (9) [63].

$$f = \frac{\int_0^{\pi/2} I_{\varphi} \sin \varphi \cos^2 \varphi d\varphi}{\int_0^{\pi/2} I_{\varphi} \sin \varphi d\varphi} \quad (9)$$

### References Chapter-3

1. G. Mohapatra, F. Sommer, E.J. Mittemeijer, *Thermochim. Acta*, 453 (2007) 57–66
2. *Standard Practice for Quantitative Measurement and Reporting of Hypo-eutectoid Carbon and Low-Alloy Steel Phase Transformations*, American Society for Testing and Materials (ASTM), Designation: A1033-10, Published in April 2010
3. G. Mohapatra, F. Sommer, E.J. Mittemeijer, *Thermochim. Acta*, 453 (2007) 31-41
4. Y.C. Liu, F. Sommer, E.J. Mittemeijer, *Thermochim. Acta*, 413 (2004) 215-225
5. T.G. Kollie, *Phys. Rev. B*, 16 (1977) 4872- 4881
6. B. Hallstedt, N. Dupin, M. Hillert, L. Hoglund, H. L. Lukas, J. C. Schuster, N. Solak, *Computer Coupling of Phase Diagrams and Thermochemistry*, 31 (2007) 28-37
7. L. Leibowitz, R.A. Blomquist, *J. Nucl. Mater.*, 167 (1989) 76-81
8. Designation: E228, Standard Test Method for Linear Thermal Expansion of Solid Materials with a Push-Rod Dilatometer, April 1, 2011. Published April 2011.
9. G. Mohapatra, PhD Thesis, “Phase Transformation Kinetics; the Role of Stress” Dissertation, Universität Stuttgart, Bericht Nr. 192, November 2006
10. L. Zhao, *Mater. Sci.* 37 (2002) 1585-1591
11. M. Takahashi, H. K. D. H. Bhadeshia, *J. Mater. Sci. Lett.*, 8 (1989) 477- 478
12. S.J. Lee, M.T. Lusk, Y.K. Lee, *Acta Mater.*, 55 (2007) 875-882
13. D.W. Suh, C.S. Oh, H.N. Han, S. J. Kim, *Acta Mater.*, 55 (2007) 2659-2669
14. J.Z. Zhao, C. Mesplont, B.C. De Cooman. *Mater. Sci. Eng. A*, 332 (2002) 110-116
15. A. Kop, J. Sietsma, S. Van Der Zwaag, *Mater. Sci.*, 36 (2001) 519-526
16. J.Z. Zhao, C. Mesplont, C. De Cooman, *Material Processing Technology*, 129/1-3(2002) 345-348
17. A.S. Akbari, *RWTH Aachen Institute of Ferrous Metallurgy, Matr.-Nr. 268696*
18. P. Suwanpinij, N. Togobytska, C. Keul, W. Weiss, U. Prahl, D. Homberg, W. Bleck, *ISSN 0946-8633, No. 1306, WIAS Berlin, 2008*
19. C.K. Chow, C.E. Coleman, M.H. Koike, A.R. Causey, C.E. Ells, R.R. Hosbons, S. Sagat, V.F. Urbanic, D.K. Rodgers, (ASTM), *STP 1295 (1996) 469-491*

20. P. Motycka, M. Kover, *Recent Trends in Structural materials, Plzeň, Czech Republic, EU, COMAT-2012, 21-22 November, 2012*
21. R.N. Singh, P. St°ahle, A.R. Massih, A.A. Shmakov, *J. Alloys Compd.*, 436 (2007) 150-154
22. P. E. J. Flewitt, *J. Appl. Cryst.* 5 (1972) 423-425
23. G.F. Slattery, *J. Less Common Metals*, (1964) 195-208
24. Designation: E228, Standard Test Method for Linear Thermal Expansion of Solid Materials with a Push-Rod Dilatometer, *April 1, 2011. Published April 2011*
25. F.M. Haggag, “*Nondestructive Determination of Yield Strength and Stress-Strain Curves of In-Service Transmission Pipelines Using Innovative Stress-Strain Microprobe Technology*” (1999), Report No. ATC/DOT/990901
26. Standard Test Methods for Tension Testing of Metallic Materials (ASTM), Designation: E8/E8M – 09, approved Dec. 1, 2009, Published December 2009
27. F.M. Haggag, J. A. Wang, Proc., doi,10.1117/12.259096, *SPIE 2945 (1996) 217-228*
28. F.M. Haggag, L.D Phillips, IPC04-0345, *Proceedings of IPC 2004, American Society for Mechanical Engineering (ASME), International Pipeline Conference Oct, 2004*
29. F.M. Haggag, L.D Phillips, IPC04-0357, *Proceedings, IPC 2004, American Society for Mechanical Engineering (ASME), International Pipeline Conference Oct.2004*
30. W.R. Corwin, F. M. Haggag, and W. L. Server, *American Society for Testing and Materials, (ASTM) STP 1204, (1993) 27- 44*
31. F.M. Haggag, *American Society for Mechanical Engineering (ASME), Pressure Vessel Piping (PVP)-429 (2001) 99-104*
32. F.M. Haggag, *Proceedings 3<sup>rd</sup> Int. conf. Trends in Welding Research, July (1992) 629-635*
33. F.M. Haggag, *ASM International, Advanced Materials and Processes, (2006) 41-43*
34. F.M. Haggag, *Final Report, The U.S. Department of Energy, DOE/ER/82115-2,(1999)1-40*
35. F.M. Haggag, K.L. Murty, “*Nondestructive Evaluation and Materials Properties III*”, *JOM, (1997), 101-106*
36. F.M. Haggag, A.S. Kumar, D.S. Gelles, R.K. Nanstad, E.A. Little, *American Society For Testing and Materials (ASTM), STP 1175, (1993) 172-185*

37. K.L. Murty, M.D. Mathew, Y. Wang, V.N. Shah, F.M. Haggag, *Int. J. Pressure Vessels and Piping*, 75 (1998) 831-840
38. Standard Test Method for Brinell Hardness of Metallic Materials, Designation: *American Society for Testing and Materials (ASTM)*, E 10-10, June 1, 2010. Published June 2010
39. H. Takahashi, T. Shoji, X. Mao, Y. Hamaguchi, T. Misawa, M. Saito, T. Oku, T. Kodaria, F. Fukaya Kioshi, H. Nishi, M. Suzuki, “*Recommended practice for Small Punch (SP) testing of metallic materials (Draft)*”, *JAERI-M-88-172 (Report)*, September, (1988) 1-19
40. X. Mao, H. Takahashi, *J. Nucl. Mater.*, 150 (1987) 42-52
41. K. Kumar, K. Madhusoodanan, B.B. Rupani, *BARC, Found. day Sp.285 Oct.2007*
42. J. Kameda and X. Mao, *J. Mater. Sci.*, 27 (1992) 983-989
43. Chubb W. Chubb, G.T. Muehlenkamp, G.T. Manning, *Battelle Memorial Institute Report BMI- (1955) 987*
44. D.H. Sastry, *Mater. Sci. Eng., A*, 409 (2005) 67-75
45. T.R.G. Kutty, C.B. Basak, A. Kumar, H.S. Kamath, *J. Nucl. Mater.*, 408 (2011) 90-95
46. 20-J. Larsen-Badse, *ORNL-TM-1862 Report*, (1967); also paper presented at the *Annual Meeting of AIME, Los Angeles*
47. J.C.M. Li, *Mater. Sci. Eng. A*, 322 (2002) 23-42
48. R.N. Singh, S. Mukherjee, R. Kishore, B.P. Kashyap, *J. Nucl. Mater*, 345 (2005) 146–161
49. T.H. Hyde, W. Sun, DOI: 10.1243/03093247JSA502, *Department of Mechanical, Materials and Manufacturing Engineering, University of Nottingham, UK, J. Strain Analysis*, 44 (2009) 171-185
50. T. H. Hyde, W. Sun, A.A. Becker, *Int. J. Mech. Sci.* 38, No.10, (1996) 1089-1102
51. Y.J. Liu, B. Zhao, B.X. Xu, Z.F. Yue, *Mater. Sci. Eng. A*, 456 (2007) 103-108
52. T.H. Hyde, W. Sun, J.A. Williams, *A review, Inter. Mater. Rev.*, 52(4) (2007) 213-255
53. T.H. Hyde, W. Sun, *Inter. J. Pressure Vessels and Piping*, 86 (2009) 757-763
54. T.O. Mulhearn, D. Tabor, *J. Inst. Metals*, 89 (1960-1961) 7-12
55. T.R.G. Kutty, C. Ganguly, *J. Nucl. Mater.*, 182 (1991) 258-260
56. T.R.G. Kutty, C. Ganguly, *J. Nucl. Mater.*, 207 (1993) 345-349
57. T.R.G. Kutty, K. Ravi, C. Ganguly, *J. Nucl. Mater.*, 265 (1999) 91-99

58. K. B. Khan, T.R.G. Kutty, M.K. Surappa, *Mater. Sci. and Eng. A*, 427 (2006) 76-82
59. I.M. Hutchings, *J. Mater. Res.*, 24, No. 3, (2009) 581-589
60. J. R. Cahoon, *Metall. Trans.* 3 (1972) 3040
61. Standard Test Method for Knoop and Vicker's Hardness of Materials, (*ASTM*), *International*, Designation: E384-11<sup>ε1</sup> approved Aug. 1, 2011. *Published August 2011, editorially corrected in March 2011*
62. Y. Jinyuan, PhD Thesis "Crystallographic Texture and Creep Anisotropy in Cold Worked and Recrystallised ZIRLO" Department of Nuclear Engineering North Carolina State University, March, 2005.
63. J.J Kearns "Thermal expansion and preferred orientation in Zircaloy" TID 4500 (46<sup>th</sup> edition), Contract No. AT-11-1-GEN-14, November 1965. *Scientific and Technical information, National Bureau of Standards, US Department of Commerce, Verginia, USA*

## CHAPTER 4: Heat Treatment and Microstructural Evolution in Zr-2.5%Nb Pressure Tube Material

.....

### 4.1 Objectives

The objective of this part of the work was to study the effect of various heat treatments particularly from the ( $\alpha+\beta$ ) phase field of the Zr-2.5%Nb alloy on the microstructural and texture changes. The soaking temperature within the ( $\alpha+\beta$ ) phase field would influence the fractions of primary  $\alpha$  and  $\beta$  phases, because of sharp slope of the ( $\alpha+\beta$ ) solvus line i.e.  $\beta$ -transus boundary of the Zr-Nb system. On the other hand, the cooling rates adopted would influence the morphologies of the  $\beta$  phase transformation products. In addition, modification in texture can also occur under certain conditions. Therefore, the main interest in this part of the thesis was to study the microstructural and textural evolution through a systematic variation in soaking temperatures and also the cooling rates. Since, the phase boundaries of the Zr-Nb binary system are the strong functions of oxygen and iron concentrations, initially the objective was to establish a partial CCT diagram for the selected Zr-2.5%Nb alloy to have accurate knowledge of  $\beta$ -transus boundary. This work provides wider knowledge base on the microstructural and texture changes due to different heat treatments which is necessary for the development of heat treated pressure tubes.

### 4.2 Background

The Zr-2.5%Nb pressure tube is a dual phase alloy in which variety of microstructures can be obtained through different heat treatment parameters. The final microstructure and the texture are the two important factors that dictate the short term and long term mechanical properties and also play a role in the in-reactor deformation behavior of the pressure tubes. The previous post irradiation study by Chow *et. al* [1] and Takayama [2] reported lower in-reactor creep rates for the heat treated pressure tubes compared to those fabricated from conventional cold worked route. The obvious reasons for such lower creep rates must be attributed to the final microstructure and texture obtained due to specific heat treatments during the manufacture of the pressure tube. As discussed earlier the data available on the microstructural and texture evolution

is limited and also discrete which was the motivation behind this part of the work. Therefore, a systematic study of effect of soaking temperatures and the cooling rates on the morphological changes in the microstructures reported in this chapter bears utmost importance particularly for the development of creep resistant Zr-2.5%Nb alloy.

As discussed in the literature review in chapter-2 the increasing amounts of oxygen expands the  $(\alpha+\beta)$  phase region of the Zr-Nb system resulting in higher  $\beta/(\alpha+\beta)$  transus temperature, while the presence of iron would lower the same [3]. Therefore, the determination of partial CCT diagram was initiated to have accurate knowledge of  $\beta/(\alpha+\beta)$  transus boundary for the alloy selected for heat treatment studies. The following subsections discuss the determination of  $\beta/(\alpha+\beta)$  transus boundary, heat treatments within  $(\alpha+\beta)$  phase field followed by microstructural and texture study on these heat treated samples.

### 4.3 Determination of partial CCT diagram for Zr-2.5%Nb alloy

The experimental details of determination of partial CCT diagram and  $\beta$  transus boundary for the Zr-2.5%Nb alloy using quenching dilatometry has been described in the section 3.1.5. Fig. 3.5 (c) shows the dilatometric curve ( $\Delta l$  vs.  $t$ ) recorded for one of the experiments. From all the experiments, it was observed that, during heating the transformation  $(\alpha_{Zr}+\beta_{Nb}) \rightarrow (\alpha_{Zr}+\beta_{Zr})$  occurred in the small temperature range between 707°C and 729°C which is indicated by sharp decrease in specific volume of the specimen in the  $\Delta l$  vs.  $t$  plot. This transformation temperature was identified by the sharp slope change in the  $\Delta l$  vs.  $t$  plot as shown in Fig. 3.5 (c). On continued heating beyond 729°C the transformation  $(\alpha_{Zr}+\beta_{Nb}) \rightarrow (\alpha_{Zr}+\beta_{Zr})$  showed continued decrease in volume (indicated by decrease in  $\Delta l$ ) which is associated with decrease in specific volume of the product phase  $\beta_{Zr}$  at the expense of  $\alpha_{Zr}$  [4]. With the continued heating another sharp slope change occurred in the range 887°C and 898°C in the  $\Delta l$  vs.  $t$  plot but in the opposite direction (see Fig. 3.5 (c)) indicating the end of  $(\alpha_{Zr}+\beta_{Nb}) \rightarrow (\alpha_{Zr}+\beta_{Zr})$  transformation. Beyond 898°C the all specimens showed thermal expansion of  $\beta_{Zr}$  phase which is evident from the constant slope of  $\Delta l$  vs.  $t$  plot.

The cooling part of dilation curves in the  $\Delta l$  vs.  $T$  plots showed different dilation characteristics depending on cooling rate adopted for all the specimens. During cooling from 1063°C the increase in specific volume due to  $\beta_{Zr} \rightarrow \alpha_{Zr}$  transformation was more dominant compared to thermal contraction of the transformation products, as  $\alpha_{Zr}$  phase has relatively low density compared to  $\beta_{Zr}$  phase [7]. Thus, from the sharp slope changes in  $\Delta l$  vs.  $T$  plots, it was possible to identify the start and end points of the  $\beta_{Zr}$  transformation using the graphical method [5-8]. Fig. 4.1 (a) shows a typical cooling part of dilation curve ( $\Delta l$  vs.  $T$ ) for one of the experiments and the method of identifying the transformation start and end temperatures [6-8]. Depending on different cooling rates adopted the transformation  $\beta_{Zr} \rightarrow \alpha_{Zr}$  produced slope change in the  $\Delta l$  vs.  $T$  plots in different temperature ranges which are shown in Figs. 4.1 (b-c).

At slower cooling rates such as 0.06°C/s, the transformation rate was relatively slower due to lower thermodynamic driving force generally prevalent at lower degrees of under cooling. Therefore, the transformation occurred at relatively higher temperatures and over a longer duration of time resulting in shallow slope change in the dilation curve. With the increase in cooling rates the transformation occurred at lower temperature ranges and also over shorter duration of time due to higher degrees of under cooling resulting in relatively sharper slope changes in dilation curves (See Fig. 4.1. (b-c)). However, at much higher cooling rates such as 50, 100 and ~200°C/s the dilation curves showed stepped slope changes at temperatures higher than  $\beta/(\alpha+\beta)$  boundary. These transformations are similar to the one observed by Hunt *et.al* [9] in the thermal arrest points for the Zr-2.5%Nb alloy samples during the study of CCT diagrams. Hunt *et.al* [9] interpreted that the initial formation of  $\alpha_{Zr}$  nuclei at  $\beta_{Zr}$  boundaries might be responsible for such thermal arrest points. Therefore, in the present study the stepped slope changes observed at temperatures higher than  $\beta/(\alpha+\beta)$  boundary can be attributed to formation of  $\alpha_{Zr}$  nuclei at  $\beta_{Zr}$  grain boundaries [9].

The  $\beta$  transus temperatures determined from the cooling part of the dilation curves were plotted as typical *Temperature vs. log<sub>10</sub> (time)* to establish the partial CCT diagram as shown in Fig.4.2. The plot (Fig.4.2) shows the start temperatures for different cooling rates and was used to identify as  $\beta$  transus boundary for the alloy which served the basis for the heat treatment studies.

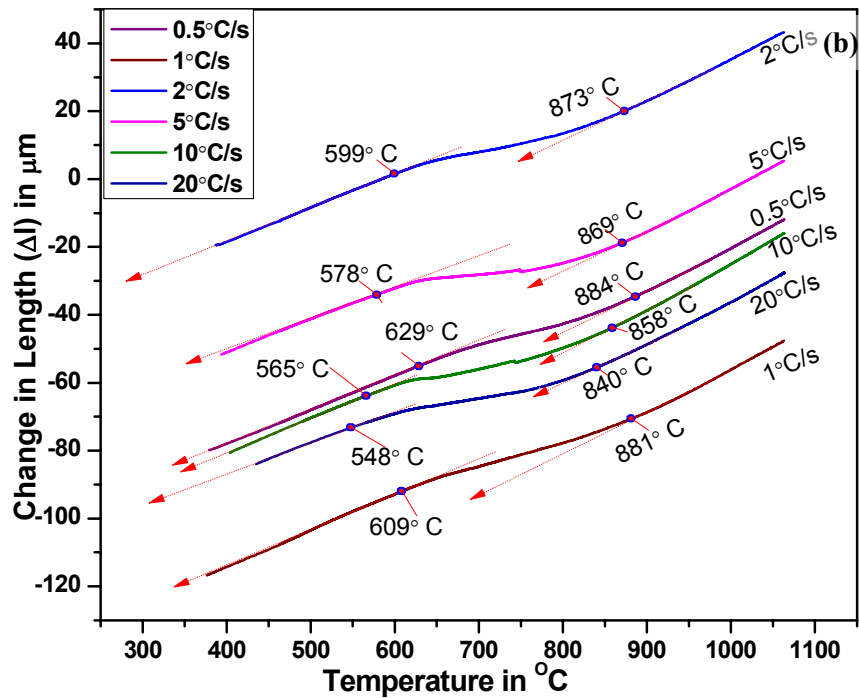
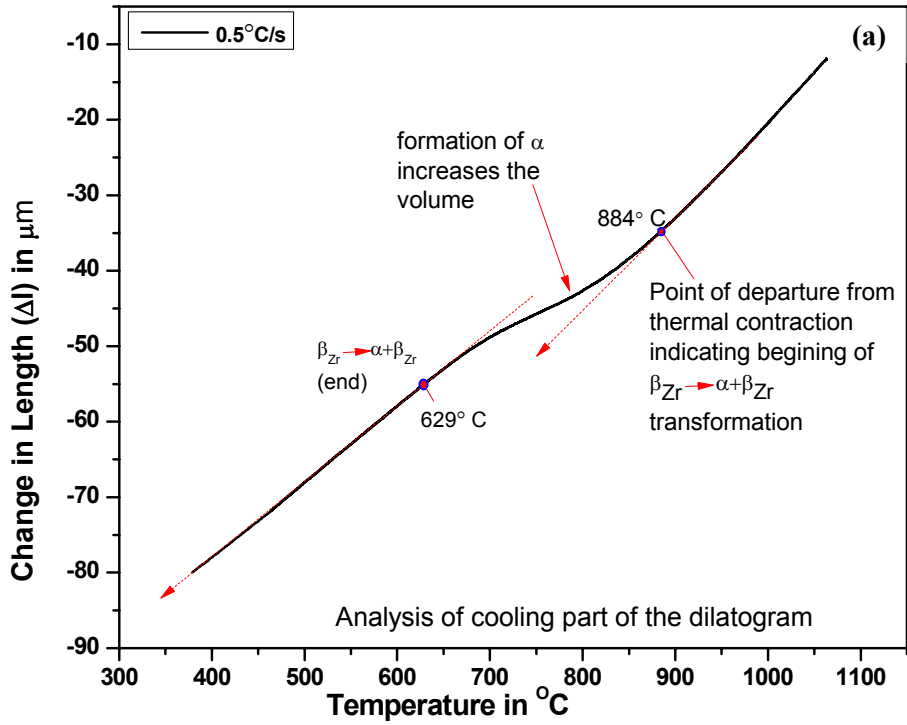


Fig. 4.1 (a) Analysis of cooling part of a typical  $\Delta l$  vs.  $T$  curve for  $\beta_{\text{Zr}} \rightarrow \alpha_{\text{Zr}} + \beta_{\text{Zr}}$  transformation start and end points, (b) analysis for  $\beta_{\text{Zr}} \rightarrow \alpha_{\text{Zr}} + \beta_{\text{Zr}}$  transformation start and end points for the cooling rates, between 0.5  $^{\circ}\text{C/s}$  and 20 $^{\circ}\text{C/s}$

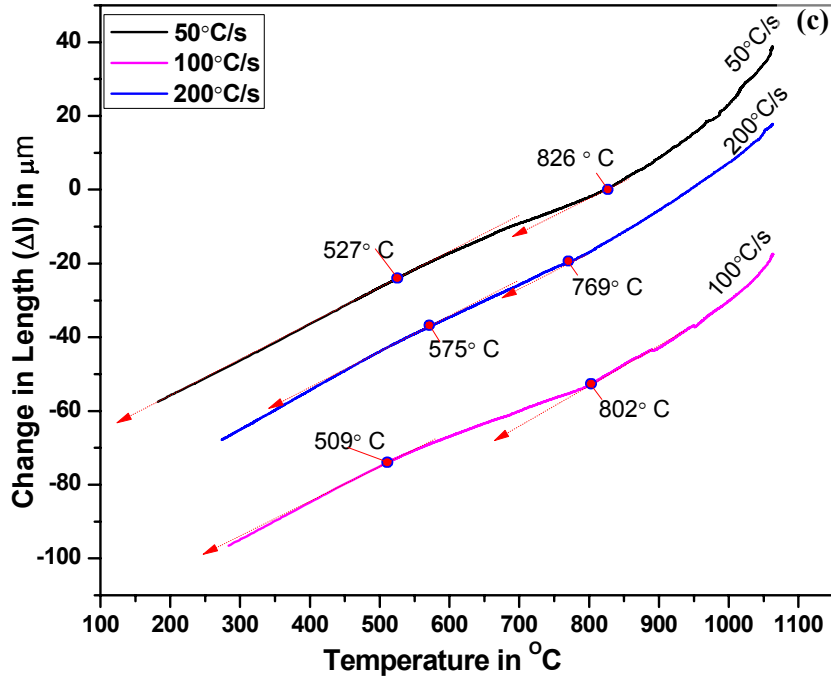


Fig.4.1 (c) Analysis of cooling part of  $\Delta l$  vs.  $T$  curve for  $\beta_{Zr} \rightarrow \alpha_{Zr}$  transformation start and end points for the cooling rates between 50 °C/s and 200 °C/s

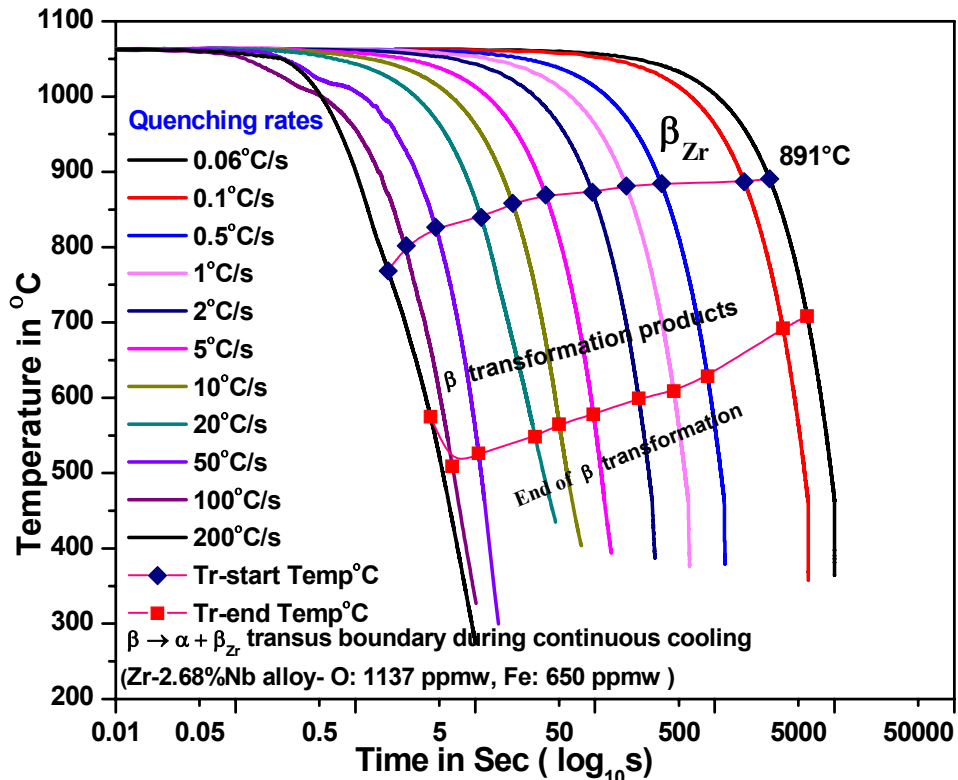
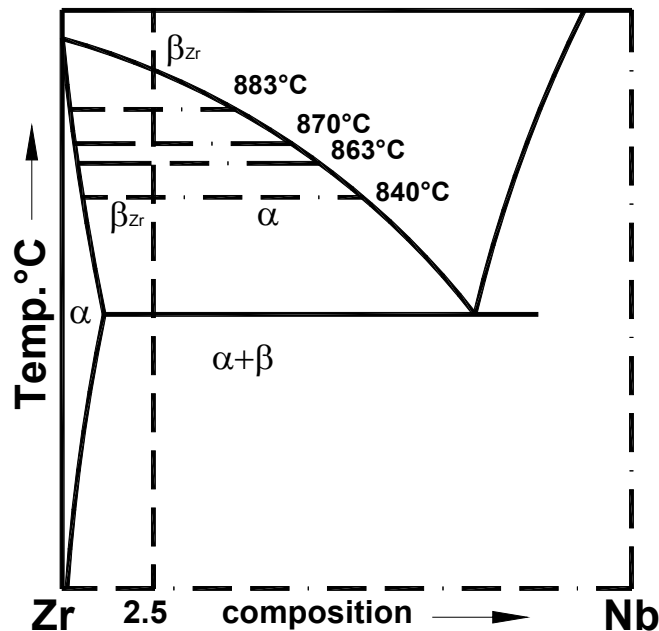


Fig. 4.2 Partial CCT diagram for the Zr-2.5% Nb PT alloy selected for the heat treatment study

#### 4.4 Heat treatments from the ( $\alpha+\beta$ ) phase field of Zr-2.5%Nb alloy

Since heat-treatments of zirconium-niobium alloys usually consist of a solution treatment in the upper portion of the ( $\alpha+\beta$ ) region of the phase diagram, the soaking temperatures 840, 863, 870, 883°C were chosen for the heat treatment in the present study. Selection of these temperatures was based on the  $\beta$  transus start temperature of 891°C established for the slowest cooling rate of 0.06°C/s for the alloy. The experimental part of the heat treatment has been discussed in the section 3.1.6. The main objectives of this part of the study was to investigate the effect of soaking temperatures and the cooling rates on the distribution and morphologies of  $\beta_{Zr}$  phase transformation products and also textural changes occurring due to the heat treatments. The results of heat treatments by quenching dilatometry and microstructural textural examinations by electron microscopy techniques have been discussed in the following sections.

##### 4.4.1 Dilatometric curves of ( $\alpha+\beta$ ) heat treatment experiments



*Fig. 4.3 Schematic presentation of Zr- rich region of the Zr-Nb system showing effect of soaking temperature on fractions of  $\alpha$  and  $\beta$  phases and their compositions*

Different soaking temperatures in ( $\alpha+\beta_{Zr}$ ) phase field influenced the fractions of primary  $\alpha_{Zr}$  and  $\beta_{Zr}$  in the sample (see Fig.4.3), before being subjected to cooling, while different cooling rates

adopted from these soaking temperatures influenced the morphologies of  $\beta_{Zr}$  phase transformation that led to formation of Widmanstätten- $\alpha$  along with network of  $\beta$  or martensite ( $\alpha'$ ) depending on cooling rates adopted [4, 10].

Fig.4.4 (a), shows a typical output of dilatometry curves for one of the heat treatment experiments. The heating part of dilatograms for all the samples showed  $(\alpha_{Zr}+\beta_{Nb})\rightarrow(\alpha_{Zr}+\beta_{Zr})$  transformation dilation similar to the one observed during determination of  $\beta$ -transus boundary for the alloy discussed in section 3.1.4 (see Fig. 3.5 (c)). However, in the case of soaking in the  $(\alpha+\beta)$  phase field, it was observed that the  $(\alpha_{Zr}+\beta_{Nb})\rightarrow(\alpha_{Zr}+\beta_{Zr})$  transformation continued isothermally at the selected soaking temperatures as seen in Fig.4.4 (a). It was observed that, during the soaking time for 30 min at 883°C the dilation curve remained nearly flat (see Fig.4.4 (a)) indicating quick equilibration of transformation at such higher soaking temperature.

Fig.4.4 (b) shows a typical dilatogram of cooling part of a specimen for the cooling rates 25°C/s from all the soaking temperatures studied. These curves show typical nucleation and growth type of transformation of  $\beta_{Zr}\rightarrow(\alpha_{Zr}+\beta_{Zr})$ , where the fraction transformed builds up at the expense of parent  $\beta_{Zr}$  resulting in progressive increase in the specific volume. At every instant on the dilation curve, the length change of the specimen is due to three factors. First being, the thermal contraction of existing phases i.e. primary  $\alpha$  and the  $\beta$ -phase transformed products and untransformed  $\beta_{Zr}$ . Second being, the volume change due to  $\beta_{Zr}\rightarrow\alpha_{Zr}$  (known as *transformation strain*) which is a more dominant physical change and hence would produce pronounced positive change in the specimen length. This is because, *bcc*  $\beta_{Zr}$  phase is denser phase and has ~2.6% smaller lattice parameter compared to *hcp*  $\alpha_{Zr}$  and hence the deviation in the dilation curve would be observed [7]. Third being change in specific volume of  $\alpha_{Zr}$  and  $\beta_{Zr}$  phases due to increased 'Nb' content at the lower temperatures in the  $(\alpha+\beta)$  phase field [11-13] (see Fig. 4.3).

Fig. 4.5 (a) shows one of the typical set of cooling part of the dilation curves, with slope changes indicating transformation of  $\beta_{Zr}$  phase in different temperature range when cooled at different rates from the soaking temperature 883°C. At slower cooling rate such as 0.5°C/s due to the low degrees of under cooling, the transformation  $\beta_{Zr}\rightarrow(\alpha_{Zr}+\beta_{Zr})$  reached completion at higher temperature (Fig. 4.5 (a)), whereas at higher cooling rates such as 10 and 25°C/s it was observed

that due to higher degrees of undercooling, the same transformation occurred at lower temperatures (Fig. 4.4 (b) and Fig. 4.5 (a)).

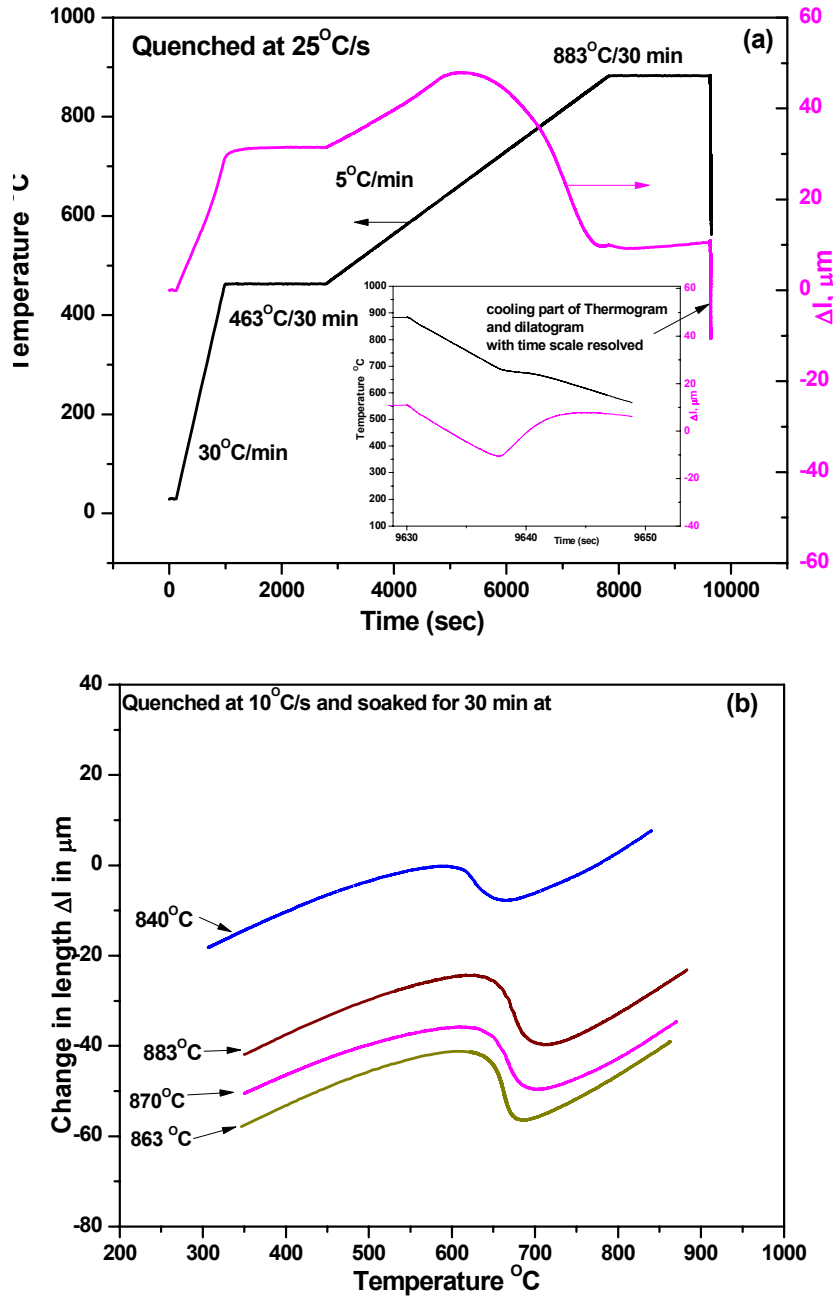


Fig. 4.4 (a) Typical thermogram and dilatogram recorded for one of the samples that was soaked at 883°C (within the  $(\alpha+\beta)$  phase field) and quenched at 25°C/s, (b) Slope changes in the cooling part of dilation curves showing transformation of  $\beta_{Zr} \rightarrow \alpha_{Zr} + \beta_{Zr}$  phase for the cooling rate 10°C/s from different soaking temperatures

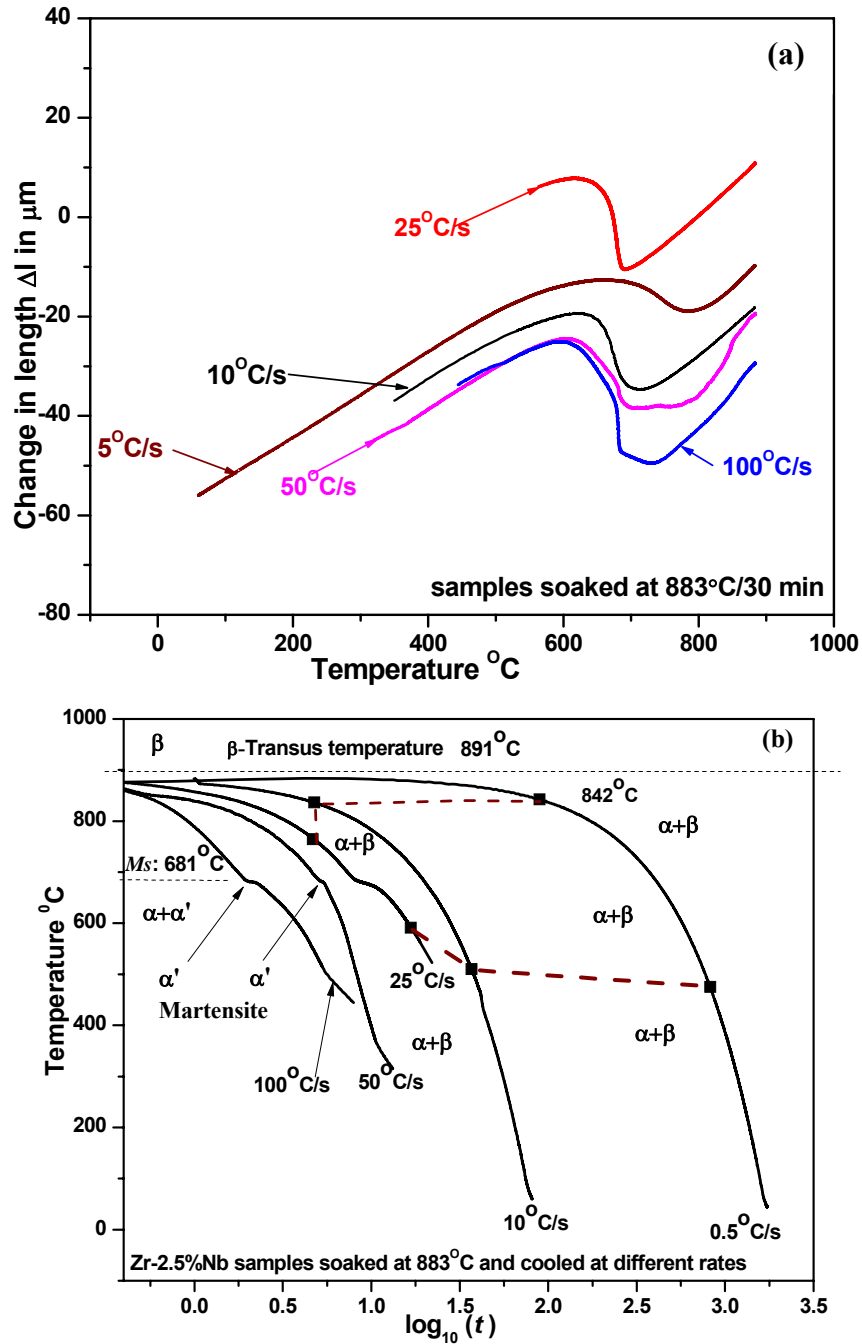


Fig. 4.5 (a) The slope changes in the cooling part of dilatograms showing transformation of  $\beta_{\text{Zr}}$  phase when cooled at different rates from the soaking temperature  $883 \pm 0.5^{\circ}\text{C}$ . The significant increase in volume (i.e. increase in length) during cooling may be attributed to formation of  $\alpha_{\text{Zr}}$  at slower cooling rates and  $\alpha'$  at relatively higher cooling rates, (b) A partial CCT diagram for the Zr-2.5%Nb alloy for the condition soaked in  $(\alpha+\beta)$  phase field at  $883^{\circ}\text{C}$  and quenched at different rates. The martensite start temperature is observed at  $681^{\circ}\text{C}$  for this alloy and is also observed to be independent of cooling rates beyond  $50^{\circ}\text{C/s}$ .

With increase in cooling rates to 50 and 100°C/s, the dilatograms showed marked difference in  $\beta_{Zr}$  transformation characteristics with multiple stepped slope changes for all the soaking temperatures studied (see Fig.4.5 (a)). Such sharp multiple steps on the dilation curves may be attributed to formation of  $\alpha_{Zr}$  at the  $\beta_{Zr}$  boundaries and also  $\beta_{Zr}$  phase undergoing martensitic ( $\alpha'$ ) transformation in successive stages. Fig.4.5 (b) shows the cooling part of the thermograms recorded for these samples (soaked at 883°C) in the form of typical continuous cooling transformation diagram. The plot shows the temperature ranges of  $\beta_{Zr}$ -transformation products such as  $\alpha$ ,  $\beta$  and martensite ( $\alpha'$ ) for different cooling rates adopted in the study. These transformation temperatures were also determined according to the method described in section 3.1.5 Fig. 3.5 (c). Similar transition temperatures were observed even for the case of different soaking temperatures such as 870, 863 and 840°C. It was observed that the martensite start ( $M_s$ ) temperature of 681°C identified by sharp increase in volume in the dilatogram and thermal arrest points in the thermograms for the quenched samples remained nearly same for all the lower soaking temperatures studied.

#### 4.5 Microstructural evolution in Zr-2.5%Nb alloy due to heat treatments

The bright field TEM micrographs presented in Fig 4.6 to 4.9 provide the finer details of distribution of the  $\alpha$  and  $\beta$  phases, their size and morphologies for the samples heat treated in the ( $\alpha+\beta$ ) phase field using dilatometry. These micrographs describe the microstructural evolution as a function of cooling rates and soaking temperatures (*from the  $\alpha+\beta$  phase field*) used in the study. Table-4.1, 4.2 and 4.3 provide the details of effect of cooling rate on the grain size of the transformed  $\alpha$  phase and also the effect of soaking temperature between 883 and 863 °C in the  $\alpha+\beta$  phase field on the fraction of primary  $\alpha$  (*approximated from SEM image analysis*). As expected from the Zr-rich region of Zr-Nb phase diagram [14] and as schematically presented in Fig.4.3, the samples soaked at 883°C had relatively low fraction of primary  $\alpha$  at room temperature (see Table-4.2) as it was closest to the  $\beta$ -transus temperature of 891°C established for the same alloy in this study (see section 4.3). At lower soaking temperatures, such as 870 °C and 863°C, the volume fraction of primary  $\alpha$  phase increased (Tables -4.2 and 4.3) particularly

for the cases of lower cooling rates as  $\alpha$  phase tends to grow on the existing primary  $\alpha$  phase as seen in the Fig.4.6 (a), (b), 4.7 (a), 4.8 (a).

The effect of cooling rate on the size and morphology of the transformed products is shown as in the case of two extreme rates of cooling in Fig.4.10 (a-b). It is evident that the higher rate of cooling ( $100^{\circ}\text{C/s}$ ) from the soaking temperature of  $883^{\circ}\text{C}$  results in much finer martensite, in contrast to large Widmanstätten plates obtained through relatively much slower cooling rate of  $0.5^{\circ}\text{C/s}$ . Statistical measurement of grain size distribution, using EBSD, in these two extreme cases revealed a mean size ratio of 5 in case of both  $\alpha$  and  $\beta$  phases. Thus the present study reveals maximum window of grain sizes that can be achieved from the quenching process for a soaking of 30 min. This is because of the fact that  $100^{\circ}\text{C/s}$  and  $0.5^{\circ}\text{C/s}$  represent two reasonably extreme cooling rates achievable in practice for the production of full scale pressure tube. The wide difference observed in grain sizes between the aforementioned samples is expected to have an important influence on their properties.

The samples cooled at  $50^{\circ}\text{C/s}$  and  $100^{\circ}\text{C/s}$  showed predominantly martensitic transformation (Fig.4.6 (d), (e) and 4.7 (c)). At higher cooling rate of  $100^{\circ}\text{C/s}$ , internally twinned martensite plates were observed (Fig.4.6 (e)), whereas internally slipped martensite were the major features observed in samples subjected to relatively lower cooling rates of  $50^{\circ}\text{C/s}$  together with a minor fraction of primary  $\alpha$  phase (Figs. 4.6 (d), (e), 4.7 (c), 4.8 (c), (d) and 4.9 (c)) [15]. The martensite plates were seen to have formed in self accommodating morphologies (Fig. 4.6 (d)), thereby reducing the transformation strain energies [16]. In contrast at much slower cooling rates such as  $0.5^{\circ}\text{C/s}$  large Widmanstätten  $\alpha$  lamellae were obtained (see Fig. 4.6 (a)). With a decrease in cooling rates from  $25^{\circ}\text{C/s}$ . The width of the Widmanstätten  $\alpha$  plates increased (Table-4.1 and 4.3) and their morphology progressively changed from being sharp straight lamellae to more irregular-shaped lamellae (Fig. 4.6 (a), (b), (c), Fig. 4.7 (a), (b)).

The mixed structures of finer Widmanstätten  $\alpha$  lamellae and martensite were obtained even for the cooling rate of  $25^{\circ}\text{C/s}$  at the lower soaking temperatures as in the case of  $870^{\circ}\text{C}$ ,  $863^{\circ}\text{C}$  and  $840^{\circ}\text{C}$  soaked samples (Fig. 4.7 (b), 4.8 (b) and 4.9 (b)).

Comparison of Fig. 4.6 (c), 4.7 (b) and Fig. 4.9 (b) reveal that the probability of martensitic transformation is higher with lowering of soaking temperature for a given cooling rate. This may

be attributed to the higher ‘Nb’ content in the  $\beta$  phase at the lower soaking temperatures which might provide the driving force for martensitic transformation. In general, the Widmanstätten  $\alpha$  lamellae became finer with lower soaking temperature (Fig.4.6 (b), 4.7 (a), 4.8 (a) and 4.9 (a)). At lower soaking temperature, higher incidence of internally twinned martensite was observed due to matrix (*untransformed  $\beta$ -phase*) being stronger (Fig. 4.8 (b)) [15]. Such a wide range of microstructural changes in the alloy samples due to various heat treatment conditions are expected to have influence on the mechanical properties.

On the basis of these observations it may be concluded that in order to obtain primary  $\alpha$  and martensitic microstructure, a lower soaking temperature in the  $\alpha+\beta$  phase field followed by a minimum cooling rate of 25°C/s is required. This is an important result from practical point of view for the design of quenching operation of pressure tubes.

*Table-4.1: Effect of cooling rate on microstructural features for 883±0.5°C soaked specimens*

Cooling rate (°C/sec)	Microstructure	Primary $\alpha$ vol. fraction (%) - (Approximated from SEM image analysis)	Grain size $\alpha$ (nm) -primary	Size: $\alpha$ Widmanstätten width (nm)	Grains size and % of the phases observed
100	$\alpha$ + Internally twinned martensite	3-5	200-400		Grain size prior $\beta$ ~10-15 $\mu\text{m}$ Grain size $\alpha$ ~1-3 $\mu\text{m}$
50	$\alpha$ + Internally slipped martensite	3-5	200-400		Primary $\alpha$ percentage ~ 3% Martensite plates 0.5-3 $\mu\text{m}$
25	$\alpha$ + Widmanstätten	3-7	200-500	10-80	Grain size: prior $\beta$ ~10 $\mu\text{m}$ . Grain size $\alpha$ ~1-3 $\mu\text{m}$ .
10	$\alpha$ + Widmanstätten	3-8	300-600	10- 100	Primary $\alpha$ = 5-8% Widmanstätten lamellae
0.5	$\alpha$ +Widmanstätten	3-10	300-900	100-300	dimensions : Length =10 to 20 $\mu\text{m}$ Width ~ 1-2 $\mu\text{m}$

*Table-4.2: Effect of cooling rate on microstructural features for 870±0.5°C soaked specimens*

Cooling rate (°C/sec)	microstructure	primary $\alpha$ vol. fraction (%) (approximated from SEM image analysis)
100	$\alpha$ + Internally twinned martensite	15-20
50	$\alpha$ +Internally slipped martensite	15-20
25	$\alpha$ + slipped martensite	15-20
10	$\alpha$ +Widmanstätten	15-25

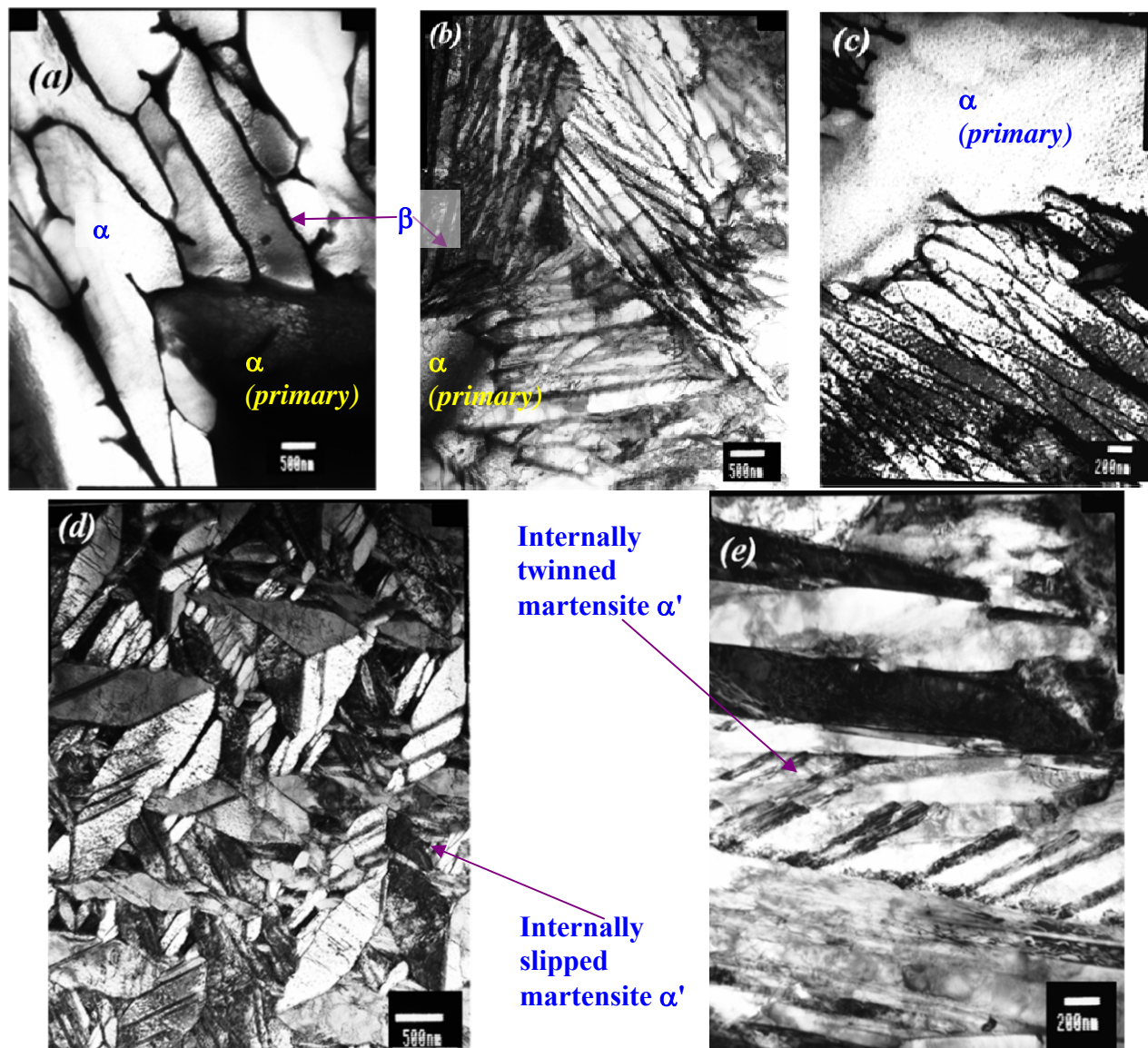


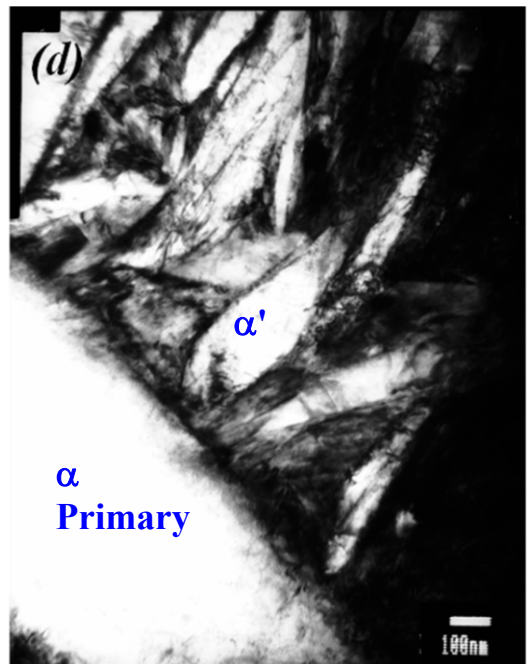
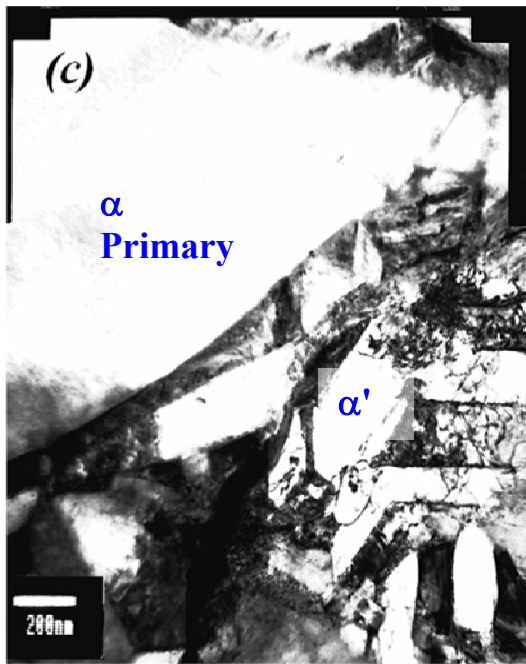
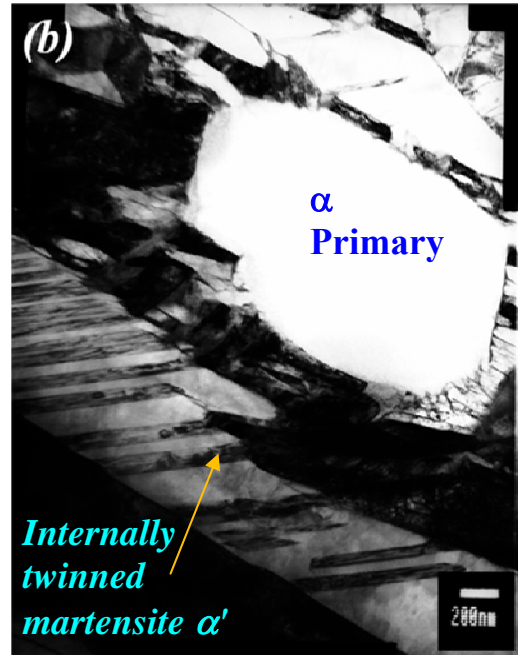
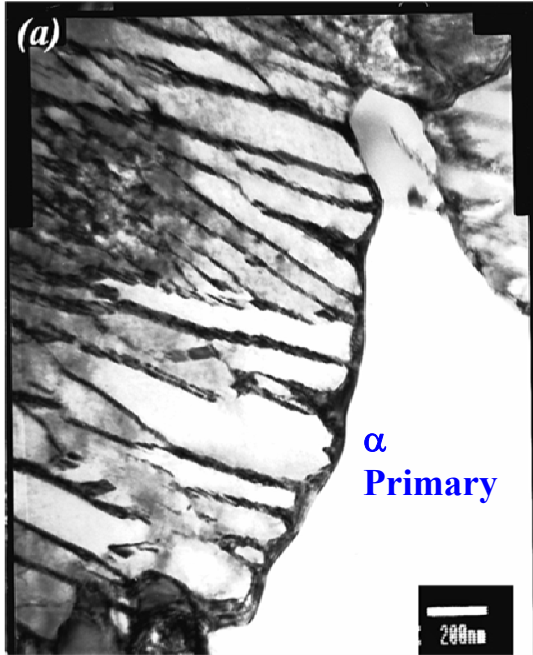
*Fig. 4.6 Bright field TEM micrographs showing distribution and morphology of primary  $\alpha$  and  $\beta$  phase transformed products  $\alpha$ ,  $\beta$  and  $\alpha'$  for the samples soaked  $883\pm 0.5^\circ\text{C}$  and cooled at, (a)  $0.5^\circ\text{C/s}$ , (b)  $10^\circ\text{C/s}$ , (c)  $25^\circ\text{C/s}$ , (d)  $50^\circ\text{C/s}$  and (e)  $100^\circ\text{C/s}$ .*

*Table-4.3: Effect of cooling rate on microstructural features for  $863\pm 0.5^\circ\text{C}$  soaked specimens*

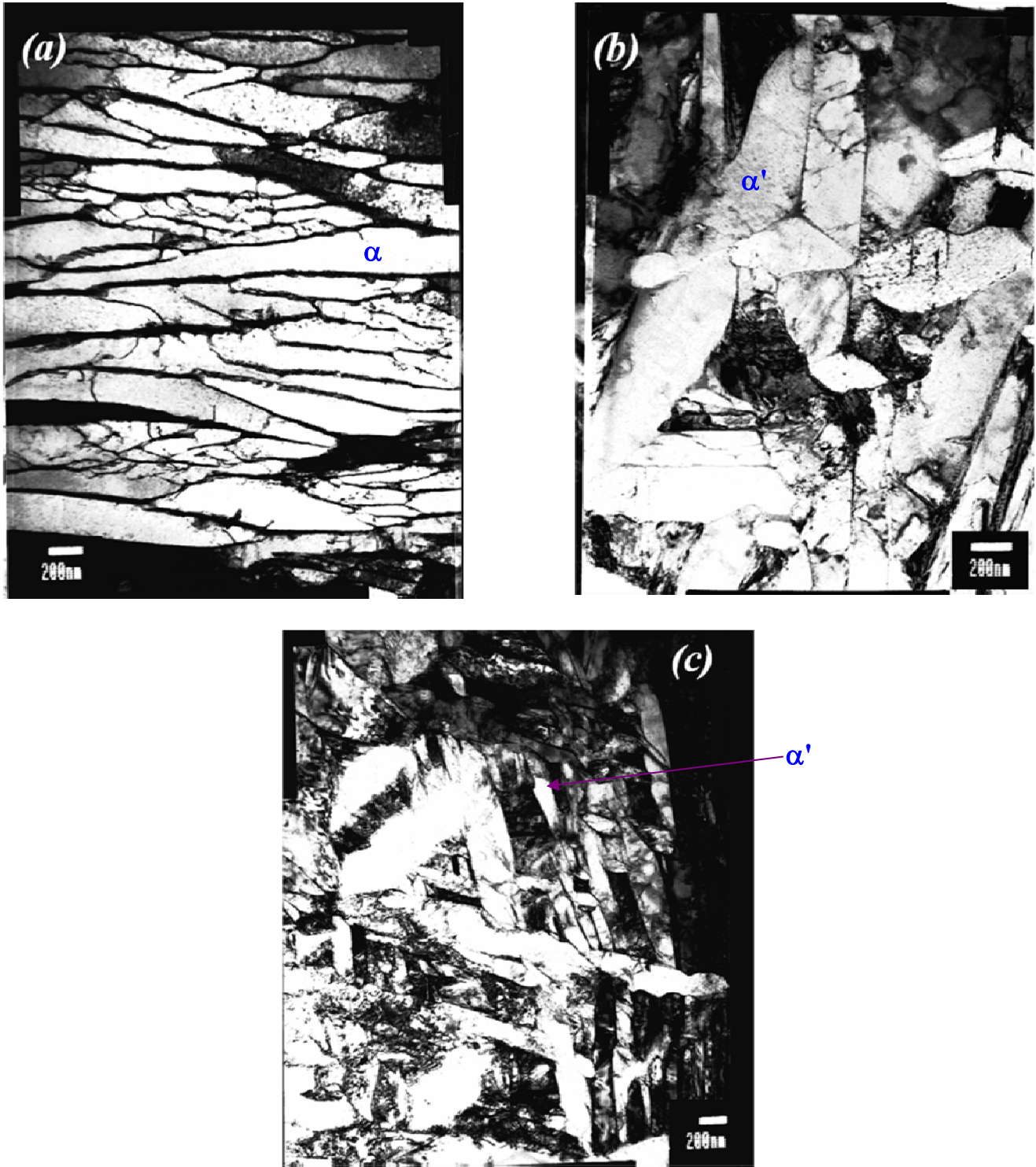
Cooling rate ( $^\circ\text{C/sec}$ )	microstructure	vol. fraction (%) - primary $\alpha$ (approximated from SEM image analysis)	Size: of Primary $\alpha$ (nm)	Size of Widmanstätten $\alpha$ width (nm)
100	$\alpha$ + martensite	18-22	300-700	No Widmanstätten $\alpha$
50	$\alpha$ + martensite	18-23	300-700	
25	$\alpha$ + martensite	18-23	300-700	Not significantly present
10	$\alpha$ + Widmanstätten	20-28	300-900	10- 80



Fig. 4.7 Bright field TEM micrographs showing distribution and morphology of primary  $\alpha$  and  $\beta$ -phase transformed products  $\alpha$ ,  $\beta$  and  $\alpha'$  for the samples soaked  $870\pm 0.5^\circ\text{C}$  and cooled at, (a)  $10^\circ\text{C/s}$ , (b)  $25^\circ\text{C/s}$  and (c)  $50^\circ\text{C/s}$



*Fig. 4.8* Bright field TEM micrographs showing distribution and morphology of primary  $\alpha$  and  $\beta$ -phase transformed products  $\alpha$ ,  $\beta$  and  $\alpha'$  for the samples soaked  $863 \pm 0.5^\circ\text{C}$  and cooled at, (a)  $10^\circ\text{C/s}$ , (b)  $25^\circ\text{C/s}$ , (c)  $50^\circ\text{C/s}$  and (d)  $100^\circ\text{C/s}$



*Fig. 4.9 Bright field TEM micrographs showing distribution and morphology of primary  $\alpha$  and  $\beta$  phase transformed products  $\alpha$ ,  $\beta$  and  $\alpha'$  for the samples soaked  $840\pm 0.5^\circ\text{C}$  and cooled at, (a)  $10^\circ\text{C/s}$ , (b)  $25^\circ\text{C/s}$  and (c)  $50^\circ\text{C/s}$*

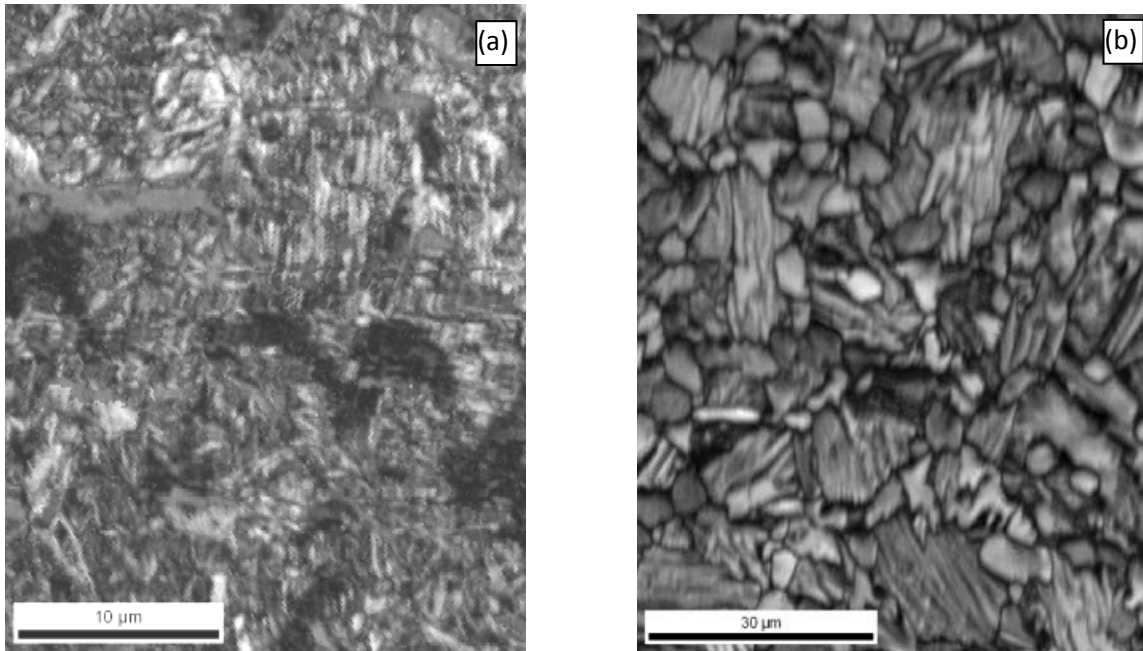


*Fig. 4.10 Image quality maps obtained from EBSD of (a) sample quenched from 883°C at a rate of 100°C/s (b) sample quenched from 883±0.5°C at a rate of 0.5°C/s*

#### **4.6 Texture evolution in Zr-2.5%Nb alloy due to heat treatments**

The texture evolution study was carried out using EBSD technique for a few of the selected samples adopting the procedure mentioned in the reference [17] and the manual of TSL-OIM. The results of Kearn's texture parameters obtained for the samples are tabulated in Table-4.4. It is clear that the starting material is highly textured, with majority of the basal poles (*i.e.*, normals of  $(0002)_\alpha$  plane) oriented along the circumferential direction of the tube. Such texture is expected, as the tube had gone through extrusion and pilgering during its fabrication. Quenching of samples with a rate of 50°C/s and 100°C/s, have resulted in considerable randomisation of the texture as indicated by nearly similar values of basal pole fractions ( $f_a$ ,  $f_r$ ,  $f_t$ ) along the three principal directions of the samples. Slower rate of quenching, on the other hand, resulted in similar fraction of basal poles to be aligned along the radial and circumferential directions ( $f_r$ ,  $f_t$ ) leaving axial component ( $f_a$ ) largely unaltered. These observations can be rationalised based on the differences in  $\beta$  to  $\alpha$  transformation characteristic at these widely different quenching conditions. For cooling rates of 50°C/s and above, as shown in Fig. 4.10 (a), transformation is largely martensitic in nature and the transformation products consisted of very fine distribution

of the various variants of the martensite plates. It has been shown in a number of studies that the  $\beta$  to  $\alpha$  transformation follows burger orientation relationship given by  $(0001)_\alpha // (110)_\beta$  and  $[2\bar{1}\bar{1}0]_\alpha // [111]_\beta$ . Theoretically, a single  $\beta$  grain can yield as many as 6 variants of  $\alpha'$  needles satisfying this crystallographic relationship. Even if there is considerable degree of variant selection, significant randomisation is expected if a large number of fine grains are generated from the parent  $\beta$  grains. This indeed is the case in case of cooling rates exceeding  $50^\circ\text{C/s}$  and thus explains the nearly random texture observed in these samples. Sample, cooled at  $0.5^\circ\text{C/s}$ , however, did not show appreciable modification in texture, especially along the axial component.

*Table-4.4: Kearns texture parameters for the samples subjected to various cooling rates*

Sample condition Soaking Temp. $^\circ\text{C}$ /cooling rate ( $^\circ\text{C/s}$ )	Kearns texture parameters (Standard deviation (SD) 0.02)		
	$(f_a)$ Axial direction	$(f_r)$ Radial direction	$(f_t)$ circumferential direction
As received sample	0.05	0.35	0.60
$883^\circ\text{C}-100^\circ\text{C/s}$	0.27	0.39	0.32
$883^\circ\text{C}-50^\circ\text{C/s}$	0.36	0.36	0.28
$883^\circ\text{C}-0.5^\circ\text{C/s}$	0.1	0.45	0.45

This can be attributed to the predominantly Widmanstätten nature of the transformation, coupled with the relatively large size (*consequently fewer number of product grains*) of the transformed product. Hence the degree of texture randomisation is very low in this sample.

#### **4.7 Effect of cold working on texture modification of heat treated Zr-2.5% Nb alloy**

As discussed in the earlier subsections, the Zr-2.5% Nb pressure tube is presently being fabricated using well established route consisting of hot extrusion followed by two stage cold pilgering (*cold work*) and stress relieving treatment for the PHWRs. The effect of cold working on the texture modification of the Zr-2.5%Nb alloy after the heat treatment in the  $\alpha+\beta$  phase field would be an important part of the work which can provide input for the manufacture of heat treated pressure tube. It is well known that the final microstructure and also the texture of the alloy is largely controlled by the ratio of reduction in wall thickness ( $R_w$ ) and reduction in tube diameter ( $R_D$ ) during pressure tube fabrication [18-20]. Therefore, the aim of this part of the work was to have better understanding on the texture evolution as a function of cold work on the heat treated Zr-2.5%Nb pressure tube samples.

#### 4.7.1 Effect of cold deformation on texture evolution of ( $\alpha+\beta$ ) heat treated Zr-2.5%Nb alloy

Three samples cold worked to  $\sim 9.6$ ,  $\sim 12$  and  $\sim 28.6\%$  along with the as heat treated sample were initially electro polished adopting the standard procedure as discussed in subsection 3.7. The samples were then subjected to EBSD scanning for studying texture evolution as a function of cold work through microtextural examination. The EBSD scans obtained for the reflections from radial-transverse plane of the samples were analysed for determining Kearn's texture parameters adopting standard procedures. It is to be noted here that, the dilatometry samples were extracted from the axial direction for heat treatment and the specimens were cylindrical, therefore the identification of radial and transverse directions of the tube on the specimen was not possible. Therefore, the Kearn's texture parameters obtained for the axial direction of the sample which coincides with the pressure tube axis were used to correlate with the amount of cold work in the sample. As discussed earlier, the general microstructure of Zr-2.5%Nb alloy pressure tube fabricated from cold worked and stress relieved route possess elongated  $\alpha_{Zr}$  plates that constitutes over 90% of the volume and remaining 10% of  $\beta_{Zr}$  phase is present in the form of thin filaments around the  $\alpha_{Zr}$  phase [21, 22].

*Table -4.5: Kearn's Texture parameter ( $f_a$ ) for the cold worked samples after heat treatment*

Sample condition	% Cold Work	( $f_a$ ) Axial direction (SD 0.02)
Starting material ( <i>as fabricated</i> )	0	0.05
As heat Treated ( <i>soaked at 870°C/30 min and cooled at 25°C/s</i> )	0	0.04
1	$\sim 9.6$	0.05
2	$\sim 12$	0.10
3	$\sim 28.6$	0.27

The preferred orientation of the  $\alpha_{Zr}$  phase resulting from a series of thermomechanical treatments during the pressure tube fabrication makes it highly textured material with predominantly transverse orientation of basal poles [21, 22]. The texture parameters for the starting material (*as received*) as determined by XRD technique are presented in Table-4.4, and Table-4.5 provides the texture parameters determined after the compression testing of the samples to different amounts. The image quality maps obtained for the as heated treated condition as well as

compression tested samples are presented in Fig. 4.11 (a-d). The correlation of texture parameter ( $f_a$ ) with the percentage of cold work is shown in Fig. 4.11(e).

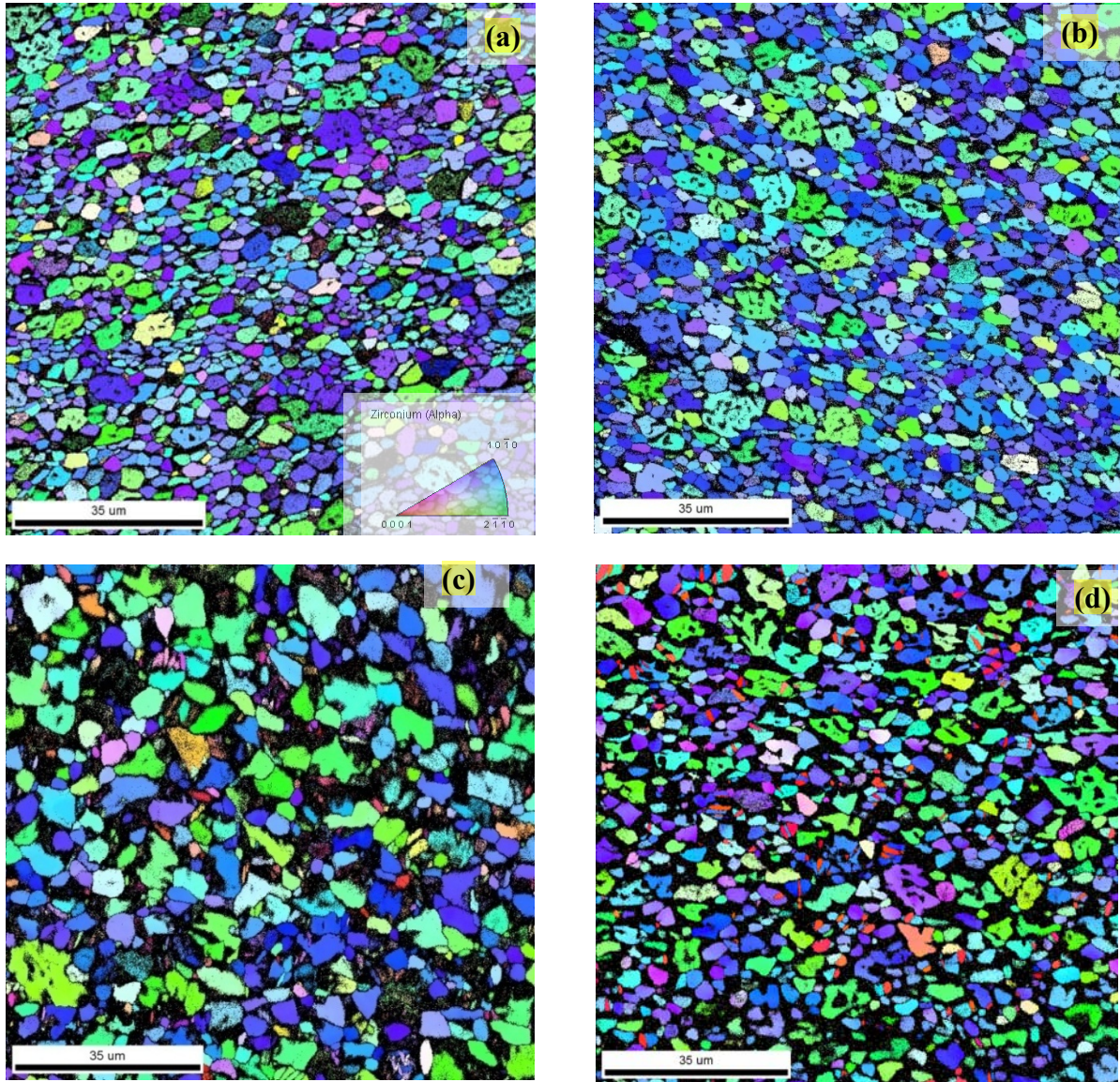


*Fig. 4.11 Image quality maps from the EBSD scans for the Zr-2.5%Nb alloy samples heat treated at  $870\pm 0.5^\circ\text{C}/30$  min and cooled at  $25^\circ\text{C}/\text{s}$  followed by Cold Working (CW) to different levels (a) as heat treated (0% CW) (b)  $\sim 9.6\%$  CW, (c)  $\sim 12\%$  CW, (d)  $\sim 26.8\%$  CW*

It can be seen from the results that the  $f_a$  values for the starting material (before the heat treatment, Table 4.4) and for the heat treated condition (soaked at  $870^\circ\text{C}/30\text{min}$  and cooled at  $25^\circ\text{C}/\text{s}$ ) and cold worked condition up to  $\sim 9.6\%$  and  $\sim 12\%$  showed insignificant change

indicating no considerable modification in the texture (Table 4.5). Whereas at ~28.6% of cold work the  $f_a$  value showed considerable increase (see Fig. 4.11(e)).

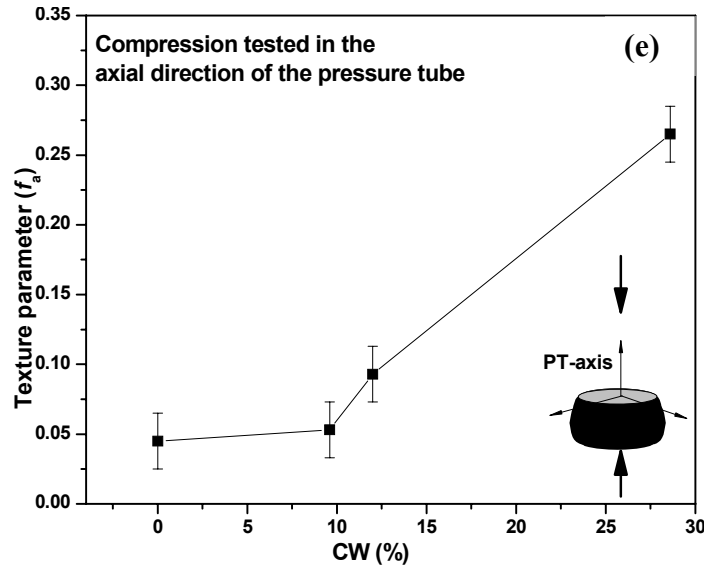


Fig. 4.11 (e) Correlation of Texture parameter ( $f_a$ ) with %CW showing increasing trend

Since the specimen were axially loaded with respect to pressure tube axis during the compression testing, majority of the  $\alpha_{Zr}$  crystallites in the radial –transverse plane experienced the tensile stresses along their c-axis due to the Poisson’s effect, causing elongation or flow of the material in the directions along radial-transverse plane. The observed modification in the crystallographic texture with the increasing amounts of cold work can be explained on the basis of deformation mechanisms operative in the alloy. It is well known that the c/a ratio for the  $\alpha_{Zr}$  phase is 1.593 which is less than the ideal ratio of 1.633 for the hcp structure. This makes prismatic slip a dominant slip system operative in the deformation of the Zr-2.5%Nb alloy [18]. However, such deformation systems (*primary slip systems*) are limited (*only two in number*) in the  $\alpha_{Zr}$  and are also not symmetric as compared to metals with cubic structure [18, 19]. The two available slip systems are not sufficient to satisfy the Von Mises criterion which requires at least five independent slip systems for uniform plastic deformation in polycrystalline materials [20]. Therefore, the deformation in hcp metals like Zr-2.5%Nb alloy is mainly contributed by the combined effect of slip and twinning. The extensive study by Tenckhoff [18] on the deformation mechanisms and associated texture developments in the Zr alloys, has described that, initially the deformation proceeds primarily on the prism planes in the  $\langle a \rangle$  directions of the hcp lattice at low

deformation rates. However, under constraints i.e. when the slip is inhibited, the pyramidal planes  $\{\bar{1}011\}$  and  $\{1\bar{2}11\}$  with  $\langle c+a \rangle$  directions become operative to produce deformation by twinning [18, 19, 21, 23]. Although the amount of strain resulting from twinning is small, it can cause large rotation of lattice and play an important role in favorably orienting additional slip systems with the stress axis. The twinning can also initiate new slip systems even at the stress concentration regions such as twin boundaries and dislocation interaction regions. These newly oriented slips systems can become responsible for continuing further deformation [18, 19, 24].

The deformation by prismatic slip although can cause rotation of lattice, the orientation changes of the crystallites are relatively low compared to the effect of twinning [18, 25]. It is reported that twinning is expected to be activated at ~5% deformation. The previous study carried out on the Zr-2.5Nb bar specimens having high concentration of basal poles along the tensile axis by Cheadle *et.al* [25], has revealed that textural changes associated with twinning for plastic strains less than 10% was insignificant. In the present study as well, it has been observed the samples compression tested up to ~9.6% and ~12% cold work showed insignificant change in texture and is in agreement with finding by Cheadle *et.al* [25].

Tenckhoff [18] study has established that for orientation of basal poles in the 50-90° from the normal direction (*i.e. direction of application of compressive load*) irrespective of azimuthal position of basal poles the  $\{10\bar{1}2\} \langle \bar{1}011 \rangle$  (*pyramidal*) twins become operative resulting in tensile strain along the c-axis of the  $\alpha_{Zr}$  crystallites. Due to the tensile strain in the c-directions, the pyramidal twin systems cause rotation of the basal poles by ~85° with respect to the direction of compression. Therefore, in the present study, the observed modification in texture parameter ( $f_a$ ) in the case of specimen subjected to ~28.6% of cold work (Fig.4.11 (e)) can be attributed to considerable extent of lattice rotation of such  $\alpha_{Zr}$  crystallites with respect to compression axis [18].

#### 4.8 Summary of the work

1. Partial CCT diagram for the Zr-2.5%Nb alloy containing 1137 ppmw oxygen and 650 ppmw of 'Fe' has been determined using quenching dilatometry.

2. It was established that the  $\beta$  transus temperature i.e  $\beta_{Zr} \rightarrow (\alpha + \beta_{Zr})$  regime for the alloy starts below 891°C for all cooling rates.
3. The transformation characteristics of the Zr-2.5% Nb alloy containing 1137 ppmw of oxygen and 650 ppmw of 'Fe' was ascertained during quenching from 883, 870, 863 and 840°C in the  $\alpha + \beta_{Zr}$  phase field, at different rates using quenching dilatometry and electron microscopy.
4. The specimens cooled from  $\alpha + \beta_{Zr}$  phase field at rates 25°C/s and slower, showed smooth dilation curve particularly for the case of samples soaked close to  $\beta$ -transus temperature such as 883°C indicating characteristic nucleation and growth type of transformation leading to Widmanstätten type of product. For quenching rates  $>25^\circ\text{C/s}$  multiple steps were observed on the dilatograms for the case of samples soaked at lower temperatures in the  $(\alpha + \beta)$  phase field which may be attributed to successive generation of martensite formation.
5. For a given soaking temperature within  $\alpha + \beta_{Zr}$  region, at cooling rates  $<25^\circ\text{C/s}$ , predominantly Widmanstätten structure resulted. The morphology of Widmanstätten  $\alpha$  changed from finer and straight lamellae to wider and irregular shape with cooling rate decreasing from 25°C/s. Mixed structures of finer Widmanstätten  $\alpha$  and martensite were observed at quenching rates 25°C/s. For quenching rates 50°C/s and 100°C/s the microstructure was predominantly martensite along with primary  $\alpha$ .
6. For a given quenching rate the probability of martensite formation increased with decreasing soaking temperatures in the  $\alpha + \beta_{Zr}$  region. This may be attributed to increased 'Nb' content in  $\beta_{Zr}$  providing the driving force at the lower soaking temperatures.
7. The microtextural study on the specimens heat treated close to  $\beta$ -transus temperature (*i.e. soaked at 883°C*) indicated that the texture tended to randomise at higher cooling rates such as 50°C/s and 100°C/s, while little change was seen at lower cooling rates.
8. The study on effect of cold deformation on textural evolution of  $(\alpha + \beta)$  heat treated samples showed that axial component of the texture parameter ( $f_a$ ) remained nearly unaffected up to 12% CW, whereas at higher amount of CW 28.6% the ( $f_a$ ) component showed increase. This is an important result considering thermomechanical treatments of the heat treated alloy.

## References Chapter-4

1. C.K. Chow, C.E. Coleman, M.H. Koike, A.R. Causey, C.E. Ells, R.R. Hosbons, S. Sagat, V.F. Urbanic, D.K. Rodgers, (*ASTM*), *STP 1295 (1996)* 469-491
2. K. Takayama, "Post-Irradiation Examination And Evaluation of Zr-2.5%Nb Pressure Tube of FUGEN", *XA9846758*, 181-192
3. M. Griffiths, J.E. Winegar, A. Buyers, *J. Nucl. Mater.*, 383(1-2) (2008) 28-33
4. G.F. Slattery, *J. Less Common Metals*, (1964) 195-208
5. P. Suwanpinij, N. Togobytska, C. Keul, W. Weiss, U. Prah, D. H"omberg, W. Bleck, *ISSN 0946-8633*, No. 1306, *WIAS Berlin*, 2008
6. A.S. Akbari, *RWTH Aachen Institute of Ferrous Metallurgy*, Matr.-Nr. 268696
7. P. Suwanpinij, N. Togobytska, C. Keul, W. Weiss, U. Prah, D. H"omberg, W. Bleck, *ISSN 0946-8633*, No. 1306, *WIAS Berlin*, 2008
8. P. Motycka, M. Kover, *Recent Trends in Structural materials*, Plze"n, Czech Republic, EU, *COMPACT-2012*, 21-22 November, 2012
9. C.E.L. Hunt, P. Niessen, *J. Nucl. Mater.*, 38 (1971) 17-25
10. N. Saibaba, S.K. Jha, S. Tonpe, Kumar Vaibhaw, V. Deshmukh, S.V. Ramana Rao, K.V. Mani Krishna, S. Neogy, D. Srivastava, G.K. Dey, R.V. Kulkarni, B.N. Rath, E. Ramadasan, S. Anantharaman, *J. (ASTM), International*, DOI: 10.1520/JAI103213, (*JAI Paper ID JAI103213*, 8, No. 6, (2011))
11. R. Tewari, D. Srivastava, G.K. Dey, J.K. Chakravarty, S. Banerjee, *J. Nucl. Mater.*, 383 (2008) 153-171
12. D.W. Suh, C.S. Oh, H.N. Han, S. J. Kim, *Acta Mater.*, 55 (2007) 2659-2669
13. P. E. J. Flewitt, *J. Appl. Cryst.* 5 (1972) 423-425
14. H. Okamoto, *Alloy phase diagrams*, *ASM International*, *ASM hand book*, 3 (1992)
15. N. Saibaba, S.K. Jha, S. Tonpe, Kumar Vaibhaw, V. Deshmukh, S.V. Ramana Rao, K.V. Mani Krishna, S. Neogy, D. Srivastava, G.K. Dey, R.V. Kulkarni, B.N. Rath, E. Ramadasan, S. Anantharaman, *J. (ASTM), International*, (*JAI*), *Paper ID JAI103213*, 8, Issue 6 (2011)
16. D. Srivastava, K.Madangopal, S. Banerjee, S. Ranganathan, *Acta Metall, Mater. Vol. 41*, No. 12 (1993) 3445-3454

17. K.V. Mani Krishna, D. Srivastava, G.K. Dey, V. Hiwarkar, I. Samajdar, N. Saibaba, *J. Nucl. Mater.* 414 (2011) 492–497
18. E. Tenckhoff, *J. (ASTM), International, (JAI) Paper ID JAI 12945, 2, No.4 (2005)*
19. K. L. Murty, I. Chari, *Progress in Nuclear Energy, 48 (2006) 325-359*
20. C.J. Cochrane, PhD Thesis “*Effect of Process Parameters on Deformation of Zr-2.5wt%Nb Alloy*”, Department of Mechanical and Materials Engineering, Queen's University Kingston, Ontario, Canada, October 2013
21. S. Cai, PhD Thesis, “*Evolution of Interphase and Intergranular Strain in Zr-Nb alloys During Deformation at room Temperature*”, Oct 2008, Dept. of Mechanical and Materials Eng. University Kingston Canada, Publication Ref, ISBN, 0494443162, 9780494443163
22. W. Li, Thesis “*Effect of Texture on Anisotropic Thermal Creep Of Pressurised Zr-2.5%Nb Tubes*”, Queen’s University Kingston, Ontario, Canada August, 2009
23. S. Cai, M.R. Daymond, R.A. Holt, M.A. Gharghouri, E.C. Oliver, *Mater. Sci. Eng. A, 501 (2009) 166-181*
24. L.B. Addessio, E. K. Cerreta, G. T. Gray, III, *Metall. Mater. Trans. A, 36A (2005) 2893-2903*
25. B. A. Cheadle, C. E. Ells, W. Evans, *J. Nucl. Mater* 23 (1967) 199-268

## **CHAPTER 5: Determination of Correlation Parameters for Evaluation of Mechanical Properties by Small Punch Test (SPT) and Automated Ball Indentation (ABI) Test for Zr-2.5%Nb Pressure Tube Material**

.....

### **5.1. Objectives**

Considering that precise heat treatment conditions can be maintained in the small size specimen volume, the quenching dilatometer was used for heat treatment of Zr-2.5%Nb alloy pressure tube samples which has been discussed in chapter-4. This systematic heat treatment study catered samples for the structure and property correlation studies. Since, the heat treated dilatometry specimens were small in size, the miniature specimen testing techniques such as ABI and SPT were selected for characterisation of mechanical properties such as yield strength (YS) and ultimate tensile strength (UTS). Since these techniques are non conventional, it was essential to establish the correlations using some standard testing method. Therefore, in this part of the work, the main objective was to determine the correlation parameters for evaluation of basic mechanical properties YS and UTS of Zr-2.5%Nb alloy using ABI and SPT.

### **5.2. Background**

Generally, conventional tension tests provide stress-strain curves and strength values which are the mainstay of worldwide design codes for the design and manufacture of many components [1]. However, in recent times the miniature techniques have become increasingly popular as they can provide mechanical property data that are in good agreement with the conventionally established values and also are generally reproducible when carried out under the controlled conditions. The miniature specimen testing techniques are essentially innovative and nonconventional techniques, developed for evaluation of mechanical properties of small size specimens through establishment of correlations using some conventional test methods such as ASTM approved methods [2-9]. The ABI technique has been successfully used by many authors [2-5,10] for evaluation of mechanical properties of small test pieces through correlations with conventional methods. Similarly, the SPT technique has also been successfully used by many authors [11, 12] through correlations for mechanical property characterisation.

The correlation parameters for a given miniature testing technique are material specific and need to be determined separately for different class of materials [5, 10, 13, 14]. No work pertaining to correlations for evaluation of mechanical properties of anisotropic Zr-base alloys using ABI and SPT has been reported in the open literature which was the main motive behind this work. Secondly, ABI and SPT techniques are best suited for studying the texture effect on the mechanical properties of anisotropic Zr-2.5%Nb alloy by testing along orthogonal directions of the tube [10] which was also another motive behind this work. Thirdly, it was also of interest to understand the sensitivity of these techniques to variations in microstructures so that these techniques can be adopted for performance evaluation of components and material development studies [1, 15, 16].

### 5.3. Microstructures of heat treated specimens

Figs. 5.1, represents the microstructure of the various samples, generated by heat treatment from  $\alpha+\beta$  phase field. It is clear that heat treatment has resulted in a wide range of microstructures. The furnace cooled sample (*cooling rate: 0.15°C/s*) developed coarse Widmanstätten  $\alpha$  grains surrounded by thin filaments of  $\beta$ , as shown in Fig.5.1 (a). The morphology of Widmanstätten  $\alpha$  grains became finer when cooling rate increased to 28°C/s, as seen from micrographs in Figs. 5.1(a), (b). At cooling rate 55°C/s the transformation was predominantly martensitic along with primary  $\alpha$  (see Fig.5.1(c)). Fig.5.1 (d) depicts the formation of very fine martensitic structure along with primary  $\alpha$  in case of water quenched sample (i.e., sample with highest cooling rate of the present study). Thus, this set of samples represents a fairly wide range of microstructures and therefore was suitable for meeting the objective of the present study.

Table-5.1: Kearn's texture parameters for the starting material Zr-2.5%Nb PT spool piece

$(f_a)$ Axial direction	$(f_r)$ Radial direction	$(f_t)$ Circumferential direction
0.05	0.35	0.6

It may be noted here that the samples for present study were extracted from an as fabricated pressure tube, which was highly textured (as shown in the Table-5.1). In this context it becomes pertinent to investigate the role of loading direction (both for ABI, SPT) on the correlation parameters.

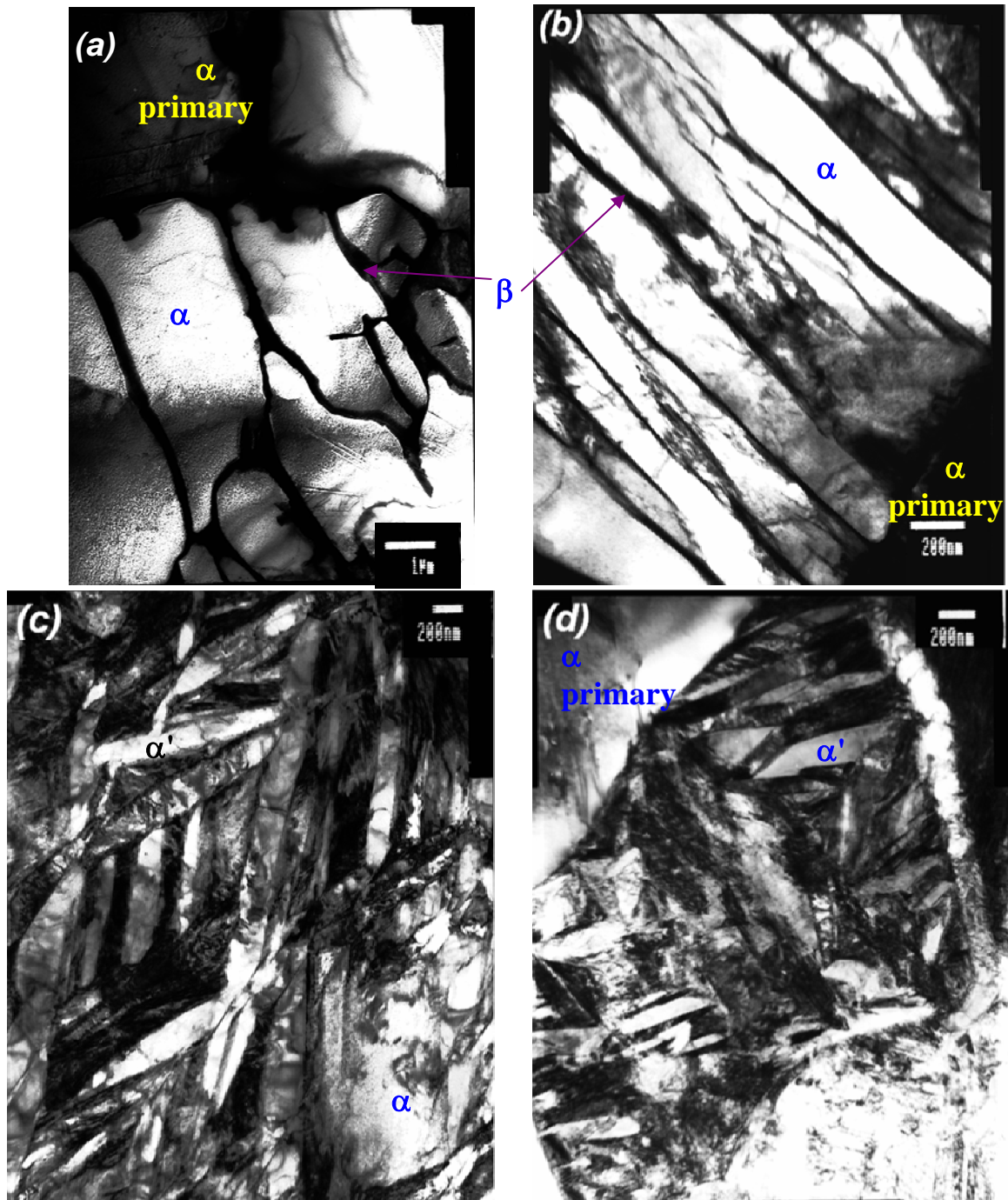


*Fig. 5.1 Bright field TEM micrographs showing distribution and morphology of primary  $\alpha$  and  $\beta$ -phase transformed products  $\alpha$ ,  $\beta$  and  $\alpha'$  for the samples soaked 880°C and cooled at, (a) furnace cooled (0.15 °C/s), (b) 28°C/s, (c) 55°C/s and (d) water quenched sample*

## 5.4 Evaluation of Mechanical Properties of heat treated specimens

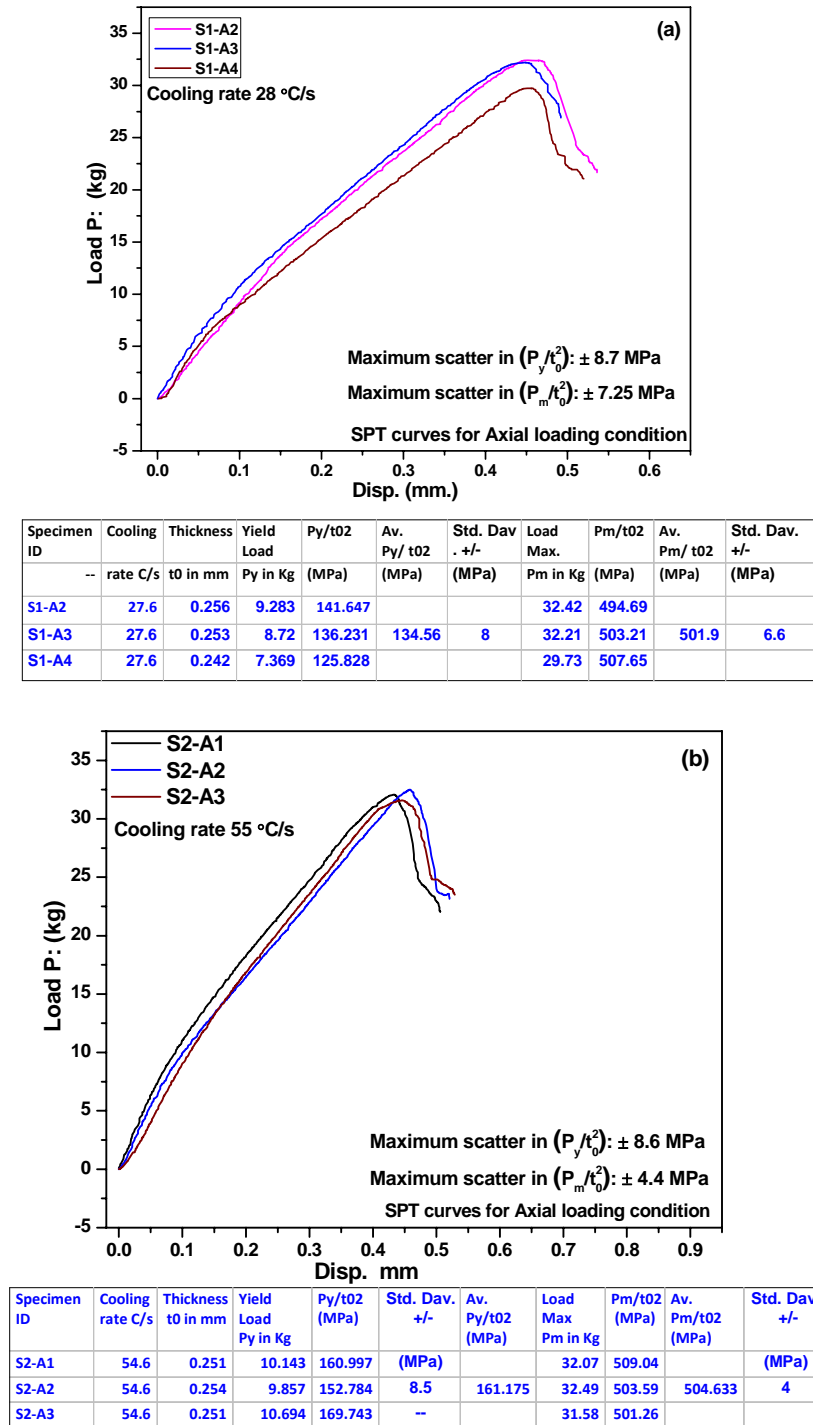
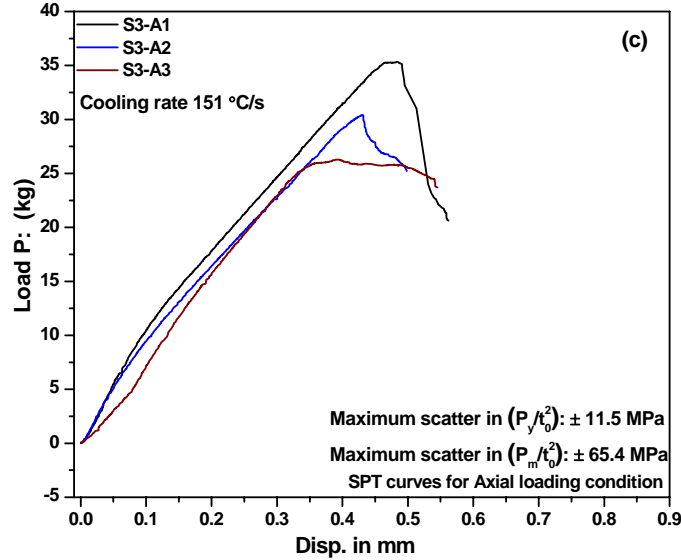
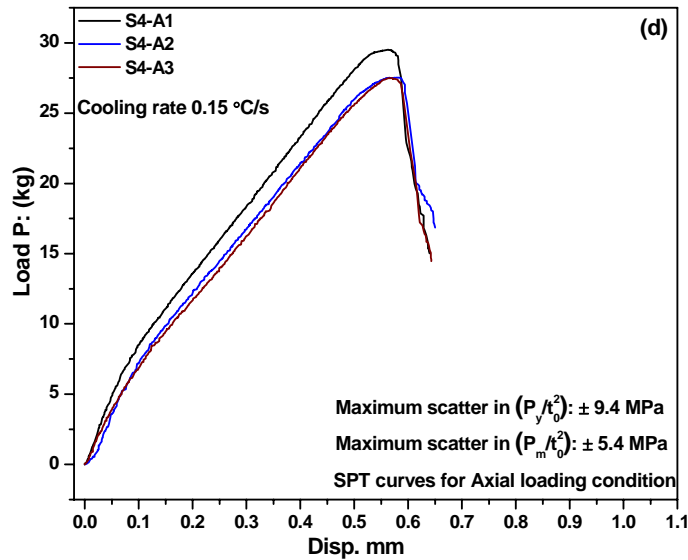


Fig. 5.2 SPT Load vs. displacement curves obtained for Zr-2.5%Nb alloy specimens heat treated at 880°C (axial loading), (a) Quenched at 28°C/s and (b) Quenched at 55 °C/s

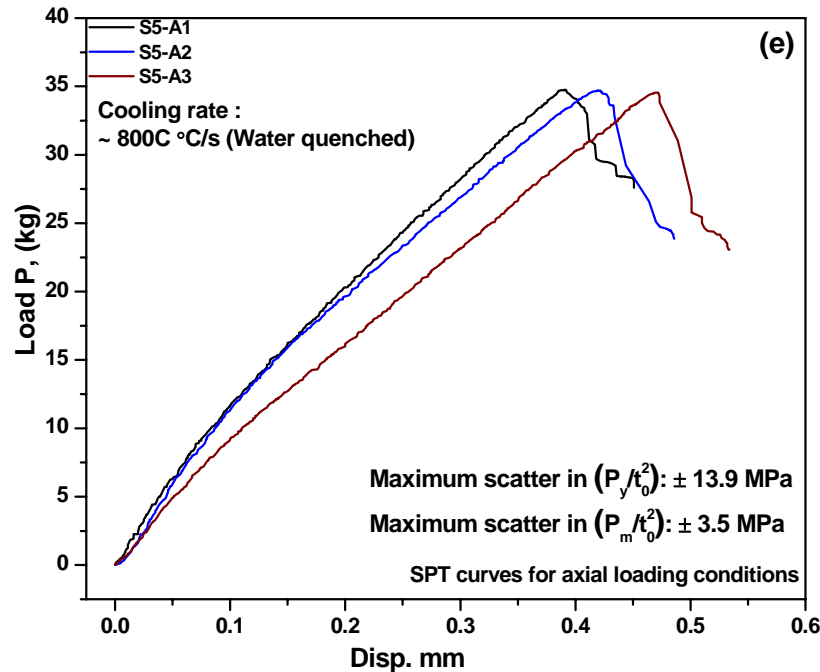


Specimen ID	Cooling rate C/s	Thickness t0 in m	Yield Load Py in Kg	Py/t02 (MPa)	Av. Py/ t02 (MPa)	Std. Dav. +/- (MPa)	Load Max Pm in Kg	Pm/t02 (MPa)	Av. Pm/ t02 (MPa)	Std. Dav. +/- (MPa)
S3-A2	151	0.244	9.385	157.636			30.4	510.615		
S3-A3	151	0.243	10.5	177.818	169.1	10.4	26.29	445.223	510.6	67
S3-A1	151	0.247	10.492	171.975			35.33	579.095		



Specimen ID	Cooling rate C/s	Thickness t0 in mm	Yield Load Py in Kg	Py/t02 (MPa)	Av. Py/ t02 (MPa)	Std. Dav. +/- (MPa)	Load Max Pm in Kg	Pm/t02 (MPa)	Av. Pm/ t02 (MPa)	Std. Dav. +/- (MPa)
S4-A1	0.15	0.251	7.766	123.268			29.51	468.405		
S4-A2	0.15	0.244	7.16	120.263	117.05	8.3	27.53	462.409	467.9	5.5
S4-A3	0.15	0.241	6.25	107.608			27.49	473.305		

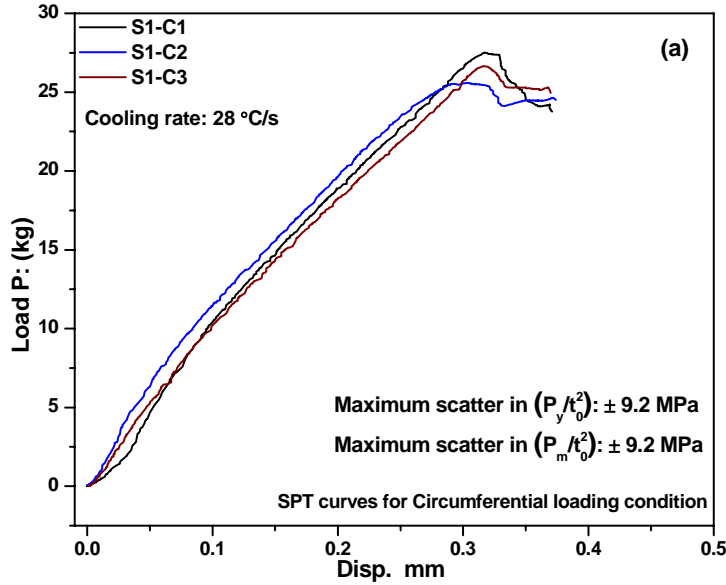
Fig. 5.2 SPT Load vs. displacement curves obtained for Zr-2.5%Nb alloy specimens heat treated at 880°C (axial loading), (c) Quenched at 151°C/s and (d) Cooled at 0.15°C/s



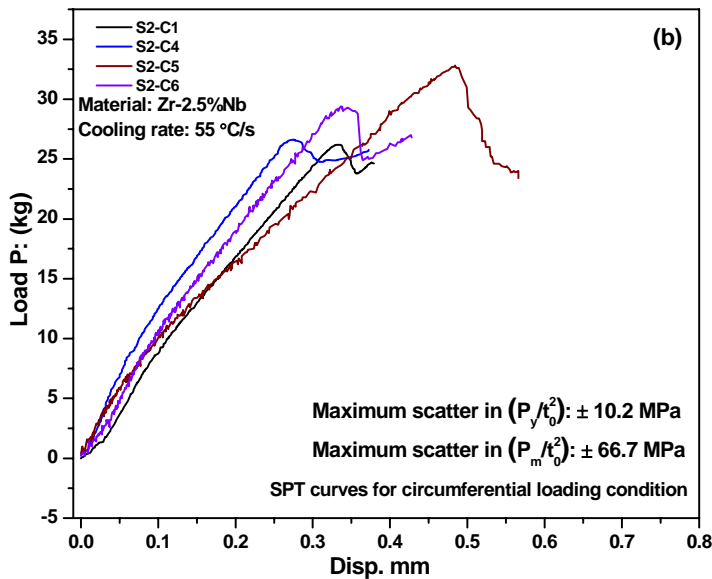
Specimen ID	Cooling rate	Thickness t0	Yield Load	Py/t02	Av. Py/t02	Std. Dav. +/-	Load Max	Pm/t02	Av. Pm/t02	Std. Dav. +/-
--	C/s	in mm	Py in Kg	(MPa)	(MPa)	(MPa)	Pm in Kg	(MPa)	(MPa)	(MPa)
S5-A1	800	0.255	11.527	177.27			34.74	534.256		
S5-A2	800	0.256	12.465	190.201	176.21	14.5	34.71	529.633	530.763	3
S5-A3	800	0.255	10.484	161.23			34.549	528.4		

Fig. 5.2 SPT Load vs. displacement curves obtained for Zr-2.5%Nb alloy specimens heat treated at 880°C (axial loading) and (e) Water quenched (~800°C/s)

Figs. 5.2 and 5.3 shows the SPT load displacement ( $P$  vs.  $\delta$ ) curves obtained for the heat treated specimens used in the study. Fig. 5.2 (a-e) show the SPT results for the loading condition axial with respect to pressure tube axis, while Fig. 5.3 (a-e) shows the same results for the loading condition circumferential with respect to pressure tube axis. Each figure also shows an inscribed table containing details of  $P_y$ ,  $P_m$ ,  $(P_y/t_0^2)$  and  $(P_m/t_0^2)$  values evaluated and the standard deviation of these values. The conventional tension tests carried out on the heat treated specimens provided the expected results as seen from Figs. 5.4 to Fig. 5.8. The effect of cooling rate showed a clear increase in strength values, (*i.e.*,  $\sigma_y$  and  $\sigma_{UTS}$  values) for both the directions of loading in all the three kinds of tests. This result is consistent with the microstructure evolving from coarse and irregular Widmanstätten  $\alpha$  to finer, sharp and straight lamellae and then to predominantly martensitic structure with the cooling rates increasing as seen from Fig. 5.1 (a-d).

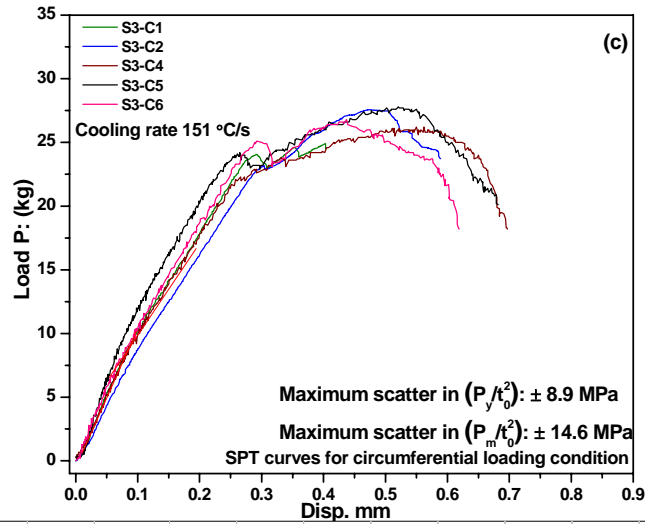


Specimen ID	Cooling rate C/s	Thickness t0 in mm	Yield Load Py in Kg	Py/t02 (MPa)	Av. Py/ t02 (MPa)	Std. Dav. +/- (MPa)	Load Max Pm in Kg	Pm/t02 (MPa)	Av. Pm/t02 (MPa)	Std. Dav. +/- (MPa)
S1C1	27.6	0.252	8.434	132.811			27.51	433.201		
S1C2	27.6	0.248	7.842	127.504	125.53	8.4	25.6	416.233	425.39	8.6
S1C3	27.6	0.25	7.268	116.288			26.67	426.72		

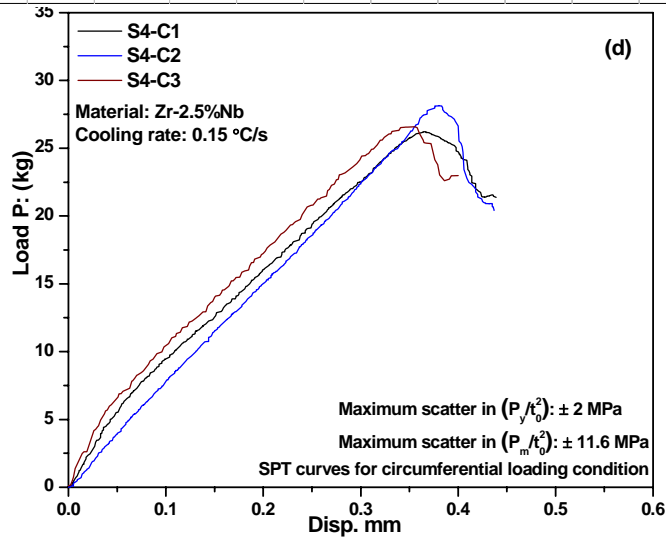


Specimen ID	Cooling Rate C/s	Thickness t0 in mm	Yield Load Py in Kg	Py/ t02 (MPa)	Av. Py/ t02 (MPa)	Std. Dav. +/- (MPa)	Load Max Pm in Kg	Pm/ t02 (MPa)	Av. Pm/ t02 (MPa)	Std. Dav. +/- (MPa)
S2C1	54.6	0.254	8.893	137.842			26.2	406.101		
S2C4	54.6	0.256	8.46	129.089	139.24	7.7	26.76	408.325	445.64	50
S2C5	54.6	0.253	9.16	143.105			32.8	512.428		
S2C6	54.6	0.254	9.48	146.94			29.4	455.701		

Fig. 5.3 SPT Load vs. displacement curves obtained for Zr-2.5%Nb alloy specimens heat treated at 880°C (Circumferential loading), (a) Quenched at 28°C/s and (b) Quenched at 55 °C/s

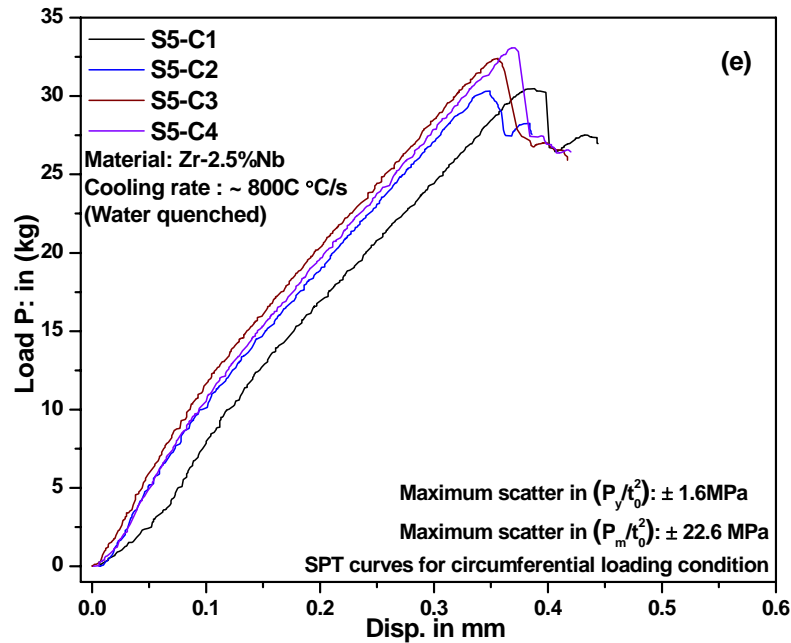


Specimen ID	Cooling Rate	Thickness t0	Yield Load	Py/t02	Av. Py/t02	Std. D av. +/-	Load Max	Pm/t02	Av. Pm/t02	Std. D av. +/-
--	C/s	t0 in mm	Py in Kg	(MPa)	(MPa)	(MPa)	Pm in K	(MPa)	(MPa)	(MPa)
S3C1	151	0.242	8.836	150.878						
S3C2	151	0.25	8.889	142.22	145.38	6	27.56	440.96	--	
S3C4	151	0.253	9.426	147.26					430.02	13.2
S3C5	151	0.253	9.608	150.10			27.76	433.68	--	
S3C6	151	0.254	8.803	136.44			26.8	415.40	--	



Specimen ID	Cooling Rate	Thickness t0	Yield Load	Py/t02	Av. Py/t02	Std. Dav. +/-	Load Max	Pm/t02	Av. Pm/t02	Std. Dav. +/-
--	C/s	t0 in m	Py in Kg	(MPa)	(MPa)	(MPa)	Pm in K	(MPa)	(MPa)	(MPa)
S4C1	0.15	0.253	6.828	106.67	--		26.23	409.78	--	
S4C2	0.15	0.255	7.191	110.58	108.67	2.7	28.133	432.64	421.39	16
S4C3	0.15	0.251	6.853	108.77			26.571	421.75		

Fig. 5.3 SPT Load vs. displacement curves obtained for Zr-2.5%Nb alloy specimens heat treated at 880°C (circumferential loading), (c) Quenched at 151°C/s, (d) Cooled at 0.15°C/s



Specimen ID	Cooling Rate	Thickness	Yield Load	Py/t02	Av. Py/ t02	Std. Dav. +/-	Load Max.	Pm/t02	Av. Pm/ t02	Std. Dav. +/-
--	C/s	t0 in mm	Py in Kg	(MPa)	(MPa)	(MPa)	Pm in Kg	(MPa)	(MPa)	(MPa)
S5C1	800	0.256	10.691	163.132			30.486	465.179		
S5C2	800	0.253	10.309	161.056	162.829	1.4	30.32	462.647	483.713	23
S5C3	800	0.257	10.863	164.469			32.41	506.335		
S5C4	800	0.255	10.577	162.661			33.07	500.689		

Fig. 5.3 SPT Load vs. displacement curves obtained for Zr-2.5%Nb alloy specimens heat treated at 880°C (axial loading), (e) Water quenched (~800°C/s)

The effect of texture was clearly seen as the circumferential direction strength values by conventional tensile test and ABI were higher compared to the axial direction strength values for the same specimen condition. In the case of ABI tests the yield parameter “A” values obtained for both the direction of loading showed increase with increase in cooling rates which may be attributed to the morphological changes in  $\alpha$  and  $\beta$  phase as discussed for conventional tension test results. The yield parameter values obtained for circumferential direction of loading were higher compared to axial loading condition for the same heat treatment condition indicating the effect of preferred orientation of grains. This difference has been reflected in the correlation parameters established for the two directions of loading as seen in Fig. 5.4(a) and (b).

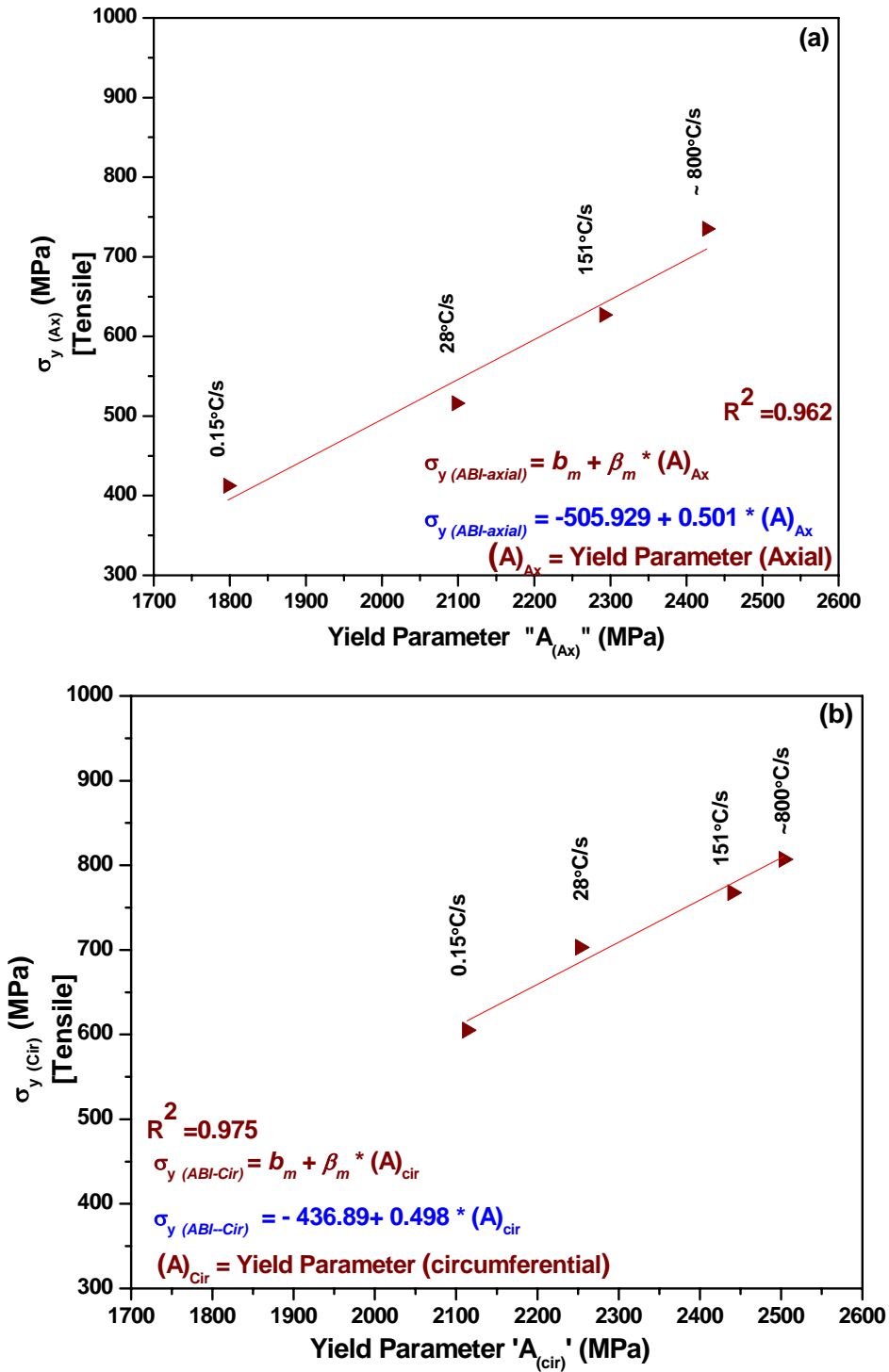


Fig. 5.4 Correlation parameters for determination of  $\sigma_y$  by ABI (a) Axial-loading and (b) Circumferential loading

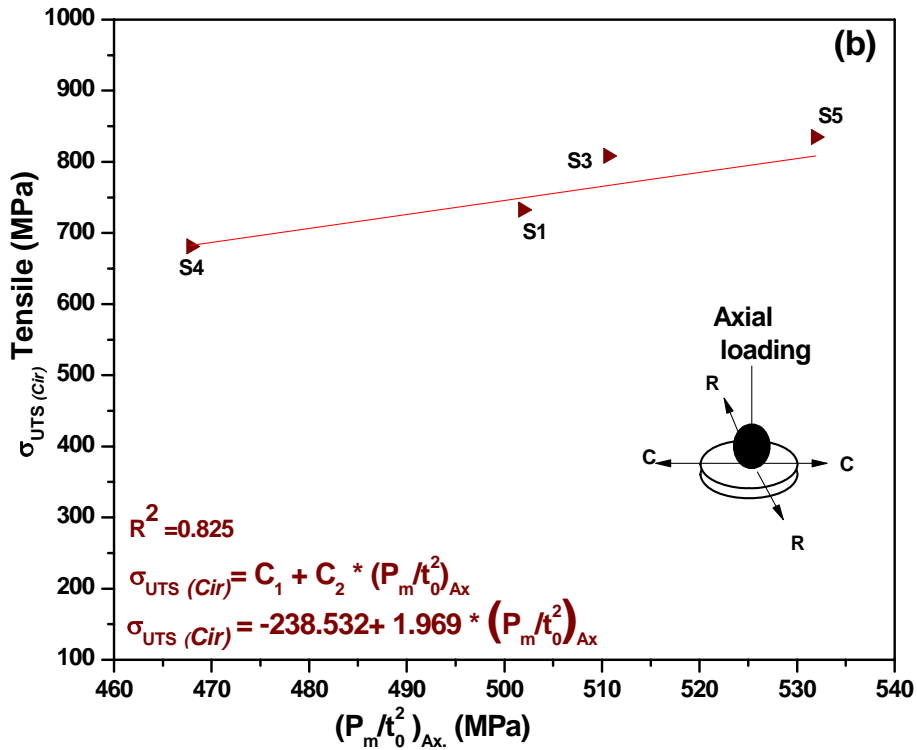
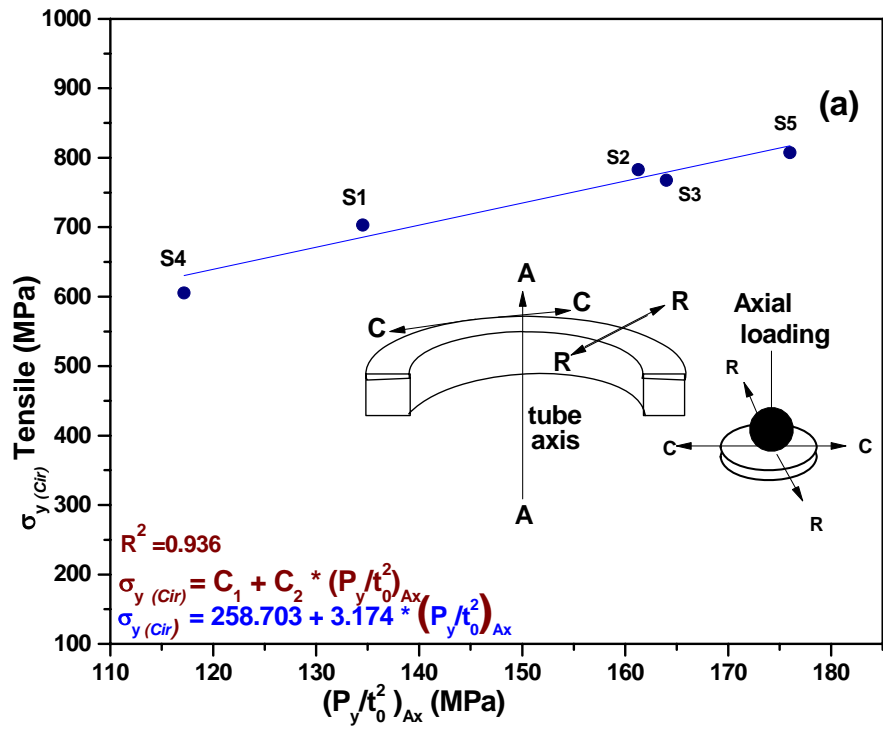


Fig. 5.5(a) SPT: Correlation parameters for evaluation of  $\sigma_y$  for - (Axial loading), (b) SPT; Correlation parameters for evaluation of  $\sigma_{UTS}$ -(Axial loading)

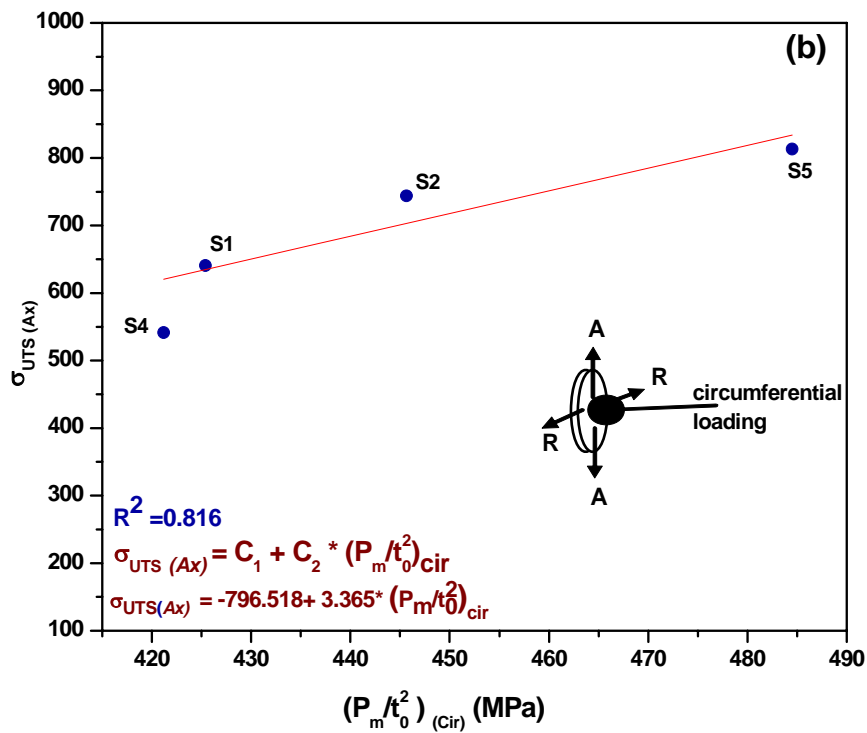
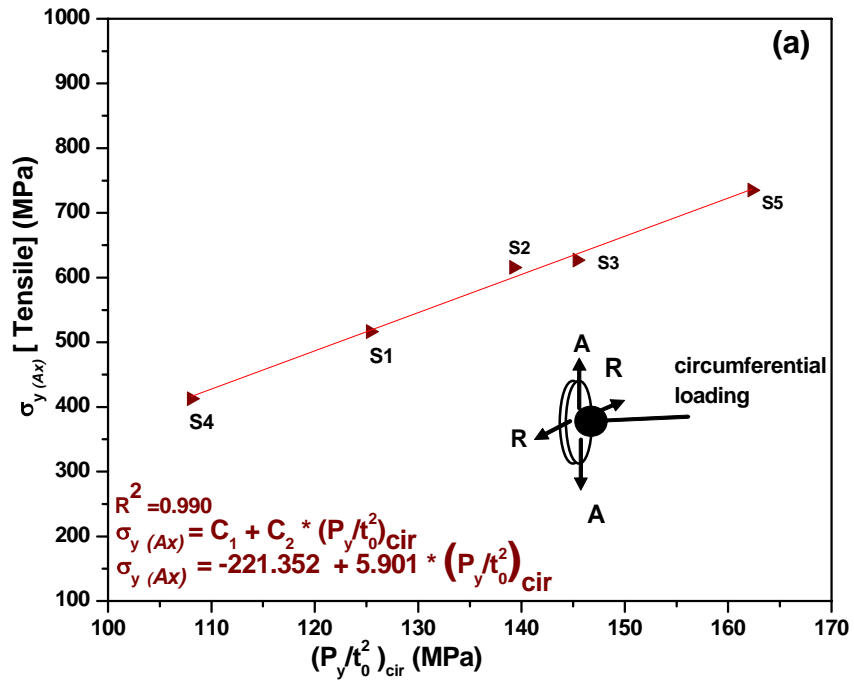


Fig. 5.6(a) SPT, Correlation parameters for evaluation of  $\sigma_y$  for -(Circumferential loading),  
 (b) SPT, Correlation parameters for evaluation of  $\sigma_{UTS}$  – (Circumferential loading)

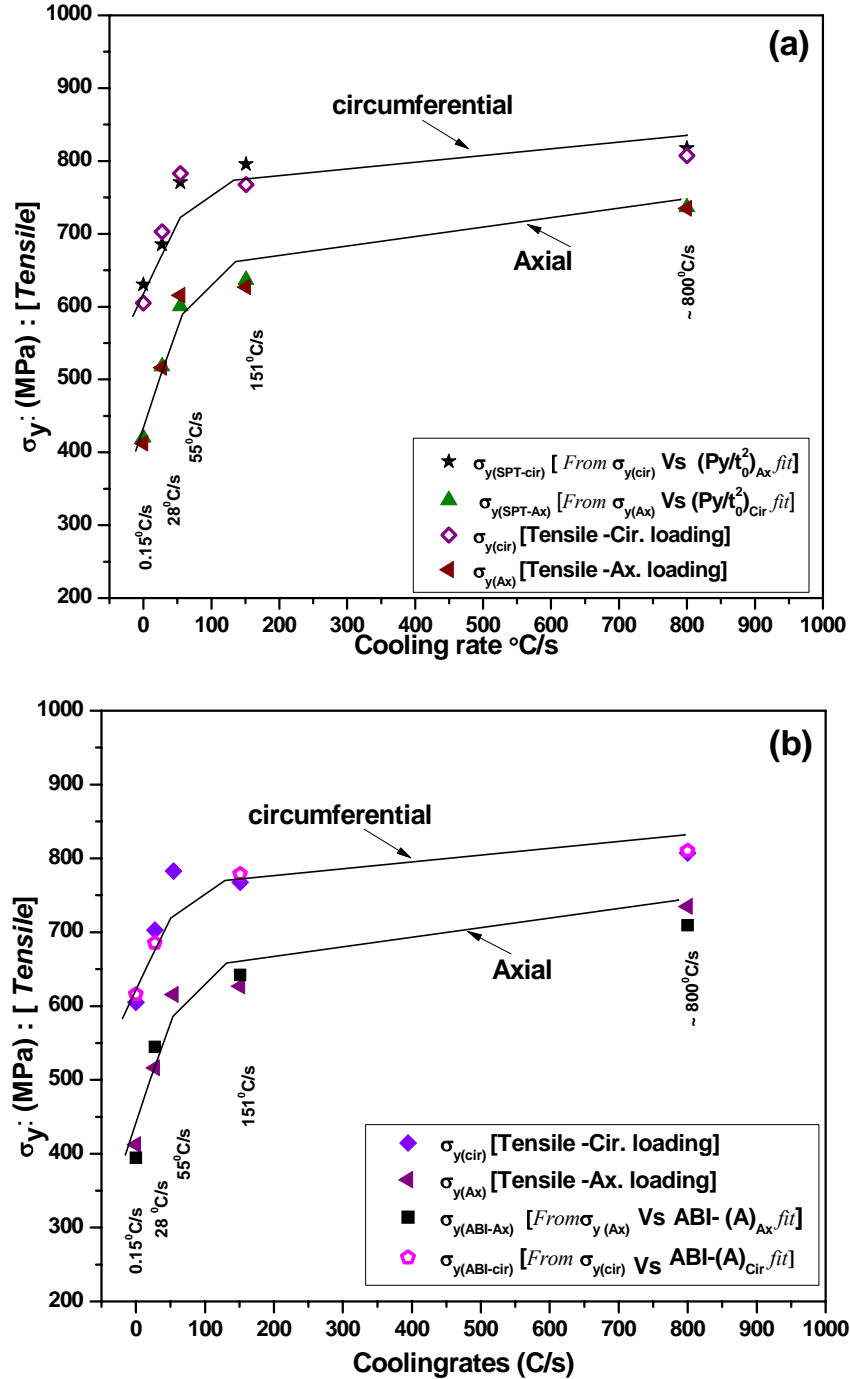


Fig.5.7(a) Comparison of Tensile and SPT derived directional  $\sigma_y$  values for different heat treated conditions, (b) Comparison of Tensile and ABI derived directional  $\sigma_y$  values for different heat treated conditions

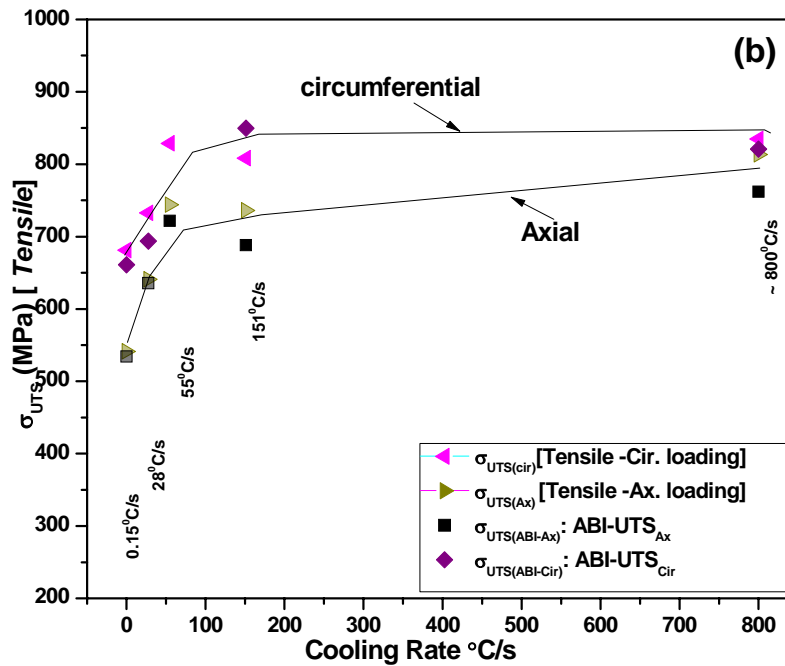
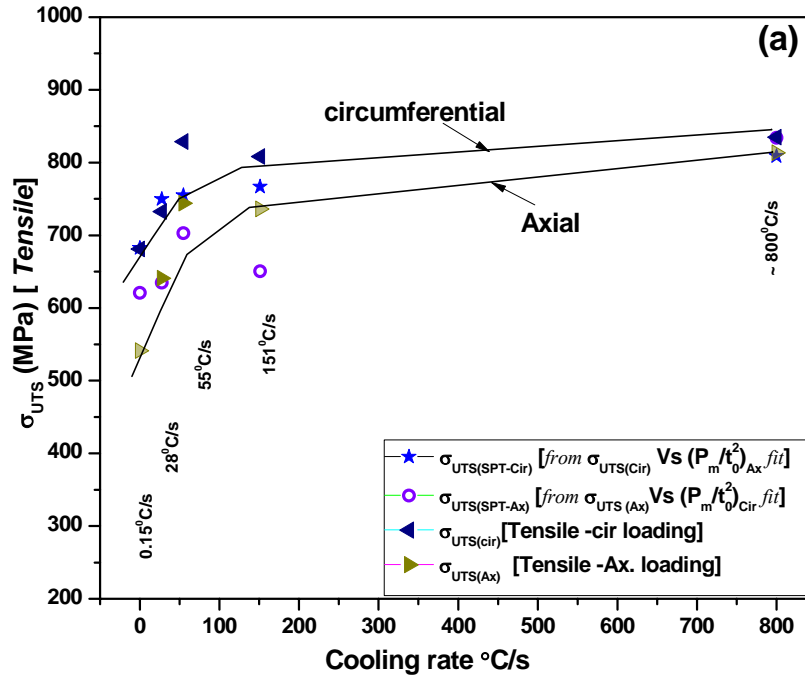


Fig. 5.8(a) Comparison of Tensile and SPT derived directional  $\sigma_{UTS}$  values for different heat treated conditions, (b) Comparison of Tensile and ABI derived directional  $\sigma_{UTS}$  values for different heat treated conditions

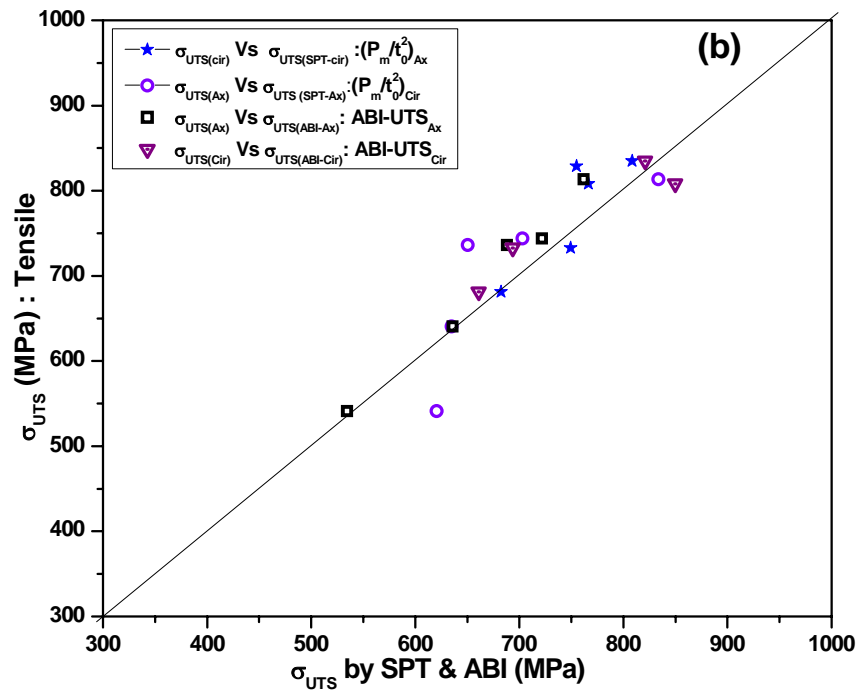
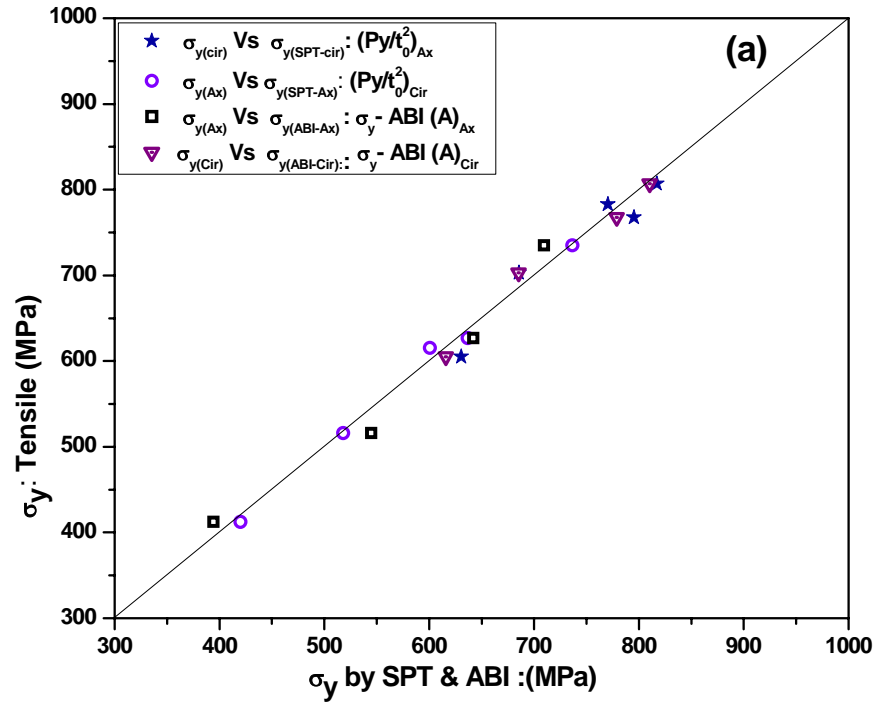


Fig. 5.9 Comparison of axial and circumferential direction mechanical property data, (a) SPT and ABI- derived  $\sigma_y$  data with tensile  $\sigma_y$  data, (b) SPT and ABI- derived  $\sigma_{UTS}$  data with tensile  $\sigma_{UTS}$  data

Figs. 5.5 (a) and (b) and Fig. 5.6 (a) and (b) show the responses of SPT carried out on the heat treated specimens. In general it was seen that the average values of  $(P_y/t_0^2)$  and  $(P_m/t_0^2)$  increased with increasing cooling rates for both the direction of loading owing to the morphological changes in the  $\alpha$  and  $\beta$  phases as discussed earlier. However, on comparison of average values of  $(P_y/t_0^2)$  and  $(P_m/t_0^2)$  obtained for the two directions of loading, it was observed that for axial loading condition the values of  $(P_y/t_0^2)$  and  $(P_m/t_0^2)$  were placed higher compared to the circumferential direction of loading for each heat treated condition, which is a unique finding in this study, and is dealt with in the discussion in section 5.7.

Haggag [17] had presented correlation parameters for evaluation of YS for the steel material using ABI, and many authors [11, 18-21] have presented similar results for steel material using SPT where direction of loading was of no concern as polycrystalline steel with cubic crystallographic structure is expected to behave like isotropic material on macroscopic scale. However from the results in the present study suggest that direction of loading needs to be adequately considered to arrive at true mechanical properties while testing anisotropic material.

*Table-5.2: Correlation parameters for evaluation of axial and circumferential  $\sigma_y$  by ABI*

Loading direction	Mechanical property	Correlation parameters		
		$b_m$	$\beta_m$	Regression
Axial	$\sigma_{y(Ax)} = b_m + \beta_m A_{(Ax)}$	-505.929	0.501	$R^2 = 0.962$
Circumferential	$\sigma_{y(cir)} = b_m + \beta_m A_{(cir)}$	-436.89	0.498	$R^2 = 0.975$

### 5.5 Determination of correlation parameters for ABI for evaluation of $\sigma_y$

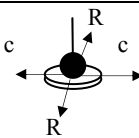
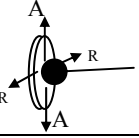
For determining the correlation parameters for evaluation of  $\sigma_y$  of Zr-2.5%Nb alloy using ABI the procedure described by the authors at [2, 13, 17] was adopted. The exercise involved regression analysis of various tensile yield strength values (measured from conventional specimens with different heat treatments) and the corresponding (*average values*) yield parameter value “A” obtained from the ABI tests. Fig. 5.4(a) and (b) show the linear regression of the form  $\sigma_y = b_m + \beta_m A$  for the axial and circumferential loading conditions, where  $b_m$  and  $\beta_m$  are the linear correlation parameters known as yield point offset constant and material-type constant specific to particular type or class of material respectively [5, 6, 17]. Table-5.2 provides

the values of correlation parameters established for evaluation of  $\sigma_y$  by ABI for the two directions of loading studied.

### 5.6 Determination of correlation parameters for SPT for evaluation of $\sigma_y$ and $\sigma_{UTS}$

In the case of SPT, for the axial loading condition, the average values of  $(P_y/t_0^2)_{Ax}$  and  $(P_m/t_0^2)_{Ax}$  were correlated with the corresponding circumferential direction tensile  $\sigma_{y(cir)}$  and  $\sigma_{UTS(cir)}$ , respectively. The results of linear regression correlation parameters obtained from this regression analysis are shown in graphs in Fig.5.5(a) and (b) and also in Table-5.3. The general form of correlation for  $\sigma_y$  and  $\sigma_{UTS}$  is expressed as  $\sigma = C_1 + C_2 \times (P/t_0^2)$ . Similarly Fig.5.6(a) and (b) show the linear correlation results for circumferential loading condition, where average values of  $(P_y/t_0^2)_{cir}$  and  $(P_m/t_0^2)_{cir}$  were correlated with axial direction tensile  $\sigma_{y(Ax)}$  and  $\sigma_{UTS(Ax)}$ , respectively, (where  $t_0$  = average initial thickness of the specimen in mm).

Table-5.3: Correlation parameters for evaluation of axial and circumferential  $\sigma_y$ ,  $\sigma_{UTS}$  by SPT

Loading direction	convention	Mechanical property	Correlation parameters		
			C <sub>1</sub>	C <sub>2</sub>	Regression
Axial loading		$\sigma_{y(cir)} = C_1 + C_2 \times [P_y/t_0^2]_{Ax}$	258.703	3.174	$R^2 = 0.936$
		$\sigma_{UTS(cir)} = C_1 + C_2 \times [P_m/t_0^2]_{Ax}$	-238.532	1.969	$R^2 = 0.825$
Circumferential loading		$\sigma_{y(Ax)} = C_1 + C_2 \times [P_y/t_0^2]_{cir}$	-221.352	5.901	$R^2 = 0.990$
		$\sigma_{UTS(Ax)} = C_1 + C_2 \times [P_m/t_0^2]_{cir}$	-796.5175	3.365	$R^2 = 0.816$

### 5.7 Discussion

Development of correlation parameters for the purpose of evaluation of mechanical properties of anisotropic Zr-2.5%Nb pressure tube alloy by miniature specimen testing techniques, SPT and ABI is of practical significance considering their application to testing of irradiated specimens. Most of the earlier studies have dealt with development of correlations for evaluation of mechanical properties of macroscopically isotropic materials such as steels. No such study has been reported in the open literature, which deals with mechanical property characterisation of anisotropic Zr-2.5%Nb pressure tube alloy using miniature specimen testing techniques such as SPT and ABI. Considering, significant crystallographic texture that is generally present in Zr-

2.5%Nb pressure tube alloy due to preferred orientation of  $\alpha_{Zr}$  phase, the issue of direction of load application during testing bears importance. Therefore, it becomes important to study the correlations with respect to direction.

For example, comparing the correlation parameters  $b_m$  and  $\beta_m$  established for the two directions of loading for ABI tests (Table-5.2), clearly shows that the correlations are highly sensitive to the direction of loading. However, it may also be noted that  $\beta_m$  value for the class of material, (*Zr-2.5%Nb pressure tube alloy*) is nearly same for the two directions of loading, while values of  $b_m$  differed by  $\sim 200$  MPa between these two directions of loading. Thus these results ascertain that

- (a) The ABI test is sensitive enough to capture the anisotropy in mechanical properties
- (b) Correlation parameters must be established taking direction of loading into account, which is a requirement specific for textured materials.

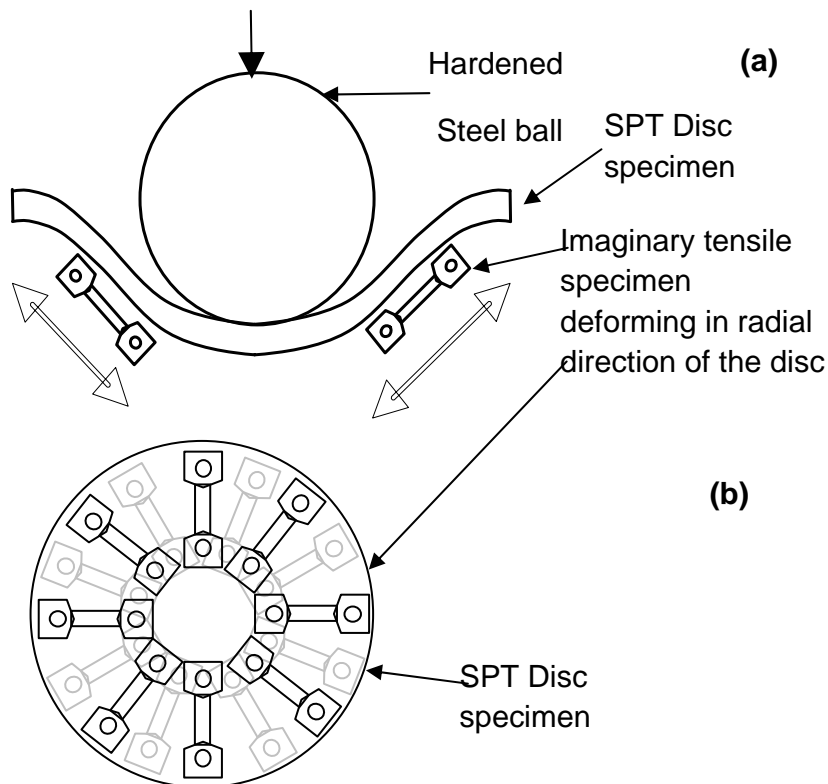


*Fig. 5.10 (a and b) A schematic of SPT specimen deformation during a test compared to tensile deformation in the radial direction.*

Further, due to the kind of texture one would expect that circumferential direction to be stronger (due to higher concentration of basal poles along the circumferential direction, see Table-5.1).

Indeed the tensile data does support this premise. However, SPT results, appear to contradict this aspect as the yield load and load maximum were found to be higher in case of loading along axial direction in comparison with circumferential loading for the same specimen condition. This apparent contradiction can however be rationalised in the following way.

During SPT, the disc specimen undergoes deformation under biaxial stress state [12, 20-22]. Since, the disc is constrained at center and periphery, there exists a tensile stress along the radial direction of the disc (*i.e. from centre to periphery*) during the test. Thus, one can imagine the disc specimen to be composed of a large number of tiny tensile elements radially arranged as shown schematically in Fig. 5.10 (b) and (c). These imaginary tiny tensile specimens undergo elongation due to the tensile forces acting in the radial direction when the hardened steel ball is forced using a plunger at a constant speed. The membrane stretching, necking and fracture that occur during continued deformation of the disc are analogous to uniform elongation, necking and fracture that occur during a conventional tension test. These imaginary radial direction tensile members can be resolved into two principle directions of the pressure tube *i.e.* along the (R-R) direction coinciding with tube's radial direction and along (C-C) direction coinciding with the tube's circumferential direction as shown in Fig. 5.5 (a) and Table-5.3. Therefore the SPT output obtained for an axial loading condition is the net effect of tensile deformation of these radial members resolved in the (C-C) and (R-R) directions, which can be compared with the deformation characteristics of circumferential direction for conventional tensile specimen corresponding to the same heat treatment condition (Fig.5.5(a)). Similarly, it is obvious that for the circumferential loading condition, the SPT output is due to the net effect of tensile deformation of the radial members resolved in (A-A) and (R-R) directions as shown in Fig.5.6 (a), which can be compared with the tensile deformation characteristics of axial direction conventional tensile specimen for the corresponding heat treatment condition.

Here (A-A) direction of the disc coincides with the pressure tube axis as shown in Fig.5.6 (a). On the basis of this analogy it can be ascertained that due to relatively higher texture effects along (C-C) and (R-R) directions, compared to (A-A) and (R-R) directions, the  $(P_y/t_0^2)$  and  $(P_m/t_0^2)$  for the axial loading condition are placed higher than the circumferential loading condition for all the heat treatment conditions. Hence, in a SPT for the axial loading condition, actually the

circumferential direction mechanical properties are established and visa a versa. Based on this analysis the  $(P_y/t_0^2)$  and  $(P_m/t_0^2)$  obtained for axial direction of loading have been correlated to the corresponding circumferential direction conventional tensile data and vice a versa for establishing correlation parameters for evaluation of mechanical properties  $\sigma_y$  and  $\sigma_{UTS}$  (*for the two directions of loading*). From the results presented in Fig. 5.5 (a), (b) and Fig. 5.6 (a) and (b), it can be seen that the scatter in the  $(P_m/t_0^2)$  values for both the direction of loading was relatively higher compared to the  $(P_y/t_0^2)$  values particularly in the case of circumferential loading condition. In the previous studies by the authors [19, 21] similar kind of scatter in  $(P_m/t_0^2)$  values was observed in relatively more isotropic materials such as steels. These authors [19, 21] have attributed this scatter to substantial thickness reduction in the plastic instability regime of the deforming disc. In addition, combination of multi-axial stress state within the sample, the strain localisation resulting from neck formation and crack growth behavior would also contribute to such observed scatter [19, 21].

### **5.8 Inter comparison of mechanical property data derived from tensile, ABI and SPT**

Using the correlation parameters established for the alloy for SPT in this study, the  $\sigma_y$  and  $\sigma_{UTS}$  values for the two directions of loading were evaluated for the heat treated specimens used in this study. Similarly, using the correlation parameters established for evaluation of yield strength by ABI, the  $\sigma_y$  values for the same heat treated specimens was also evaluated for both the loading directions. As shown in Fig. 5.7(a) and (b), comparison of tensile  $\sigma_y$  data with SPT derived  $\sigma_y$  data and ABI derived  $\sigma_y$  data, respectively, for both the directions of loading show excellent agreement with each other. Similarly Fig. 5.8(a) and (b) shows the comparison of tensile  $\sigma_{UTS}$  data with SPT derived  $\sigma_{UTS}$  data and ABI derived  $\sigma_{UTS}$  data for both the directions of loading which again show good agreement however with a relatively higher scatter. From Fig. 5.7 (a), (b) and also from Fig. 5.9 (a) it is clear that SPT and ABI derived  $\sigma_y$  data are in excellent agreement with the corresponding tensile  $\sigma_y$  data. Hence, it can be ascertained that the correlation parameters established for evaluation of  $\sigma_y$  by these techniques for both the directions of loading are satisfactory. Fig. 5.8 (a), (b) and Fig.5.9 (b) show the comparison of SPT derived  $\sigma_{UTS}$  data established through currently determined correlation parameters and ABI derived  $\sigma_{UTS}$

data. Therefore, it can be ascertained that  $\sigma_{UTS}$  values were by and large in good agreement but with relatively higher scatter. The  $\sigma_y$  and  $\sigma_{UTS}$  data obtained for the water quenched condition for the axial direction of loading (*by miniature tests*) at room temperature closely agreed with that established by Saibaba *et.al* [23] from the conventional tension tests carried out on water quenched and aged (540°C/24hrs) specimens. Thus, this result indicates that, proper values of correlation parameters have been arrived at for the two miniature techniques ABI and SPT. The overall study indicated that ABI and SPT techniques are sensitive to the small changes in mechanical properties and can be adopted to study the effect of orientation on the mechanical properties of small specimens.

## 5.9 Summary of the work

1. Empirical correlations for evaluation of basic mechanical properties  $\sigma_y$  and  $\sigma_{UTS}$  of anisotropic Zr-2.5%Nb alloy have been established for SPT and ABI test techniques for axial and circumferential directions of loading using recommended procedure. In the case of ABI the difference in yield strength off set constant  $b_m$  between the two directions of testing indicated intrinsic difference in yield behavior attributing to effect of texture in the alloy.
2. The strength values obtained using tensile and ABI tests were higher for circumferential compared to axial direction, whereas the strength representing values ( $P_y/t_0^2$ ) and ( $P_m/t_0^2$ ) by SPT showed opposite effect for the sample conditions. This contradiction has been rationalised on the basis of biaxial deformation of the disc specimen experiencing orientation effects.
3. The strength values by SPT, ABI and conventional tensile tests showed increasing trend with the increase in cooling rates for both directions tests, which can be attributed to finer morphology of Widmanstätten  $\alpha$  and  $\beta$  phases and also predominantly martensitic structure obtained at cooling rates greater than 50°C/s.
4. Comparison of ABI and SPT derived  $\sigma_y$  and  $\sigma_{UTS}$  data and the corresponding tensile data for both direction tests showed a good agreement indicating proper empirical correlation

parameters have been arrived at for evaluation of mechanical properties of the alloy. The overall study indicated that ABI and SPT techniques are sensitive to the changes in mechanical properties due to microstructure and texture effects in the alloy. Thus these techniques can be adopted for mechanical property characterisation of anisotropic Zr-2.5%Nb alloy materials using direction specific correlation parameters.

## References Chapter-5

1. T.H. Hyde, W. Sun, J.A. Williams, DOI: 10.1179/174328007 X160317, *International Materials Reviews*, 52 No 4, (2007) 213-255
2. F.M. Haggag, J. A. Wang, Proc., doi,10.1117/12.259096, SPIE 2945 (1996) 217-228
3. F.M. Haggag, L.D Phillips, IPC04-0345, *Proceedings of IPC 2004, American Society for Mechanical Engineering (ASME), International Pipeline Conference Oct, 2004*
4. F.M. Haggag, L.D Phillips, IPC04-0357, *Proceedings, IPC 2004, American Society for Mechanical Engineering (ASME), International Pipeline Conference Oct.2004*
5. W.R. Corwin, F. M. Haggag, and W. L. Server, *American Society for Testing and Materials, (ASTM) STP 1204, (1993) 27- 44*
6. F.M. Haggag, *American Society for Mechanical Engineering (ASME), Pressure Vessel Piping (PVP)-429 (2001) 99-104*
7. F.M. Haggag, *Proceedings 3<sup>rd</sup> Int. conf. Trends in Welding Research, July (1992) 629-635*
8. F.M. Haggag, *ASM International, Advanced Materials and Processes, (2006) 41-43*
9. F.M. Haggag, *Final Report, The U.S. Department of Energy, DOE/ER/82115-2, (1999) 1-40*
10. F.M. Haggag, K.L. Murty, "Nondestructive Evaluation and Materials Properties III", *JOM, (1997), 101-106*
11. Y. Xu, G. Ning, C. Zhang, Q. Yu, *Int. J. Pressure Vessels and Piping, 77 (2000) 715-721*
12. X. Mao, H. Takahashi, *J. Nucl. Mater., 150 (1987) 42-52*
13. K.L. Murty, M.D. Mathew, Y. Wang, V.N. Shah, F.M. Haggag, *Int. J. Pressure Vessels and Piping, 75 (1998) 831-840*
14. H. Takahashi, T. Shoji, X. Mao, Y. Hamaguchi, T. Misawa, M. Saito, T. Oku, T. Kodaria, F. Fukaya Kioshi, H. Nishi, M. Suzuki, "Recommended practice for Small Punch (SP) testing of metallic materials (Draft), JAERI-M-88-172 (Report), September, (1988) 1-19

15. F.M. Haggag, A.S. Kumar, D.S. Gelles, R.K. Nanstad, E.A. Little, (*ASTM*), *STP 1175*, (1993) 172-185
16. G.E. Lucas, *J. Nucl. Mater.*, 117 (1983) 327-339
17. F.M. Haggag, “*Nondestructive Determination of Yield Strength and Stress-Strain Curves of In-Service Transmission Pipelines Using Innovative Stress-Strain Microprobe Technology*” (1999), Report No. ATC/DOT/990901
18. K. Kumar, K. Madhusoodanan, B.B. Rupani, *BARC, Found. day Sp.285 Oct.2007*
19. J. Kameda and X. Mao, *J. Mater. Sci.*, 27 (1992) 983-989
20. X. Mao, M. Saito, H. Takahashi, *Scripta Metall.* 25 (1991) 2481-2485
21. E. Fleury, J.S. Ha, *International J. Pressure Vessels and Piping*, 75 (1998) 699-706
22. X. Mao, H. Takahashi, T. Kodaira, *Mater. Sci. Eng. A*, 150 (1992) 231-236
23. N. Saibaba, S.K. Jha, S. Tonpe, K. Vaibhaw, V. Deshmukh, S.V. Ramana Rao, K.V. Mani Krishna, S. Neogy, D. Srivastava, G.K. Dey, R.V. Kulkarni, B.N. Rath, E. Ramadasan, S. Anantharaman, *J. (ASTM), International, (JAI) Paper ID JAI103213, DOI: 10.1520/JAI103213*, 8, No. 6, (2011)

## **CHAPTER 6: Mechanical Properties of Zr-2.5%Nb Pressure Tube Material Subjected to Heat Treatments in $\alpha+\beta$ Phase field**

### **6.1 Objectives**

Dimensional changes in pressure tubes during service are the strong functions of microstructure characterised by morphologies and distribution of various phase constituents, crystallographic texture and dislocation density and type, majority of which are dictated by the fabrication history [1-6]. The controlled heat treatment conditions can result in the evolution of microstructure which can influence both short term and long term mechanical properties and also the in-reactor deformation behaviour. Therefore, the main objective of this part of the thesis was to study the microstructure and mechanical property correlations of the Zr-2.5%Nb pressure tube alloy subjected to various heat treatments. The structure and property correlation study presented in this chapter provides wider data and knowledge base for the development of creep resistant pressure tube alloy.

### **6.2 Background**

It has been reported that the Zr-2.5%Nb pressure tubes in the heat treated condition have shown superior performance with lower deformation rates [7]. Such better creep rates have been indicated to be due to the final microstructure resulting from heat treatments in the ( $\alpha+\beta$ ) phase field. As discussed in Chapter-2 the literature pertaining to heat treatments and structure property correlations is discrete. Therefore the understanding in this subjected domain was restricted which was the main motive behind the study of structure and property correlations being discussed in this chapter. It has been shown in chapter-4 that, various heat treatments from the ( $\alpha+\beta$ ) phase field using quenching dilatometry resulted in wide range of microstructures. Different soaking temperatures influenced the fraction of primary  $\alpha$  and  $\beta$  phases and their compositions, while different cooling rates adopted influenced the nature of  $\beta$ -phase transformation leading to wide range of morphologies and distribution of transformed  $\alpha$  and  $\beta$  phases. These heat treated dilatometry specimens served as source material for the structure and property correlation study.

For characterising these small size specimens for mechanical properties such as  $\sigma_y$  and  $\sigma_{UTS}$ , the miniature techniques such as SPT and ABI were adopted using appropriate correlations established earlier in the present study (refer chapter-5). Table 6.1 (a) provides the correlation parameters used for the determination of  $\sigma_y$  and  $\sigma_{UTS}$  by SPT and Table 6.1 (b) provides the correlation parameters for evaluation of  $\sigma_y$  by ABI.

*Table-6.1 (a): Correlation parameters for evaluation of  $\sigma_y$  and  $\sigma_{UTS}$  by SPT for loading along axial direction of the pressure tube (for tensile  $\sigma_y$  range 600 and 810 MPa and  $\sigma_{UTS}$  range, 683 and 835 MPa)*

Correlation parameters for evaluation of $\sigma_y$		Correlation parameters for evaluation of $\sigma_{UTS}$	
C1 (Intercept: MPa)	C2 (Slope)	C3 (Intercept: MPa)	C4: (slope)
258.703	3.174	-238.532	1.969

*Table-6.1 (b): Correlation parameters for evaluation of  $\sigma_y$  by ABI for loading along axial direction with of the pressure tube (for tensile  $\sigma_y$  range 412 and 735 MPa)*

$b_m$ (Yield strength off set constant specific to Zr-2.5%Nb alloy, MPa)	$\beta_m$ (Material specific constant for Zr-2.5%Nb alloy; represented by slope)
-505.929	0.501

### 6.3 Evaluation of mechanical properties of heat treated specimens by ABI and SPT

Figs. 6.1 (a-d) and Figs. 6.2 (a-d) show the effect of cooling rate on the mechanical properties ( $\sigma_y$  and  $\sigma_{UTS}$ ) of the alloy material, derived from ABI and SPT, respectively. The maximum scatter in the  $\sigma_y$  and  $\sigma_{UTS}$  values by SPT were  $\pm 4.6\%$  and  $\pm 6.1\%$  (max), respectively, while for ABI-derived  $\sigma_y$  and  $\sigma_{UTS}$  data, the maximum scatter was observed to be  $\pm 4.4$  and  $\pm 3.8\%$ , respectively. It is apparent from these figures that, the strength values obtained from these two techniques indicated an increasing trend with the increase in cooling rates, for the four soaking temperatures studied. For the samples cooled at 50 °C/s and 100 °C/s the mechanical properties were stronger and remained the same within a small scatter range compared to the strength values obtained at lower cooling rates for all the soaking temperatures studied. Fig. 6.3 (a-d) and Fig. 6.4 (a-d) show the effect of soaking temperature on the mechanical properties derived from ABI and SPT for the cooling rates of 10 °C/s, 25 °C/s, 50 °C/s and 100 °C/s. Although the  $\sigma_{UTS}$  values determined by SPT had a relatively higher scatter of  $\pm 6.1\%$  (max) as compared with  $\sigma_y$  values, which was  $\pm 4.6\%$  (max), the results by and large indicated a decreasing tendency with

the increasing soaking temperatures. However, the ABI-derived  $\sigma_y$  and  $\sigma_{UTS}$  values were apparently unaffected with increasing soaking temperatures.

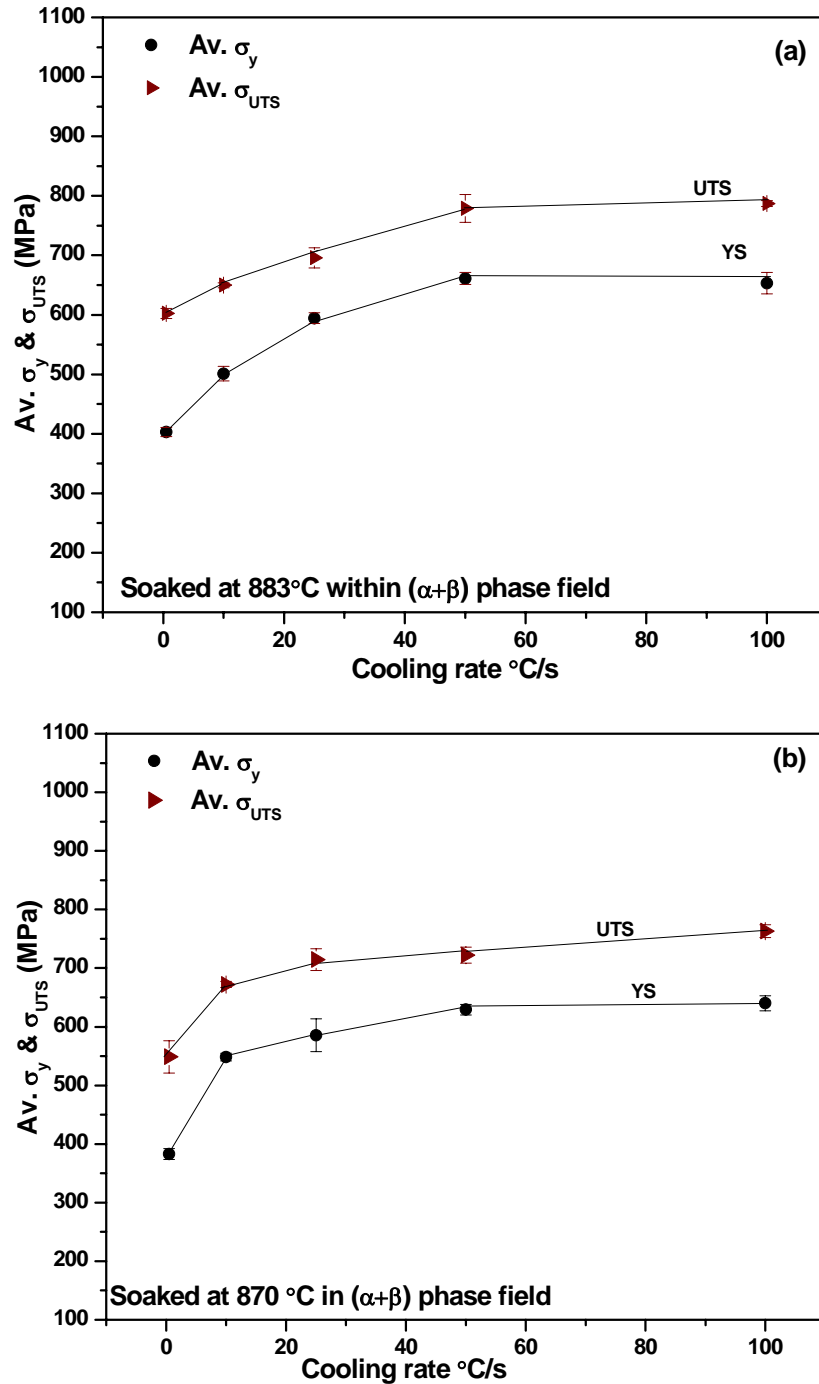


*Fig. 6.1 Effect of cooling rate on mechanical properties  $\sigma_y$  and  $\sigma_{UTS}$  of the Zr-2.5%Nb pressure tube samples by ABI for the samples soaked within the  $(\alpha+\beta)$  phase field at (a) 883°C, (b) 870°C*

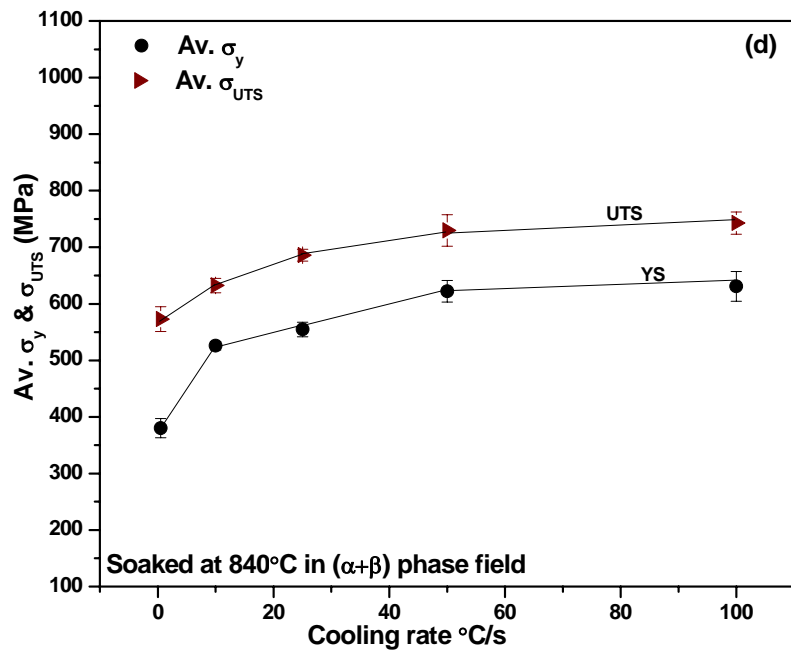
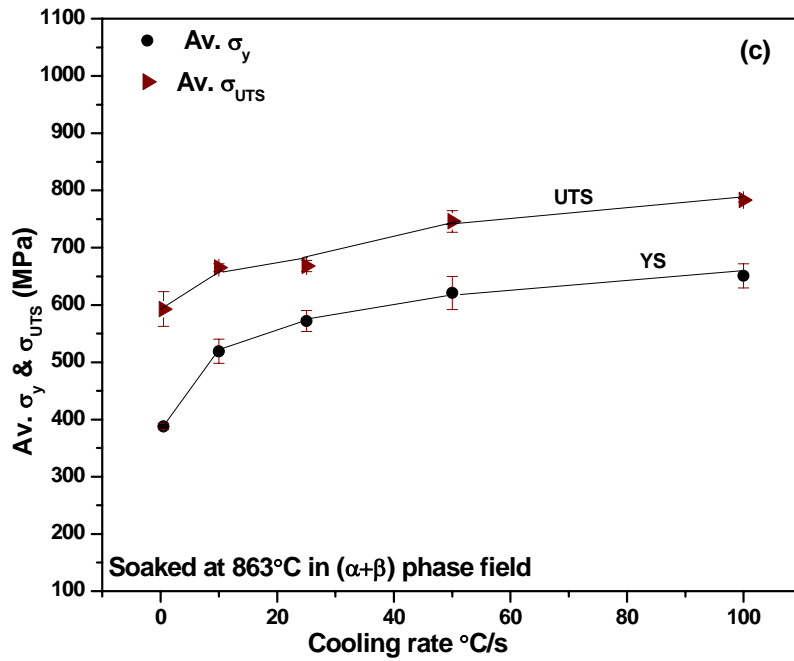


*Fig. 6.1 Effect of cooling rate on mechanical properties  $\sigma_y$  and  $\sigma_{UTS}$  of the Zr-2.5%Nb pressure tube samples by ABI for the samples soaked within the  $(\alpha+\beta)$  phase field at (c) 863°C, (d) 840°C*

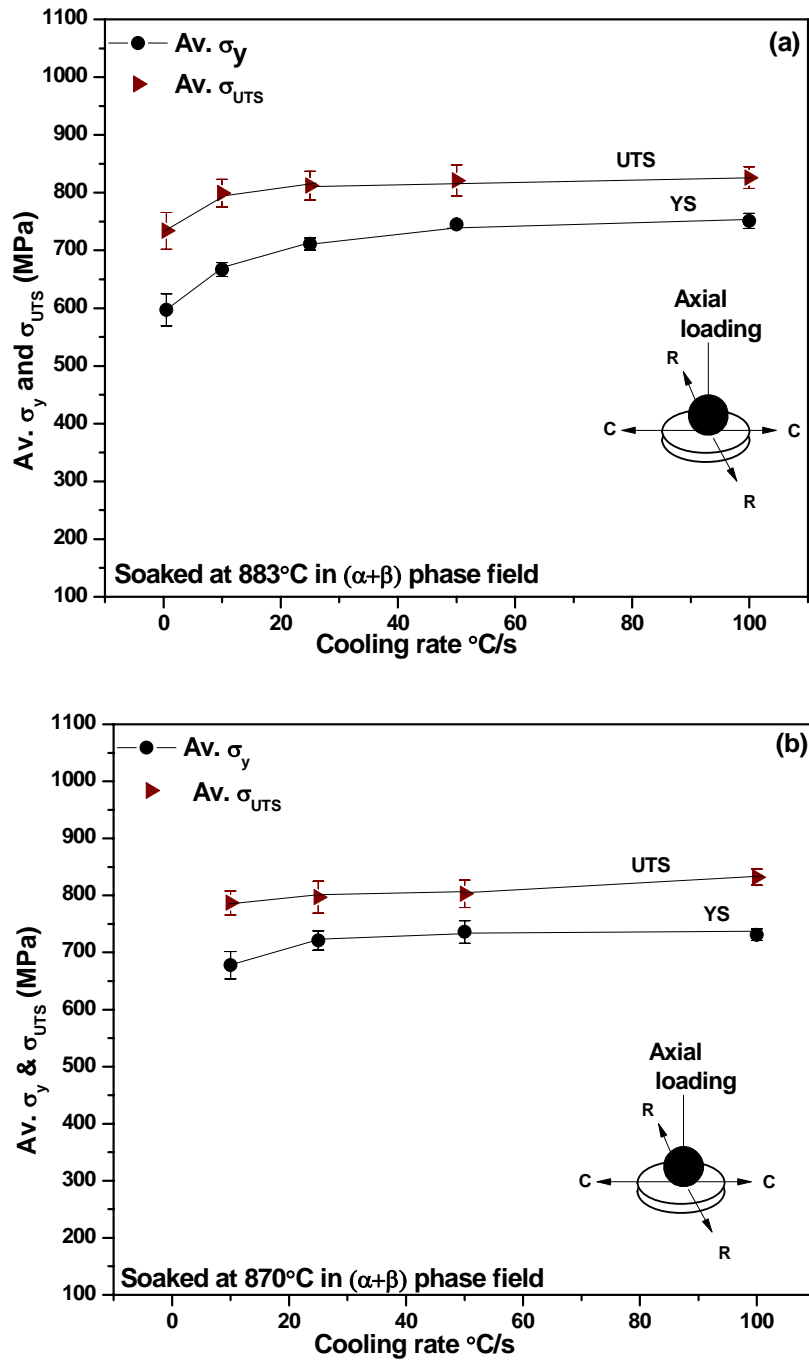


*Fig. 6.2* Effect of cooling rate on mechanical properties  $\sigma_y$  and  $\sigma_{UTS}$  of the Zr-2.5%Nb pressure tube samples by SPT for the samples soaked within the ( $\alpha+\beta$ ) phase field at (a) 883°C, (b) 870°C

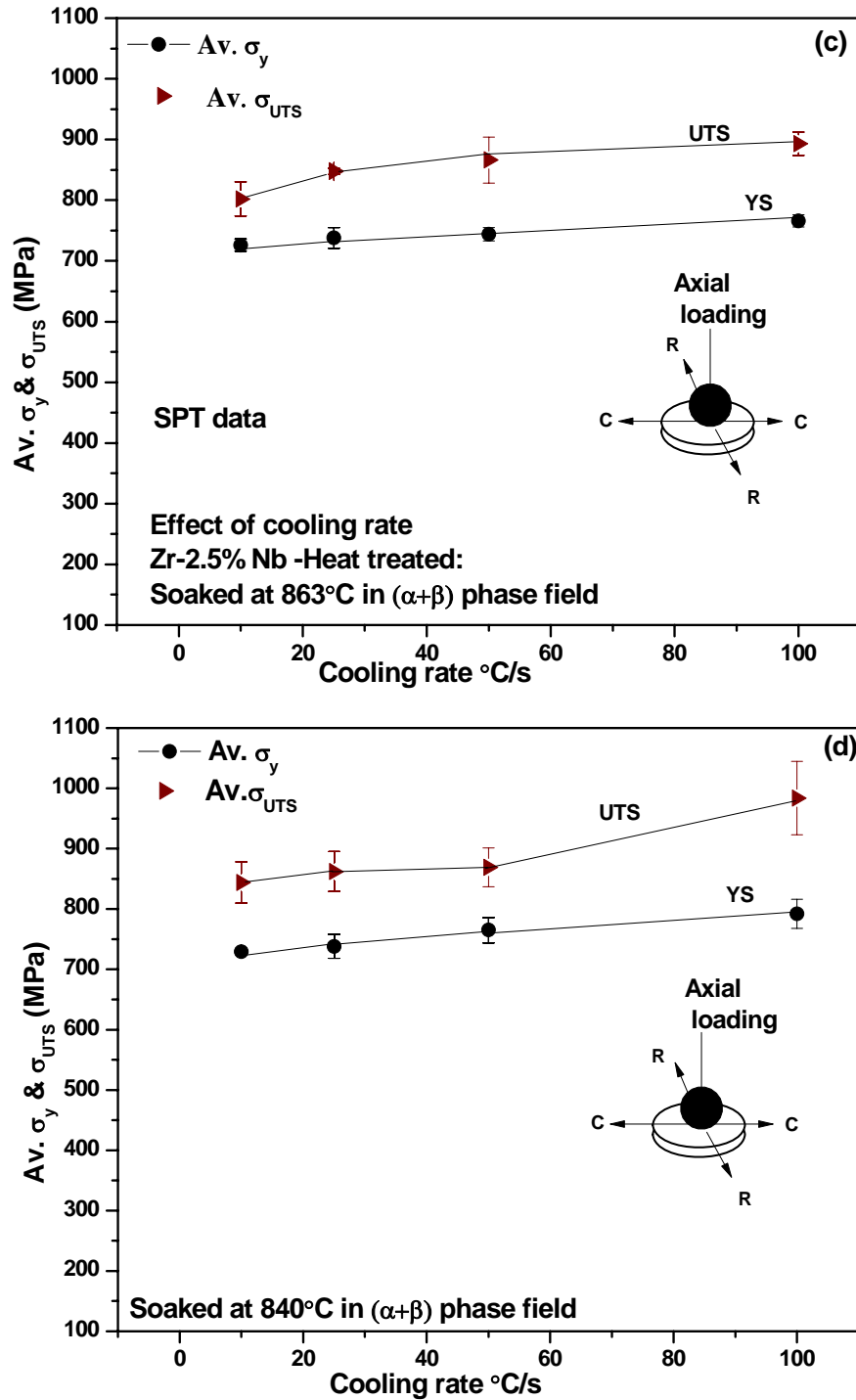


*Fig. 6.2 Effect of cooling rate on mechanical properties  $\sigma_y$  and  $\sigma_{UTS}$  of the Zr-2.5%Nb pressure tube samples by SPT for the samples soaked within the  $(\alpha+\beta)$  phase field at (c) 863°C, (d) 840°C*

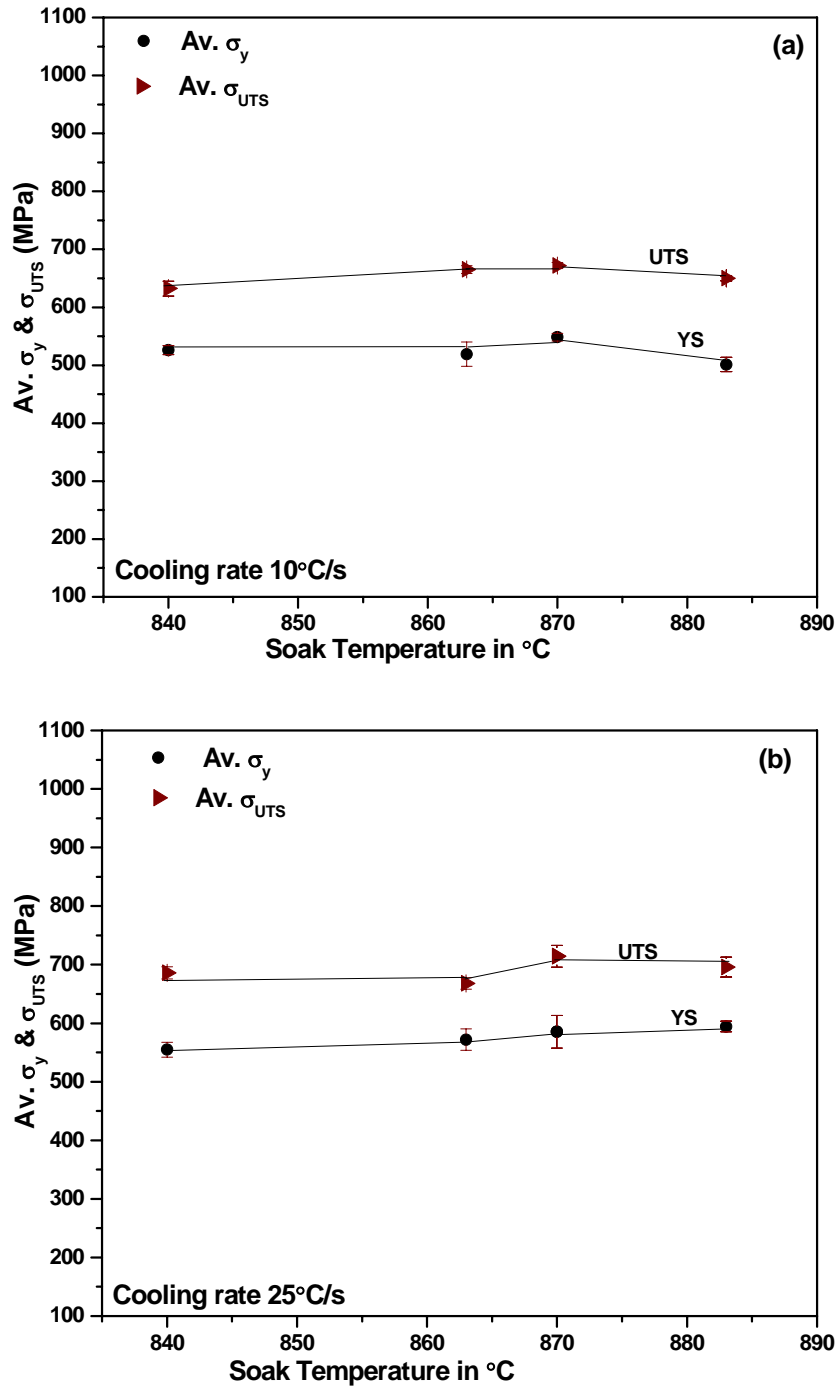


Fig. 6.3 Effect of soaking temperatures on mechanical properties  $\sigma_y$  and  $\sigma_{UTS}$  of the ( $\alpha+\beta$ ) heat treated Zr-2.5%Nb pressure tube samples by ABI, for the cooling rates (a) 10°C/s, (b) 25°C/s

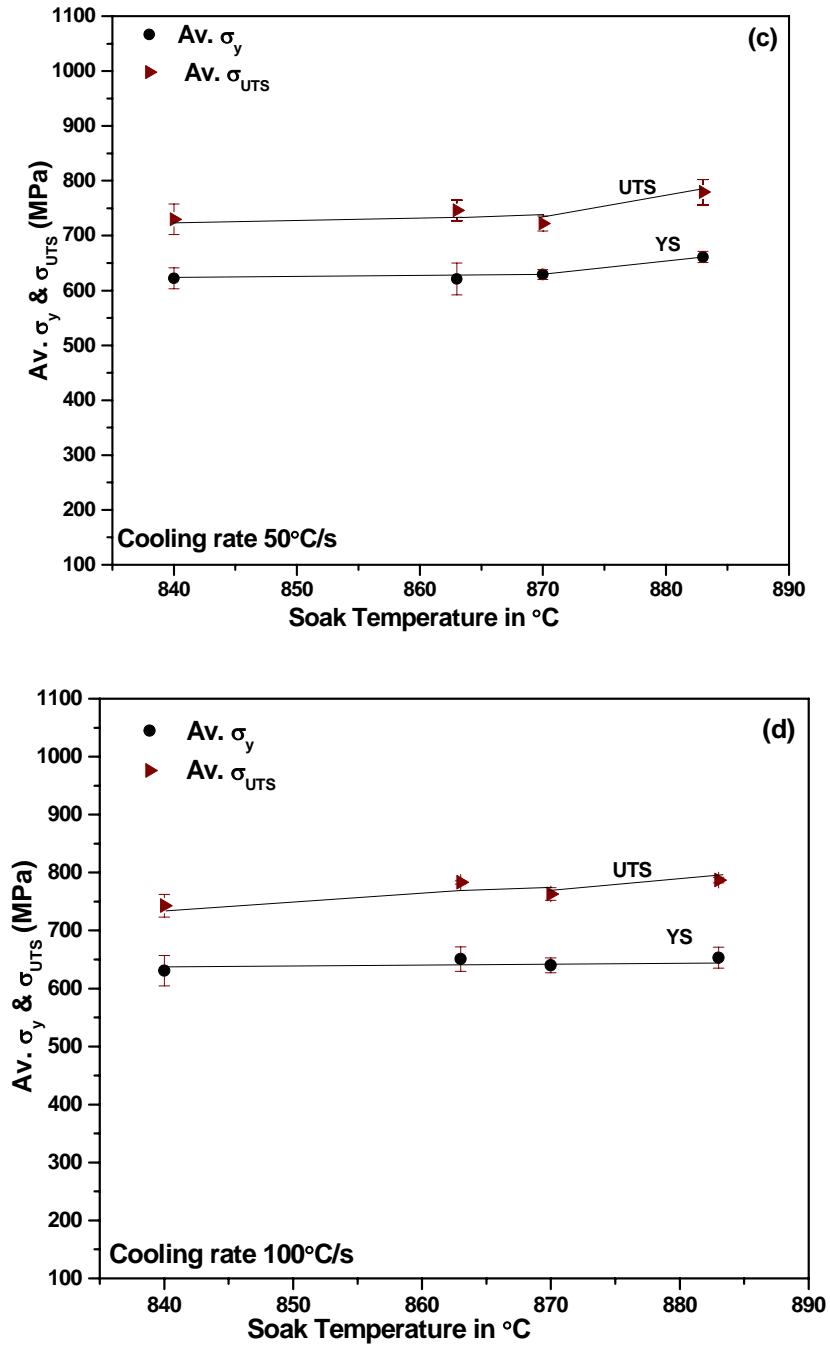


Fig. 6.3 Effect of soaking temperatures on mechanical properties  $\sigma_y$  and  $\sigma_{UTS}$  of the  $(\alpha+\beta)$  heat treated Zr-2.5%Nb pressure tube samples by ABI, for the cooling rates (c) 50°C/s, (d) 100°C/s

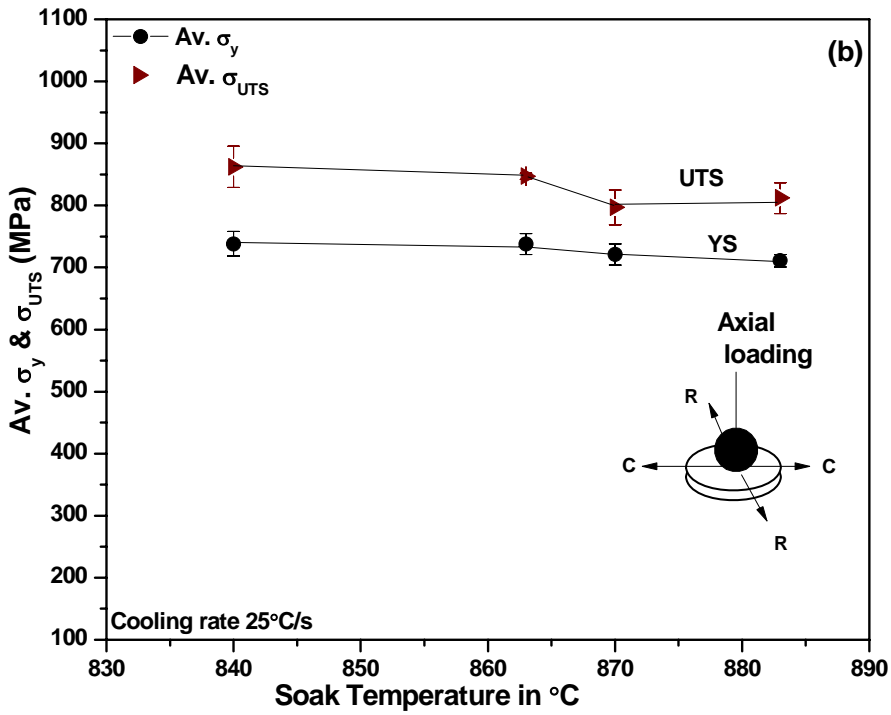
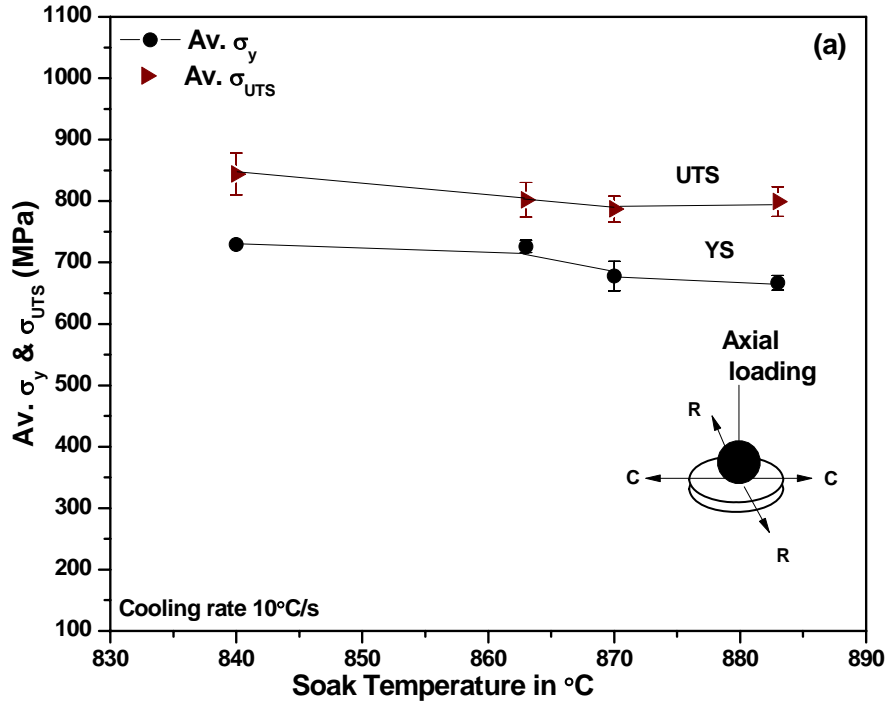


Fig. 6.4 Effect of soaking temperatures on mechanical properties  $\sigma_y$  and  $\sigma_{UTS}$  of the  $(\alpha+\beta)$  heat treated Zr-2.5%Nb pressure tube samples by SPT, for the cooling rates (a) 10°C/s, (b) 25°C/s

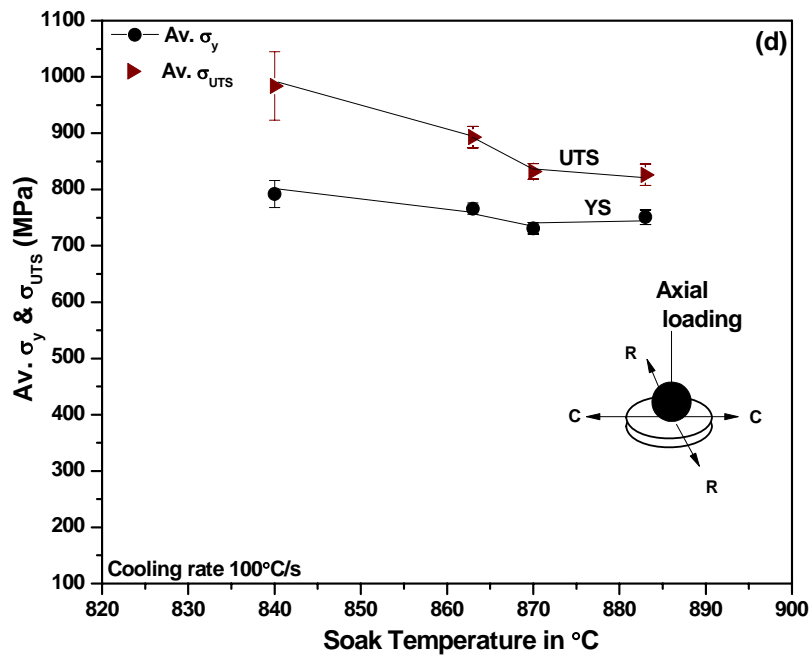
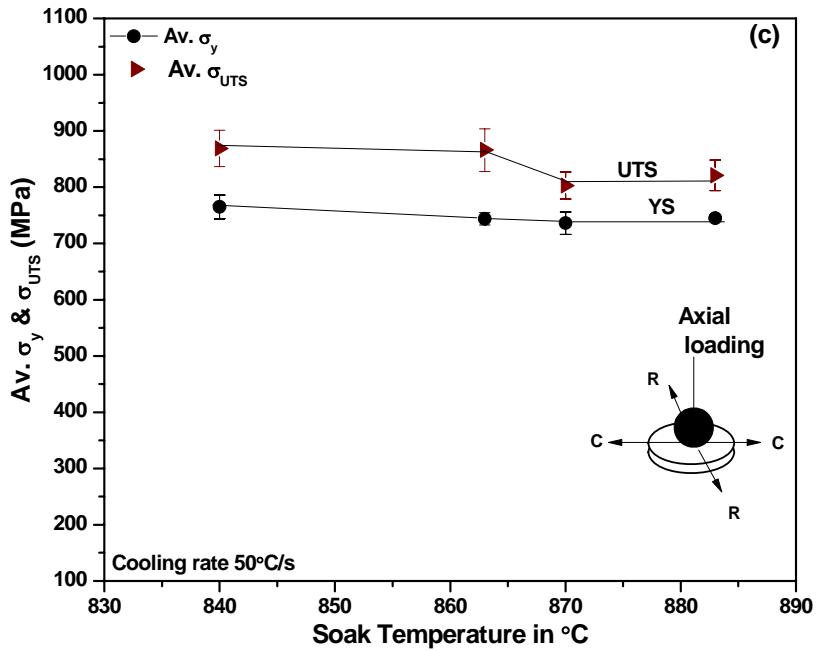


Fig. 6.4 Effect of soaking temperatures on mechanical properties  $\sigma_y$  and  $\sigma_{UTS}$  of the  $(\alpha+\beta)$  heat treated Zr-2.5%Nb pressure tube samples by SPT, for the cooling rates (c) 50°C/s and (d) 100°C/s

## 6.4 Discussion

The mechanical properties of Zr-2.5%Nb pressure tube alloy are dependent on crystallographic texture, the microstructure of  $\alpha$  and  $\beta$  phases and also their interactions during deformation [8]. The present work is an attempt to address issue of effect of microstructural variations on the mechanical properties through a systematic study. In the following discussion, the effect of soaking temperatures in the ( $\alpha+\beta$ ) phase field and different cooling rates adopted on the morphologies and distribution of  $\alpha$  and  $\beta$  phase transformation products have been correlated with the mechanical properties of the alloy.

Being dual phase material consisting of inherently anisotropic  $\alpha$  (*hcp*) and relatively isotropic  $\beta$  phases and crystallographic texture, the deformation mechanisms in Zr-2.5%Nb alloy are much more complicated than cubic polycrystalline or single-phase materials. During deformation the loads tend to partition unequally between the  $\alpha$  and  $\beta$  phases due to their different elastic and plastic properties [8] and also between grains of each phase with different crystal orientations. This results in anisotropic stress-strain behavior [8]. Therefore, while dealing with mechanical properties of anisotropic materials like Zr-2.5%Nb alloy, the direction of load application on the specimen bears importance. The heat treatment was carried out in a quenching dilatometer which uses smaller geometry ( $\phi 3.0$  mm and 10.0 mm long) of samples. Therefore, in the present study, the miniature techniques like ABI and SPT were adopted for characterisation of mechanical properties of these miniature samples. In both kinds of tests the specimen loading condition was along the axis of the dilatometry specimens which coincides with the axis of the pressure tube.

Both miniature specimen testing techniques, the ABI and SPT are essentially nonconventional methods which require correlations using some conventional testing methods such as those certified by ASTM for evaluation of mechanical properties. In a recent study, the authors [9] addressed the issue of correlation parameters for both ABI and SPT considering the effect of loading direction on the textured Zr-2.5%Nb alloy material [9]. Their study has established that the correlation parameters are essentially material specific and also need to be direction specific when materials are anisotropic like Zr-2.5%Nb alloy.

During a small punch test, the disc specimen undergoes deformation under biaxial stress state [10-13]. Since the disc is constrained at center and periphery, there exists a tensile stress along

the radial direction of the disc (*i.e. from centre to periphery*) during the test. Thus one can imagine the disc specimen to be composed of a large number of tiny tensile elements radially arranged as shown schematically in Fig.5.10 (a and b). These imaginary tiny tensile specimens undergo elongation due to the tensile forces acting in the radial direction of the disc specimen when the centrally placed hardened steel ball is forced using a plunger at a constant speed during the test. It shall be noted here that, the plane of the disc belongs to the radial-transverse plane of the dilatometry specimen (*i.e. cross-sectional plane of the pressure tube*) along which majority of basal poles of the  $\alpha_{Zr}$  phase are aligned owing to strong transverse texture and relatively lower radial texture (Table-4.4). Therefore, for the axial loading condition with respect to the pressure tube, during the deformation of the disc specimen, majority of basal poles are along the axis of imaginary tensile elements, indicating that majority of  $\alpha_{Zr}$  crystals are experiencing tensile force along the c-axis (*which is a stronger direction*).

On the other hand for the same loading condition in an ABI test, the fraction of basal poles in the direction of load application (*i.e. axial with respect to pressure tube*) are much less due to the kind of texture (*low  $f_a$  values as shown in Table-4.4*) generally present in the alloy. Further, the deformation in an ABI test occurs primarily in the direction of load application itself beneath the indenter which is similar to the one experienced during a uniaxial tensile test. Unlike ABI, in a SPT, the majority component of the deformation in the disc specimen occurs in a direction perpendicular to the load application under near biaxial (*tensile*) stress state. Therefore, in an ABI test for the same loading direction (*axial in the present study*) the mechanical properties established are relevant to the same direction of loading. This is unlike the case of SPT, where the mechanical properties established are relevant to circumferential direction for the same loading condition, because the strain components can be resolved along circumferential and radial directions with respect to pressure tube axis [9]. Thus the mechanical properties established by these two techniques for the same direction of loading are expected to bring out the effect of anisotropy (*i.e. due to the texture in the alloy*) in the alloy material. The authors [9] in their study have found that the strength values in a SPT were higher compared to ABI for the same sample and same loading condition owing to the effect of orientation of  $\alpha_{Zr}$  crystallites. Therefore in the present study, the direction specific correlations established at our laboratory [9]

for evaluation of mechanical properties by ABI and SPT have been used, and the results have been discussed as a function of cooling rate, soaking temperature and morphological changes of the transformed products in the following subsections.

#### **6.4.1 Effect of cooling rates on microstructures and mechanical properties**

The cooling rate from a given soaking temperature within  $\alpha+\beta$  phase field of the alloy greatly affects the microstructural features [14], such as the dimensions of the  $\alpha$  and  $\beta$  phases within the transformed  $\beta$  region (see Fig.4.6 to 4.9) and consequently have an influence on the short term and long term mechanical properties. Slower cooling rates exhibit much wider lamellae originated by a diffusion process [14] as evident in the case of sample soaked at 883 °C and cooled at 0.5°C/s (see Fig.4.6 (a)). The thickness of  $\alpha$  laths in the transformed  $\beta$  region increased considerably as the cooling rate was decreased from 25°C/s for all the soaking temperatures studied. This effect was more pronounced particularly in the case of slower cooling rates because the  $\alpha_{Zr}$  appeared to grow on the pre-existing primary  $\alpha$  (see Fig.4.6 (a), (b), 4.7 (a), 4.8 (a)). The observed increase in the width and length of  $\alpha$  lamellae (or the volume fraction of  $\alpha$ -phase) as the cooling rate is decreased can be mainly attributed to an increased diffusional transformation of  $\beta$ -phase to the  $\alpha$ -phase influencing the growth of  $\alpha$  phase due to relatively longer length of time that the specimens spend at higher temperatures during the course of cooling at slower rates such as 0.5°C/s.

The size of  $\alpha$  colonies is thought to be the most influential microstructural parameter on the mechanical properties in the lamellar microstructure because it determines the effective slip length as it influences the resistance offered to the advancing deformation front (*slip or twin*) [14]. Within the transformed  $\beta$  region, the  $\alpha$  colony size is generally decreased with increasing cooling rate as seen in the Fig. 4.6 (a-c), Fig. 4.7 (a-b) and resulting in increased  $\alpha$  colony boundaries which are the major barriers to slip [14]. Such morphological changes are expected to decrease the effective slip length [14, 15]. Both the microstructural feature i.e. the  $\alpha$  lamellae size and  $\alpha$  colony size would influence the mechanical properties. Therefore, fine  $\alpha$  lamellae and smaller  $\alpha$  colony obtained with increase in cooling rate would result in increase in the strength. This effect was clearly reflected in the mechanical properties,  $\sigma_y$  and  $\sigma_{UTS}$  values particularly for

the cooling rates of 0.5 °C/s and 10 °C/s presented in Figs. 6.1 (a), (b) (by ABI) and Fig.6.2 (a), (b) (by SPT). The finer grain size is expected to show higher strength with reasonable ductility. It can be observed from the microstructures (see Fig.4.6 (a), (b), (c), 4.7 (a), (b)) that the increase in cooling rates at a given soaking temperature caused the decrease in thickness of Widmanstätten  $\alpha$  and size of the  $\alpha$  colonies. The finer structure decreases the effective slip length, where, higher stress levels are required to overcome the barriers due to crystal boundaries. Thus the observed tendency of increase in  $\sigma_y$  and  $\sigma_{UTS}$  values with the increase in cooling rates as seen in Fig. 6.1 (a-d) and Fig. 6.2 (a-d) for all the soaking temperatures studied, can be attributed to the decrease in effective slip length and also increase in effectiveness of the different interfaces in offering resistance to the approaching deformation front (*either slip or twin*) [14, 15]. The higher cooling rates such as 50 °C/s and 100 °C/s resulted in martensitic phase (*displacive type transformation*) [16] as shown in Fig. 4.6 (d), (e), 4.7 (c), 4.8 (c), (d), 4.9 (c). The strength values obtained for these samples (see Fig. 6.2 (a-d), Fig. 6.3 (a-d)) were higher compared to other lower cooling rate conditions. The earlier studies [14, 15] have attributed higher strength of martensitic structure to solution strengthening of supersaturated  $\alpha'$  (*martensite*) like carbon in ferrite, in addition to the concentration of defects such as crystal interfaces, i.e. the lath, the plate and the twin boundaries and a higher density of dislocations caused by the rapid cooling as compared to the slower cooled  $\alpha$  structure of the same composition. On similar lines it can be stated here that the higher strength of martensite in the Zr-2.5%Nb alloy can be attributed to mainly the super-saturation of  $\alpha_{Zr}$  phase with 'Nb', and oxygen, in addition to increase of crystal interfaces and fine grain structure that offer resistance to deformation. The strength values however showed saturation beyond the cooling rate of 50 °C/s (Figs. 4.6 (d), (e), 4.7 (c), 4.8 (c), (d) and 4.9 (c)) indicating near saturation in formation of martensite. This also indicates that change in structure of martensite at still higher cooling rates does not influence the mechanical properties appreciably.

The results by SPT presented in Fig.6.2 (a-d) have shown relatively higher scatter particularly for  $\sigma_{UTS}$  values compared to the  $\sigma_y$  values. Earlier studies have attributed this kind of scatter to substantial thickness reduction in the plastic instability regime of the deforming disc, where the number of grains participating in the deformation process would substantially decrease as the

deformation proceeds [10, 17]. Further the combination of multiaxial stress state within the sample, the strain localisation resulting from the neck formation and the crack growth behavior is also expected to contribute to such observed scatter [10, 17]. Despite higher scatter in SPT derived results ( $\sigma_y$  and  $\sigma_{UTS}$  values), the influence of microstructural features on the mechanical properties as a function of cooling rate was observable and are similar to the ABI derived results presented in Fig.6.2 (a-d). Hence, experimentally it has been established that these methods corroborate qualitatively the relationship between microstructure and mechanical properties in the heat treated Zr-2.5%Nb alloy. This indicated that these techniques are sensitive to the microstructural changes in the alloy and can be adopted to characterise wide range of microstructures.

#### 6.4.2 Effect of soaking temperature on microstructure and mechanical properties

As expected from the phase diagram [18], lowering the soaking temperature within the  $\alpha+\beta$  phase field of the Zr-2.5%Nb alloy, the relative fraction of  $\alpha$  phase will increase and correspondingly  $\beta$  phase will decrease (see results in Table-4.1, 4.2, 4.3). Additionally both  $\alpha$  and  $\beta$  phases will get enriched with 'Nb' content and  $\beta$  to the higher extent (see Fig.4.5 (b)).

Comparing the Fig.4.6 (b), 4.7 (a), 4.8 (a), 4.9 (a) for the cooling rate of 10 °C/s, it is evident that the Widmanstätten  $\alpha$  plates became finer with lowering of soaking temperatures. The decrease in soaking temperature, in general, will result in decrease in temperature at which  $\beta_{Zr} \rightarrow \alpha+\beta_{Nb}$  transformation would occur due to super cooling required to initiate the transformation (this is true for lower cooling rates where diffusional transformation is dominant and results in Widmanstätten  $\alpha$  phase) [19]. At lower temperature the  $\beta$  grain size will be smaller, on cooling the  $\beta$  grains would transform to still finer  $\alpha$  and  $\beta$  phases. Thus considering the  $\beta$  grain size effect, the strength values are expected to increase with decreasing soaking temperature [14]. In case of higher cooling rates as mentioned earlier the  $\beta$  phase at lower soaking temperature will have a higher 'Nb' content. This would result in lowering of martensite start ( $M_s$ ) temperature [19]. Hence, one would expect to obtain finer martensite and more pronounced internally twinned martensite [20], as seen in the case of samples soaked at lower temperatures (863 °C and 840 °C) (see Fig. 4.8 (b) and 4.9 (c)). Hence the mixed structures of martensite and finer

Widmanstätten structure obtained for the samples soaked at lower soaking temperatures (870 °C, 863 °C and 840 °C) even at relatively slower cooling rates of 25 °C/s (see Figs. 4.7 (b), 4.8 (b) and 4.9 (b)) are expected to have influence on the mechanical properties.

One of the most important parameters that influence the mechanical properties of the dual phase microstructure is the volume fraction of primary  $\alpha$ , because this can be closely related to the partitioning effect of alloying elements [14] such as ‘Nb’, ‘O’ and ‘Fe’ in  $\alpha$  and  $\beta$  phases. It has been shown in earlier studies [1] that the properties of as fabricated tube (*crystallographic texture, mechanical properties*) are strong functions of the amount of primary  $\alpha$  phase (after heat treatment) present in the alloy, which in turn is dependent on the soaking temperature in the  $\alpha+\beta$  phase field [6]. The extensive study by Nishimura, *et.al* [21] on deformation of a series of quenched  $\beta$ -phase of Zr-Nb alloys with ‘Nb’ content ranging from 13.5wt% to 80wt% (at 290 K) showed that ‘Nb’ content in  $\beta$  phase significantly increases the strength by solute strengthening effect. At relatively lower concentration of ‘Nb’ in  $\beta_{Zr}$ , mode of deformation was predominantly slip, while at higher ‘Nb’ concentration (>40%), solute strengthening increasingly blocked dislocation slip leading to twinning [8, 21].

Hence the higher strength values ( $\sigma_Y$  and  $\sigma_{UTS}$ ) observed for the specimens soaked at lower soaking temperature as seen in the case of results from SPT (Fig.6.4 (a-d)) for the cooling rates of 10, 25, 50 and 100 °C/s, can be attributed to ‘Nb’ enrichment of  $\beta$  phase, the grain refinement effect (*finer structure*) and also the martensitic transformation. Lowering of soaking temperature would lead to increased solute strengthening effect due to ‘Nb’ enrichment of  $\beta$  phase, while the finer structure due to grain refinement effect and martensitic transformation even at slower cooling rates such as 25 °C/s will provide increased crystal barriers resulting in higher strength values. In general, the concentration of defects like crystal interfaces, dislocations (introduced during the transformation) and the effectiveness of these barriers in restricting dislocation motion differ significantly as the microstructure of the alloy is altered [15] through soaking temperature. Therefore, the soaking temperature in the  $\alpha+\beta$  phase field of the alloy is one of the controlling factors for obtaining the required structure and the properties in the alloy.

However, the strength values determined by ABI (Fig. 6.3 (a-d)) as a function of soaking temperature for the cooling rates of 10, 25, 50 and 100 °C/s adopted in the study, were

apparently unaffected, while the results from SPT for the same conditions could exhibit the effect of microstructural changes despite relatively higher scatter in the strength values. This indicated that, SPT could capture the influence of microstructure on the mechanical properties, whereas the ABI is not equally sensitive. Although it is difficult to ascertain the exact reasons for the dissimilar trends by ABI and SPT for the same conditions at this time, one of the possible reasons can be that the SPT specimen is a thin slice of disc and the deformation of the disc occurs under biaxial state of stresses, while in the case of ABI the deformation occurs under near triaxial state of stresses in a larger volume of deforming material where the sensitivity to the microstructural changes can be lower due to averaging effect.

#### **6.4.3 Effect of microstructural changes on the micro-hardness of heat treated Zr-2.5%Nb alloy sample**

The micro-hardness measurements were carried out on the same heat treated dilatometry specimens at room temperature to study the effect of microstructures using a Vicker's micro-hardness measuring equipment. The tests were performed on the metallographically prepared flat cross sectional surface of the heat treated samples using a diamond pyramid indenter and 500 g load. The tests were carried out as per the specifications in [ASTM 384 11<sup>el</sup>](#) [22]. The loading direction was axial with respect to the dilatometry sample axis which was identical as in the case of ABI tests. The purpose of hardness test by Vicker's method was to verify the mechanical response obtained from ABI tests on the heat treated samples (*for the same loading conditions*). In this part of the work the aim was to compare the hardness trends by Vicker's and the Brinell obtained during ABI testing and check the validity of the ABI derived results. [Figs. 6.5 \(a\)](#) shows the Vicker's micro hardness results for the heat treated specimens plotted as a function of cooling rate for the four soaking temperatures studied. Similarly [Fig. 6.5 \(b\)](#) shows the same kind of plots for the BHN values obtained during ABI tests on the same heat treated specimens.

The BHN hardness test carried out was as per the American Society for Testing and Materials (ASTM), standard E10-10 [23]. The trends observed in the results by Vicker's and by Brinell hardness ([Fig. 6.5 \(a-b\)](#)) indicate clearly that as the morphology of transformed  $\alpha$  and  $\beta$  phases becoming finer the hardness values showed an increase.

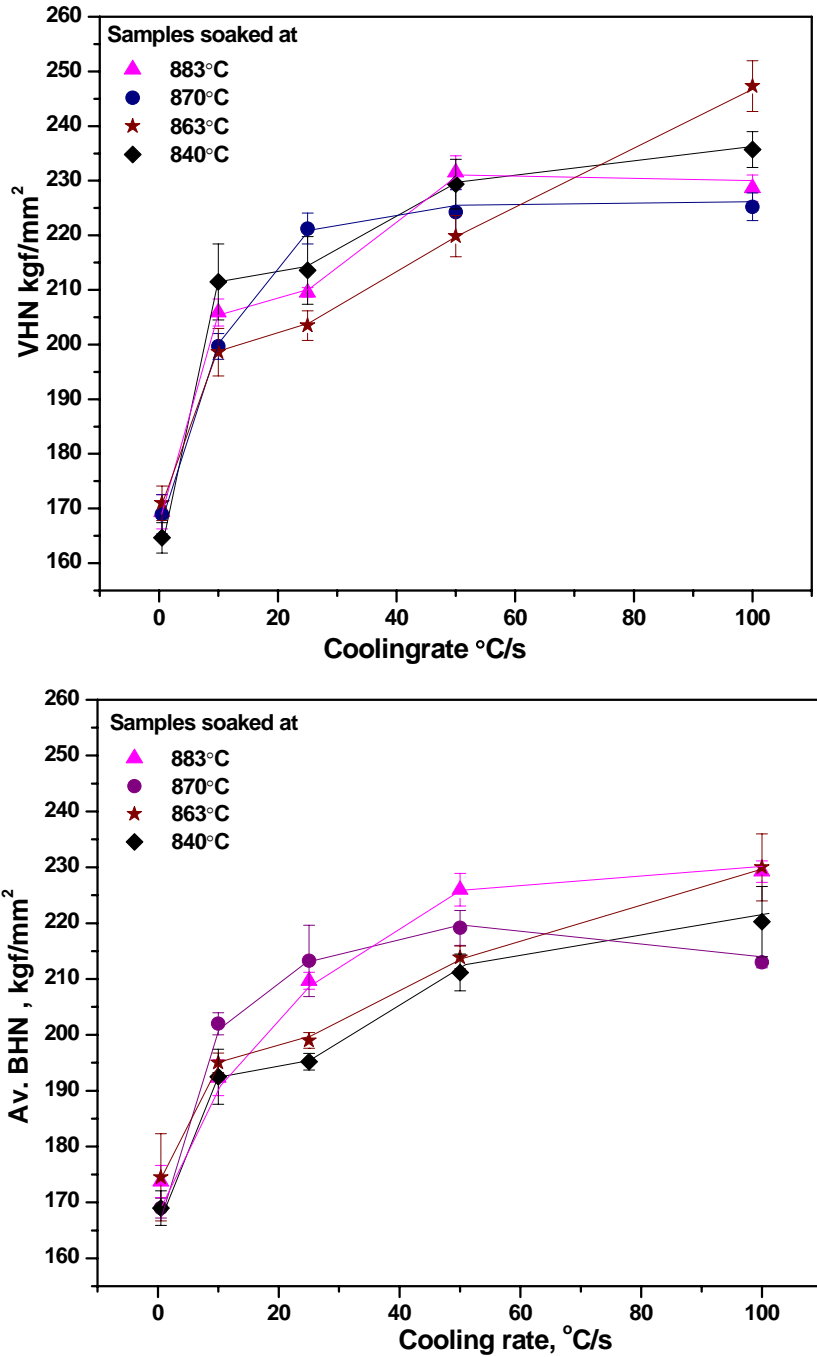


Fig. 6.5 (a) Effect of cooling rate on the Vicker's hardness (VHN) of the heat treated Zr-2.5%Nb alloy samples soaked at 883, 870, 863 and 840°C, (b) Effect of cooling rate on the Brinell hardness (BHN) of the same alloy samples obtained during ABI tests

At higher cooling rates such as 50 and 100C/s the hardness values were higher and nearly remained same as observed in the case of ABI and SPT. Thus, the results by Vicker's and Brinell

hardness tests confirm the validity of the trends observed in the mechanical properties established by ABI tests on the same heat treated samples.

## **6.5 Summary of the work**

1. The specimens of Zr-2.5%Nb alloy samples heat treated from the  $\alpha+\beta$  phase field using dilatometry were characterised for basic mechanical properties  $\sigma_y$  and  $\sigma_{UTS}$  using SPT and ABI tests. The samples heat treated from the  $\alpha+\beta$  phase field showed increasing  $\sigma_y$  and  $\sigma_{UTS}$  values with increasing cooling rates, which can be attributed to finer transformation products in the fast-cooled samples.
2. Higher strength values obtained at lower soaking temperatures for a given cooling rate can be related to both solute-strengthening effect by 'Nb' enriched  $\beta$  phase and increased effectiveness of the crystal interfaces to the deformation fronts due to finer structures.
3. This study has indicated that SPT was more effective in capturing the changes in mechanical properties due to change in microstructures as compared to ABI.

## References Chapter- 6

1. N. Saibaba, S.K. Jha, S. Tonpe, Kumar Vaibhaw, V. Deshmukh, S.V. Ramana Rao, K.V. Mani Krishna, S. Neogy, D. Srivastava, G.K. Dey, R.V. Kulkarni, B.N. Rath, E. Ramadasan, S. Anantharaman, *J. (ASTM), International, (JAI), Paper ID JAI103213, 8, Issue 6 (2011)*
2. D.K. Rodgers, C.E. Coleman, M. Griffiths, G.A. Bickel, J.R. Theaker, I. Muir, A.A. Bahurmu, S. St. Lawrence, M. Resta Levi, *J. Nucl. Mater., 383 (2008) 22-27*
3. M. Griffiths, N. Wang, A. Buyers, S.A. Donohue, *J. (ASTM), International, (JAI) Paper ID JAI101133, 5, Issue 1, (2008)*
4. G. A. Bickel, M. Griffiths, *J. (ASTM), International, (JAI) Paper ID JAI101126, 4, issue 10, (2007)*
5. C.E. Coleman, A.R. Causey, V. Fidleris, *J. Nucl. Mater., 60 (1976) 185-194*
6. M. Griffiths, N. Christodoulou, S.A. Donohue, *J. (ASTM), International, (JAI) Paper ID JAI12432, 2 No. 7, (2005)*
7. K. Takayama, "Post-Irradiation Examination And Evaluation of Zr-2.5%Nb Pressure Tube of FUGEN", *XA9846758, 181-192*
8. S. Cai, PhD Thesis, Dept. of Mechanical and Materials Eng. University Kingston Canada, Oct 2008, *Publication Ref, ISBN, 0494443162, 9780494443163*
9. R.V. Kulkarni, K.V. Mani Krishna, S. Neogy, D. Srivastava, E. Ramadasan, G.K. Dey, N. Saibaba, S.K. Jha, R.S. Shrivastaw, S. Anantharaman, *Nucl. Eng. Des., 265 (2013) 1101-1112*
10. E. Fleury, J.S. Ha, *Int. J. Pressure Vessels and Piping, 75 (1998) 699-706*
11. X. Mao, H. Takahashi, *J. Nucl. Mater., 150 (1987) 42-52*
12. X. Mao M. Saito, H. Takahashi, *Scr. Metall, 25(1991) 2481-2485*
13. X. Mao, H. Takahashi, T. Kodaira, *Mater.Sci. Eng., AI50 (1992) 231-236*
14. E. Lee, Dissertation for PhD, The Ohio State University 2004, Document number, *osu1092756139, ([http://rave.ohiolink.edu/etdc/view?acc\\_num=osu1092756139](http://rave.ohiolink.edu/etdc/view?acc_num=osu1092756139))*
15. S. Banerjee, S. J. Vijayakar, R. Krishnan, *Acta. Metall., 26 (1978) 1815-1831*
16. G.K. Dey, R.N. Singh, R. Tewari, D. Srivastava, S. Banerjee, *J. Nucl. Mater., 224 (1995) 146-157*

17. J. Kameda, X. Mao, *J. Mater. Sci.*, 27 (1992) 983-989
18. H. Okamoto, *Alloy phase diagrams, ASM International, ASM hand book, 3 (1992)*
19. D. Srivastava, PhD Thesis “ $\beta$ -phase transformation in dilute Zr-Nb alloys”, IISc, Bangalore, India (1996)
20. R.V. Kulkarni, S. Neogy, B.N. Rath, K.V. Mani Krishna, D. Srivastava, N. Saibaba, I. Samajdar, E. Ramadasan, G.K. Dey, S. Anantharaman, DOI 10.1007/s12666-011-01047, *Trans Indian Inst. Met.* 64, Issue 4-5 (2011) 395-399
21. K. Nishimura, S. Handa, O. Izumi, *J. Mater. Sci.*, 25 (1990) 384-390
22. Standard Test Method for Knoop and Vicker’s Hardness of Materials, *American Society for Testing and Materials, (ASTM) International*, Designation: E 384-11<sup>e1</sup> approved Aug. 1, 2011. Published August 2011. editorially corrected in March 2011.
23. Standard Test Method for Brinell Hardness of Metallic Materials, Designation: (ASTM), E 10-10, June 1, 2010. Published June 2010

## CHAPTER 7: Effect of Variation in Iron and Oxygen content on Phase Boundary, Physical and Mechanical Properties of Zr-2.5%Nb Pressure Tube Alloy

.....

### 7.1 Objectives

The previous work by Holt [1] has shown that both ‘Fe’ and ‘O’ have advantageous effect on irradiation creep rates of the pressure tubes (Fig. 2.10 (a-c)). Therefore, it was of interest to investigate the effect of independent variation of these elements on  $(\alpha+\beta)/\beta$  phase boundary, the physical and mechanical properties of the alloy to develop better understanding on the material’s properties and behaviour. ‘Fe’ and ‘O’ being  $\beta_{(bcc)}$  and  $\alpha_{(hcp)}$  phase stabilisers respectively, the  $(\alpha+\beta)/\beta$  phase boundary of the alloy is expected to be influenced in opposite ways depending on their concentrations. Therefore, for a selected soaking temperature within the  $(\alpha+\beta)$  phase field of the alloy, the volume fractions of  $\alpha_{Zr}$  and  $\beta_{Zr}$  phases would be influenced by the concentration of these elements, which eventually can influence the microstructure and also physical and mechanical properties of the alloy. Hence, one of the objectives of this part of the work was to study the effect of independent variation of these two elements on the  $(\alpha+\beta)/\beta$  phase boundary of the alloy particularly within the pressure tube specification range.

The variations in ‘Fe’ and ‘O’ concentrations are also expected to influence the physical property CTE of the anisotropic Zr-2.5%Nb alloy and mechanical properties such as strength, hardness and also the important long term mechanical property, the creep strength. Since the thermal and irradiation creep behavior are closely related, another objective of this part of the thesis was to study the effect of independent variation of these elements on thermal creep behavior particularly at temperatures close to reactor operation. Due to the preferred orientation of  $\alpha_{Zr}$  phase, the CTE and texture of the anisotropic Zr-2.5%Nb alloy are related. Therefore, another objective was to investigate the effect of independent variation of these elements on the CTE and texture and study the inter-correlations of these parameters.

### 7.2 Effect of ‘Fe’ and ‘O’ contents on $(\alpha+\beta)/\beta$ transus temperature of the alloy

Tables -7.1 (a) and (b) provide the ‘Fe’ and ‘O’ variation in the alloy samples respectively, selected for the study. The Figs. 7.1 (a-d) show the heating part of the dilation curves ( $\Delta l$  vs.  $t$ )

recorded for the samples belonging to the Table-7.1 (a). These figures depict the effect of 'Fe' content on the  $(\alpha+\beta)/\beta$  boundary of Zr-2.5%Nb pseudo binary system.

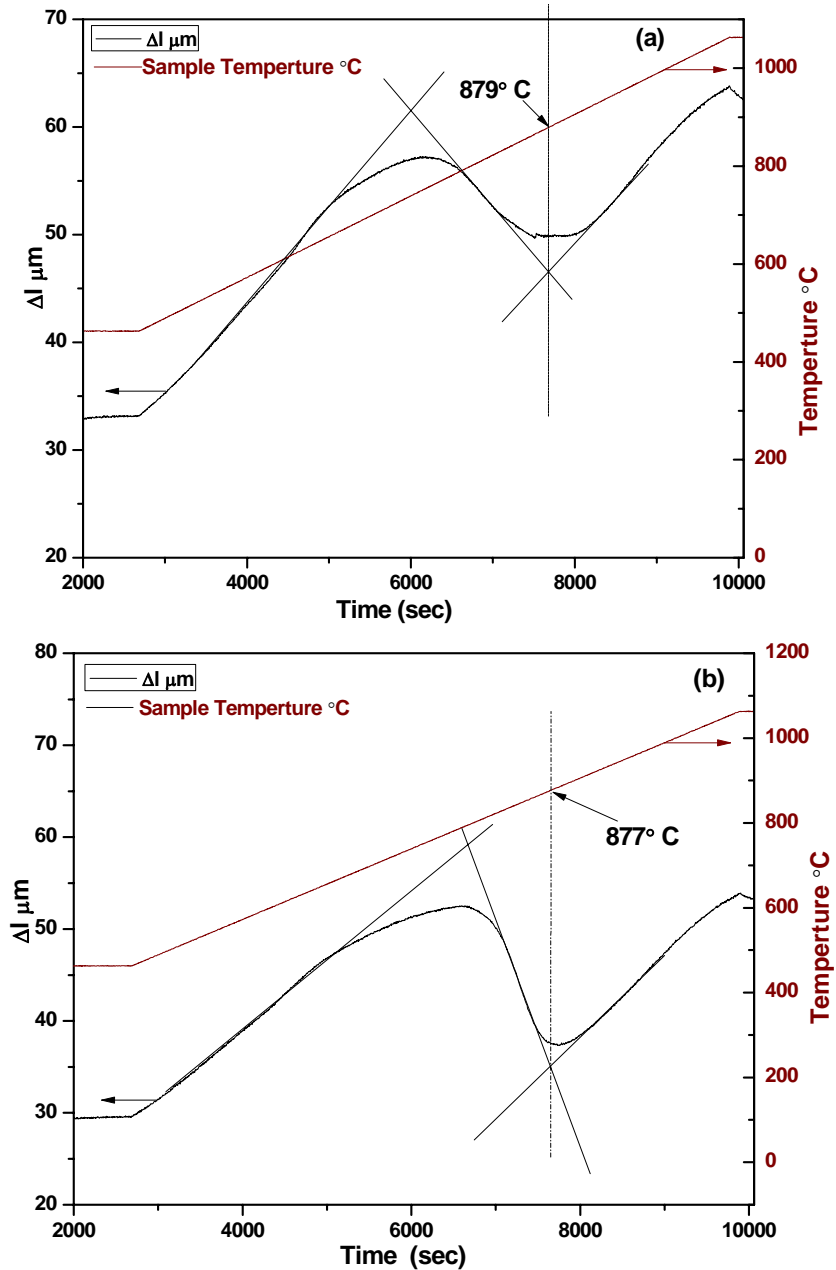


Fig. 7.1 The  $(\alpha+\beta)/\beta$  transus temperature for the Zr-2.5%Nb alloy sample containing (a) 301 ppmw of 'Fe' (Ph-1), (b) 402 ppmw of 'Fe' (Ph-2)

The dilation curves ( $\Delta l$  vs.  $t$ ) were analysed for the  $\alpha_{\text{Zr}}+\beta_{\text{Zr}} \rightarrow \beta_{\text{Zr}}$  phase transformation temperatures adopting three-tangent method and the results are presented in Table-7.1 (a). The

three-tangent method represents the  $(\alpha+\beta)/\beta$  transus temperature of the alloy when nearly complete volume of the specimen is undergoing the transformation. Fig. 7.1 (e) shows the linear fit established for the  $(\alpha+\beta)/\beta$  transus temperature as a function of 'Fe' content in the alloy which is expressed in eq. (1)

$$T_{(\alpha+\beta)/\beta} = T_{\beta} = (893.97 - Fe_{ppmw} \times 0.041) \text{ } ^\circ\text{C} \quad (1)$$

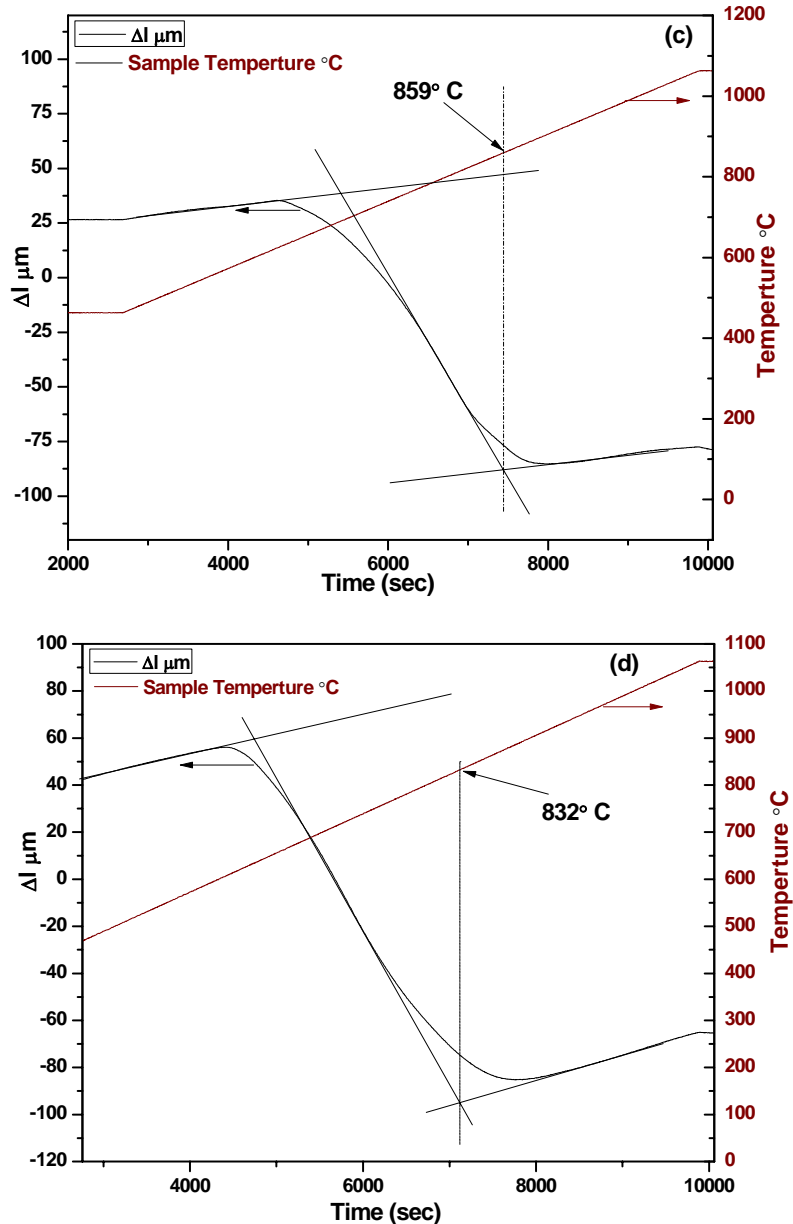


Fig. 7.1 The  $(\alpha+\beta)/\beta$  transus temperature for the Zr-2.5%Nb alloy sample containing (c) 1100 ppmw of 'Fe' (Ph-3), (d) 1336 ppmw of 'Fe' (Ph-4)

The slope of the linear fit indicated a decrease in the  $(\alpha+\beta)/\beta$  transus temperature by  $\sim 4^\circ\text{C}/100$  ppmw of 'Fe' in the alloy. This is one of the essential information for determining parameters for thermo-mechanical treatments of heat treated pressure tube. The Fig. 7.2 (a-e) show the heating part of  $\Delta l$  vs.  $t$  curves recorded for the 'O' variation samples listed in Table-7.1 (b). Analysis of these dilation curves ( $\Delta l$  vs.  $t$ ) for  $\alpha_{\text{Zr}}+\beta_{\text{Zr}}\rightarrow\beta_{\text{Zr}}$  phase transformation temperatures was also carried out by three-tangent method. A linear fit of  $(\alpha+\beta)/\beta$  transus temperature as a function of 'O' content in the alloy samples was established which is expressed in eq. no. (2), and the fit is shown in Fig.7.2 (f).

$$T_{(\alpha+\beta)/\beta} = T_{\beta} = (735.12 + O_{\text{ppmw}} \times 0.135) ^\circ\text{C} \quad (2)$$

Table-7.1 (a) Zr-2.5%Nb alloy samples with 'Fe' variation, 'O' and Nb varied in the range of  $1018 \pm 20$  ppmw and  $2.65 \pm 0.05\%$

Sample Ref. No.	Fe- content, ppmw	$(\alpha+\beta)/\beta$ Transus temperature in $^\circ\text{C}$
Ph-1	301	880
Ph-2	402	877
Ph-3	1100	859
Ph-4	1336	832

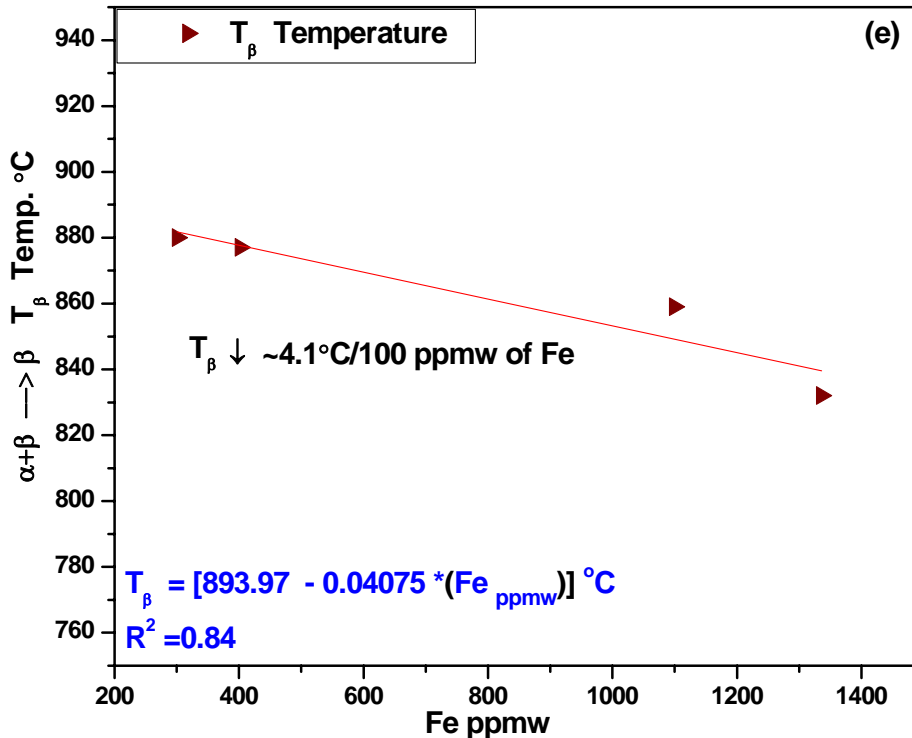


Fig. 7.1 (e) Linear fit of  $(\alpha+\beta)/\beta$  transus temperature vs. 'Fe' content in the Zr-2.5%Nb alloy samples

Table-7.1 (b) Zr-2.5%Nb alloy samples with oxygen content variation. 'Fe' and 'Nb' content varied within  $330 \pm 20$  ppmw and  $2.60 \pm 0.04\%$ , respectively in these samples

Sample Ref. No.	Oxygen content, ppmw	$(\alpha+\beta)/\beta$ Transus temperature in °C
Ph-5	930	858
Ph-6	963	865
Ph-7	967	867
Ph-8	1003	870
Ph-9	1073	880

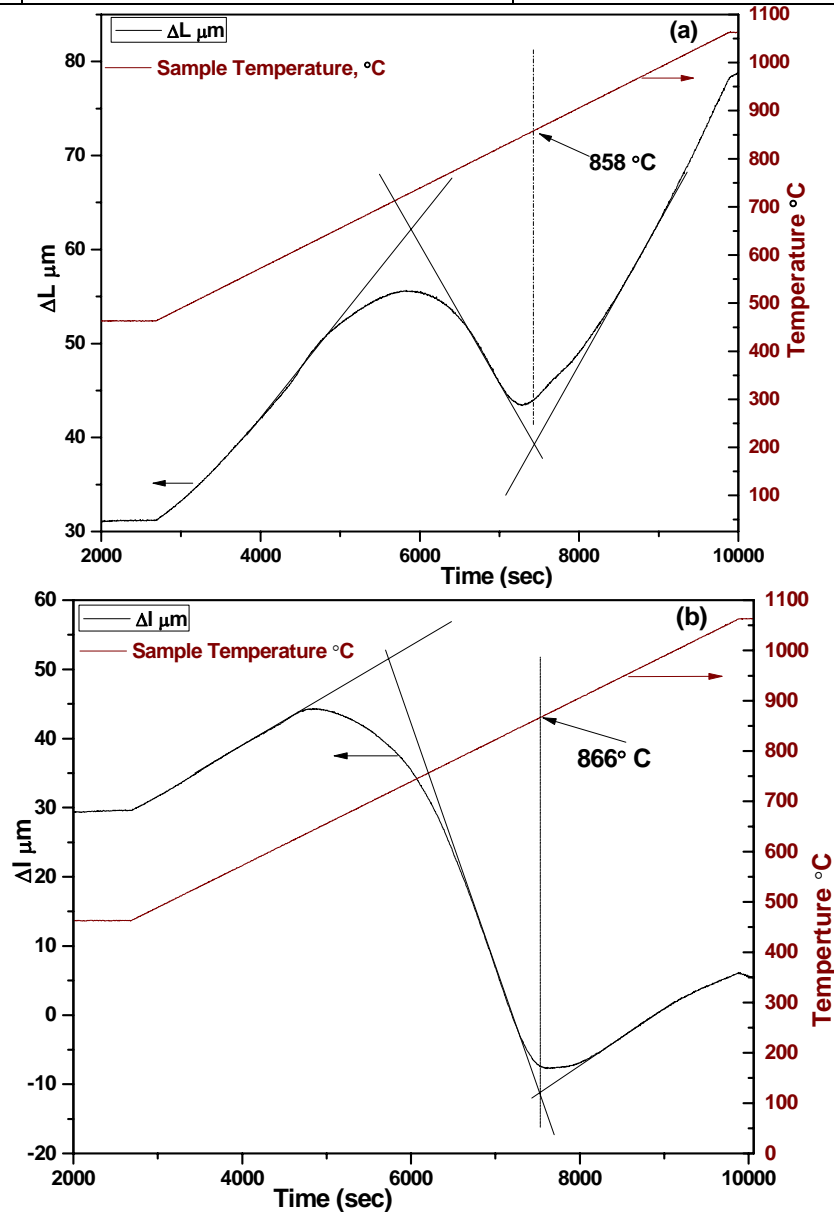


Fig. 7.2 The  $(\alpha+\beta)/\beta$  transus temperature for the Zr-2.5%Nb alloy sample containing (a) 930 ppmw of oxygen (Ph-5), (b) 963 ppmw of oxygen; (Ph-6)

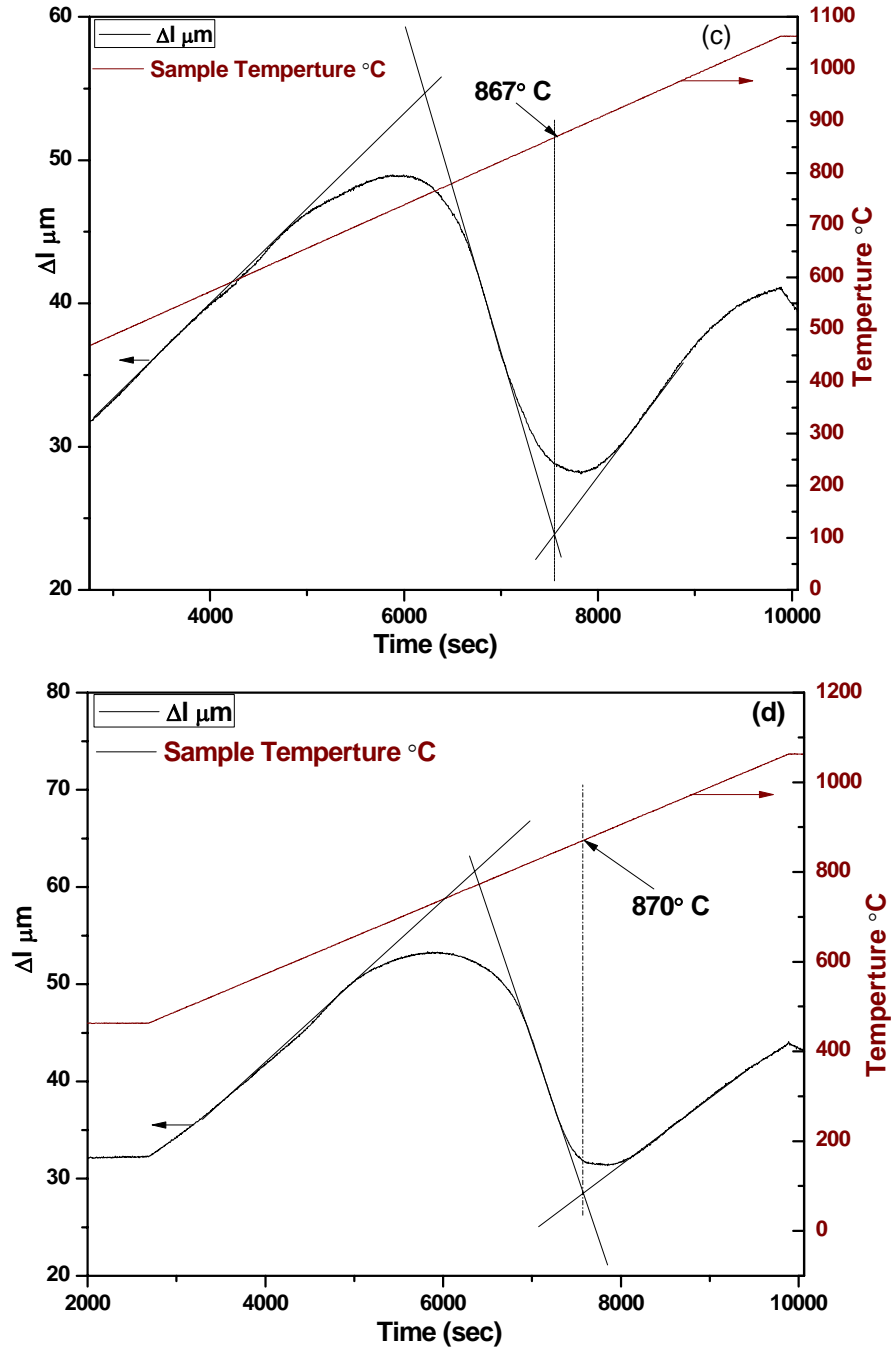


Fig. 7.2 The  $(\alpha+\beta)/\beta$  transus temperature for the Zr-2.5%Nb alloy sample containing (c) 967 ppmw of oxygen; (Ph-7), (d) 1003 ppmw of oxygen; (Ph-8)

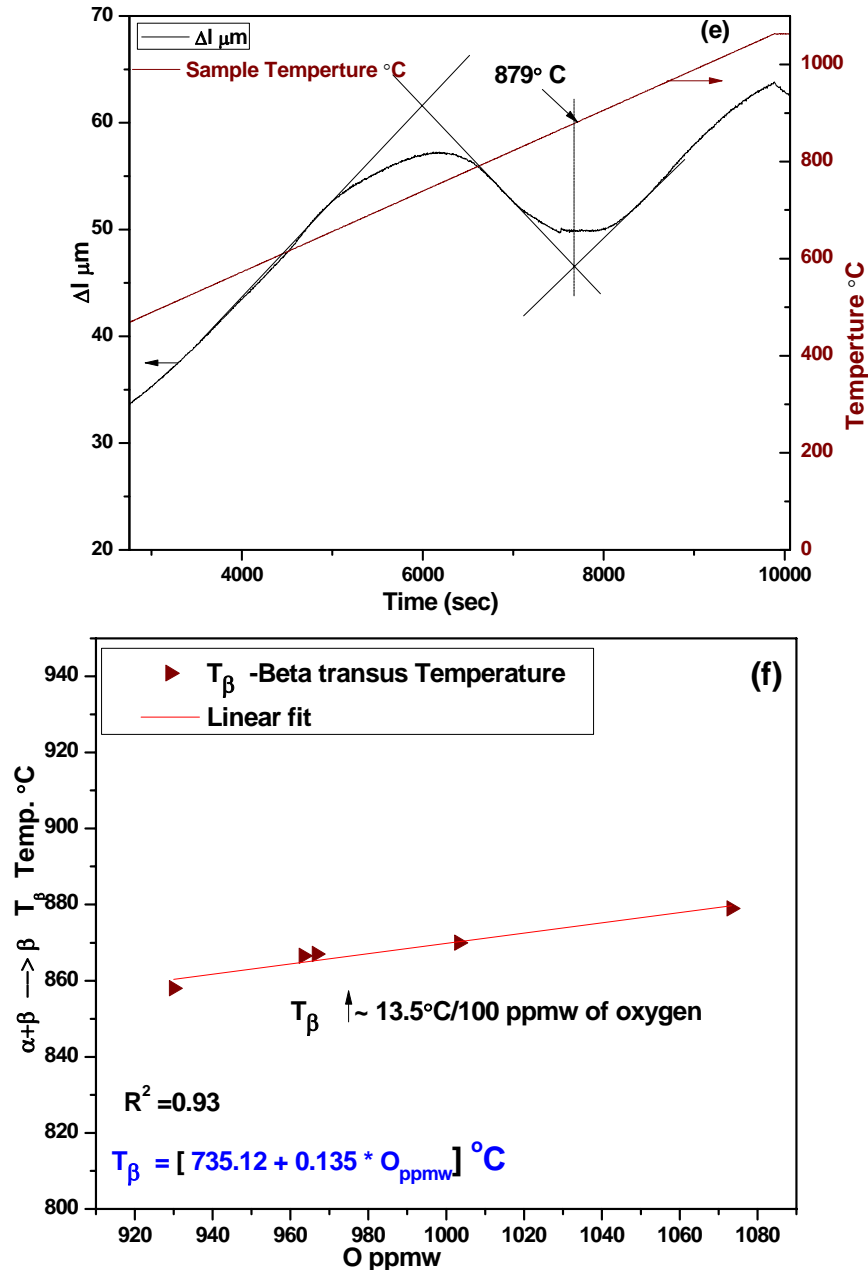


Fig. 7.2 The  $(\alpha+\beta)/\beta$  transus temperature for the Zr-2.5%Nb alloy sample containing (e) 1073 ppmw of oxygen; (Ph-9, (f) Linear fit of  $(\alpha+\beta)/\beta$  transus temperature vs. 'O' content in the Zr-2.5%Nb alloy

The positive slope of the linear fit in Fig. 7.2 (f) indicated an increase in  $(\alpha+\beta)/\beta$  transus temperature by  $\sim 13.5^{\circ}\text{C}/100$  ppmw of oxygen in the alloy material. The observed increase in slope of  $(\alpha+\beta)/\beta$  phase boundary of the Zr-Nb system with increasing 'O' content is similar to

the results of phase diagram calculations by Fidleris [2]. The positive slope of  $(\alpha+\beta)/\beta$  transus temperature vs. O content in eq. (2) is in agreement with the previous finding by Fidleris [2] and Pe´rez and Massih [3] that oxygen expands the  $(\alpha+\beta)$  phase region. Fidleris [2] predicted an increase of  $(\alpha+\beta)/\beta$  transus temperature by  $\sim 7^\circ\text{C}/100$  ppmw oxygen from phase diagram calculations of Zr-Nb-O ternary system, whereas in the present study the experimentally established results showed an increase of  $\sim 13.5^\circ\text{C}/100$  ppmw of oxygen. The lower value predicted by Fidleris [2] may be attributed to theoretical calculation considering ternary system of pure elements. Pe´rez and Massih [3] observed the increase in  $(\alpha+\beta)/\beta$  transus temperature to follow Arrhenius relationship with oxygen content. However, in the present study due to relatively smaller range of variation of oxygen considered the linear fit was used to explain the effect on  $(\alpha+\beta)/\beta$  transus temperature. Now, for the Zr-2.5%Nb alloy containing  $930\pm 26$  ppmw of ‘O’ and 650 ppmw of ‘Fe’ the eq. (1) gives  $T_\beta = 893 - (0.041 \times 650) = 867^\circ\text{C}$ . If the ‘O’ content in this alloy is increased from 930 to 1137 ppmw then, according to eq.(2)  $T_\beta$  should increase by  $(13.5/100) \times 207 = 27^\circ\text{C}$ . Therefore, for the Zr-2.5%Nb alloy containing 1137 ppmw of ‘O’ and 650 ppmw of ‘Fe’ the b-transus temperature is  $T_\beta = 867 + 27 = 894^\circ\text{C}$ . This result is close to  $891^\circ\text{C}$  established for the alloy with the same composition as described in section 4.3. This study has provided valuable input on the effects of ‘Fe’ and ‘O’ on the  $(\alpha+\beta)/\beta$  phase boundary essential for determining parameters for thermomechanical treatments of the pressure tube alloy.

### **7.3 Effect of ‘Fe’ and ‘O’ on the thermal creep behavior of Zr-2.5%Nb alloy**

Although the mechanisms involved in irradiation creep of a pressure tube are complex, understanding of irradiation creep in Zr-2.5%Nb pressure tubes can be improved by a thorough understanding of its thermal creep behaviour, because these two phenomena are closely related [4-6]. Therefore, the objective of present work was to study the effect of ‘Fe’ and ‘O’ content variations, (*within the range of specification*) on the thermal creep behavior of the alloy particularly at temperatures close to reactor operation. Such data would be useful for modeling and predicting the irradiation behavior of the pressure tubes. The experimental part of thermal creep study carried out using the miniature techniques has been described in section 3.8 and 3.9.

### 7.3.1 Impression creep tests on the Zr-2.5%Nb alloy samples with varying 'Fe' contents

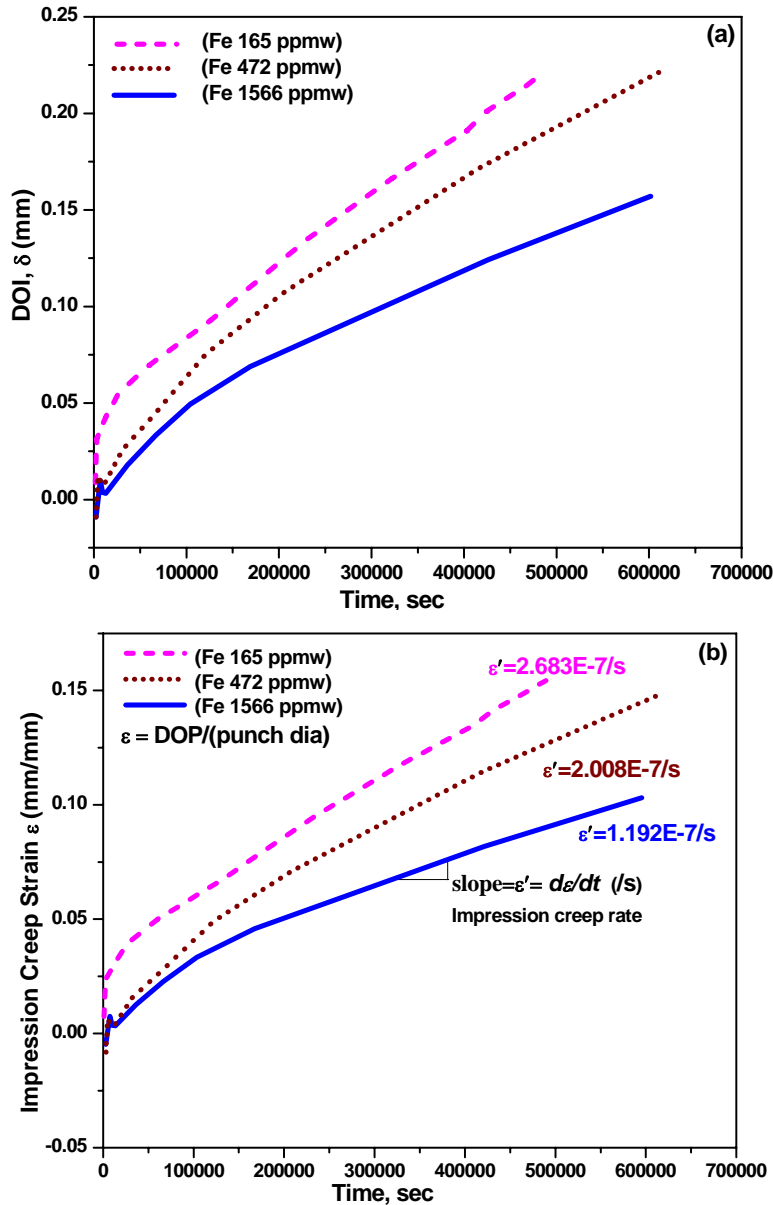


Fig. 7.3 Impression creep test results in the form of (a) Depth Of Penetration (DOP) vs. time and (b) creep stain ( $\epsilon$ ) vs. time

Fig. 7.3 (a) shows the basic output of impression creep tests in the form of DOP ( $\delta$ ) vs. time ( $t$ ) for the three samples listed in Table-3.4 (a). The stress and strain parameters between impression creep test and conventional uniaxial tensile creep test are related by relations in eq. (3), (4), (5) [7-11].

$$\sigma_i = c_I \sigma_t \quad (3)$$

$$\varepsilon = \text{DOP}/d = \text{DOP}/a \quad (4)$$

$$\dot{\varepsilon} = d\varepsilon/dt \quad (5)$$

In eq. (3), the punching stress defined as  $\sigma_i = \text{Load}/\text{cross sectional area of the flat punch}$ , is related to the corresponding conventional uniaxial tensile stress ' $\sigma_t$ ' through a constant ' $c_I$ ' known as conversion factor. The previous studies by Sastry and co-workers [7, 12] have established the value of  $c_I$  to be 3 for the isotropic materials and between 3.5 and 4 for the anisotropic materials. Since, Zr-2.5%Nb alloy is an anisotropic material with predominantly transverse texture, the conversion factor  $c_I$  has been taken as 3.5 for evaluation of  $\sigma_t$  in the present work. Therefore, for the punching stress value of  $\sigma_i = 400$  MPa and  $c_I = 3.5$ ,  $\sigma_t$  value of 114 MPa results from eq. (3), which is close to the operating stress level in the hoops direction of the pressure tube. In eq.(4), ' $d$ ' is the depth of plastic zone beneath the punch, which is nearly equal to the diameter of the punch ' $a$ ' as established from the metallographic investigations by Yang *et.al* [13]. Using this value in relationships in eq. (4) the basic output of impression creep test were converted to creep strain  $\varepsilon$  vs.  $t$  which is shown in Fig. 7.3 (b). Therefore, the impression strain rate  $\dot{\varepsilon}$  at the test temperature of 400°C is the slope of  $\varepsilon$  vs.  $t$  curves in Fig. 7.3 (b) i.e.  $\dot{\varepsilon} = d\varepsilon/dt$ . The Fig. 7.4 (a) presents the plot of steady state impression creep rate ( $\dot{\varepsilon} = d\varepsilon/dt$ ) vs. 'Fe' content in the alloy samples which shows decreasing trend with the increase in 'Fe' content. Fig. 7.4 (b) presents the in-reactor axial creep rate ( $\dot{\varepsilon}_i$ ) data for the corresponding operating pressure tubes with their 'Fe' content. It is seen that the  $\dot{\varepsilon}_i$  vs. Fe content also shows a decreasing trend. This irradiation creep data corresponds to the operating conditions of 300°C and has been normalised with average peak fluence of the respective channel after 3340 effective full power days (EFPDs) of operation [14].

It is known that the potential factors that influence the creep deformation in a polycrystalline anisotropic alloy are the texture, the metallurgical variables such as distribution of different phases, the grain size, shape and their morphologies, the pre-existing dislocation structure, the extent of alloying additions and also impurity levels, in addition to the test parameters such as stress level and test temperature [1, 4, 6, 15]. The microstructural study on some of the representative samples used in the thermal creep study was carried out using Transmission

Electron Microscopy (TEM). Figs.7.5 (a-c) show micrographs of the microstructures of these samples. The distribution of  $\alpha$  and  $\beta$  phases in these microstructures is similar to those of Zr-2.5%Nb pressure tubes of CANDU PHWRs discussed by Li [4] in the author's thermal creep study and also by Cai [16]. Fig. 7.5 (a-c) show that microstructural features such as grain size, distribution and morphologies of  $\alpha_{Zr}$  and  $\beta_{Zr}$  phases in these samples are similar. The width of  $\alpha_{Zr}$  plates is observed to be in the range of 200-300 nm with thin filaments of  $\beta_{Zr}$  present around it in all the three microstructures. Therefore, it can be stated that the 'Fe' and 'O' content variation within range studied has not caused significant change in the microstructure. Table-3.4 (a) and 7.2 (b), show, the texture parameters and dislocation density determined for these sample materials. These tables show that the texture parameters for all these samples varied in a small range. The dislocation density evaluated using X-ray line profile analysis for the crystallographic planes  $[11\bar{2}0]$  exhibited no specific trend as a function of 'Fe' and 'O' contents in the alloy. The sample to sample variation in dislocation densities had a standard deviation of  $3.45 \times 10^{16}$  at a mean value of  $6.83 \times 10^{16} \text{ m}^{-2}$  for the 'Fe' variation set of samples (Table-3.4 (a)). Similarly for the 'O' variation set of samples the dislocation density had a standard deviation of  $1.15 \times 10^{16}$  at a mean value of  $7.91 \times 10^{16} \text{ m}^{-2}$  (Table-7.2 (b)). Therefore, it can be reasonably assumed that the microstructure, texture and dislocation densities in these samples have similar effect on the creep behaviour. Hence the observed trends in the thermal creep results have been discussed in relation to the effect of variation in minor alloying elements 'Fe' and 'O' contents in the alloy.

In addition to the microstructural parameters, the alloying elements such as 'Nb', 'Fe' and 'O' are also expected to influence the thermal creep behavior of the alloy strongly [2, 17]. Generally, the 2.5% overall 'Nb' content in the as fabricated alloy is partitioned mainly between the  $\alpha_{Zr}$  and  $\beta_{Zr}$  phases such that the  $\alpha_{Zr}$  phase has  $\sim 0.6 \text{ wt\%}$  'Nb', while the  $\beta$ -phase contain  $\sim 20 \text{ wt\%}$  Nb [16]. After autoclaving at  $400^\circ\text{C}$ , the metastable  $\beta_{Zr}$  phase partially transforms towards the equilibrium  $\alpha_{Zr}$  and  $\beta_{Nb}$  that contain  $\sim 95 \text{ wt\%}$  Nb and combination of 'Nb' depleted  $\omega$  phase (*a metastable hexagonal phase of intermediate 'Nb' content*) and  $\beta_{Zr}$  with enriched 'Nb' content at  $\sim 50 \text{ wt\%}$  [16]. Thus, all the 'Nb' content in the pressure tube alloy is in solution with both  $\alpha_{Zr}$  and  $\beta_{Zr}$  phases. Oxygen is another alloying element whose maximum solubility in  $\alpha_{Zr}$  phase is 6.75 wt.% (29 at.%) in a wider range of temperature [18]. At reactor operating temperatures and at test

temperatures in the present study, ‘O’ is mainly concentrated in the  $\alpha_{Zr}$  phase in the form of interstitial solute and is depleted in  $\beta_{Zr}$  phase [16, 19]. On the other hand, iron being a  $\beta$  phase stabiliser, it is mainly concentrated in the  $\beta$ -phase. ‘Fe’ is also found at the  $\alpha$ - $\alpha$  grain boundaries in the form of fine precipitates [19].

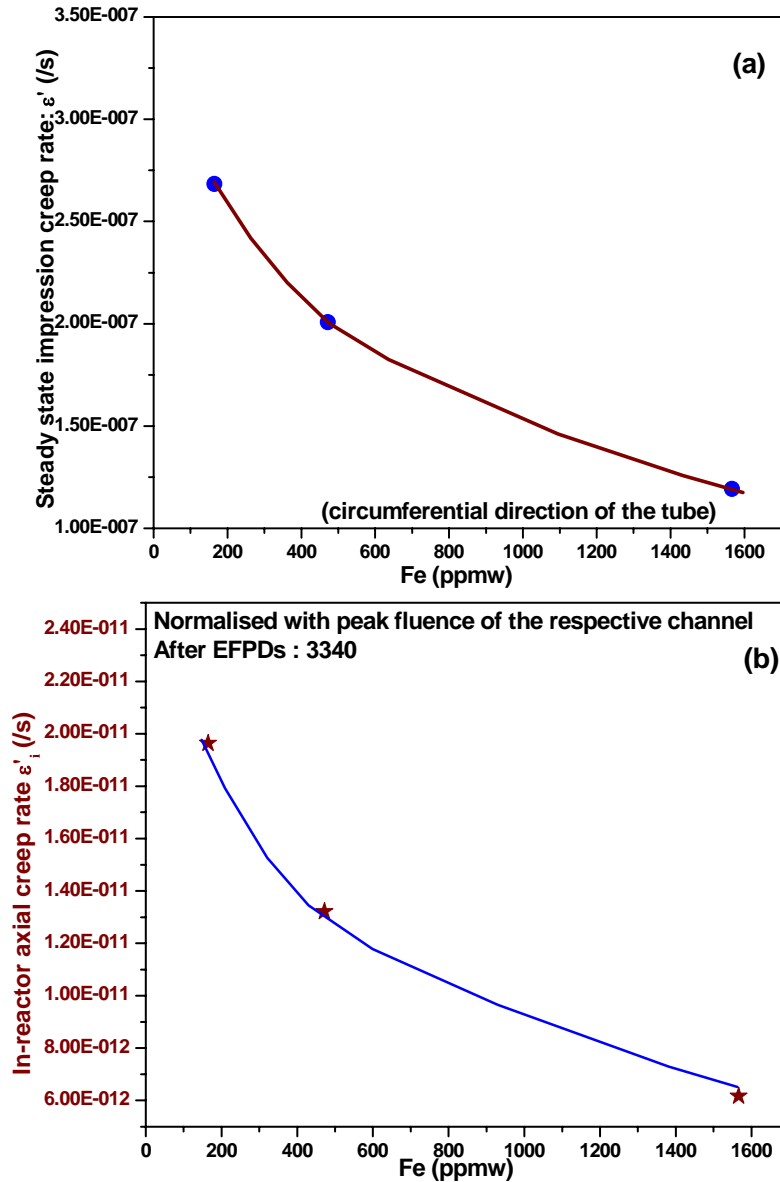
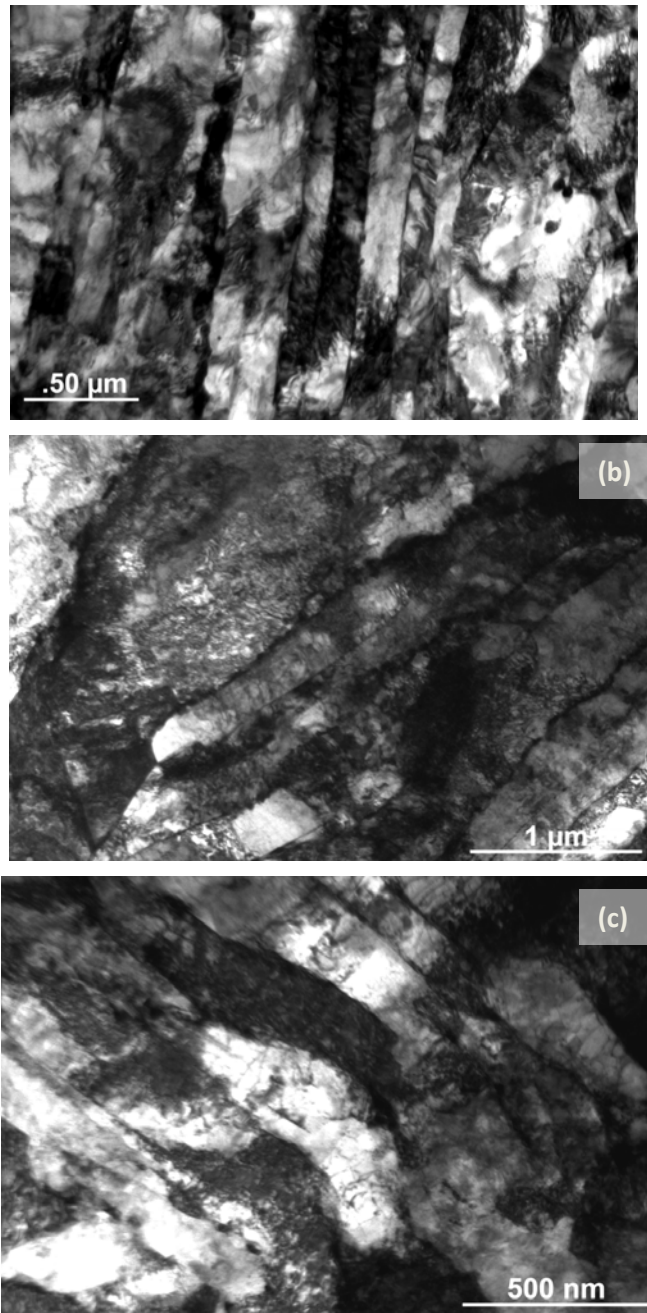


Fig. 7.4 Increasing ‘Fe’ content in the Zr-2.5%Nb alloy showing decreasing trend in (a) Steady state impression creep strain rate  $\dot{\epsilon}$  (at 400°C) in the circumferential direction, (b) In-reactor creep rate,  $\dot{\epsilon}_i$  of the pressure tubes in the axial direction (reactor operating temperature 300°C) normalised with peak fluence of the respective channel after 3340 EFPD



*Fig. 7.5(a-c) typical microstructure of the off cut samples used for the thermal creep study indicating similar distribution and features of  $\alpha_{Zr}$  and  $\beta_{Zr}$  phases*

The maximum solubility of iron in  $\alpha_{Zr}$  phase below monotectoid temperature is only 0.02wt% [20, 21], while in  $\beta_{Zr}$  it is between 0.2 wt% and 0.5wt% [20]. Hence, all the ‘Fe’ content in the dual phased Zr-2.5%Nb alloy is expected to be partitioned between  $\beta$  and  $\alpha$  phases limiting maximum up to the solubility limits at the test temperature. Thus, in the present study the

concentration levels of ‘Nb’, ‘Fe’ and ‘O’ belonged to the solute range of the alloy system and influenced the thermal creep behavior of the alloy accordingly. The effect of ‘Nb’ on the thermal creep behaviour of the samples has been considered similar for all the samples as its concentration has varied in a narrow range. Hence, the observed change in thermal creep behaviour has been mainly related to the effect of independent variation in ‘Fe’ and ‘O’ contents in the alloy. In the following, the deformation mechanisms being discussed have been mainly related to the microstructural aspects of the hexagonal close packed  $\alpha_{Zr}$  phase as it constitutes over ~90% of the volume [4, 16].

***Effect of iron content on the creep behavior of Zr-2.5%Nb pressure tube alloy***

In all the three impression creep curves presented in Fig. 7.3 (b), it was observed that, after an initial transient condition, where the creep rate  $\dot{\epsilon}$  decreased with time, a steady state was attained. This initial decrease in strain-rate is generally attributed to the formation of well-defined dislocation network, and thus a more creep-resistant substructure is developed [4, 5]. The steady state part of the creep curve (see Fig. 7.3 (b)), can be attributed to a balance between two competing processes i.e. strain hardening and recovery processes that extend over a long period of time. The deformation process leads to strain hardening effect due to increased resistance to the dislocation movements by crystal interfaces, lattice imperfections such as interstitial and substitutional atoms, precipitates, in addition to the interaction between dislocations from different slip systems of different orientations. On the other hand, the recovery processes at the given test temperature involves thermally activated annihilation of dislocations and defects and facilitate further deformation. The steady state region of the impression creep represented by the linear part of  $\epsilon$  vs  $t$  curves (Fig. 7.3 (b)) are generally correlated with the steady state creep rate  $\dot{\epsilon}_t$  of the conventional uniaxial creep test through a conversion factor  $c_2$  as expressed in eq. (6).

$$\dot{\epsilon}_t = c_2 \dot{\epsilon} = c_2 (d\epsilon/dt) \quad (6)$$

However, in the present study, since the comparison of impression creep strain rate  $\dot{\epsilon}$  was sufficient to explain the effect of iron content in the alloy on the thermal creep behaviour of the alloy, the extensive study involving evaluation of conversion factors has not been attempted. Although creep deformation under a constant stress occurs at all temperature, it only becomes important for temperatures greater than about 0.4  $T_m$  ( $T_m$  = absolute melting temperature) where

diffusion of species in the alloy become significant and contribute to the deformation process [5]. At different levels of stress and temperature, different mechanisms may operate in creep deformation [4]. The dominant deformation mechanism prevalent under the given test conditions are generally described by the deformation maps for the given alloy.

Li [4] studied thermal creep behavior of Zr-2.5%Nb pressure tube alloy under transverse stresses of 100~325MPa at 300~400°C and indicated that dislocation creep is the likely dominant mechanism at these testing conditions. In another work, Kim *et.al* [17] studied the effect of the alloying elements ‘Cu’, ‘Fe’ and ‘Nb’ on the thermal creep behavior of Zr-alloys in the temperature range between 280°C and 330°C and stress level range of 100 to 140 MPa who also referred dislocation climb and glide as the likely mechanism under the testing conditions selected. In another systematic study by Murty *et. al* [22] on Zr-1Nb-1Sn-0.2Fe alloy the authors established different regimes of deformation mechanisms depending on the stress and temperature, which has been taken as reference to identify the dominant deformation mechanism in the present study. According to Murty *et. al* [22], for test temperature 400°C and the impression stress level  $\sigma_i=400$  MPa (i.e.  $\sigma_t=114$  MPa) used in the present work would correspond to the regime of dislocation glide plus climb as the rate-controlling mechanism [17]. Further, Zr-2.5%Nb alloy samples studied is regarded as Class A alloy (i.e. solid solution alloys) as all the alloying elements, ‘Fe’, ‘O’ and ‘Nb’ are in solid solution with  $\alpha_{Zr}$  and  $\beta_{Zr}$  phases [17]. The alloying element ‘Nb’ in Zr-2.5%Nb alloy is known to increase the creep strength [17] significantly. Since the ‘Nb’ and oxygen content in the alloy samples have varied in a small range, their effect on thermal creep behavior has been considered identical in these samples. Hence, the observed change in creep behavior of these samples has been attributed to variation in ‘Fe’ content in the alloy.

As discussed before, creep behavior in these alloy samples is governed by the rate of dislocation glide, which is controlled by the rate of diffusion of solute atoms. At the test temperature of 400°C, the thermally activated movements of solute atoms can cause rearrangement in the lattice which eventually may lead to de-pinning effect on the dislocations on the active slip systems. This kind of creep mechanism is usually referred as viscous glide [17]. On the basis of these theories, it can be hypothesised that the solute atoms iron, oxygen are expected to be locked on

to (*pin down*) the dislocation glide and climb systems and thermally activated solute atom rearrangements might cause de-pinning effect which can be the rate controlling factor for the creep deformation in the present study.

Since, 'Fe' is present as interstitial solute in the  $\alpha_{Zr}$  lattice [20], the increase in overall 'Fe' content in the alloy, would increase the interstitial 'Fe' content in the  $\alpha_{Zr}$  lattice limiting to the Terminal Solid Solubility (TSS) at the test temperature of 400°C. The, increased interstitial 'Fe' is expected to provide increased resistance to dislocation movement due to pinning effect on the active slip systems in the  $\alpha_{Zr}$  lattice. In addition, the increase in 'Fe' content in the  $\beta_{Zr}$  phase (*that is present around the  $\alpha_{Zr}$  phase*) would make it stronger and hence would act as strong barrier for the movement of dislocations at the  $\alpha_{Zr}$  grain boundaries. Thus, the observed decrease in creep rate as a function of 'Fe' content (Figs. 7.3 (b) and 7.4 (a)) in the alloy can be attributed to increased solute strengthening effect on  $\alpha_{Zr}$  and  $\beta_{Zr}$  phases.

The effect of 'Fe' content on the in-reactor axial creep rates of the pressure tubes is also showing clear decrease with the increase in 'Fe' content in the alloy as seen in (Fig. 7.4 (b)). This result is similar to the observation by Holt [1]. Although the mechanism by which the irradiation creep is influenced due to 'Fe' content in the alloy is not clearly established, Holt [1] proposed that, if 'Fe' concentration is more than the solubility limit in the alloy it may result in fine 'Fe' bearing precipitates which might provide sites for recombination of vacancies and the self interstitials produced during neutron irradiation. Thus, the presence of higher amounts of 'Fe' may retard such damage rate and hence decrease the irradiation creep rate. Zou *et.al* [23] in their SIMS study on the Zr-2.5%Nb alloy material found excess 'Fe' in the  $\alpha_{Zr}$  matrix more than the TSS limit. Zou *et.al* [23] explained that, this excess of 'Fe' can be simply the property of more complex alloys formed locally, or it may be possible that 'Fe' is finely distributed in some complex state in the  $\alpha_{Zr}$  matrix. However, no such evidence of complex states or precipitates could be established by the authors Zou *et.al* [23] in their Transmission Electron Microscopy (TEM) studies. Further, Zou *et.al* [23] interpreted from the previous work on Zr-Fe systems that extended annealing of the Zr-2.5%Nb alloy material may result in a continuous reduction of residual 'Fe' by diffusion to adjacent free surfaces such as  $\alpha$ -grain boundaries and may form  $Zr_3Fe$  precipitates. These precipitates can play an important role of recombination sites and

retard the irradiation creep [1, 23]. Zou *et.al* [23] also made a reference of positron annihilation spectroscopic (PAS) measurements by Eldrup *et. al* [24], who proposed that the vacancies and self-interstitials formed during irradiation, may interact with ‘Fe’ in the bulk  $\alpha$ -lattice. This may result in formation of highly mobile ‘Fe’ and vacancy defects. The interaction of ‘Fe’ and vacancies would accelerate and control net vacancy migration in a given direction during irradiation. Thus on the basis of these theories it can be stated that ‘Fe’ in some form in the  $\alpha_{Zr}$  lattice might be playing an important role in providing increased recombination sites with the increase in ‘Fe’ content and retard the in-reactor deformation rates.

Further, if it is believed that the fine ‘Fe’ bearing precipitates are formed locally as described by Zou *et al.*[23], then the observed decrease in thermal creep rate with increase in ‘Fe’ content in the alloy can be attributed to the precipitation strengthening effect. Thus the study has indicated that increasing amounts of ‘Fe’ in the Zr-2.5%Nb alloy decrease both thermal and in-reactor creep rates.

### **7.3.2 Hot hardness tests on the Zr-2.5%Nb alloy samples with varying ‘O’ contents**

The study of effect of oxygen on thermal creep of the alloy was carried out in two steps. In the first step a number of Zr-2.5%Nb alloy samples listed in [Table-7.2 \(a\)](#) were subjected to Vicker’s micro-hardness measurements at room temperature to understand the effect of oxygen on the mechanical behavior of the alloy. In the next step, three of these samples with oxygen content variation covering entire range as listed in [Table-7.2 \(b\)](#) were subjected to time dependent constant load hardness tests at two test temperatures, namely 300°C and 400°C using the Vicker’s hot hardness measuring equipment. The [Table-7.2 \(b\)](#) also provides the texture and dislocation density determined using X-ray diffraction method. It is seen from this table that the texture has varied in a small range while the dislocation density had a small sample to sample variation with a standard deviation  $1.15 \times 10^{16}$  at a mean value of  $7.91 \times 10^{16}$ . This indicates that these parameters had similar influence on the thermal creep behaviour and hence the observed trend in the results has been discussed in relation to the effect of variation in ‘O’ content in the alloy. [Fig. 7.6](#) shows the room temperature VHN as a function of oxygen content for the alloy samples listed in [Table-7.2 \(a\)](#).

*Table-7.2 (a): Zr-2.5%Nb pressure tube samples with oxygen variation and the room temperature hardness values by Vicker's*

Sample ID	'O' ppmw (Std. Dev. of 'O' measurement $6 \times 10^{-4}$ ppmw)	Vicker's Hardness (VHN) $\text{kgf/mm}^2$ at room temperature (Average of 3 measurements)
1*	1587	264
2	1288	262
3	980	253
4	974	242
5*	929	240
6	893	241
7*	743	235
* Samples chosen for the indentation creep studies		

The result shows a clear increase in Vicker's Hardness number hardness (VHN) with the increase in oxygen content in the alloy. Fig. 7.7 (a) and (b) show the time dependent micro-hardness data for the test temperatures, 300°C and 400°C, respectively, plotted as  $\ln(H)$  vs.  $\ln(t)$  along with the linear fits for the three samples Table-7.2 (b). The  $\ln(H)$  vs.  $\ln(t)$  linear plots showed different intercept values (*intrinsic hardness*) on the  $\ln(H)$  axis at both the test temperature 300°C and 400°C which were proportional to the oxygen content in the alloy samples. This indicated a clear strengthening effect of 'O' content on the mechanical behaviour of the alloy. Therefore, it was observed that, the sample with 1587 ppmw of oxygen exhibited higher hardness values at both the test temperatures 300°C and 400°C and at all the dwell times studied, compared to the samples containing 929 of oxygen under the same test conditions. Similarly, the  $\ln(H)$  vs.  $\ln(t)$  data for the sample containing 929 ppmw at both test temperatures were placed higher compared to the same data for the sample containing 743 ppmw (Fig. 7.7 (a) and (b)). The slopes of the linear fits at 300°C for all the samples were nearly same indicating that the dominant deformation mechanisms are same. Similarly, slopes of the linear fits at 400°C were also nearly same for all the samples, but were relatively higher compared to 300°C data as seen in  $\ln(H)$  vs.  $\ln(t)$  plots in Fig. 7.7 (a), (b) and Fig.7.8 (a-c).

In general the hardness can be related to the physical and mechanical properties of the materials such as thermal conductivity, electrical resistivity, yield and ultimate tensile strengths, fatigue strength, creep, and rupture properties [25]. At an elevated temperature, as the indenter sinks into the test piece with increasing dwell time, the size of the indentation would increase (*i.e decrease*

in hardness with dwell time) which is regarded as the measure of creep [8, 12, 25-32]. From, the Mulheran and Tabor [33] relationship that relates the hardness, temperature and dwell time of the indenter, if the test temperature  $T$  is maintained constant, the  $\ln(H)$  vs.  $\ln(t)$  results in a linear fit and the slope of the fit is related to  $(n+0.5)$ . Generally, the  $\ln(H)$  vs.  $\ln(t)$  linear fits in a given temperature range may remain parallel if the mechanisms of deformation remains unchanged. Conversely, at a given test temperature, the alloy samples with varying composition, can also result in different linear fits depicting the effect of alloying elements on the hot hardness behavior. Because, the hot hardness is also a sensitive method of identifying the change in mechanical behavior of a material due to alloying addition [12, 25, 31, 34, 35]. In the present study this particular approach has been adopted for the analysis of  $\ln(H)$  vs.  $\ln(t)$  linear fits as a function of oxygen content in the samples.

#### ***Effect of oxygen on room temperature hardness***

The increase in VHN values with the increase in oxygen content in the alloy as seen in Fig. 7.6 is similar to the previously reported results by Kelly *et al.* [36]. The authors work showed that the VHN values at room temperature varied linearly over a wide range of oxygen concentration from 350 to 5000 ppmw. The oxygen levels studied in the present work and that by Kelly *et al.* [36] correspond to the solute range, as the solid solubility limit of oxygen in  $\alpha_{Zr}$  is much higher (~6.75%) [1, 18]. Oxygen is less associated with the  $\beta_{Zr}$  phase and is mainly concentrated in the  $\alpha_{Zr}$  phase in the octahedral interstitials [1, 36-38]. Being a dominant phase, the observed effect of oxygen on the mechanical behavior of the Zr-2.5%Nb alloy is mainly related to the mechanical response of the  $\alpha_{Zr}$  phase. These octahedral sites are spherically symmetric when the axial ratio is ideally of 1.633 [38]. Although in  $\alpha_{Zr}$ , the  $c/a$  ratio (1.593) being less than ideal value [5, 6, 16, 39, 40], the stress field induced by the presence of oxygen in the  $\alpha_{Zr}$  lattice is spherically symmetric in a crude approximation. The increase of oxygen in the lattice does not alter this situation considerably, since  $c/a$  remains almost constant even with increasing alloying additions [38]. According to Dasgupta *et al.* [38], in spite of almost symmetrical distortion in the  $\alpha_{Zr}$  lattice due to insertion of oxygen, the volume change produced in the lattice must be interacting strongly with the stress field of dislocations. This expected phenomenon was considered to be responsible for high value of activation energy (as oxygen concentration increased) as observed

by Dasgupta *et.al* [38]. Therefore, it is likely that, the oxygen in the  $\alpha_{Zr}$  lattice would pin the dislocations strongly [38] and result in increase in hardness with increase in oxygen content at all test temperatures studied. Thus, it can be concluded that the observed increase in hardness of Zr-2.5%Nb alloy at room temperature with the increase in oxygen content can be attributed to increased solute hardening effect.

According to the another model proposed by Kelly *et.al*, [36] a single oxygen occupying the octahedral site in  $\alpha_{Zr}$  lattice would produce symmetric distortion, as a consequence, there is no first order reaction between solitary interstitial oxygen and the screw dislocations. Therefore, the single oxygen in the  $\alpha_{Zr}$  lattice cannot explain the observed hardening behavior of the alloy in the study by Kelly *et.al* [36]. However, according to the mechanism proposed by Kelly *et.al*, the interstitial pair is assumed to be formed with a probability that oxygen ions occupy adjacent sites in the  $\alpha_{Zr}$  lattice. This theory is based on the fact that, the pair of interstitials can produce an asymmetric or “tetragonal” distortion in the  $\alpha_{Zr}$  lattice [36] and the strength of the alloy is linearly related on the square root of the interstitial concentration (i.e. oxygen concentration). Thus, in the present study the interstitial pair theory can also explain the observed hardening as a function of oxygen concentration, through its asymmetric distortion in  $\alpha_{Zr}$  lattice [36].

#### ***Effect of oxygen on time dependent hot hardness***

Although creep deformation under a constant stress occurs at all temperature, it only becomes important for temperatures greater than about  $0.4 T_m$  ( $T_m =$  *melting temperature of the test material on absolute scale*) where diffusion of atoms in the alloy becomes significant and contributes to the deformation process [5]. The test temperatures 300 and 400°C selected for the study correspond to the homologous temperature of  $<0.36 = T/T_m$ , where T is the test temperature on absolute scale. Dasgupta *et.al* [38] proposed that, increasing the temperature, it is possible that, dislocations get unpinned from some pinning centers through thermal activation alone and can overcome the energy barrier at much lower stresses [38]. On the other hand, increase in oxygen content in the alloy, would increase the pinning centers on more lattice points of  $\alpha_{Zr}$  phase. It can therefore be argued based on Dasgupta *et.al* [38] findings the sample containing 1587 ppmw of ‘O’ is expected to have relatively higher number of lattice points (*in  $\alpha$ -Zr lattice*)

at which pinning effect would occur as compared with the sample containing 929 ppmw of ‘O’ at both test temperatures.

*Table-7.2 (b): Description and microstructures of Zr-2.5% Nb pressure tube samples with ‘O’ content variation used for thermal creep study by indentation creep test method.*

Sample ID	‘O’ ppmw Std. deviation: $6 \times 10^{-4}$ ppmw)	Vicker’s Hardness Number $kgf/mm^2$ at room temperature (Average of 3 measurements)	$f_t$	$f_r$	$f_a$	Dislocation density ( $m^{-2}$ ) determined from X-ray line profile analysis	
						Plane: $[11\bar{2}0]$	Std. Devi.
*1	1587	264	0.50	0.34	0.11	$7.91 \times 10^{16}$	$1.15 \times 10^{16}$
*5	929	240	0.51	0.37	0.10		
*7	743	235	0.53	0.36	0.09		

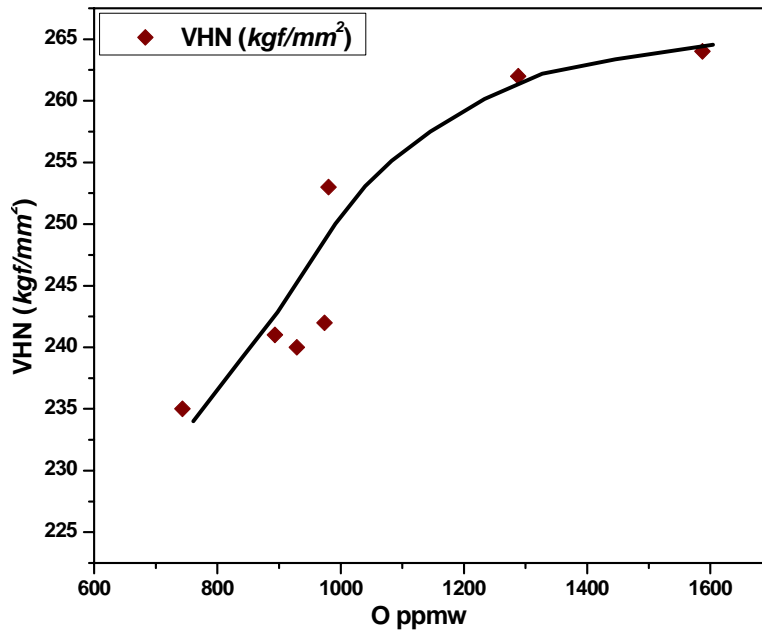


*Fig. 7.6 Room temperature Vicker’s Hardness of Zr-2.5%Nb alloy samples showing increasing trend with oxygen content in the range 743 to 1587 ppmw*

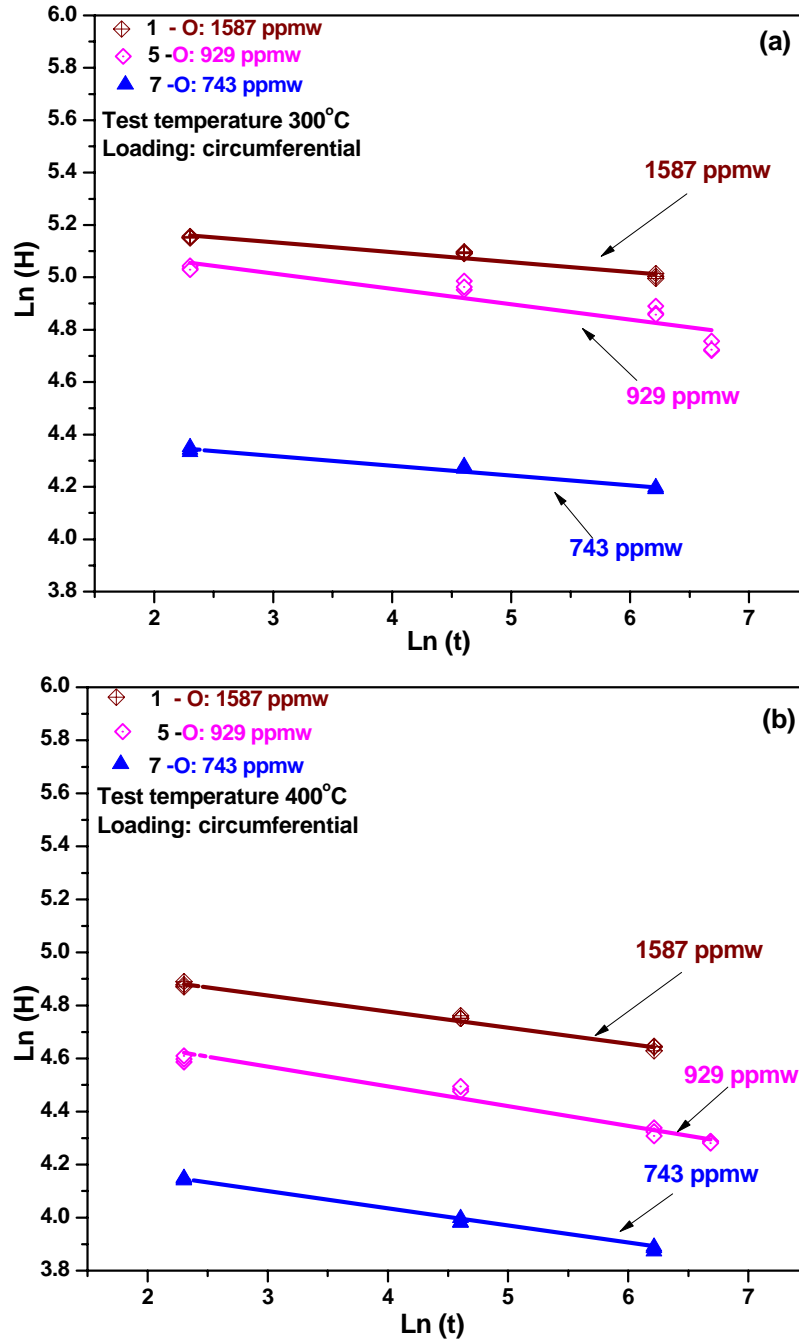


Fig. 7.7  $\ln(H)$  vs.  $\ln(t)$  showing decrease in hardness with dwell time for all the three Zr-2.5%Nb alloy samples at the test temperature (a) 300°C, (b) 400°C

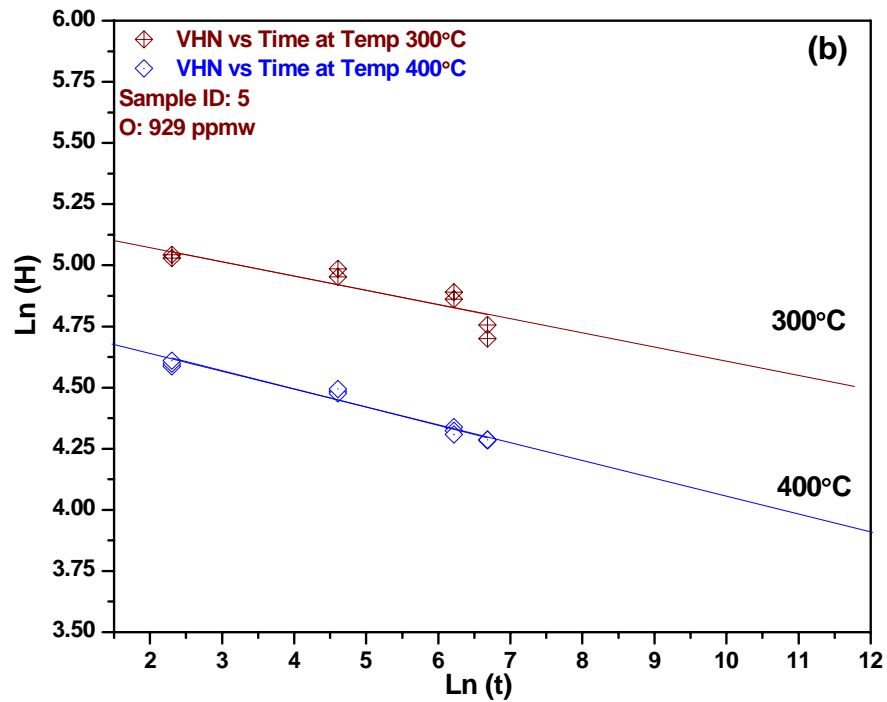
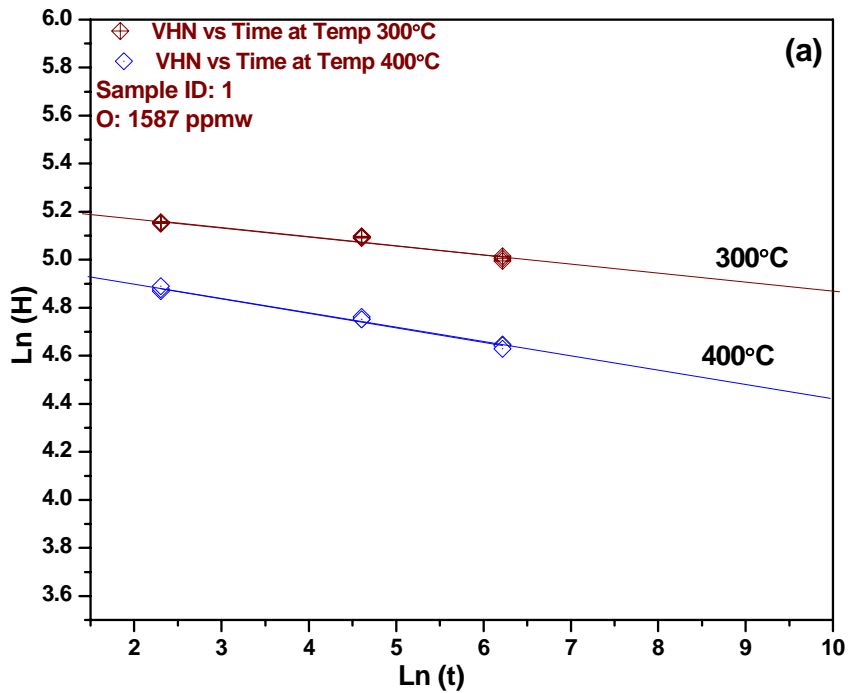


Fig. 7.8  $\ln(H)$  vs.  $\ln(t)$  plot showing decrease in hardness with time at the test temperatures 300°C and 400°C for the Zr-2.5%Nb alloy sample containing (a) 1587 ppmw of oxygen and (b) 929 ppmw of oxygen.

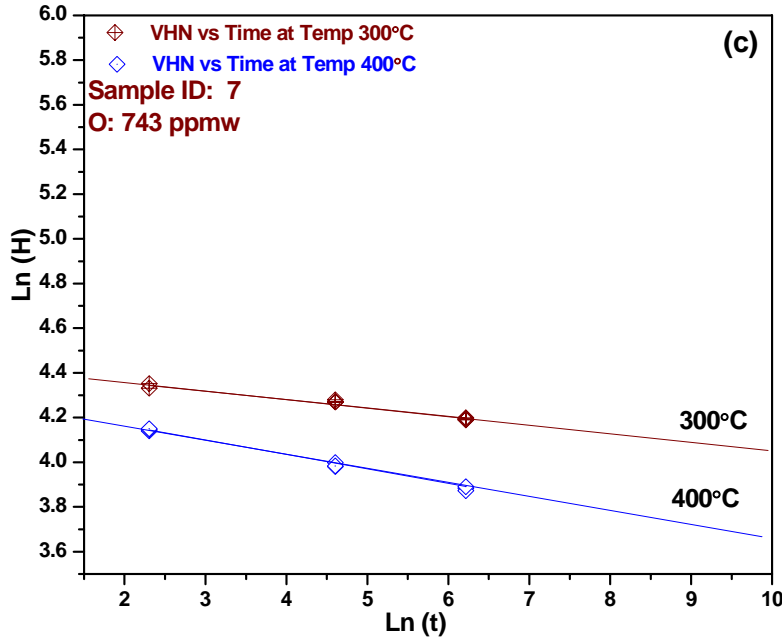
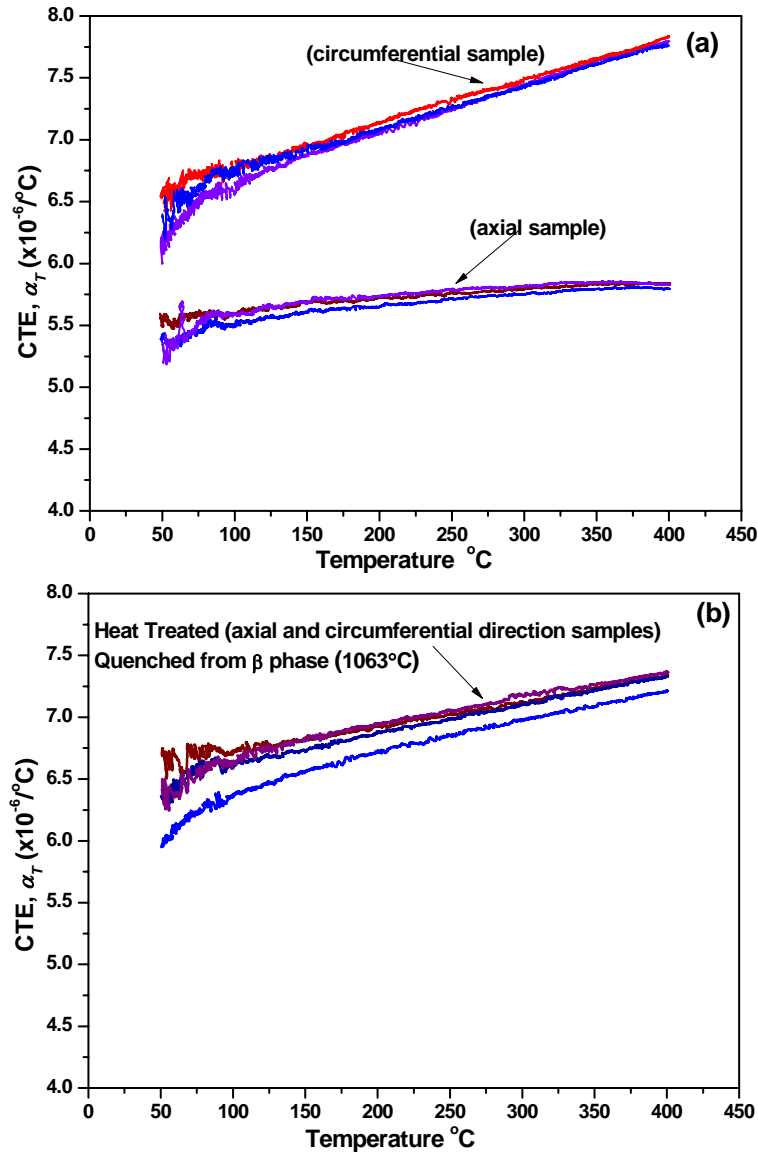


Fig. 7.8  $\ln(H)$  vs.  $\ln(t)$  plot showing decrease in hardness with time at the test temperatures 300°C and 400°C for the Zr-2.5%Nb alloy sample containing (c) 743 ppmw of oxygen

Increased pinning centers would increase the resistance to the dislocation movements resulting in higher strength and hardness in general. Therefore, at the test temperatures 300 and 400°C, the sample with 1587 ppmw of ‘O’ has exhibited higher hardness at all the dwell times studied compared to the sample containing 929 ppmw of ‘O’. Exactly the same analogy can be applied to explain the observed higher hardness values for the sample containing 929 ppmw ‘O’ compared to the one containing 743 ppmw of ‘O’. The results in Fig.7.7 (a) and (b) also show that, slope of  $\ln(H)$  vs  $\ln(t)$  is relatively lower for the test at 300°C compared to the slope at 400°C test for the given sample. Figs. 7.8 (a-c) also show this observation for each of the samples studied. This relative small increase in slope (-ve) indicates that the material is becoming relatively softer at 400°C. This can be attributed to the increased thermally activated recovery processes at 400°C compared to the condition at 300°C, which might be leading to increased annihilation of dislocations from the pinning centers in the  $\alpha_{Zr}$  lattice [38]. Thus, the hot hardness study has shown that oxygen plays an important role in improving creep resistance through solute strengthening effect. The strong interaction of distortion in  $\alpha_{Zr}$  lattice due to insertion of oxygen with the stress field of the dislocations at all test temperatures is responsible for such solute strengthening effect. The in-reactor axial creep rates for the operating pressure

tubes corresponding to these samples exhibited marginal variation at the mean value of  $1.485 \times 10^{-11}/s$  with a standard deviation of  $4.08 \times 10^{-12}/s$ . This result indicates that, ‘O’ content variation within the specification range has lesser role in influencing the irradiation creep behaviour of the pressure tube alloy unlike the case of effect of ‘Fe’ variation, where decrease in irradiation creep rates were quite significant (see Fig. 7.4).

#### 7.4 Effect of ‘Fe’ and ‘O’ on CTE and texture of Zr-2.5%Nb pressure tube alloy



*Fig.7.9 Typical experimental CTE curves (up to 400 $^{\circ}C$ ) for the axial and circumferential directions of Zr-2.5%Nb pressure tube samples (a) as fabricated showing large difference slopes indicating texture effects, (b) heat treated ( $\beta$ -quenched from 1063 $^{\circ}C$ ) showing similar slopes indicating similar texture*

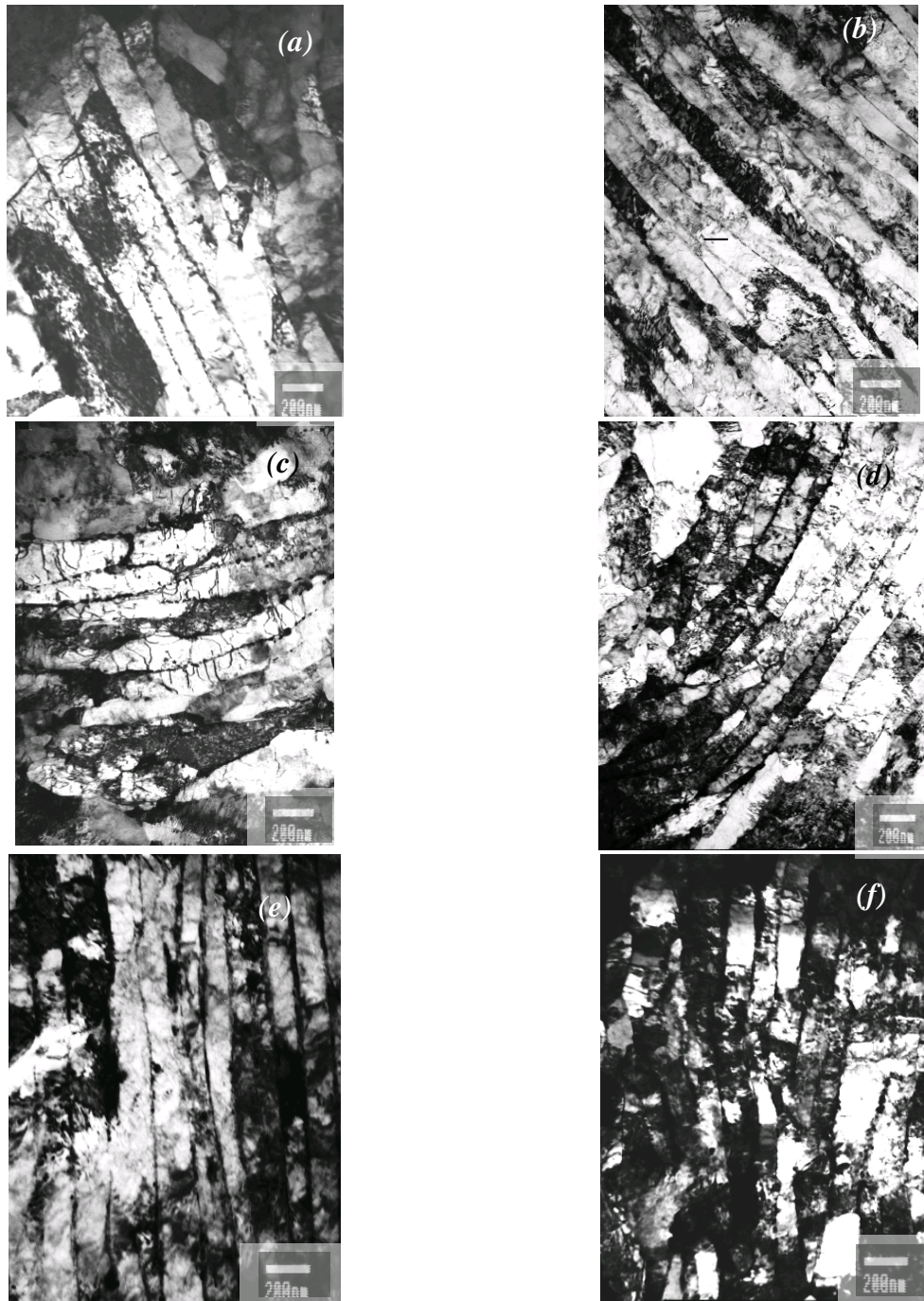
The as-fabricated Zr-2.5%Nb alloy pressure tube is anisotropic in nature, which is largely attributed to the pronounced preferred orientation of  $\alpha_{Zr}$  phase resulting from manufacturing schedules [1, 16, 39- 43]. As a result, not only mechanical properties such as yield strength (YS), ultimate tensile strength (UTS) and ductility are anisotropic, the physical properties such as CTE, thermal conductivity, electrical resistivity and elastic moduli are also anisotropic [44, 45]. It has been observed that the strong (0002) transverse texture of typical PHWR pressure tube results in good transverse tensile strength and low circumferential strain due to irradiation creep [4, 46] during the service. However, such texture has been observed to exhibit higher axial elongation rates [4, 46]. Thus, texture is one of the controlling factors for the in-reactor deformation behavior of the Zr-2.5%Nb pressure tube alloy. The texture parameter and CTE in a given principal direction of an anisotropic component is expected to correlate [47]. Further, the alloying additions can also influence the CTE of the alloy. Hence, it was of interest to study the inter-correlation of CTE, texture parameters, the in-reactor deformation rates and the iron and oxygen contents in the pressure tube alloy. The literature review indicated that, no such detailed interrelation study has been reported in the open literature, which was the main motive in initiation of this work.

Thus the, objective of this part of the work was to study the effect of independent variation in ‘Fe’ and ‘O’ contents (*within the specification range*) on the CTE and texture parameters of the as fabricated Zr-2.5%Nb pressure tube samples and also correlate with the in-reactor axial deformation rates. The inter-correlation study presented in this section can provide inputs for predicting and modeling the alloy behavior under irradiation.

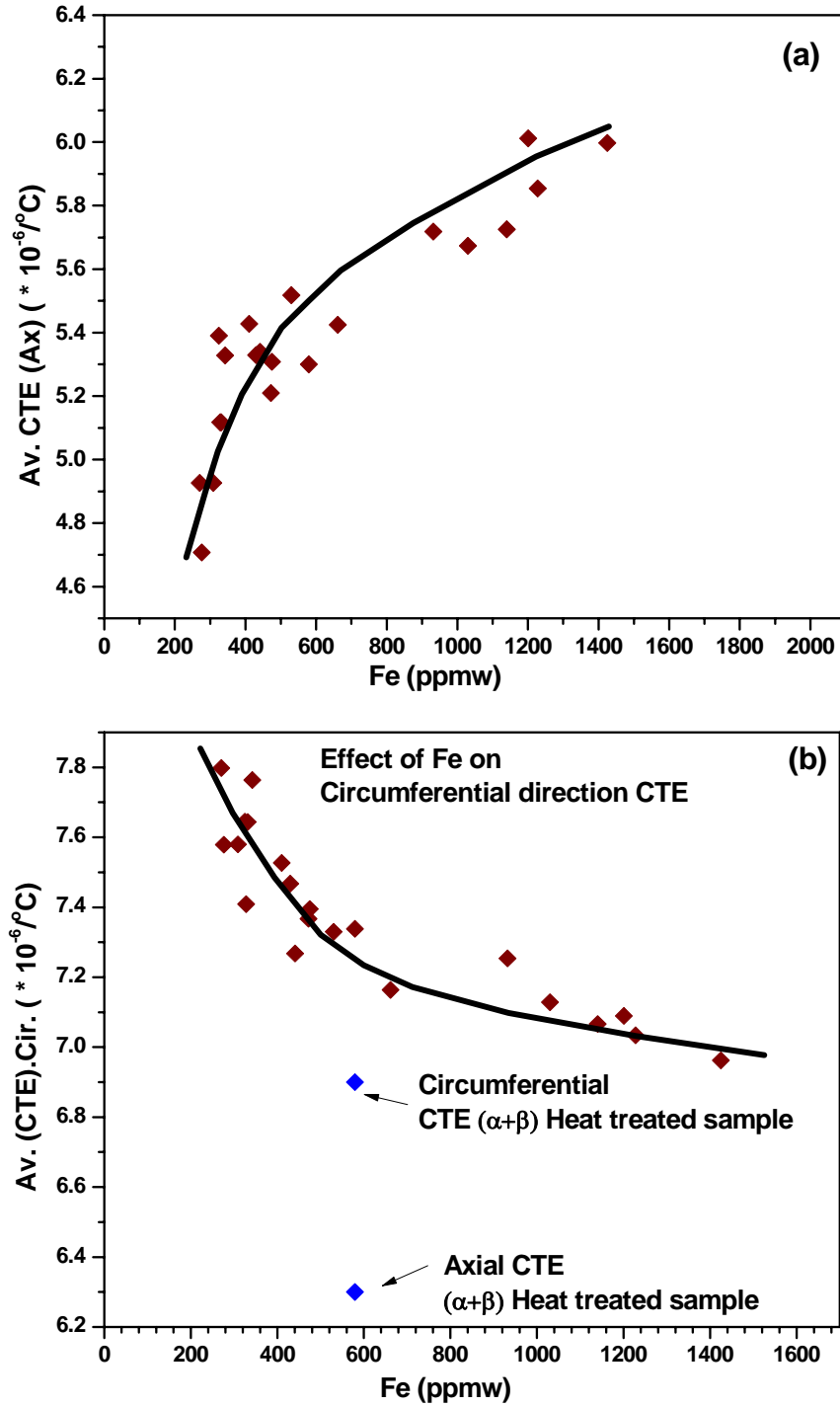
#### **7.4.1 CTE, texture measurements and microstructural examination**

Fig. 7.9 (a) shows typical CTE curves for the axial and circumferential directions for one of the off cut samples studied. The circumferential CTE curves show higher values and also higher slope compared to the axial direction CTE curves. Similarly, Fig. 7.9 (b) shows the CTE curves for the axial and circumferential direction of the Zr-2.5%Nb pressure tube sample subjected to  $\beta$ -quenching from 1063°C. The average CTE between 100 and 400°C has been determined as per ASTM E228 [48] and has been used as representative value (see subsection 3.1.8).

## Microstructures



*Fig. 7.10 (a-f) Typical microstructure of the off cut samples used for the thermal expansion studies indicating similar distribution and features of the  $\alpha_{Zr}$  and  $\beta_{Zr}$  phases*



*Fig. 7.11* Effect of increasing 'Fe' content in Zr-2.5%Nb alloy showing (a) increasing trend in axial direction CTE, (b) decreasing trend in circumferential direction CTE. This plot also shows nearly similar values of CTE for both axial and circumferential directions for a sample containing 579 ppmw of 'Fe' after heat treatment at 880°C in the ( $\alpha+\beta$ ) phase field followed by quenching at ~150°C/s.

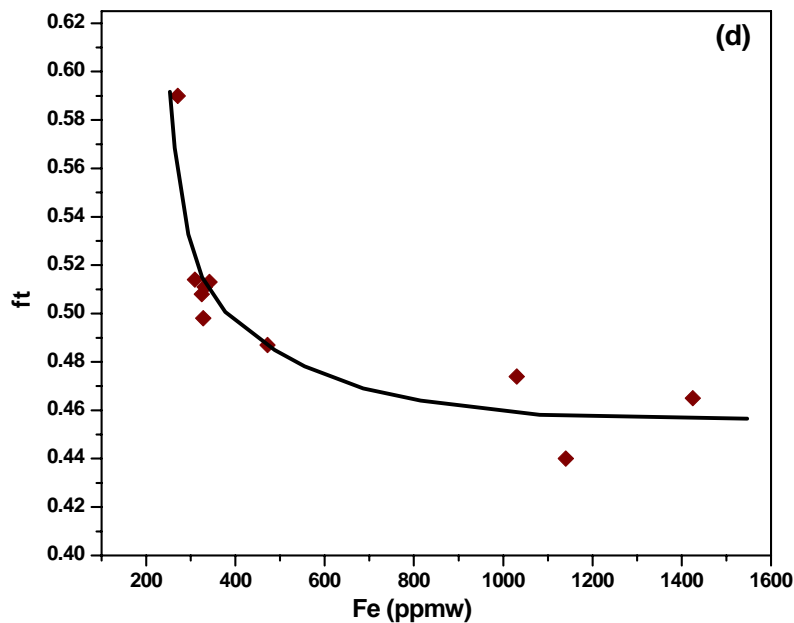
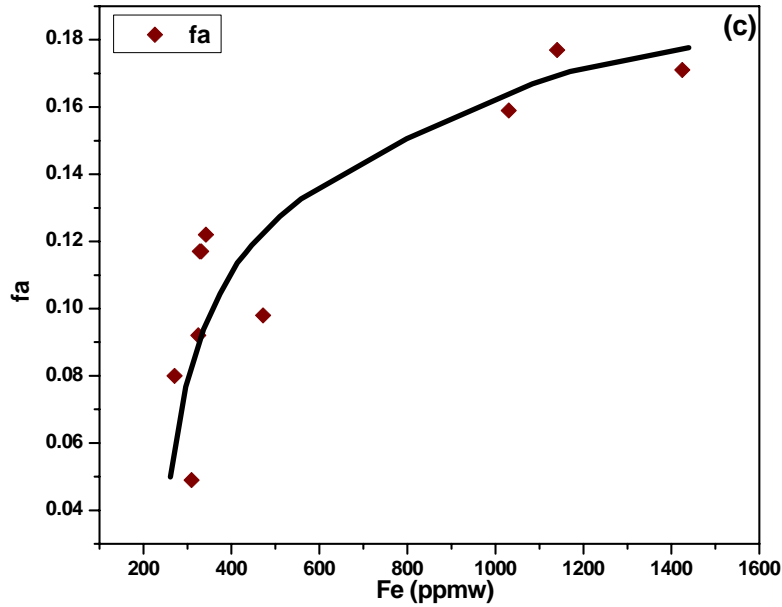


*Fig. 7.11(c) Correlation of axial texture parameter ( $f_a$ ) with 'Fe' content of as fabricated Zr-2.5%Nb pressure tube samples, (d) Correlation of circumferential texture parameter ( $f_i$ ) with 'Fe' content of as fabricated Zr-2.5%Nb pressure tube samples*

Fig.7.10 (a-f) show TEM micrographs of microstructures of some of the Zr-2.5%Nb alloy off cut samples used in this study. These micrographs show similar microstructural features such as distribution and morphologies of the  $\alpha_{Zr}$  and  $\beta_{Zr}$  phases. Therefore it can be assumed that small variations in Fe and O contents have not lead to significant change in microstructure.

### CTE and texture measurements

Fig.7.11 (a) and (b) show the average CTE values for axial and circumferential directions as a function of ‘Fe’ content in the pressure tube samples. The axial CTE values exhibited increasing trend (Fig. 7.11 (a)) while circumferential CTE exhibited decreasing trend (Fig. 7.11 (b)) with the increase in ‘Fe’ content in the alloy. The plot 7.11 (b) also shows the average values of axial and circumferential CTE for the samples heat treated at 880°C in the ( $\alpha+\beta$ ) phase field and quenched at  $\sim 150^\circ\text{C/s}$  which were  $6.3$  and  $6.9 \times 10^{-6}/^\circ\text{C}$  respectively. This result also shows a clear effect of heat treatment on the CTE which can be attributed to the modification in the texture and microstructure. Similarly, Figs. 7.11 (c) and (d) show the measured texture parameters  $f_a$  and  $f_t$  values for few of the selected samples (texture data taken from the internal reference [49]), as a function of ‘Fe’ content which were also studied for CTE.

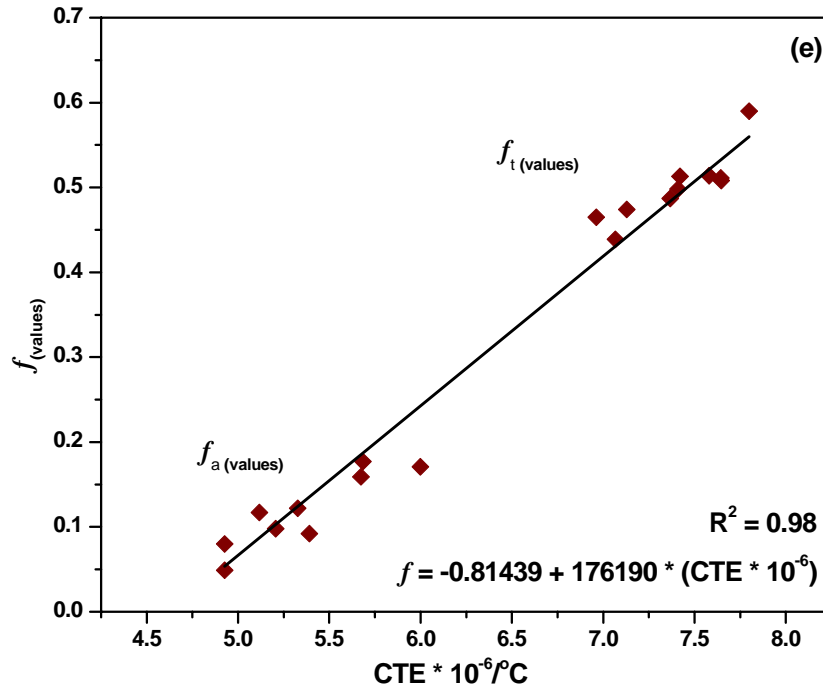


Fig. 7.11 (e) Correlation of texture parameters  $f_a$  and  $f_t$  values with CTE values in the corresponding direction (Fe-variation set of samples)

The  $f_a$  values in Fig. 7.11 (c) and  $f_t$  values in Fig. 7.11 (d) also exhibited increasing and decreasing trends respectively with the increase in ‘Fe’ content in the alloy similar to the trends exhibited by axial and circumferential CTE in Figs. 6 (a) and (b) respectively. A good linear relationship has also been observed between texture parameters ( $f_{values}$ ) and corresponding CTE

as seen in Fig. 7.11 (e). This result is similar to the one reported by Kearns [47] for  $\alpha_{Zr}$  phase of the Zircalloy-4. In this part of the study the axial and circumferential CTE values had standard deviations of  $0.08/^{\circ}\text{C}$  and  $0.26/^{\circ}\text{C}$  respectively, whereas texture parameter measurements had a standard deviation of 0.02. Unlike the effect of 'Fe' content variation on the CTE and texture parameters of the alloy, the variation in oxygen content in the alloy did not show any definite correlation with either CTE or with texture parameters as seen in Fig.7.12 (a-c).

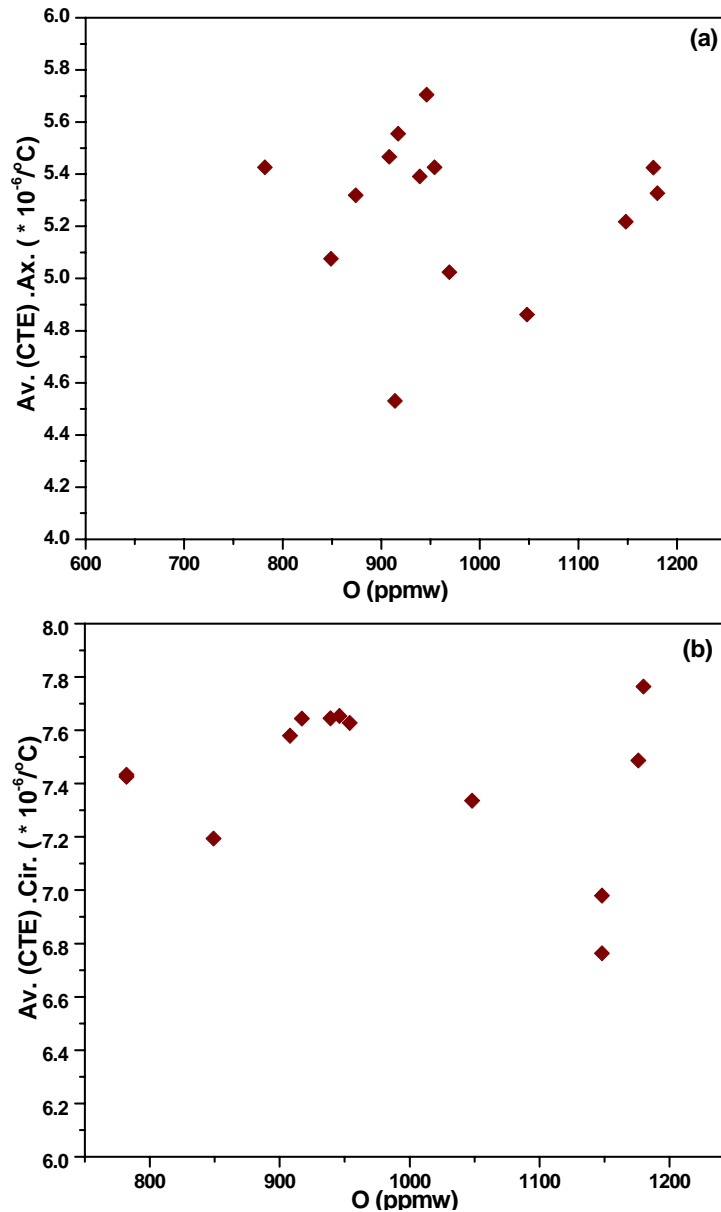


Fig. 7.12 (a) Effect of oxygen on CTE of as fabricated Zr-2.5%Nb pressure tube samples for the (a) axial direction (b) for the circumferential direction

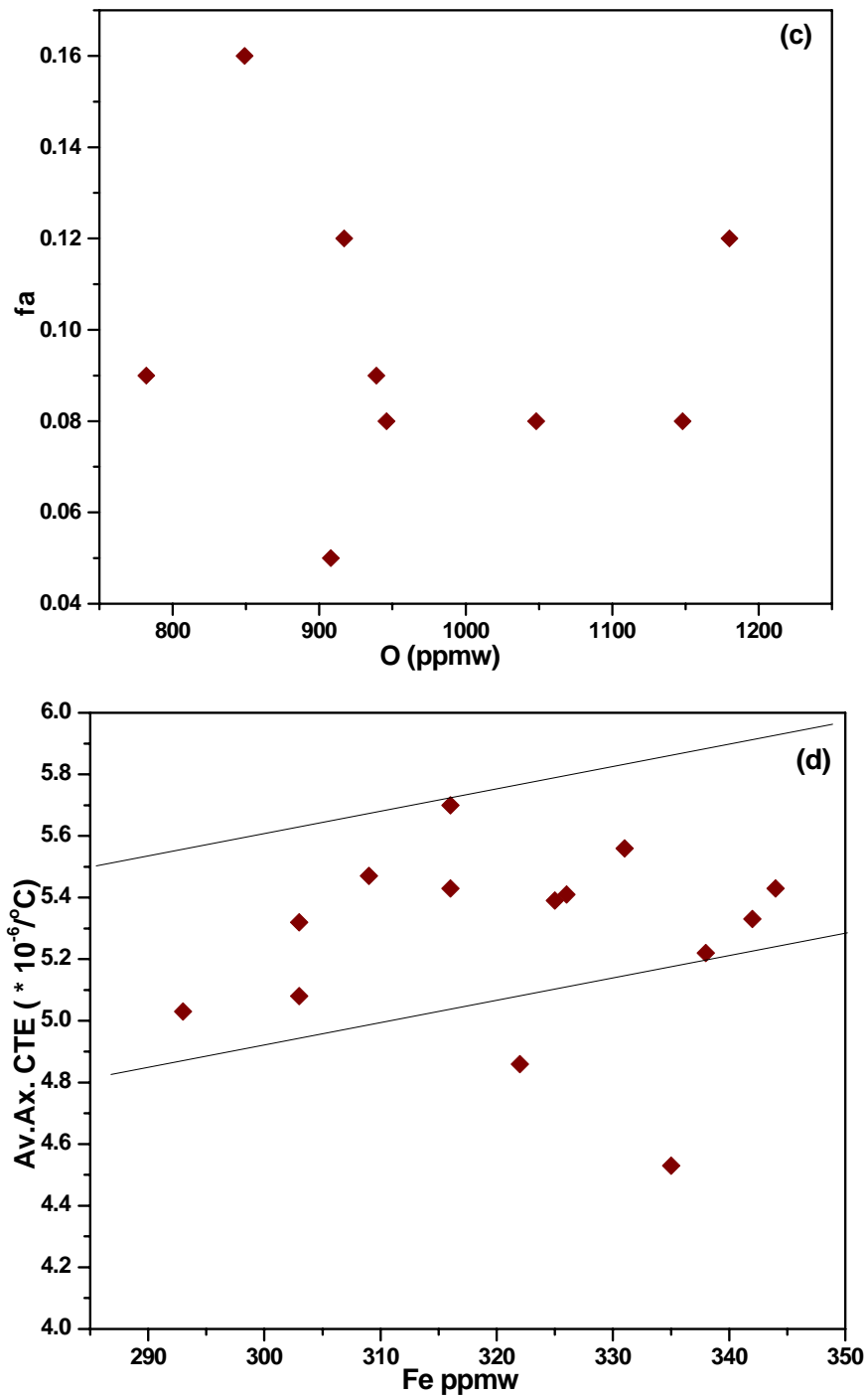
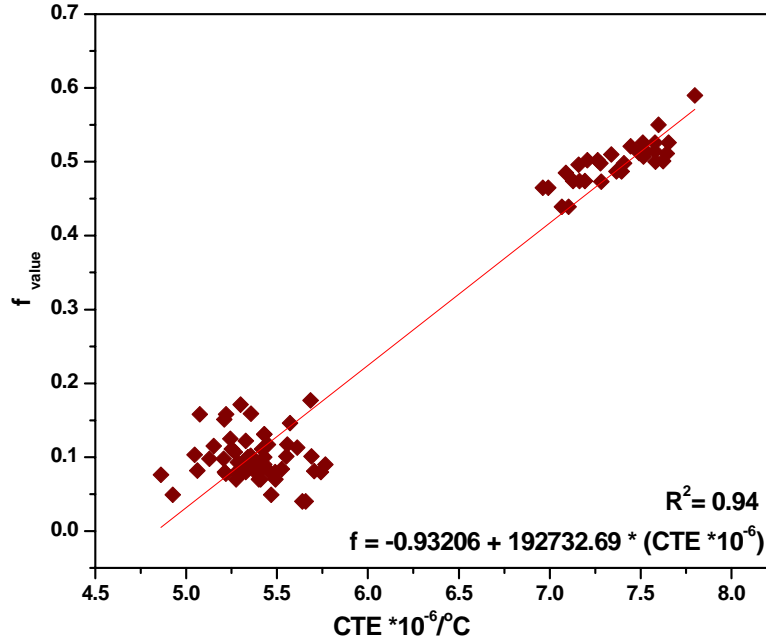


Fig. 7.12 (c) Correlation of texture parameter ( $f_a$ ) [49] with oxygen content showing scatter, (d) Effect of small variation of 'Fe' content on the axial CTE of oxygen variation samples



*Fig.13 Correlation of  $f_{\text{values}}$  with CTE for the (randomly selected samples) showing linear linear fit*

To understand the possible reasons for such scatter in the results, the axial CTE data for these samples were plotted against their corresponding ‘Fe’ content, although it varied in a small range of  $322 \text{ ppmw} \pm 16 \text{ ppmw}$  as seen in Fig. 7.12 (d). The plot showed a weaker but relatively better correlation with ‘Fe’ content as compared to the effect of oxygen content variation seen in Fig. 7.12 (a-b). Fig. 7.13 shows the correlation of CTE vs. texture parameters ( $f_{\text{values}}$ ) measured for a number of randomly selected samples (*texture data taken from the internal reference [49]*). A regression analysis of the data points in Fig. 7.13 provided a linear fit with a regression coefficient of  $R^2=0.94$  indicating a good correlation between these two parameters.

The CTE is described as thermo-elastic property that shows response of the material geometry when the temperature is changed and hence is an important physical property of the solids in design and engineering. From the view point of material science, it is fundamental. Therefore it is worth studying its relation with the microstructure and texture of anisotropic solid materials [50] like the Zr-2.5%Nb pressure tube alloy. The thermal expansion of a solid is a property arising strictly due to the anharmonicity of the lattice vibration [45, 51]. As an example, with the increasing temperature, the lattice constant ‘ $a$ ’ of crystalline material usually increases (*provided*

no phase transformation occurs), because the lattice separation becomes wider, producing a positive thermal expansion in most materials (see Fig.7.14).

At the crystalline level, the linear thermal expansion coefficient of a solid material is defined as  $\alpha_T = (\Delta a/a_0) / \Delta T$ , where ‘ $a_0$ ’ is the lattice parameter at 293K and  $\Delta a$  is the change in lattice parameter due to change in temperature  $\Delta T$  of the solid [52]. In the case of anisotropic materials like ‘Zr’, ‘Ti’, ‘Mg’, ‘Cd’ etc the ‘ $\alpha_T$ ’ is strongly dependent on crystallographic directions, where the intratomic separations (i.e. lattice parameters) and hence anharmonicity of vibration are different with rising temperature. It is well known fact that in the Zr-2.5%Nb pressure tube alloy, the dominant  $\alpha_{Zr}$  (hcp) phase is crystallographically anisotropic with lattice parameters  $a=0.323$  nm and  $c=0.515$  nm [53]. Therefore, CTE in the ‘ $a$ ’ and ‘ $c$ ’ directions of the  $\alpha_{Zr}$  lattice must be considerably different attributing to large difference in lattice separation in these two directions [47, 53, 54]. Tomé *et.al* [55] has reported the CTE in the ‘ $a$ ’ and ‘ $c$ ’ directions of the  $\alpha_{Zr}$  lattice as  $\alpha_a=5.8 \times 10^{-6}/^\circ\text{C}$  and  $\alpha_c=10.3 \times 10^{-6}/^\circ\text{C}$  respectively. This implies that, if the concentration of basal pole orientations (i.e. (0002) texture) of the  $\alpha_{Zr}$  crystallites varies in a given direction in different pressure tube samples, the CTE for these samples in that direction must also reflect the corresponding change.

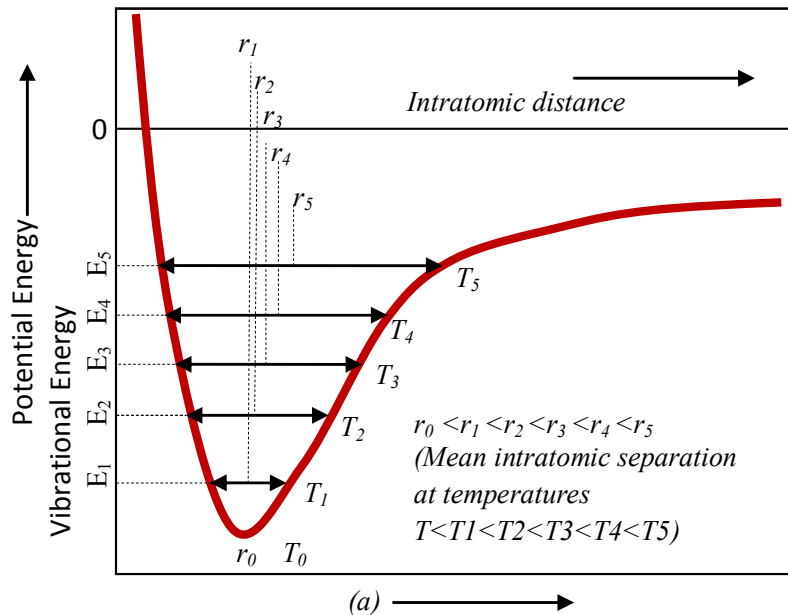


Fig. 7.14 A conceptual plot of potential energy versus intratomic distance, demonstrating the anharmonic increases in intratomic separation with rising temperature.

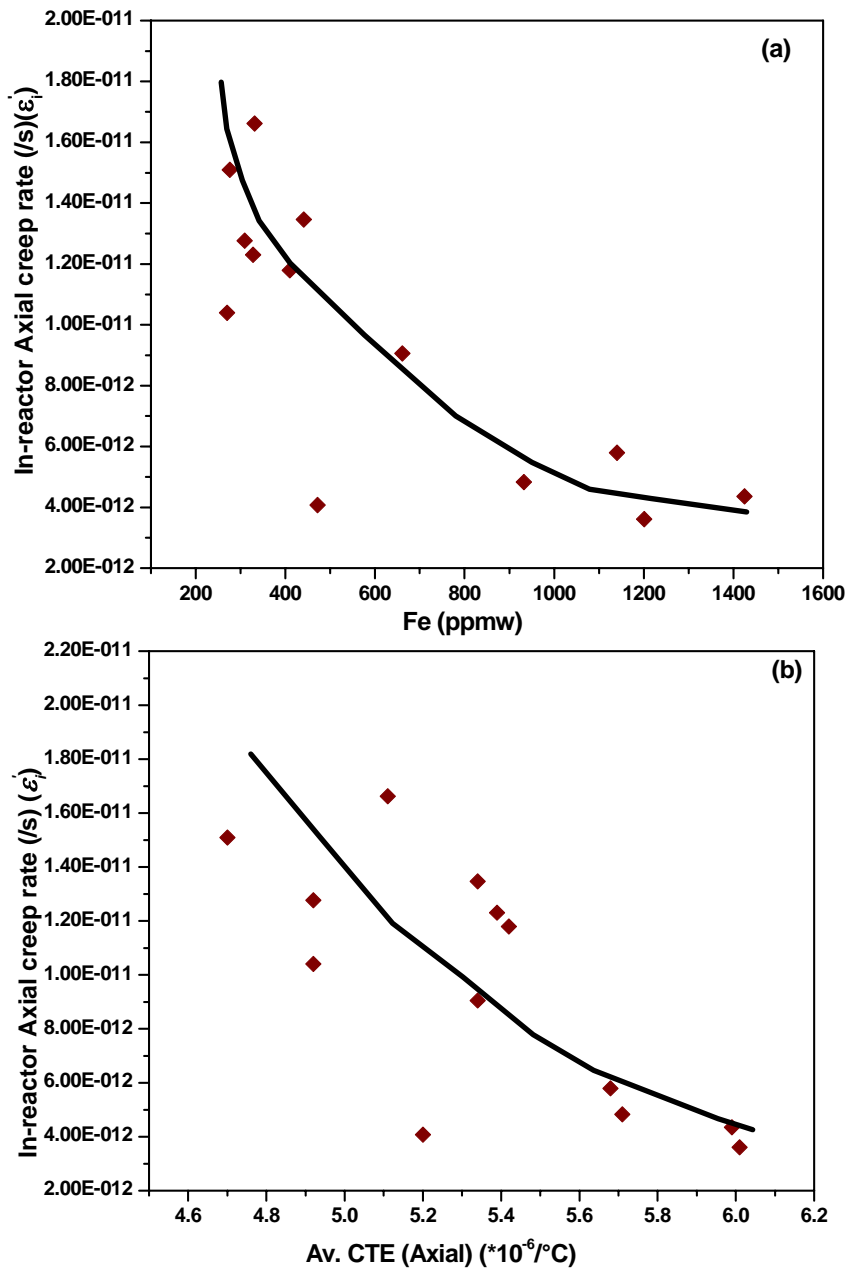
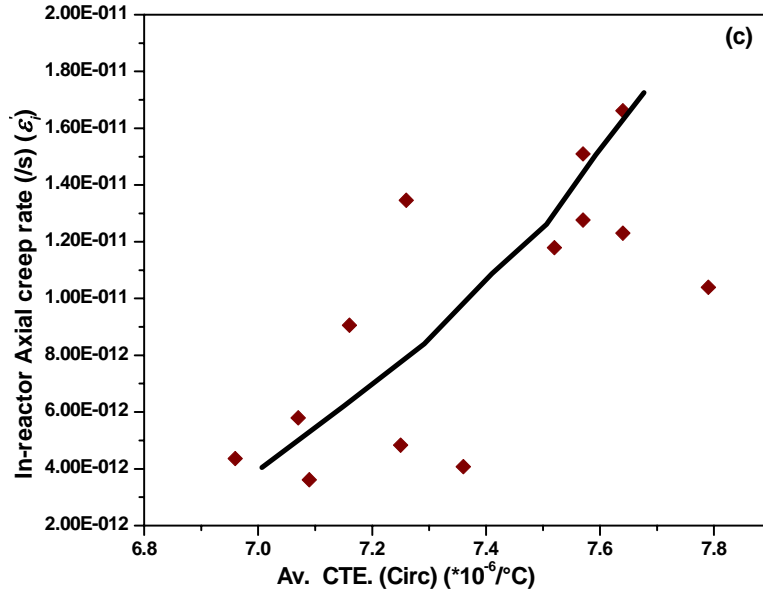


Fig. 7.15 Correlation of axial direction irradiation creep rate ( $\dot{\epsilon}_i$ ) of Zr-2.5%Nb pressure tubes with their (a) 'Fe' content, (b) axial direction CTE ('Fe' variation samples), Note: ( $\dot{\epsilon}_i$ ) data presented in the study has been normalised with channel peak fluence after 3340 EFPD



*Fig. 7.15(c) Correlation of ( $\dot{\epsilon}_i$ ) with circumferential CTE ('Fe' variation samples)*

Conversely, the linear thermal expansion coefficient ' $\alpha_T$ ' i.e CTE measured in some direction of the component is often used as a criterion for information on the degree of preferred orientation of a phase in the material [56]. The typical axial and circumferential CTE results presented in Fig. 7.9 (a) clearly show the effect of such preferred orientation with strong transverse texture which generally exists in the as fabricated (*cold worked route*) Zr-2.5%Nb alloy pressure tubes. The higher CTE and higher slope of circumferential CTE vs. Temperature curves can be attributed to the higher concentration of basal pole orientations (*(0002) texture*) in the circumferential direction of the pressure tube. In contrast, the negligible slope of CTE vs. Temperature curves observed in the axial direction clearly indicates much less concentration of basal poles in that direction which is generally the case with as-fabricated pressure tubes. On the other hand it can be seen in Fig.7.9 (b) that the slopes of the CTE curves for the axial and circumferential directions of the ( $\alpha+\beta$ ) heat treated samples are similar. This result shows a clear effect of heat treatment and observed similar CTE behavior can be attributed to the microstructural and textural changes. This result also indicated that CTE is sensitive to the microstructural changes produced due to heat treatments. Nevertheless, the results in Fig.7.9 (a), (b) explain that the variation in slope of CTE vs. Temperature curves can be a measure of variation in texture parameters in the corresponding directions of the pressure tube.

#### 7.4.2 Effect of 'Fe' content on CTE and texture of Zr-2.5%Nb pressure tube alloy

The results presented in Figs. 7.11 (a-d) indicate that, 'Fe' in Zr-2.5%Nb pressure tube alloy has definite role in influencing both CTE and texture parameters. It is well known that 'Fe' is a  $\beta$ -phase stabilizer and is mainly concentrated in the  $\beta$ -phase [17, 57]. Perovic *et.al* [19] and Hood [20] have indicated that the maximum solubility of 'Fe' in  $\alpha_{Zr}$  phase below monotectoid temperature of Zr-2.5%Nb alloy is only 0.02wt%, whereas in  $\beta_{Zr}$  phase it is between 0.2 wt% and 0.5wt% [19, 20]. Hence, all the 'Fe' in the alloy is expected to be partitioned mainly between  $\alpha$  and  $\beta$  phases limiting maximum up to the terminal solubility (TSS) at the test temperatures. Upon increasing the 'Fe' content in the alloy, its concentration both in  $\alpha_{Zr}$  and  $\beta_{Zr}$  phases are expected to increase. Further, it is to be noted here that, 'Zr' belongs to group of IVB elements of the periodic table which characterises  $\alpha_{Zr}$  to be an 'open' metal, due to its unusually larger ratio of ionic to atomic radii as compared with other 'normal' *hcp* metals such as 'Mg', 'Zn' and 'Cd' in the same group.

Thus, in open metals, the elements with smaller atomic radii such as 'Fe', which normally occupy substitutional sites, are able to dissolve interstitially because of larger size difference [20, 58- 59]. Hood [20] has shown that 'Fe' has slightly bigger atomic diameter than the spherical octahedral site of the  $\alpha_{Zr}$  lattice [20]. Hence, in Zr-2.5%Nb alloy, 'Fe' forms interstitial solid solution with the  $\alpha_{Zr}$  lattice [20], while in  $\beta_{Zr}$  (*bcc* structure) 'Fe' is expected to form substitutional solid solution.

Theoretically, the presence of any alloying element in the lattice of a host material either in substitutions or in interstitials is expected to cause dilatation in the parent lattice and hence can influence the thermal expansion characteristics [60]. The extent to which the CTE is influenced depends on the extent and nature of interaction of alloying additions with the host lattice [60]. However, this cannot conclusively explain the opposing trends observed in axial and circumferential CTE and texture parameters with the increase in 'Fe' content of the alloy (Figs. 7.11 (a-d)).

These observed trends in (Fig. 7.11 (a-d)) may be related to the mechanical behavior of the alloy during thermomechanical treatments, similar to the one observed in the case of  $\alpha$ -Ti (*hcp*) alloys

[61], because,  $\alpha_{Zr}$  (*hcp*) also has similar crystallographic characteristics as  $\alpha$ -Ti. It has been shown in  $\alpha$ -Ti alloys that, addition of Al (*substitutional*) reduced the stacking fault energies [61], thereby enhancing twinning ability of the alloy. Similarly, Wang *et.al* [62, 63] study has also reported the influence of impurities on twinning behavior of ‘Mg’ alloys (*hcp*). According to these authors [61- 63], the stacking fault energy,  $\gamma_{sf}$  is an important property that dictates the deformation mechanisms in the *hcp* alloys. Wang *et.al* [62, 63] found that, alloying was an efficient way to improve the ductility of ‘Mg’ alloys. Alloying provided additional deformation modes, such as non-basal slip in ‘Mg’ and mechanical twinning through reduction in stacking fault energies  $\gamma_{sf}$  [62, 63]. It is well understood from the extensive study on deformation texture by Tenckhoff [64] that, twinning invariably results in considerable texture modifications in the Zr-2.5%Nb alloy. In the case of Zr-2.5%Nb alloy, one of the most prevalent twinning systems in  $\alpha_{Zr}$  (*hcp*) is  $\{10\bar{1}2\} \langle 10\bar{1}1 \rangle$  which is known as tensile twin [37, 64, 65]. Activation of such twinning systems or other favorable twinning systems through addition of alloying elements may result in considerable reorientation of basal poles (*rotation by 85.2 degrees*) during thermomechanical treatments leading to modification in texture [64].

Presently there are no reported literature on the effect of ‘Fe’ content on the stacking fault energies of  $\alpha_{Zr}$  lattice and its consequent effect on twinning behaviour and texture modifications. Therefore, it is assumed here that, interstitial ‘Fe’ might be playing a role in reducing the stacking fault energies of the dominant  $\alpha_{Zr}$  lattice and might be promoting the twinning activity on some twinning systems of the alloy during thermomechanical treatments similar to the one observed in the case of  $\alpha$ -Ti alloys. Thus, increased interstitial ‘Fe’ in the  $\alpha_{Zr}$  lattice might be increasing the twinning activity during thermomechanical treatments, leading to increased reorientation of basal poles [37, 64, 65]. Such reorientation might be causing axial component  $f_a$  to increase, as a consequence the circumferential component  $f_t$  might decrease with the increase in ‘Fe’ content as seen in Figs. 7.11 (c-d) because  $f_a + f_r + f_t = 1$  [47]. The linear correlation presented in Fig. 7.11 (e) and the overall results in Figs. 7.11 (a-d) together show a good interrelationship between CTE, texture parameters  $f_a$  and  $f_t$  and ‘Fe’ content in the alloy.

### 7.4.3 Correlation of ‘O’ content with CTE and texture of Zr-2.5%Nb alloy

Oxygen is known to be a  $\alpha$ -phase stabiliser in the Zr-Nb system and is mainly concentrated in the octahedral interstitials of the  $\alpha_{Zr}$  (*hcp*) lattice [66]. The presence of ‘O’ in the  $\alpha_{Zr}$  can cause lattice dilation, and hence can influence the thermal expansion behavior of the given alloy [60]. The previous study by Conrad [67] on the lattice parameters of  $\alpha$ -Ti (*hcp*) has shown that the presence of ‘O’ in the  $\alpha$ -Ti lattice would produce a volume dilation of  $\sim 0.13 \text{ \AA}^3$ /per at% of oxygen through an increase in lattice parameters  $a_o$  and  $c_o$ . It is known that such lattice dilation should influence the CTE along crystallographic directions of the alloy. In the present study, the analysis of axial and circumferential CTE data as a function of ‘O’ content in the Zr-2.5%Nb alloy samples did not reveal any systematic trend as seen in (Fig.7.12 (a-b)) which is unlike the observed effect of ‘Fe’ content variation. However, it was observed that, the axial CTE values of these samples when correlated with their ‘Fe’ contents, although it varied in much smaller range of  $322 \pm 16$  ppmw, exhibited a weaker but reasonably better correlation as seen in Fig. 7.12 (d). This finding indicates that, although ‘O’ content varied in a wider range, its effect on the CTE was suppressed, possibly by much stronger influence of ‘Fe’ and other impurities.

Similarly, the plot of texture parameter  $f_a$  as a function of oxygen content as seen in Fig. 7.12 (c) also showed considerable scatter as compared with much stronger effect of ‘Fe’ content variation as seen in Fig. 7.11 (c). This observed scatter of  $f_a$  values as a function of ‘O’ content may also be explained in relation with twinning behaviour of the alloy similar to the case of effect of ‘Fe’ as discussed in the previous section. It has been reported that, increasing addition of ‘O’ to  $\alpha$ -Ti alloy suppressed the twinning ability of the alloy [37, 58]. This is because ‘O’ in the interstitials restricts the sites for shuffling of atoms that is necessary for twinning to occur [37]. On the basis of this observation it can be argued here that, in the case of  $\alpha_{Zr}$  as well which has similar crystallographic characteristics, the interstitial ‘O’ might be suppressing the twinning ability and therefore might be restricting the texture modification during thermomechanical treatments. Hence, the observed scatter in the  $f_a$  values as a function of ‘O’ content in Fig. 7.12 (c) can be reasonably attributed to the decreasing twinning ability of the  $\alpha_{Zr}$ .

#### 7.4.4 Correlation of CTE and texture parameters

The texture parameters  $f_a$  and  $f_t$  values and the corresponding CTE values in the Fig.7.13 and also in Fig. 7.11 (e) (for Fe variation set of samples) have exhibited a good linear correlation for the Zr-2.5%Nb pressure tube samples. Although Zr-2.5%Nb pressure tube is a dual phase alloy with predominantly  $\alpha_{Zr}$  and with relatively smaller fraction of  $\beta_{Zr}$  phase [4, 16, 40] the linear correlation obtained in Fig.7.13 and Fig. 7.11 (e) corroborate with the previously work on  $\alpha_{Zr}$  phase of Zircaloy-4 reported by Kear's [47]. The observed linear correlation of  $f_{\text{values}}$  from the two directions with the corresponding CTE values in Fig.7.13 and Fig. 7.11 (e) can be attributed to the systematic change in effective fraction of basal poles of the  $\alpha_{Zr}$  phase in these directions of the pressure tube [16, 47, 53]. Relatively higher scatter observed in the axial direction  $f_{\text{values}}$  (i.e.  $f_a$  values) vs. CTE plot in Fig.7.13 can be attributed to the influence of small variations in manufacturing parameters that generally exist and also errors associated with texture parameter measurement. The liner expression in Fig.7.13 with a regression coefficient of  $R^2 = 0.94$  is an important result in this work, as it can be used for evaluation of texture parameters,  $f_a$  and  $f_t$  values, if the CTE values in the respective directions are known with reasonably good accuracy. According to Kear's [47], on substituting  $f=1$  in the liner relationship of  $f_{\text{values}}$  vs. CTE (see Fig.7.11 (e) and Fig.7.13) the CTE value must correspond to the c-axis of the single crystal of  $\alpha_{Zr}$ . It was observed that the CTE values of  $10.29 \times 10^{-6}/^\circ\text{C}$  and  $10.02 \times 10^{-6}/^\circ\text{C}$  were obtained on substituting  $f=1$  in the linear relationships presented in (see Fig.7.11 (e) and Fig.7.13). These results are in very good agreement with the CTE value for the c-axis of the  $\alpha_{Zr}$  phase reported by Tomé *et.al* [55]. Thus, these results validate the accuracy of CTE measurement and also the linear relationship of  $f_{\text{values}}$  vs. CTE established in the present study.

#### 7.4.5 Inter-correlation of in-reactor axial creep rate, CTE, texture parameters, 'Fe' and 'O' contents in the alloy

The in-reactor axial creep rate ( $\dot{\epsilon}_i$ ) data for the pressure tubes presented in this study is normalised with peak fluence of the respective channels after 3340 Effective Full Power Days (EFPDs) of operation [14]. It is well known that the values of  $\dot{\epsilon}_i$  represent the combined effect of irradiation creep, irradiation growth and thermal creep [4, 68]. Generally, under normal operating

conditions the contribution of irradiation creep is about 70% of the total deformation, while irradiation growth and thermal creep contribute to about 20% and 10%, respectively [4, 68]. Since the operating conditions of all these channels were similar the effect of thermal creep to the total deformation has been considered similar and also negligible. Therefore, in the following the variation in in-reactor axial creep rates being discussed in the present context of inter-correlation study has been considered to involve mainly irradiation creep and irradiation growth. The effect of 'Fe' content on the axial direction irradiation creep rate ( $\dot{\epsilon}_i$ ) of the pressure tubes is shown in the plot of  $\dot{\epsilon}_i$  vs. 'Fe' content in Fig. 7.15 (a). The plot shows a clear decreasing trend of  $\dot{\epsilon}_i$  with the increase in 'Fe' content of the pressure tubes. This result is similar to the previous post irradiation observations on the reactor operated pressure tubes reported by Holt [1]. It is to be noted here that, the plot of  $\dot{\epsilon}_i$  vs. axial CTE also exhibited a good correlation with a decreasing trend (see Fig. 7.15 (b)), while  $\dot{\epsilon}_i$  vs. circumferential CTE exhibited increasing trend as seen in Figs. 7.15 (c). Since,  $f_{\text{values}}$  and CTE correlated linearly in Fig. 7.11 (e), for the 'Fe' variation set of samples, it implies from Fig. 7.15 (b) and (c) that  $\dot{\epsilon}_i$  actually exhibit decreasing trend with  $f_a$  values and increasing trend that with  $f_t$  values. The increasing trend of  $\dot{\epsilon}_i$  with circumferential CTE in Fig. 7.15 (c) is the consequence of increase in  $f_a$  causing corresponding decrease in  $f_t$  values as seen in Fig. 7.11 (d), because  $f_a + f_r + f_t = 1$  [47].

In the previous studies, Roy *et.al* [69] and Holt [1] have indicated that, the direction which shrinks during irradiation corresponds to the direction of highest thermal expansion coefficient i.e. along basal pole direction. Thus, higher values of CTE in Fig.7.15 (b) or the higher  $f_a$  values as seen in Fig.7.11 (c) correspond to higher concentration of basal poles in the axial direction, which might be responsible for some degree of shrinkage along the tube axis [4]. Thus, this phenomenon may result in some degree of decrease in the axial creep rate which accounts for the irradiation induced growth part [4, 68]. Although, the phenomenon by which 'Fe' content in the  $\alpha_{Zr}$  lattice of the alloy can influence the remaining part of irradiation induced deformation is not well established, the authors wish to describe probable mechanisms based on the reported post irradiation observations. Holt [1] proposed that, if 'Fe' concentration is more than the solubility limit in the alloy it may result in fine 'Fe' bearing precipitates. Such precipitates might provide sites for recombination of vacancies and self interstitials produced during neutron irradiation and

thus can retard the damage rate and consequently deformation rate. The authors Zou *et.al* [23] in their SIMS study on the Zr-2.5%Nb alloy material, found excess ‘Fe’ in the  $\alpha_{Zr}$  matrix, more than the Terminal Solid Solubility (TSS) limit, which they explained that, it could be due to some ‘Fe’ bearing complexes formed locally. These ‘Fe’ bearing complexes within the  $\alpha_{Zr}$  phase and also the  $Zr_3Fe$  precipitates that may be formed at the grain boundaries due to diffusion of ‘Fe’ to the grain boundaries might serve as sites for recombination of both types of irradiation induced defects and hence can retard the damage rate. Zou *et.al* [23], also made a reference of positron annihilation spectroscopic (PAS) measurements by Eldrup *et. al* [24], who proposed that ‘Fe’ in the  $\alpha$ -lattice may control the net vacancy migration in a given direction (*anisotropic*) during irradiation and aid in defect annihilation process and hence retard defect aided deformation process. Thus the observed decreasing trend in in-reactor axial creep rates ( $\dot{\epsilon}_i$ ) (Fig. 7.15 (a)), can be attributed to the combined effect of decrease in effective damage rate caused by recombination of defects at the ‘Fe’ bearing sites as well as due to the increase in  $f_a$  values (see Fig. 7.11 (c)) as the ‘Fe’ content increased.

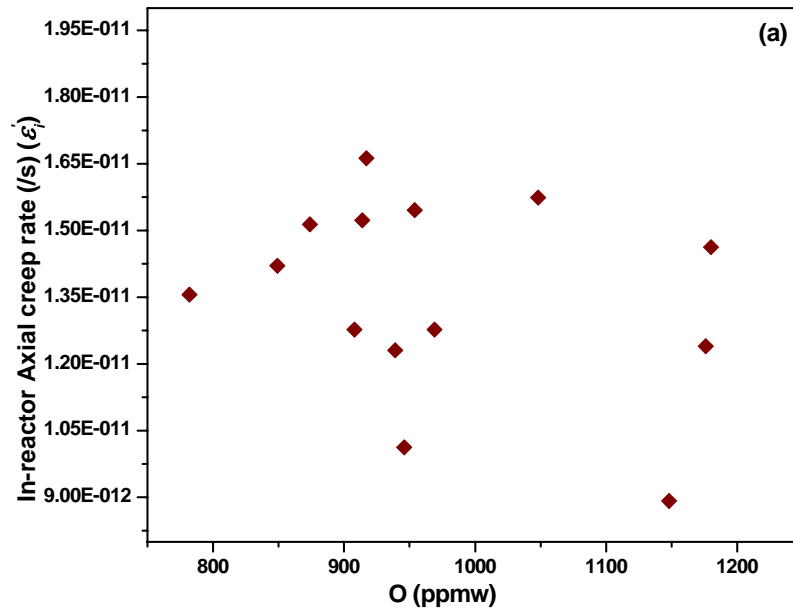


Fig. 7.16 (a) Effect of oxygen on ( $\dot{\epsilon}_i$ ) of Zr-2.5%Nb pressure tubes

Good correlations of  $\dot{\epsilon}_i$  with the axial and circumferential CTE in Fig. 7.15 (b-c) indicate that CTE can provide a good measure of in-reactor axial creep behavior as much as by texture parameters. Thus, the results in Fig. 7.11 (a-e), Fig.7.15 (a-c) describe the significant effect of

'Fe' content on CTE, texture parameters and  $\dot{\epsilon}_i$ . Thus, this part of the work has established that CTE is sensitive to 'Fe' content when varied independently (*within the specification range*) in the Zr-2.5%Nb pressure tube alloy.

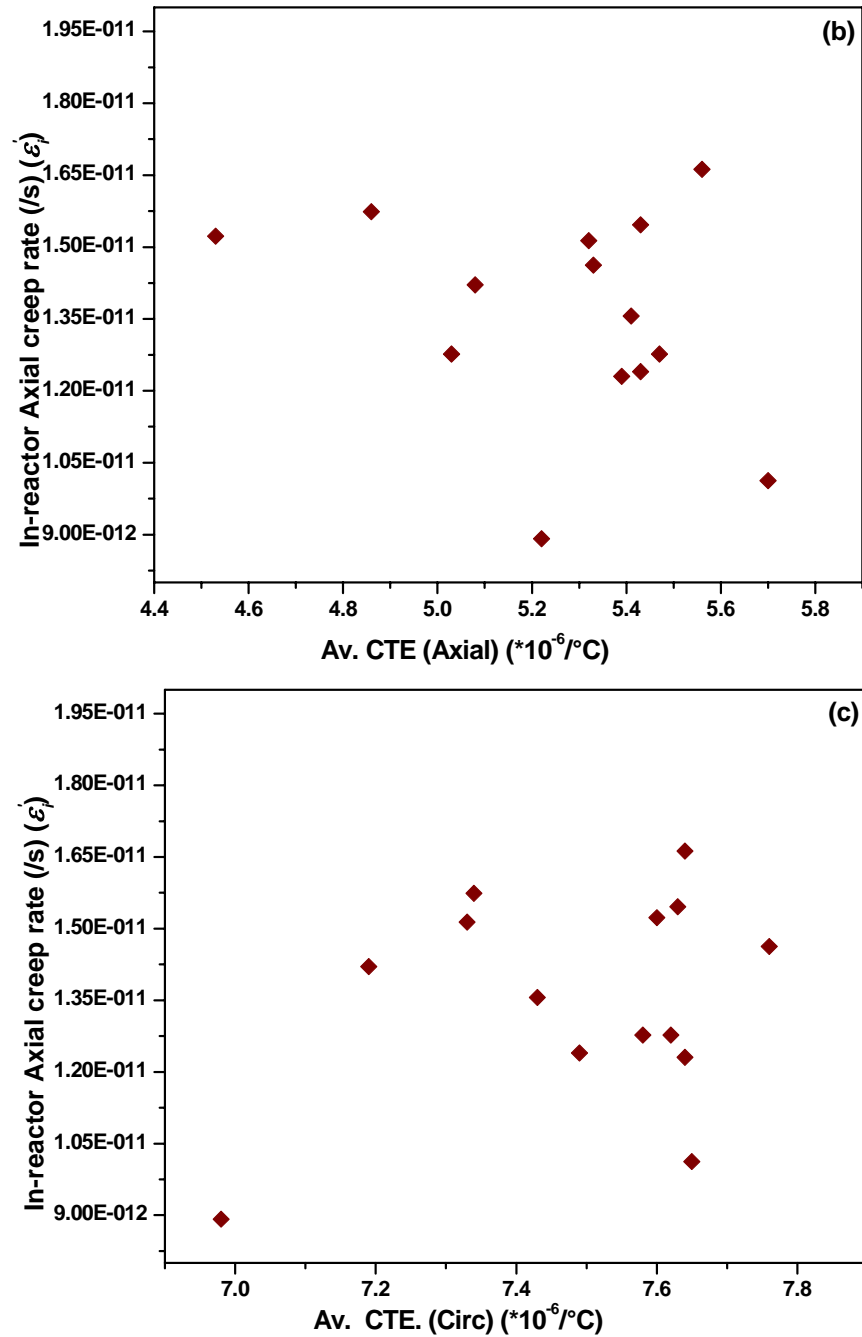


Fig. 7.16 (b) Correlation of ( $\dot{\epsilon}_i$ ) with axial direction CTE (c) with circumferential direction

The correlation of  $\dot{\epsilon}_i$  with oxygen content in Fig. 7.16 (a), and CTE in Fig. 7.16 (b-c) also exhibited no definite trend. This indicated that oxygen content variation within the specification range has lesser role to play in influencing the irradiation creep behavior as compared to contrasting effect of 'Fe' content variation in the alloy. The observed scatter can be attributed to relatively stronger effect of other alloying elements and impurities. The correlations established in this work between CTE, texture parameters, irradiation creep rates and 'Fe' content in the alloy can be useful in modeling and prediction of in-reactor behaviour of the pressure tubes. Further, this work has also established that the CTE measured in a given direction can provide a good measure of the irradiation behaviour of the pressure tube through the inter-correlations established in this study.

## 7.5 Summary of the work

1. The effect of independent variation in minor alloying elements 'Fe' and 'O' within the specification range on the  $(\alpha+\beta)/\beta$ -transus temperature was studied using dilatometry technique. The empirical relationships for the  $(\alpha+\beta)/\beta$ -transus temperature as a function of 'O' content and also as a function of 'Fe' content in the alloy have been established. The slopes of the linear relations indicated that the  $(\alpha+\beta)/\beta$ -transus temperature increased by  $\sim 14^\circ\text{C}/100$  ppmw of oxygen and decreased by  $\sim 4^\circ\text{C}/100$  ppmw of iron in the Zr-2.5%Nb alloy.
2. Effect of independent variation of 'Fe' and 'O' contents within the specification range on the thermal creep behavior of Zr-2.5%Nb alloy has been studied using impression and indentation techniques. Increasing 'Fe' content in the alloy showed decreasing trend in impression creep rates at the test temperature  $400^\circ\text{C}$  which can be attributed mainly to the solute strengthening effect. The in-reactor axial creep rates for the corresponding operating channels also showed similar behavior for the reactor operating temperature of  $300^\circ\text{C}$ . This may be attributed to 'Fe' in solid solution might be influencing diffusion of vacancies and as a precipitate it might be facilitating recombination of irradiation induced defects.
3. The room temperature Vicker's hardness of the Zr-2.5%Nb alloy samples showed a good correlation with increasing trend with increasing oxygen content (*within the specification*

range). The dwell time dependent micro-hardness data for all the three samples showed a linear decrease in  $\ln(H)$  vs.  $\ln(t)$  plots at both the test temperatures 300 and 400°C. A distinct increase in hardness values with the increase in oxygen content (up to 1587 ppmw) at both the test temperatures and at any given dwell time studied indicated a clear strong influence of oxygen on the high temperature deformation behavior. This can be attributed to solute strengthening effect. The study has established that both iron and oxygen content decrease the thermal creep rates of the Zr-2.5%Nb pressure tube alloy similar to the one observed in irradiation creep rates.

4. The effect of 'Fe' and 'O' on the CTE and texture of the anisotropic Zr-2.5%Nb pressure tube samples have been studied using dilatometry and XRD respectively. The axial and circumferential CTE values exhibited opposing trends with the increasing 'Fe' content in the alloy. Increase in 'Fe' content in the alloy showed increasing trend in  $f_a$  values with a corresponding decrease in the  $f_t$  values. The observed trends in texture parameters may be attributed to increased twinning ability due to increase in 'Fe' content in the  $\alpha_{Zr}$  phase during thermomechanical treatments.
5. The inter-correlation between CTE, texture parameters, the variation in 'Fe' content and the in-reactor deformation behavior has provided the base for prediction of performance of the pressure tubes during their service.

## References Chapter-7

1. R.A. Holt, *J. Nucl. Mater.*, 372 (2008) 182-214
2. V. Fidleris, *J. Nucl. Mater.*, 54(1974) 199-211
3. R. Jerlerud Pe´rez, A.R. Massih, *J. Nucl. Mater.*, 360 (2007) 242-254
4. W. Li, PhD Thesis, “*Effect of Texture on Anisotropic Thermal Creep of Pressurised Zr-2.5Nb Tubes*” *Queen’s University Kingston, Ontario, Canada August, 2009*
5. Y. Jinyuan, PhD Thesis, “*Crystallographic Texture and Creep Anisotropy in Cold Worked and Recrystallised Zirlo*”, *Department of Nuclear Engineering North Carolina State University Raleigh, NC 27695-7909 March, 2005*
6. B. W. Marple, Thesis for Degree of Master of Science in Nuclear Engineering, “*Creep Rupture Study of Annealed Zircaloy 4, Stress and Temperature Effects*”, *North Carolina State University, Raleigh, December, 2005*
7. D.H. Sastry, *Mater. Sci. Eng., A*, 409 (2005) 67-75
8. T.R.G. Kutty, C. Ganguly, *J. Nucl. Mater.*, 182 (1991) 258-260
9. T.H. Hyde, W. Sun, *International J. Pressure Vessels and Piping*, 86 (2009) 757-763
10. T.R.G. Kutty, C.B. Basak, A. Kumar, H.S. Kamath, *J. Nucl. Mater.*, 408 (2011) 90-95
11. K. Ghoshal, T.R.G. Kutty, S. Mishra, A. Kumar, *J. Nucl. Mater.*, 432 (2013) 20-22
12. R.S. Sundar, T.R.G. Kutty, D.H. Sastry, *Intermetallics*, 8 (2000) 427-437
13. F. Yang, J.C.M. Li, *Mat. Sci. Eng. A201* (1995) 50–57
14. Axial elongation data of operating Zr-2.5%Nb pressure tubes obtained from NPCIL through internal communication.
15. Y.H. Jeong, S.Y. Park, M.H. Lee, B.K. Choi, J.H. Baek, J.Y. Park, J.H. Kim, H.G. Kim, *J.*
16. S. Cai, PhD Thesis, “*Evolution of Interphase and Intergranular Strain in Zr-Nb alloys During Deformation at room Temperature*”, *Oct 2008, Dept. of Mechanical and Materials Eng. University Kingston Canada, Publication Ref, ISBN, 0494443162, 9780494443163*
17. H.G. Kim, Y.H. Kim, B.K. Choi, Y.H. Jeong, *J. Nucl. Mater.*, 359 (2006) 268-273
18. V. C. Marcotte, W. L. Larsen, I. E. Williams, *J. Less Common Metals*, 7 (1964) 373-382
19. A. Perovic, V. Perovic, G.C. Weatherly, G.R. Purdy, R.G. Fleck, *J. Nucl. Mater.*, 199 (1993) 102-111

20. G.M. Hood, *J. Nucl. Mater.*, 159 (1988) 149-175
21. Smithells, Metals Reference book, Edited by W.S. Gale, T.C. Totemeir, Elsevier Butterworth-Heinemann, USA and *ASM International 10* (2004) 299
22. K. L. Murty, J. Ravi, Wiratmo, *Nucl. Eng. Des.*, 156 (1995) 359- 371
23. H. Zou, G.M. Hood, J.A. Roy, R.H. Packwood, V. Weatherall, *J. Nucl. Mater.*, 208 (1994) 159-165
24. M. Eldrup, G.M. Hood, R.J. Schultz, N.J. Pedersen, *Mater. Sci. Forum 10.5-110* (1992) 997
25. R. Tewari, G.K. Dey, T.R.G. Kutty, A.K. Sengupta, N. Prabhu, S. Banerjee, *Metall. Mater. Trans. A*, 35A (2004) 205-216
26. E.R. Petty, *Acta Metall.*, 65 (1962) 25-26
27. A.G. Atkins, A. Silverio, D. Tabor, *J. Inst. Met.* 94 (1966) 369–378
28. H.D. Merchant, G.S. Murty, S.N. Bahadur, L.T. Dwivedi, Y. Mehrotra, *J. Mater. Sci.* 8 (1973) 437-442
29. T.R.G. Kutty, C. Ganguly, *J. Nucl. Mater.*, 207 (1993) 345-349
30. G. Sharma, R.V. Ramanujan, T.R.G. Kutty, G.P. Tiwari, *Mater. Sci. Eng., A*, 278 (2000) 106-112
31. K.B. Khana, T.R.G. Kutty, M.K. Surappa, *Mater. Sci. Eng., A*, 427 (2006) 76-82
32. D. Setoyama, S. Yamanaka, *J. Alloys Compd.*, 379 (2004) 193-197
33. T.O. Mulhearn, D. Tabor, *J. Inst. Metals*, 89 (1960-1961) 7-12
34. W. Chubb, G.T. Muehlenkamp, G.T. Manning, *Battelle Memorial Institute Report BMI-* (1955) 987
35. R. Roumina, B. Raeisia, R. Mahmudi, *Scripta Mater.*, 51 (2004) 497-502
36. P. M. Kelly, P. D. Smith, *J. Nucl. Mater.*, 46 (1973) 23-34
37. C.J. Cochrane, PhD Thesis “Effect of Process Parameters on Deformation of Zr-2.5wt%Nb Alloy”, Department of Mechanical and Materials Engineering, Queen's University Kingston, Ontario, Canada, October 2013
38. P. Dasgupta, V.S. Arunachalam, *J. Mater. Sci.*, 3, (May 1968) 271-281
39. E.F. Ibrahim, *J. Nucl. Mater.*, 102 (1981) 214-219

40. Bipasha Bose PhD Thesis, 2012, "Assessment of The Kinetics of Local Plastic Deformation of Zr-2.5%Nb CANDU Pressure Tube Material", The School of Graduate and Postdoctoral Studies, The University of Western Ontario, London, Ontario, Canada
41. E.F. Ibrahim, *J. Nucl. Mater.*, 118 (1983) 260-268
42. E.F. Ibrahim, R.A Holt, *J. Nucl. Mater.*, 91 (1980) 311-321
43. M. Griffiths, N. Christodoulou, S.A. Donohue, *J. (ASTM), International, (JAI) Paper ID JAI12432, 2 No. 7 (2005)*
44. IZNA-1 Special Topic Report, Mechanical Properties of Zirconium Alloys, R.B. Adamson, *Advanced Nuclear Technology International*, February 15, 2002
45. A.R. Causey, C.H. Woo, R.A. Holt, *J. Nucl. Mater.*, 159 (1988) 225-236
46. R. A. Holt, N. Christodoulou, and A. R. Causey, *J. Nucl. Mater.*, 317 (2003) 256-260
47. J.J. Kearns, U.S. Atomic Energy Commission Research and Development Report (Contract AT-11-1-GEN-14), WAPD-TM-472, Bettis Atomic Power Laboratory, November 1965.
48. Designation: E228, Standard Test Method for Linear Thermal Expansion of Solid Materials with a Push-Rod Dilatometer, *April 1, 2011. Published April 2011*
49. Sunil Kumar, "Preferred orientation parameters of KAPS-2 Zr-2.5%Nb Pressure Tubes", BARC/2005/E/025
50. W.S. Min, *Science in China (Series A)* 321 No.2, February (1989)
51. S. Sindhu, C.S Menon, *PRAMANA, Indian Academy of Sciences*, 67, No. 3 *Journal of Physics*, September (2006) 535-540
52. K. Harunai, H. Maeta, K. Ohashit, T Koiket, *J. Phys. C, Solid State Phys.* 20 (1987) 5275-5279
53. "Waterside corrosion of zirconium alloys in nuclear power plants" *IAEA-TECDOC-996, January 1998*
54. IAEA-TECDOC-1496, Thermophysical properties data base of materials for light water reactors and heavy water reactors, *Final report of a coordinated research project 1999–2005, June 2006*
55. C.N. Tomé, N. Christodoulou, P. A. Turner, M. A. Miller, C. H. Woo, J. Root, T. M. Holden, *J. Nucl. Mater.*, 227 (1996) 237-250

56. V.V. Kunchenko, N.M. Roenko, “Interrelation between Linear Thermal Expansion and Irradiation Growth rate” (UDC 539.26 : 621.039.548) Translated from *Atomnaya energiya*, 20, No. 2, February (1966) 169-170
57. M. Koppers, C. Herzig, M. Friesel, Y. Mishin, *Acta Mater.*, 45 (1997) 4181
58. R.W. Hayes, G.B. Viswanathan, M.J. Mills, *Acta Mater.*, 50 (2002) 4953-4963
59. H. Mishra, D.V.V. Satyanarayana, T.K. Nandy, P.K. Sagar, *Scripta Mater.*, 59 (2008) 591-594
60. F.C. Hull, S.K. Hwang, J.M. Wells, and R.I. Jaffee, *J. Mater. Eng.*, 9 (1987) 81-92
61. S. Zaefferer, *Mater. Sci. Eng. A*, 344 (2003) 20-30
62. C. Wang, H.Y. Wang, H.Y. Zhang, X. L. Nan, E. S. Xue, Q.C. Jiang, *J. Alloys Compd.* 575 (2013) 423–433
63. C. Wang, H.Y. Zhang, H.Y. Wang G. J. Liu, Q.C. Jiang, *Scripta. Mater.*, 69 (2013) 445-448
64. E. Tenckhoff, *J. (ASTM), International, (JAI) Paper ID, JAI 12945, 2 No.4, April (2005)*
65. K. L. Murty, I. Chari, *Progress in Nuclear Energy*, 48 (2006) 325-359
66. M. Griffiths, J.E. Winegar, A. Buyers, *J. Nucl. Mater.*, 383 (2008) 28-33
67. H. Conrad, *Prog. Mater Sci.*, 26 (1981) 123-403
68. A.R. Causey, R.A. Holt, N. Christodoulou, E.T.C. Ho, *ASTM-STP-1354 (2000) 74-84*
69. P.R. Roy, D.N. Shah, *PRAMANA*, 24, Nos. 1 and 2, January and February (1985) 397-421

## CHAPTER 8: Conclusions

.....

A comprehensive heat treatment study has been carried out from the  $\alpha+\beta$  phase field on the Zr-2.5%Nb pressure tube samples using quenching dilatometry. The microstructural and textural evolution that resulted from such heat treatments was investigated using electron microscopy techniques. The heat treated dilatometry samples were further studied for structure and mechanical property correlations using two miniature specimen testing techniques, the ABI and SPT, after establishing correlations material specific correlations adopting standard recommended procedures. The effects of independent variation in iron and oxygen content on the  $\alpha+\beta$  phase boundary, the physical property such as CTE and mechanical properties such as the thermal creep behavior of the Zr-2.5%Nb pressure tube material have been studied. Following important conclusions could be drawn based on these works;

1. Partial CCT diagram for the Zr-2.5%Nb alloy containing 1137 ppmw oxygen and 650 ppmw of Fe has been determined using quenching dilatometry. It was established that the  $\beta$  transus temperature i.e  $\beta_{Zr} \rightarrow (\alpha+\beta_{Zr})$  regime for the alloy starts below 891°C for all cooling rates.
2. The transformation characteristics of the Zr-2.5% Nb alloy containing 1137 ppmw of oxygen and 650 ppmw of ‘Fe’ was ascertained during quenching from 883, 870, 863 and 840°C ( $\pm 0.5^\circ\text{C}$ ) in the  $\alpha+\beta$  phase field, at different rates using quenching dilatometry and electron microscopy.

The specimens cooled from  $\alpha+\beta_{Zr}$  phase field at rates 25°C/s and slower, showed smooth dilation curve particularly for the case of samples soaked close to  $\beta$ -transus temperature such as 883°C indicating characteristic nucleation and growth type of transformation leading to Widmanstätten type of product. For quenching rates  $>25^\circ\text{C/s}$  multiple steps were observed on the dilatograms for the case of samples soaked at lower temperatures in the  $(\alpha+\beta)$  phase field which may be attributed to successive generation of martensite formation.

3. For a given soaking temperature within  $\alpha+\beta$  region, at cooling rates lower than 25°C/s, predominantly Widmanstätten structure resulted. The morphology of Widmanstätten  $\alpha$  changed from finer and straight lamellae to wider and irregular shape with cooling rate

decreasing from 25°C/s. Mixed structures of finer Widmanstätten  $\alpha$  and martensite were observed at quenching rates 25°C/s. For quenching rates 50°C/s and 100°C/s the microstructure was predominantly martensite along with primary  $\alpha$ .

4. For a given quenching rate the probability of martensite formation increased with decreasing soaking temperatures in the  $\alpha + \beta$  region. This may be attributed to increased 'Nb' content in  $\beta_{Zr}$  providing the driving force at the lower soaking temperatures.
5. The microtextural study on the samples soaked close to  $\beta$  transus boundary within the  $\alpha + \beta$  phase field at 883°C indicated that the texture tended to randomise at higher cooling rates such as 50°C/s and 100°C/s. Whereas, little change was seen at lower cooling rates. The texture randomisation was attributed to low fraction of primary  $\alpha$  and transformation of large number of randomly oriented fine  $\beta$  grains yielding various variants of martensitic ( $\alpha'$ ) plates which had Burgers' orientation relationship given by  $(0001)_{\alpha} // (110)_{\beta}$  and  $[2\bar{1}\bar{1}0]_{\alpha} // [111]_{\beta}$ .
6. Empirical correlations for evaluation of basic mechanical properties  $\sigma_y$  and  $\sigma_{UTS}$  of anisotropic Zr-2.5%Nb alloy have been established for SPT and ABI test techniques as a function of loading direction using recommended procedure. In the case of ABI the difference in yield strength off set constant  $b_m$ , between the two directions of testing namely the axial and circumferential directions of the pressure tube, indicated intrinsic difference in yield behavior attributing to effect of texture in the alloy.
7. The strength values obtained using tensile and ABI were higher for circumferential compared to axial direction, whereas the strength representing values  $(P_y/t_0^2)$  and  $(P_m/t_0^2)$  by SPT showed opposite effect for the same sample conditions. This contradiction has been rationalised on the basis of biaxial deformation of the disc specimen experiencing orientation effects.
8. The  $\sigma_Y$  and  $\sigma_{UTS}$  values by SPT, ABI and conventional tensile tests showed increasing trend with the increase in cooling rates for both directions tests, which can be attributed to finer

morphology of Widmanstätten  $\alpha$  and  $\beta$  phases and also predominantly martensitic structure obtained at cooling rates greater than  $50^{\circ}\text{C/s}$ .

9. Comparison of ABI and SPT derived  $\sigma_y$  and  $\sigma_{UTS}$  data and the corresponding tensile data for both direction tests showed a good agreement indicating proper empirical correlation parameters have been arrived at for evaluation of mechanical properties of the alloy. The overall study indicated that ABI and SPT techniques are sensitive to the changes in mechanical properties due to microstructure and texture effects in the alloy. Thus these techniques can be adopted for mechanical property characterisation of anisotropic Zr-2.5%Nb alloy materials using direction specific correlation parameters.
10. The specimens of Zr-2.5%Nb alloy samples heat treated from the  $\alpha+\beta$  phase field using dilatometry were characterised for basic mechanical properties  $\sigma_y$  and  $\sigma_{UTS}$  using SPT and ABI tests. In the case of SPT derived mechanical properties, higher strength values obtained at lower soaking temperatures for a given cooling rate can be related to both solute-strengthening effect by 'Nb' enriched  $\beta$  phase and increased effectiveness of the crystal interfaces to the deformation fronts due to finer structures. This study has indicated that SPT was more effective in capturing the changes in mechanical properties due to difference in microstructures as compared to ABI.
11. The effect independent variation of minor alloying elements 'Fe' and 'O' contents within the pressure tube specification range on the  $(\alpha+\beta)/\beta$ -transus temperature was studied using dilatometry technique. The empirical relationships for the  $(\alpha+\beta)/\beta$ -transus temperature as a function of 'O' content and also as a function of 'Fe' content in the alloy have been established. The (+ve) slope of the linear relationship of  $T_{\beta}$  vs. 'O' content indicated that the  $(\alpha+\beta)/\beta$ -transus temperature increased by  $\sim 14^{\circ}\text{C}/100$  ppmw. Whereas the (-ve) slope of linear relationship of  $T_{\beta}$  vs. 'Fe' content indicated that the  $(\alpha+\beta)/\beta$ -transus temperature decreased by  $\sim 4^{\circ}\text{C}/100$  ppmw of Fe in the Zr-2.5%Nb alloy.
12. Effect of independent variation of 'Fe' and 'O' contents within the specification range on the thermal creep behavior of Zr-2.5%Nb alloy were studied using impression and indentation techniques. Increasing the 'Fe' content in the alloy showed decreasing trend in

impression creep rates at the test temperature 400°C, which can be attributed mainly to the solute strengthening effect. The in-reactor axial creep rates for the corresponding operating channels also showed similar behavior for the reactor operating temperature of 300°C. This may be attributed to 'Fe' in solid solution might be influencing diffusion of vacancies. Further if 'Fe' is present in the form of precipitates, it may facilitate recombination of both kinds of irradiation induced defects.

13. The room temperature Vicker's hardness of the Zr-2.5%Nb alloy samples showed a good correlation with increasing trend with increasing oxygen content (*within the specification range*). The dwell time dependent micro-hardness data for three of these samples showed a linear decrease in  $\ln(H)$  vs.  $\ln(t)$  plots at both the test temperatures 300 and 400°C. A distinct higher hardness values at higher oxygen content at both the test temperatures and at all dwell times studied indicated a clear strong influence of oxygen content on the high temperature deformation behavior. This can be attributed to strong solute strengthening effect. The thermal creep study has established that both 'Fe' and 'O' contents decrease the thermal creep rates of the Zr-2.5%Nb pressure tube alloy.
14. The effect of 'Fe' and 'O' on the CTE and texture of the anisotropic Zr-2.5%Nb pressure tube samples were studied using dilatometry and XRD respectively. The axial and circumferential CTE values exhibited opposing trends with the increasing 'Fe' content in the alloy. Increase in 'Fe' content in the alloy showed increasing trend in  $f_a$  values with a corresponding decrease in the  $f_t$  values. The observed trends in texture parameters can be attributed to increased twinning ability due to increase in 'Fe' content in the  $\alpha_{Zr}$  phase during thermomechanical treatments.
15. The inter-correlation between CTE, texture parameters, 'Fe' content in the alloy and the in-reactor deformation behavior has provided the valuable input for modeling and also base for prediction of performance of the pressure tubes during their service.
16. Unlike the case of effect of 'Fe' content on CTE and texture, the effect of 'O' content on CTE and texture was insignificant. This may be attributed to increased oxygen content might be increasingly suppressing the twinning ability of  $\alpha_{Zr}$  phase of the alloy during thermomechanical treatments similar to the one observed in  $\alpha$ -Ti alloys.

## **FUTURE WORK**

1. Irradiation creep and thermal creep study of the Zr-2.5%Nb alloy pressure tube material with different microstructure.
2. Bulk mechanical properties of Zr-2.5%Nb pressure tube alloy with various microstructures obtained from different heat treatment conditions.
3. Development of complete CCT diagram for the Zr-2.5%Nb alloy with varying compositions of oxygen and iron contents.